UNIVERSITY OF CALIFORNIA
RIVERSIDE

Alkane Conversion on Heterogeneous Catalysts from First Principles and Descriptors

A Dissertation submitted in partial satisfaction
of the requirements for the degree of

Doctor of Philosophy

in

Chemistry

by

Victor Fung

June 2019

Dissertation Committee:
Dr. De-en Jiang, Chairperson
Dr. Gregory Beran
Dr. Francisco Zaera

The Dissertation of Victor Fung is approved.

_____

_____

_____

Committee Chairperson

University of California, Riverside

COPYRIGHT ACKNOWLEDGEMENT

ACKNOWLEDGEMENTS

First and foremost, this work would not have been possible without the guidance and mentorship of my PhD advisor Dr. De-en Jiang. I especially grateful for his continual support and pivotal role in my research and career throughout my PhD.

I would also like to acknowledge my dissertation committee members Dr. Gregory Beran and Dr. Francisco Zaera and oral qualifying exam committee members Dr. Matthew Conley and Dr. Phillip Christopher for the helpful comments and suggestions.

I thank Dr. Zili Wu for the fruitful collaborations and for his mentorship during my six-month internship at Oak Ridge National Laboratory. I also thank Dr. Franklin Tao, Dr. Jianping Xie, Dr. Peng Zhang and Dr. Felipe Polo-Garzon for productive collaborations and valuable learning experiences in the various research areas.

Finally, I would like to thank Dr. Guoxiang Hu, Dr. Runhong Huang, Dr. Cheng Zhan and all my lab mates for the enjoyable and friendly discussions over the years.

This work was supported by UCR Dean's Distinguished Fellowship, UCR Dissertation Year Program, the U.S. Department of Energy Office of Science Graduate Student Research program and funding from the Office of Basic Energy Sciences, Chemical Sciences, Geosciences, and Biosciences Division. This research used computing resources of the National Energy Research Scientific Computing Center, a DOE Office of Science User Facility.

DEDICATION

This thesis is dedicated to my parents, Mike Lai-wo Fung and Pingnan Li

ABSTRACT OF THE DISSERTATION

Alkane Conversion on Heterogeneous Catalysts from First Principles and Descriptors

by

Victor Fung

Doctor of Philosophy, Graduate Program in Chemistry
University of California, Riverside, June 2019
Dr. De-en Jiang, Chairperson

The selective conversion of alkanes to high value products remains a monumental catalytic challenge. Significant gaps in our knowledge remain regarding the mechanistic details of alkane activation and the chemical nature of the catalytically active sites for this class of reactions. In this thesis, systematic and thorough first principles studies of alkane activation on several major classes of promising materials, ranging from metal oxide surfaces to metal clusters and single metal atom sites, have provided us with the insight to tackle these open questions. To further expand these findings towards a comprehensive search of catalytically active materials, we developed chemical and catalytic descriptors which can predict these properties at a fraction of the computational cost. We find on oxide surfaces, the homolytic C-H activation pathway is favored, and correlated with the reducibility of the lattice oxygen. We identify hydrogen adsorption energy and vacancy

formation as strongly correlated energetic descriptors for C-H activation energy and CH_3 adsorption energy, which we use to predict catalytic properties of doped Co_3O_4 and compositionally diverse perovskite surfaces. To provide a structure-activity link between the oxygen and alkane activation, we developed a generally applicable coordination number descriptor, 'ACN,' which can quickly predict C-H activation barriers on various oxides. Furthermore, we identify a bulk descriptor, the metal-oxygen crystal orbital Hamilton population, which is correlated to the adsorption energy of radical adsorbates such as hydrogen and methyl. Meanwhile on metal clusters, structural fluxionality plays a pivotal role in catalytic performance. In the model system of $Pt_{10\text{-}13}$, we utilize various structural features to identify Pt_{10} as a magic number cluster with low fluxionality which can explain its experimental inertness to alkanes. On single atoms, we demonstrate how heterolytic C-H cleavage pathway can be tuned through the metal d-orbital occupation and the substrate electronic band gap. These findings have allowed us to identify promising single atom catalysts with the elusive low-temperature methane activation ability. The work in this thesis aims to provide valuable descriptors and design principles for alkane activation and theoretical predictions of promising catalysts.

TABLE OF CONTENTS

List of Tables

List of Figures

1 Introduction

1.1 Heterogeneous catalysis

Catalysis, derived from the Greek word καταλεινν, was first coined by Berzelius in 1835 in which he described it as the "the property of exercising on other bodies an action which is very different from chemical affinity. By means of this action, they produce decomposition in bodies, and form new compounds into the composition of which they remain apart." (Berzelius 1836) This idea of 'catalytic power' attributes certain substances as having the ability to "to awaken affinities, which are asleep at a particular temperature."[1] Prior to this definition, the concept chemical reactions occurring only when in contact with a specific substance had been proposed by Mitscherlich, known as 'contact theory' or 'contact action.'[2] However, catalysis as a phenomenon had already been thoroughly utilized for many millennia, though had not yet been characterized as such. The earliest catalytic processes used by humanity were biological in nature, from the enzymatic production of alcoholic beverages with yeast, to other foodstuffs such as bread, vinegar and cheese. The first intentional use of inorganic catalysts could possibly be traced back to the 16th century with the sulfuric acid catalyzed conversion of alcohol to ether by Valerius Cordus.[3-4] Half a century after Berzelius, Ostwald argued "catalysis is the acceleration of a chemical reaction… which occurs without alteration of the general energy relations."[5] In our modern definition of catalysis, it is the process of increasing the rate of a reaction via a catalyst by providing an alternative reaction pathway with a lower activation energy without changing the thermodynamics of the reaction. Catalysts can be

homogeneous or heterogeneous, in which they are either in the same or different phase as the reactant molecules, respectively.

Today, up to 90% of industrial chemical processes use heterogeneous catalysis[6] with an estimated global market share of 20 billion USD. One of the prime advantages of heterogeneous catalysts is the easy separation of the gaseous or liquid products from the solid catalyst and the higher stability of the catalysts at elevated temperatures and under harsh reaction conditions. Studies in heterogeneous catalysts has yielded several Nobel prizes, for Haber in 1918, Bosch in 1931, Langmuir in 1932, and Ertl in 2007. One of the most prominent examples of these is the catalytic nitrogen fixation process, commonly known as the Haber-Bosch process for its primary inventors. Early breakthroughs were made by the first realization by Haber and Nernst over the need for high pressures based on the Le Chatelier principle in 1903, followed by small-scale production several years later.[7] Following further improvements beyond Os based catalysts and overcoming engineering challenges of high pressure reactors by Mittasch and Bosch respectively, this process eventually replaced the more inefficient Birkeland–Eyde and the Franck-Caro cyanamide processes to become the predominant method to fix nitrogen. The importance of this catalytic process cannot be overstated: two-fifths to one-half of the world's population exists today due to the Haber-Bosch process due to its role as a "detonator of population explosion" by providing a source of synthetic fertilizer.[8-9] Today, hydrogen from coal gasification or natural gas steam reforming and nitrogen distilled from the air are reacted at temperatures of 700-800K and pressures of 100-250 atm over primarily Fe promoted catalysts.

However, the specific mechanism and understanding of the catalytic process was only accomplished nearly a century later in large part from studies by Ertl and coworkers.[10] Much of these insights were made possible through advancements in surface chemistry. In particular, the development of ultra-high-vacuum conditions made it possible to study clean catalytic surfaces without contamination coupled with characterization by low-energy electron diffraction, Auger electron spectroscopy and field emission and field ion microscopy.[11] Ertl's work on Fe single crystals yielded the first complete energy scheme and reaction pathway for ammonia synthesis.[12-15] In it and subsequent works by other researchers, the extreme structural sensitivity of this reaction was observed.[16-19] In particular, the rate determining step of N_2 dissociation requires the presence of highly uncoordinated metal sites at the steps and kinks in order to progress. Subsequent computational modelling of N_2 to NH_3 conversion on these step sites yielded good agreement with experimental results.[20]

The purpose of the above example of catalytic nitrogen fixation is to highlight the economic importance of catalysis, and the scientific hurdles which needed to be overcome in order to achieve detailed understanding of the process. In particular, computational studies have proven to be invaluable in this scientific process and the elucidation of the catalytic mechanisms. Compared to the history of catalysis, computational modelling has become a feasible approach for only a fraction of that period, but as computational hardware and theoretical methods continue to improve, its impact on the field continues to grow. The early attempts of finding viable catalysts were trial-and-error based studies requiring painstaking experimental tests of possible

candidates. For ammonia synthesis, the first viable and economical catalyst for the Haber-Bosch process was found through almost 20000 tests on thousands of catalysts over a period of several years.[21] Today, through computational modelling, it is now possible to understand, design and test catalysts completely *in silico* without external experimental input (termed 'first-principles,' see Chapter 2).

1.1.1 Surfaces

Surfaces comprise of the portion of the heterogeneous catalyst which is accessible by the reactant. With the exception of amorphous catalysts, most naturally forming and stable surfaces exist as a low-index facet cleaved from a bulk single crystal. For example, single crystal surfaces such as Ni (111) and Pt (111) provide simple model systems for study in surface chemistry. As mentioned previously, different surface facets can have dramatic differences in catalytic activity due to different concentration and local structure of exposed active sites. Various synthesis methods or post-synthesis treatments have been able to control the facet of exposed surfaces for the purpose of tuning catalytic behavior for metals and metal oxide nanoparticles.[22-26]

In many cases surfaces deviate from the pristine form, often by the formation of kinks or other defects. On oxides, these defects primarily take the form of oxygen vacancies, which are formed from a combination of high temperatures, reacted molecules desorbing, or both. In fact, it is most often the defect or high-index sites which provide the observed catalytic activity of a solid. This was recognized perhaps as early as the 1920s by Taylor

who deduced from CO adsorption on quartz and nickel that only “a small fraction of the surface is active” on specific sites on specific arrangements and spacings.[27]

Further complications arise when the as-cleaved surfaces reconstruct to form more stable motifs or overlayers.[28] Compared to the stable (111) facet, the (110) and (100) facets of noble metals may tend to reconstruct.[28-32] The presence of specific adsorbates, such as CO which can strongly bind to the metal, can also promote surface reconstruction schemes.[33-34] In metal oxides, reconstruction is a major phenomenon due to the possibility of cleaving polar surfaces which can lead to a diverging electrostatic potential or ‘polar catastrophe.’[35-37] Reconstruction is one such mechanism of polar compensation, which leads to a distinct geometry on the topmost several layers.[38-40] These reconstructions are important to take into consideration when studying the surface activity and catalysis.

1.1.2 Clusters

Metal clusters, specifically those in the sub-nanometer range represent a remarkably promising but complex system of study which is distinct from surfaces in several respects. First, they often exhibit unique physical and chemical properties which are distinct from the bulk. The high degree of surface to bulk atoms and coordinative unsaturation also suggests a great potential for high catalytic activity. Furthermore, sub-nanometer clusters exhibit properties which can change dramatically from one size to another, varying by only a single atom.[41-46] Therefore, minor changes in cluster size and composition to tune its catalytic properties is an appealing mode for creating more active

catalysts.[44, 47-49] Metal clusters as a class of materials can exhibit two extremes in terms of its structural properties and dynamics. On one hand, magic-number and/or ligand-protected metal clusters can be structurally precise down to the atomic level. On the other, most bare/unprotected metal clusters exhibit significant structural fluxionality at sizes under 50-100 atoms which precludes any identification of a single stable structure.

For ligand-protected metal nanoclusters, significant advances in the past decade have allowed for the synthesis of atomically precise clusters containing Cu, Ag, Au and various metal dopants from tens to hundreds of atoms.[50-53] Using X-ray crystallography and neutron diffraction, the atomic structure can furthermore be solved, allowing for precise structure-activity correlations for these systems. In particular, and their well-define structures make it amenable for molecular level understanding of catalysis on these clusters, which are active for a variety of reactions[50, 54]

Despite being structurally imprecise or dynamic, significant advances have also been made in the study of unprotected subnanometer clusters. Computational studies also need to consider the structural fluxionality of these systems. In particular, global optimization (see Chapter 2.4) is often necessary to sample the stable and energetically competitive cluster geometries prior to studying its chemical and catalytic properties.

For real catalysis, metal clusters must be placed on a support, usually a metal oxide, in order to stabilize the particles and retard sintering under reaction conditions. The support may also intentionally or unintentionally play a significant role in altering the properties of the metal cluster, as well as provide additional active sites for the catalytic

reaction on its surface or at the interface with the cluster. Additionally, for specific combinations of metals and supports, a strong metal-support interaction (SMSI) may manifest,[55] which can lead to the formation of oxide overlayers over the cluster and drastically change its catalytic properties. The computational modeling of supported metal clusters remains an ongoing and unresolved challenge (see chapter 1.2) due to the large system sizes of supported cluster models. Currently, simulations involving clusters larger than 10-20 atoms on a support are the exception rather than the norm due to the need to run cost-intensive global optimization or molecular dynamics to capture the structural dynamics of these clusters.

1.1.3 Single-atoms

Single atom catalysts refer to a class of materials where the active atoms for a specific catalytic reaction are (intentionally) singly dispersed in a framework or support, such as a metal oxide surface. The term single atom catalyst has only recently achieved widespread usage in the field since the past 5-10 years from the writing of this thesis.[56] This is in large part due to improved synthesis techniques and more importantly advances in characterization with atomic level resolution to provide proof for this label. One such method is high-angle annular dark-field scanning transmission electron microscopy (HAADF-STEM), which can distinguish the single metal atoms from the support atoms when the difference in atomic number is sufficiently high. Another is synchrotron X-ray absorption spectroscopy which can identify oxidation states and local coordination environment of the single atom from X-ray absorption near-edge structure (XANES) and extended X-ray absorption fine structure (EXAFS), respectively. The appeal of single

atom catalysts is the hypothetical 100% utilization of the (often precious) metal atoms analogous to what can be observed in homogeneous catalysts, while retaining certain benefits of heterogeneous catalysts such as ease of separation and improved stability. Furthermore, the properties of the single atom can be tuned electronically by changing the nature or geometry of the support.

Prior to atomic resolution characterization and the widespread usage of the single-atom label, substitutionally doped oxides had been synthesized and characterized for catalysis for many years.[57] These studies have used doping primarily as a means of altering the existing properties of a base oxide rather than creating a new catalyst centered around the catalytic properties of the single atom. Furthermore, less importance is given to the isolated nature of the dopants, which is not necessary for doped oxides to function property. In the context of catalytic reactions which occur over the lattice oxygen of metal oxides, particularly following the Mars-van-Krevelen mechanism, the dopant acts indirectly on catalysis by tuning the properties and activity of the neighboring oxygen. One such example is the doping of stable oxides such as MgO and CaO with alkali dopants such as Li to create a high-performing catalyst for methane oxidative coupling to ethylene pioneered by Lunsford and coworkers.[58-61] An early computational example is the doping of CeO_2 with various transition metals for oxidative coupling by Janik and coworkers.[62-64]

A large number of recent literature studies for single atoms has demonstrated their effectiveness for a variety of catalytic reactions. The earliest reports of single atom catalysts include Rh on MgO for propane combustion,[65] Pd on MgO for acetylene cyclo-

trimerization,[66] and Au and Pt on CeO_2 for water-gas shift.[67] More recent work in single atom catalysts include Pt, Au, Pd or other transition metal single atoms on oxides such as FeO_x,[68-69] Fe_3O_4,[70] TiO_2,[71-72] CeO_2,[73] $Ni(OH)_x$,[74] ZrO_2,[75] SiO_2,[76-77] Al_2O_3,[78-79] and 2D materials including MXenes,[80] MoS_2[81-83], graphene,[84] and g-C_3N_4.[85] Another sub-class of single atoms feature the metal atom supported in another metal, forming a so-called 'single atom alloy.'[86-89] Here, single atoms of reactive metals such as Pt, Pd and Ni can be placed in an otherwise inert metal support such as Cu to improve stability and poisoning resistance. Furthermore, spillover of reactant intermediates and bifunctional properties between the single atom and the support can be observed.

1.2 Computational surface chemistry and catalysis

Computational studies have provided a path towards the understanding of catalysis to the atomic level. Over the past two to three decades, computational modeling, primarily via first principles techniques, has grown exponentially become a widely accepted technique for the field of catalysis.[90-93] This has been made possible in large part with the development and widespread development of density functional theory (DFT).

1.2.1 Surface properties and reactions

A typical workflow for a contemporary computational study on heterogeneous catalysts will now be described briefly. Technical details for the procedures outlined can be found in Chapter 2.

1. The system (i.e. the catalytically relevant region) must first be identified and built within the confines of computational feasibility. Identifying the catalytically

relevant region is not a trivial step; often insights from a combination of experimental studies are needed, starting from determining the crystal structure, the surface structure geometry down to the exposed surfaces/sites of the catalyst. Oftentimes such data is not available, especially when predicting new, unstudied catalysts is the goal. In such cases, further work is needed to determine the thermodynamic stability and overall feasibility of the models synthesized *in silico* which we will not go into too much detail.

Another consideration is the system size; typical ranges go from 100-200 atoms for contemporary studies. Although electronic structure and adsorption calculations can be performed up to 500-1000 atoms in contemporary first principles studies, a significant limiting factor for the system size in a computational catalysis work is the cost of the transition state search. For heterogeneous catalysts, the model to be used will usually take the form of a slab several atomic layers thick (in the z-direction); the surface properties of the slab can be highly thickness dependent – in such cases the thickness will need to be determined via an energy convergence criterion. The area of the slab (the x and y-direction) must also be chosen to avoid interactions between periodic images (unless coverage effects is one of the goals of the study).

2. The adsorption or bond-activation sites must either be verified or found starting from the initial reactants to the intermediates and products. This is often the most expensive portion of a study in terms of human resources. For nearly all systems studied today, a full potential energy scan or global optimization of adsorbates on

the surface is not possible due to computational cost. Instead, adsorbates are placed on the surface and relaxed locally through geometry optimization via the input and intuition of the computational chemist. Then, the relative energies are compared to obtain the most stable configurations for subsequent study; multiple likely candidates are often chosen if the energies are similar.

3. Probing reaction pathways and barriers occurs concurrently with the previous step. This is often the most expensive portion in terms of computational resources due to the cost of the transition state search methods (see Chapter 2.2 for details). Nudged elastic band (NEB) for example, requires the simultaneous optimization of several linked geometries, which has a multiplicative effect on the computational cost. Typical studies will first find the most stable initial reactant geometries and intermediate geometries and calculated the reaction barrier from the reactant to the intermediates. However, this may not necessarily lead to the most favored reaction path with the lowest barriers; as a result several competing pathways should be tested simultaneously even if they are thermodynamically less attractive. Sometimes the final and initial states may not be intuitive, saddle point searching methods such as the dimer method do not require a final state and can be used to explore unexpected pathways. Ab inito molecular dynamics simulations can also be used to that effect.
4. Obtaining kinetics is the last step of the study once the DFT-obtained adsorption energies and reaction barriers are complete. Microkinetics and kinetic Monte Carlo (KMC) are the two most commonly used kinetic modelling techniques used

for catalysis. Whereas microkinetics is a mean field technique, kinetic Monte Carlo can explicitly account for surface diffusion, coverage and adsorbate-adsorbate interactions. Both techniques generally require an exhaustive list of elementary steps and their corresponding thermodynamic quantities and energy barriers; this is especially the case for KMC.

Comparisons with experimental studies can take many forms.[92] First, adsorption calculations can yield adsorption geometries and adsorption energies, which can be matched with experimental microcalorimetric or TPD results along with RAIRS and EELS/HREELS for surface structure. Computational studies can also yield predicted vibrational frequencies using the harmonic approximation which can be compared with FTIR or neutron scattering data. Reaction mechanism studies can also yield predictions of stable intermediates and rate determining steps. These intermediate species can be observed via operando spectroscopy and SSITKA experimentally.[94] Rate determining steps can be compared with experimental observations and kinetic isotope effect studies.

It is important to point out that the example study outlined here is only a small window into the study of computational heterogeneous catalysis. There exists a significant gap between model surface slabs and real catalysts under working conditions.[95] Obtaining the structure and morphology of working catalysts remains an ongoing experimental and theoretical challenge. As DFT is a 0K method, bridging the temperature and pressure gap is also necessary for valid predictions. A fine balance must be struck between computational feasibility and modelling accuracy while keeping in mind the limitations of any simulation method.

1.2.2 Descriptors

Although ab-initio calculations are now routinely performed to map out reaction pathways and obtain activation barriers for catalytic predictions, it is still highly impractical to perform the entire calculation steps as a means of screening different materials. One popular approach uses 'descriptors' which are specific features (such as an adsorption energy) correlated to a more general property (such as catalytic activity/activation barriers) usually via linear correlation.

1.2.2.1 Linear scaling relationships

Linear scaling relations underlie most descriptors for adsorbates on surfaces. These are broadly defined as linear correlations between adsorption energies for two or more adsorbates on various surfaces.[96] The major benefit of linear scaling relationship is the reduction of the parameter space down to one or two key properties, usually adsorption energies, for which other energies can be obtained from. These linear scaling relationships based on thermodynamic quantities have been applied extensively for a wide number of systems, particularly for the transition metals,[97-99] though correlations on transition metal compounds have also been observed.[100-104]

Most descriptors of reaction barriers derive from the Brønsted-Evans-Polanyi (BEP) relationship[101, 105-108] where the activation barrier E_a is related to the enthalpy of the reaction ΔH via this expression:

$$E_a = E_0 + \alpha \Delta H$$

where α is conventionally defined as the position of the transition state along the reaction coordinate from 0 to 1. In computational studies, E_0 and α are usually empirically determined via linear regression from a set of training data. BEP relations work best (if at all), when the transition state remains similar through the different studied systems (i.e. on metals). One of the main benefits of the BEP relationship is the ability to affordably obtain E_a from ΔH once E_0 and α have been found. This is due to the usually 1-2 orders of magnitude higher computational cost to obtain E_a compared to adsorption energies. BEP relationships, along with the broader linear scaling relationships for adsorbates, can be used to provide affordable and sufficiently accurate thermodynamic and kinetic input for various microkinetic and KMC models for high-throughput screening.

Today, thousands of papers have been published which reference or utilize linear scaling relationships in some form or another, which is too extensive to list here.[91, 109] Its widespread observation and adoption is evidence to suggest that these correlations between many thermodynamic and even kinetic properties of surface reactions must be an enduring and possibly universal one. This is true to the extent where many recent studies have focused now on trying to 'break' these linear scaling relationships, in order to access higher catalytic activities.[110-117]

1.2.2.2 Catalytic descriptors and volcano relations

Many descriptors of overall catalytic performance follow a 'volcano plot' where the peak performance is found at an intermediate value on the x-axis. This phenomenon can be attributed to the Sabatier principle.[118-120] In this model, the optimal catalyst is proposed

to follow a ‘Goldilocks principle’ where the adsorption of intermediates with the catalyst should be just right: too strong and the product fails to desorb, too weak and the reactant fails to dissociate. This is observed for both traditional thermal catalysis[119, 121-122] as well as electrocatalysis, including the oxygen reduction reaction[123-124] and the hydrogen evolution reaction.[125]

1.2.2.3 Electronic and coordinative descriptors

In many cases, adsorption and bond activation on surfaces follows the same chemical rules which can be linked to their electronic properties. Especially for metals, many such theories exist which can explain the varying adsorption energies of adsorbates on their surfaces. The earliest of such theories proposed to provide a rigorous theoretical explanation for these scaling relationships were based on that of bond-order conservation[126] Shustorovich and van Santen[127-132] and the effective medium theory.[97, 133] In both approaches, there is an ‘optimal’ bond-order or electronic density of a surface atom, which is shared between the surface-surface bonds (such as metal-metal bonds) and the surface-adsorbate bonds, and can be described via a linear analytic expression.

A further extension of this model linking adsorption to electronic states obtained from first principles is the d-band theory for metals.[134-135] This model is based on the observation that adsorbate interactions with a metal surface lead to the interaction between the adsorbate and metal s state(s) and the metal d state(s) to form bonding and anti-bonding states. The primary difference between metals and surface atoms lies in the change in position and filling of the d states. When the position of the d states or “d-band center” is

lower relative to the fermi level, the anti-bonding states are correspondingly lowered, and become progressively more occupied by electrons from the substrate, thereby weakening the interaction. Conversely, a higher d-band center corresponds to fewer filled anti-bonding states and a stronger adsorption energy.

This approach can be taken to an even greater extreme by relating the information regarding the coordinative environment of the metal site to the adsorption energies directly – often referred to as coordination number descriptors or structural descriptors. A number of recent studies have used the first metal coordination shell,[136] the first and second coordination shells,[137-138] and metal site orbital characteristics[139] to predict adsorption energies. For metals, the underlying reason why coordination number can predict adsorption energies is again related to their electronic properties, and strong correlations between coordination and d band position can be found.[137]

Applying electronic models for adsorption analogous to the d-band theory to non-metallic systems such as oxides remains an ongoing, non-trivial, challenge.[96, 140-143] Much focus in the literature has been in predicting the adsorption properties of the metal sites in a metal oxide; including the d-election descriptors proposed by Shao-Horn et al. or Calle-Vallejo et al.[140, 144-147] applied to perovskite systems.

1.3 Alkane activation and conversion

Alkanes are abundant energy resources which are primarily sourced from oil and natural gas. Natural gas in particular is composed of a majority of methane, followed by other light alkanes such as ethane and propane. Estimates of known natural gas reserves

are in the 10^{14} m^3 range, with an order of magnitude or higher additionally stored in the form of methane hydrates under the ocean or in permafrost. However, over 90% of natural gas is burned for heating or electricity production, and another 3% is flared. Reasons for this economic underutilization are due to its poor energy density (about ~50 times lower than oil), and unresolved scientific and engineering challenges in economical alkane conversion.

The fact that alkane, especially methane conversion, is routinely considered one of the holy grails of catalysis provides some notion of its difficulty and importance within the field.[148-152] Methane for example, is a symmetric, nonpolar molecule with a wide HOMO-LUMO gap and four stable C-H bonds with a dissociation energy of roughly 440 kJ/mol. These qualities make it resistant to both nucleophilic and electrophilic attack. Therefore, a chief property in catalyst design for alkane conversion involves finding materials and sites with facile C-H activating sites. A further issue arises from the first C-H bond being stronger than the subsequent C-H bonds, which means any intermediates following C-H activation is less stable and more easily reacted than the reactant alkane, which leads to overoxidation into the thermodynamic well of CO_2 and H_2O. Other, engineering, challenges for alkane catalysis include the ever-present issue of catalyst deactivation from coking and sintering due to high temperatures needed.

1.3.1 Conversion to products

Many possible routes exist to create industrially useful products from alkanes. For methane, these processes include steam reforming, dry reforming, partial oxidation, direct

conversion, oxidative coupling, halogenation and aromatization.[149, 152] Given the massive reserves there is a strong economic incentive for catalytic processes to convert alkanes to value added chemicals. Furthermore, there is a growing environmental incentive to avoid alkane conversion processes which are energy intensive and/or generate large amounts of greenhouse gases as the product.

The steam reforming of methane to produce syngas (H_2 and CO) is a mature technology in the industry, which provides much of the hydrogen for various processes such as ammonia and methanol production or directly to longer hydrocarbons via Fischer-Tropsch. The reaction,

$CH_4(g) + H_2O(g) \rightleftharpoons CO(g) + 3H_2(g)$; $\Delta H = 206$ kJ/mol

is endothermic and consequently thermodynamically limited and energy intensive.

Meanwhile, dry reforming is environmentally attractive due to the removal by catalytic conversion of the two major greenhouse gases CO_2 and CH_4 into syngas, however the energy required for this highly endothermic reaction must come from non-fossil fuel sources to justify this argument. The reaction,

$CH_4(g) + CO_2(g) \rightleftharpoons 2CO(g) + 2H_2(g)$; $\Delta H = 247$ kJ/mol

is similarly endothermic with the same drawbacks as steam reforming. However, a lower H_2/CO ratio in this reaction is beneficial for Fischer-Tropsch. To date, dry reforming remains challenging due to the propensity of coking and deactivation. The sources of coking are methane pyrolysis

$CH_4(g) \rightleftharpoons C(s) + 2H_2(g)$; $\Delta H = 75$ kJ/mol

and the Boudouard reaction

$2CO(g) \rightleftharpoons C(s) + CO_2(g)$; $\Delta H = -171$ kJ/mol

leading to the generation of carbon on the catalytic surfaces and necessitating high temperatures and CO_2 concentration for this process.[153] Furthermore, the chemical inertness of both CO_2 and CH_4 requires finding catalysts which can activate both molecules effectively. While pyrolysis is a detrimental side reaction leading to coking in this example, pyrolysis can be intentionally harnessed as well to produce H_2 gas.[154]

In a similar vein, another conversion process without strong oxidants is methane aromatization, which converts methane to aromatics such as benzene and hydrogen gas without O_2. For this reaction,

$6CH_4(g) \rightleftharpoons C_6H_6(g) + 9H_2(g)$; $\Delta H = 532$ kJ/mol

the endothermicity is even more severe than the above examples, and the thermodynamic limit for conversion is approximately 15%.[155] Most common catalysts take the form of metal atoms and clusters supported in zeolites such as ZSM-5,[156-157] though recent catalysts such as Fe single atoms in silica may also be promising.[158] Again, the high endothermicity, high temperatures and severe coking are major obstacles for this process.

Oxidative coupling of methane (OCM) is another appealing process to convert CH_4 directly into the ethylene, a major industrial precursor.

$CH_4(g) + 0.5O_2(g) \rightleftharpoons 0.5C_2H_4(g) + 2H_2O(g)$; $\Delta H = -139$ kJ/mol

This process was first brought to attention in the 1980s,[59, 159] whereby it received a huge surge in research interest and patent filings for OCM catalysts.[58, 160-162] Li-MgO, despite showing high activity, becomes deactivated within hours under catalytic conditions. Complex oxides containing Ti, Mn, La doped Na_2WO_4 supported on silica have been found to have promising yields and stability.[163-165] A soft limit is observed between C_2 selectivity and CH_4 conversion which prevents yields going above ~30% which was also predicted based on the homolytic C-H activation mechanism.[166] To avoid overoxidation into CO_2, sulfur has also been proposed as an oxidant; though selectivity is improved, current yields remain too low for practical application.[167] Another promising direction involves the use of ion conducting membrane reactors to control oxygen concentrations and prevent over-oxidation.[168-171]

Catalytic oxidation to methanol or formaldehyde through partial oxidation is another enticing alternative.[150]

$$CH_4(g) + 0.5O_2(g) \rightleftharpoons 0.5CH_3OH(g);\ \Delta H = -126\ kJ/mol$$

$$CH_4(g) + O_2(g) \rightleftharpoons C_2O(g) + H_2O(g);\ \Delta H = -368\ kJ/mol$$

Studies in homogenous[172-177] and biological systems[178-186] for this process shed valuable insights for application towards heterogeneous catalysts. Mimicking these systems, especially the di-copper motif in the methane monooxygenase enzyme, transition metal loaded zeolites or even MOFs have achieved a measure of success for heterogeneous methane oxidation.[187-196] Despite significant efforts, methane conversion rates remain in the single digits and far below commercial feasibility due to the higher reactivity of

methanol. The relative weakness of the methanol C-H bond with respect to methane necessitates strategies to protect methanol from further oxidation once it is produced.[116]

Alkane dehydrogenation is another important catalytic process with much room for improvement.[197-198] The most prevalent and mature process used today is steam cracking, where alkanes and steam are brought to high temperatures to undergo homogenous pyrolysis. On heterogeneous catalysts, alkanes can be dehydrogenated to ethylene via nonoxidative and oxidative pathways as seen in this example for ethane:

$C_2H_6(g) \rightleftharpoons C_2H_4(g) + H_2(g)$; $\Delta H = 136$ kJ/mol

$C_2H_6(g) + 0.5O_2(g) \rightleftharpoons C_2H_4(g) + H_2O(g)$; $\Delta H = -106$ kJ/mol

Two major commercial processes for nonoxidative dehydrogenation are the Catofin process using CrO_x/Al_2O_3 and the Oleflex process using $Pt–Sn/Al_2O_3$. Oxidative dehydrogenation is attractive due to the mild exothermicity and lower temperature requirements; coke formation can also be suppressed. Replacing O_2 with the milder CO_2 as the oxidant has also been studied in the literature, with the goal of increasing selectivity.

1.3.2 C-H activation

Regardless of the final product for an alkane conversion process, the C-H bond must be cleaved before any further reaction may occur; C-H activation is consequently the first step in any alkane conversion reaction. Due to the strength of this bond, the first C-H activation is also often the rate-limiting step in a reaction. Therefore, a material's ability

to activate the C-H bond is a primary descriptor of its overall catalytic performance in many cases.

Prior to C-H activation, alkanes can be physisorbed or even chemisorbed onto the surface. Physisorption from weak dispersion interactions has been measured to be on the order of only 10-20kJ/mol on oxide surfaces.[199] A relation between the chain length of the alkane and physisorption strength has also been observed, likely due to the additive dispersion interactions with the surface.[200-203] Nevertheless, the physical interaction remains fairly weak. For most conventional alkane conversion processes at high temperatures, it is safe to assume the free energy of adsorption of alkanes will be positive under these conditions. In these cases, methane is likely to be activated directly upon collision with the surface rather than adsorbing first to the surface.[203]

C-H activation occurs via one of two pathways, which we will term 'homolytic' and 'heterolytic' cleavage. In the familiar language of organic chemistry, homolytic cleavage is defined as the breaking of a chemical bond by splitting the bonding electrons equally, to form two radical species. Meanwhile heterolytic cleavage splits the electrons unevenly to form an anion and cation.[204] This terminology has been adapted to C-H activation on catalysts in much the same way. Ergo, in homolytic C-H activation, a hydrogen is abstracted from the carbon by an active surface species, usually a lattice oxygen on the catalyst surface, to form a hydroxyl and a methyl radical. This radical is most likely immediately recaptured by nearby surface active sites, though it can be conceivable the liberated methyl radical can also react directly with other gas phase molecules directly. This is the most widely viewed as the favored mechanism for alkane C-H activation in

metal oxides.[58, 151, 188, 205-207] Meanwhile, in heterolytic C-H activation, the methane transition state is stabilized by a surface species (usually a metal), to form an adsorbed methyl anion. This mechanism is proposed to be favored on metals and certain oxide surfaces where the stabilization involves the insertion of a carbon-metal bond in the transition state. [161, 208-210]

For homolytic C-H activation, the ability of surface oxygen sites to catalyze this reaction has been studied extensively. Li doped MgO is one well-known system where the homolytic pathway has been proposed. It has been argued that Li doping produces electron holes at Li^+O^- centers which act as strong Lewis acids which can abstract hydrogen atoms from methane.[58, 211] However, disagreement exists regarding the true nature of Li doping and the mechanism of C-H activation. It was found that experimental barriers for H abstraction of 80-160 kJ/mol disagree with theoretical calculations finding barriers as low as 12 kJ/mol over the Li^+O^- centers. Sauer and co-workers argue lithium instead promotes morphological changes in the MgO surfaces leading to formation steps and corners which instead activate the C-H bond heterolytically with barriers of 86 kJ/mol.[212] Nevertheless, the theory is clear regarding the low homolytic C-H activation barriers which can occur over highly active oxygen sites. Mechanistic insights regarding homolytic C-H activation have also been obtained from computational and experimental oxide cluster studies in the gas phase.[213-218] The primary conclusions from these studies indicate the higher reactivity of open-shell clusters with a radical, or greater spin density, localized on the oxygen.[151, 219-220]

The reaction barriers for homolytic activation have been linked to the adsorption strength of hydrogen or vacancy formation with the active site oxygen from previous and contemporaneous computational studies.[62-63, 205-206, 221-223] The BEP relationship can explain the linear correlation between hydrogen adsorption and C-H activation barriers due to a one to one correspondence between hydrogen adsorption and the reaction energy following homolytic cleavage. This is because in homolytic cleavage, the same transient methyl radical is released regardless of the surface, and the energy of the radical can be cancelled out or considered constant in energy. To date, no studies have yet to be conducted in the literature for homolytic cleavage following a chemisorbed methane species, possibly due to the competing heterolytic pathway becoming favored.

For heterolytic C-H activation, both non-chemisorbing and chemisorbing cases have been studied in the literature. The non-chemisorbing case is the most common which accounts for the overwhelming majority of surfaces. Here, the BEP relationship is also valid, but instead of hydrogen adsorption energy the dissociation energy to form O-H or M-H and M-CH_3 is needed.[208, 221, 224] Heterolytic C-H activation can also occur via a C-H complex, sometimes also called a σ-complex or an agnostic bond.[202, 225-226] In this situation, methane and other alkanes form a chemisorbed species analogous to σ-complexes with transition metal complexes.[227-228] The nature of this complex results in an activated C-H bond which may be subsequently cleaved with far lower energy barriers than if the alkane did not form the complex. This is a consequence of a weakening of the C-H σ bond by loss of occupancy in the σ orbital and increased occupancy in the σ* antibonding orbital from electron donating and back-donation with the metal center. This

complex-mediated heterolytic mechanism has been observed in a fair number of gas-phase cluster studies.[229-232] Meanwhile, surfaces currently experimentally proven to form complexes with methane are however currently limited to PdO, RuO_2, and IrO_2.[199, 202, 233] Nonetheless, there are some 'hybrid' systems where methane complexation is predicted to occur on surfaces with supported clusters and adatoms in the past few years.[234-238] This mechanism for alkane activation is arguably an emerging topic of interest for selective alkane conversion.

References

(1) Roberts, M. W. Birth of the catalytic concept (1800-1900). *Catal. Lett.* **2000,** *67*, 1-4.

(2) Mitscherlich, E. Ueber die Aetherbildung. *Annalen der Physik* **1834,** *107*, 273-282.

(3) Ertl, G.; Knözinger, H.; Weitkamp, J., *Handbook of heterogeneous catalysis*. VCH: Weinheim, 2008.

(4) Wisniak, J. The history of catalysis. From the beginning to Nobel Prizes. *Educación química* **2010,** *21*, 60-69.

(5) Ostwald, W. Definition der Katalyse. *Z. Phys. Chem.* **1894,** *15*, 705-706.

(6) Council, N. R., *Catalysis Looks to the Future*. The National Academies Press: Washington, DC, 1992; p 96.

(7) Haber, F.; van Oordt, G. Über die Bildung von Ammoniak den Elementen. *Zeitschrift für anorganische Chemie* **1905,** *44*, 341-378.

(8) Smil, V. Detonator of the population explosion. *Nature* **1999,** *400*, 415.

(9) Erisman, J. W.; Sutton, M. A.; Galloway, J.; Klimont, Z.; Winiwarter, W. How a century of ammonia synthesis changed the world. *Nature Geoscience* **2008,** *1*, 636.

(10) Press release. https://www.nobelprize.org/prizes/chemistry/2007/press-release/ (accessed 3/12/2019).

(11) Bowker, M. The 2007 Nobel Prize in Chemistry for Surface Chemistry: Understanding Nanoscale Phenomena at Surfaces. *ACS Nano* **2007,** *1*, 253-257.

(12) Bozso, F.; Ertl, G.; Grunze, M.; Weiss, M. Interaction of nitrogen with iron surfaces: I. Fe(100) and Fe(111). *J. Catal.* **1977,** *49*, 18-41.

(13) Ertl, G. Primary steps in catalytic synthesis of ammonia. *Journal of Vacuum Science & Technology A* **1983,** *1*, 1247-1253.

(14) Ertl, G.; Lee, S. B.; Weiss, M. Kinetics of nitrogen adsorption on Fe(111). *Surf. Sci.* **1982,** *114*, 515-526.

(15) Imbihl, R.; Behm, R. J.; Ertl, G.; Moritz, W. The structure of atomic nitrogen adsorbed on Fe(100). *Surf. Sci.* **1982,** *123*, 129-140.

(16) Singh-Boparai, S. P.; Bowker, M.; King, D. A. Crystallographic anisotropy in chemisorption: Nitrogen on tungsten single crystal planes. *Surf. Sci.* **1975,** *53*, 55-73.

(17) Strongin, D. R.; Carrazza, J.; Bare, S. R.; Somorjai, G. A. The importance of C7 sites and surface roughness in the ammonia synthesis reaction over iron. *J. Catal.* **1987,** *103*, 213-215.

(18) Zaera, F.; Gellman, A. J.; Somorjai, G. A. Surface science studies of catalysis: classification of reactions. *Acc. Chem. Res.* **1986,** *19*, 24-31.

(19) Jacobs, P. W.; Somorjai, G. A. Conversion of heterogeneous catalysis from art to science: the surface science of heterogeneous catalysis. *J. Mol. Catal. A: Chem.* **1998,** *131*, 5-18.

(20) Honkala, K.; Hellman, A.; Remediakis, I.; Logadottir, A.; Carlsson, A.; Dahl, S.; Christensen, C. H.; Nørskov, J. K. Ammonia synthesis from first-principles calculations. *Science* **2005,** *307*, 555-558.

(21) Mittasch, A., *Geschichte der Ammoniaksynthese*. Verlag Chemie: 1951.

(22) Xia, Y.; Xiong, Y.; Lim, B.; Skrabalak, S. E. Shape-Controlled Synthesis of Metal Nanocrystals: Simple Chemistry Meets Complex Physics? *Angew. Chem. Int. Ed.* **2009,** *48*, 60-103.

(23) Gilroy, K. D.; Ruditskiy, A.; Peng, H.-C.; Qin, D.; Xia, Y. Bimetallic Nanocrystals: Syntheses, Properties, and Applications. *Chem. Rev.* **2016,** *116*, 10414-10472.

(24) Foo, G. S.; Hood, Z. D.; Wu, Z. Shape Effect Undermined by Surface Reconstruction: Ethanol Dehydrogenation over Shape-Controlled SrTiO3 Nanocrystals. *ACS Catal.* **2018,** *8*, 555-565.

(25) Foo, G. S.; Hu, G.; Hood, Z. D.; Li, M.; Jiang, D.-e.; Wu, Z. Kinetics and Mechanism of Methanol Conversion over Anatase Titania Nanoshapes. *ACS Catal.* **2017,** *7*, 5345-5356.

(26) Li, Y.; Shen, W. Morphology-dependent nanocatalysts: Rod-shaped oxides. *Chem. Soc. Rev.* **2014,** *43*, 1543-1574.

(27) Taylor, H. S.; Armstrong, E. F. A theory of the catalytic surface. *Proceedings of the Royal Society of London. Series A, Containing Papers of a Mathematical and Physical Character* **1925,** *108*, 105-111.

(28) Titmuss, S.; Wander, A.; King, D. A. Reconstruction of Clean and Adsorbate-Covered Metal Surfaces. *Chem. Rev.* **1996,** *96*, 1291-1306.

(29) Rost, M. J.; van Gastel, R.; Frenken, J. W. M. Anomalous Shape and Decay of Islands on Au(110). *Phys. Rev. Lett.* **2000,** *84*, 1966-1969.

(30) Vilfan, I.; Lançon, F.; Adam, E. Lattice vibrations and stability of reconstructed (110) noble metal surfaces. *Surf. Sci.* **1999,** *440*, 279-289.

(31) Deng, X.; Min, B. K.; Guloy, A.; Friend, C. M. Enhancement of O2 Dissociation on Au(111) by Adsorbed Oxygen: Implications for Oxidation Catalysis. *J. Am. Chem. Soc.* **2005,** *127*, 9267-9270.

(32) Min, B. K.; Friend, C. M. Heterogeneous Gold-Based Catalysis for Green Chemistry: Low-Temperature CO Oxidation and Propene Oxidation. *Chem. Rev.* **2007,** *107*, 2709-2724.

(33) Tao, F.; Dag, S.; Wang, L.-W.; Liu, Z.; Butcher, D. R.; Bluhm, H.; Salmeron, M.; Somorjai, G. A. Break-Up of Stepped Platinum Catalyst Surfaces by High CO Coverage. *Science* **2010,** *327*, 850-853.

(34) van Spronsen, M. A.; Frenken, J. W. M.; Groot, I. M. N. Surface science under reaction conditions: CO oxidation on Pt and Pd model catalysts. *Chem. Soc. Rev.* **2017,** *46*, 4347-4374.

(35) Noguera, C. Polar oxide surfaces. *J. Phys.: Condens. Matter* **2000,** *12*, R367-R410.

(36) Noguera, C.; Goniakowski, J. Polarity in Oxide Nano-objects. *Chem. Rev.* **2013,** *113*, 4073-4105.

(37) Goniakowski, J.; Finocchi, F.; Noguera, C. Polarity of oxide surfaces and nanostructures. *Rep. Prog. Phys.* **2007,** *71*, 016501.

(38) Wang, Y.; Cheng, J.; Behtash, M.; Tang, W.; Luo, J.; Yang, K. First-principles studies of polar perovskite KTaO3 surfaces: structural reconstruction, charge compensation, and stability diagram. *Phys. Chem. Chem. Phys.* **2018,** *20*, 18515-18527.

(39) Deacon-Smith, D. E. E.; Scanlon, D. O.; Catlow, C. R. A.; Sokol, A. A.; Woodley, S. M. Interlayer Cation Exchange Stabilizes Polar Perovskite Surfaces. *Adv. Mater.* **2014,** *26*, 7252-7256.

(40) Wang, Z.; Loon, A.; Subramanian, A.; Gerhold, S.; McDermott, E.; Enterkin, J. A.; Hieckel, M.; Russell, B. C.; Green, R. J.; Moewes, A.; Guo, J.; Blaha, P.; Castell, M. R.; Diebold, U.; Marks, L. D. Transition from Reconstruction toward Thin Film on the (110) Surface of Strontium Titanate. *Nano Lett.* **2016,** *16*, 2407-2412.

(41) Taylor, K. J.; Pettiette‐Hall, C. L.; Cheshnovsky, O.; Smalley, R. E. Ultraviolet photoelectron spectra of coinage metal clusters. *J. Chem. Phys.* **1992,** *96*, 3319-3329.

(42) Kelly, K. L.; Coronado, E.; Zhao, L. L.; Schatz, G. C. The Optical Properties of Metal Nanoparticles: The Influence of Size, Shape, and Dielectric Environment. *J. Phys. Chem. B* **2003,** *107*, 668-677.

(43) Adlhart, C.; Uggerud, E. Reactions of platinum clusters $Pt_n^{\pm}$, n= 1–21, with CH_4: to react or not to react. *Chem. Commun.* **2006**, 2581-2582.

(44) Vajda, S.; Pellin, M. J.; Greeley, J. P.; Marshall, C. L.; Curtiss, L. A.; Ballentine, G. A.; Elam, J. W.; Catillon-Mucherie, S.; Redfern, P. C.; Mehmood, F.; Zapol, P. Subnanometre platinum clusters as highly active and selective catalysts for the oxidative dehydrogenation of propane. *Nature Mater.* **2009,** *8*, 213-6.

(45) Kaden, W. E.; Wu, T.; Kunkel, W. A.; Anderson, S. L. Electronic Structure Controls Reactivity of Size-Selected Pd Clusters Adsorbed on TiO2 Surfaces. *Science* **2009,** *326*, 826-829.

(46) Haruta, M.; Yamada, N.; Kobayashi, T.; Iijima, S. Gold catalysts prepared by coprecipitation for low-temperature oxidation of hydrogen and of carbon monoxide. *J. Catal.* **1989,** *115*, 301-309.

(47) Tyo, E. C.; Vajda, S. Catalysis by clusters with precise numbers of atoms. *Nat. Nanotechnol.* **2015,** *10*, 577-588.

(48) Vajda, S.; White, M. G. Catalysis Applications of Size-Selected Cluster Deposition. *Acs Catalysis* **2015,** *5*, 7152-7176.

(49) Liu, L.; Corma, A. Metal Catalysts for Heterogeneous Catalysis: From Single Atoms to Nanoclusters and Nanoparticles. *Chem. Rev.* **2018,** *118*, 4981-5079.

(50) Li, G.; Jin, R. Atomically Precise Gold Nanoclusters as New Model Catalysts. *Acc. Chem. Res.* **2013,** *46*, 1749-1758.

(51) Jin, R.; Zeng, C.; Zhou, M.; Chen, Y. Atomically Precise Colloidal Metal Nanoclusters and Nanoparticles: Fundamentals and Opportunities. *Chem. Rev.* **2016,** *116*, 10346-10413.

(52) Dhayal, R. S.; van Zyl, W. E.; Liu, C. W. Polyhydrido Copper Clusters: Synthetic Advances, Structural Diversity, and Nanocluster-to-Nanoparticle Conversion. *Acc. Chem. Res.* **2016,** *49*, 86-95.

(53) Yao, Q.; Chen, T.; Yuan, X.; Xie, J. Toward Total Synthesis of Thiolate-Protected Metal Nanoclusters. *Acc. Chem. Res.* **2018,** *51*, 1338-1348.

(54) Tang, Q.; Hu, G.; Fung, V.; Jiang, D.-e. Insights into Interfaces, Stability, Electronic Properties, and Catalytic Activities of Atomically Precise Metal Nanoclusters from First Principles. *Acc. Chem. Res.* **2018,** *51*, 2793-2802.

(55) Tauster, S. J. Strong metal-support interactions. *Acc. Chem. Res.* **1987,** *20*, 389-394.

(56) Wang, A.; Li, J.; Zhang, T. Heterogeneous single-atom catalysis. *Nature Reviews Chemistry* **2018,** *2*, 65-81.

(57) McFarland, E. W.; Metiu, H. Catalysis by Doped Oxides. *Chem. Rev.* **2013,** *113*, 4391-4427.

(58) Lunsford, J. H. The Catalytic Oxidative Coupling of Methane. *Angew. Chem. Int. Ed.* **1995,** *34*, 970-980.

(59) Ito, T.; Lunsford, J. H. Synthesis of ethylene and ethane by partial oxidation of methane over lithium-doped magnesium oxide. *Nature* **1985,** *314*, 721-722.

(60) Lunsford, J. H. Catalytic conversion of methane to more useful chemicals and fuels: a challenge for the 21st century. *Catal. Today* **2000,** *63*, 165-174.

(61) Hutchings, G. J.; Scurrell, M. S.; Woodhouse, J. R. Oxidative coupling of methane using oxide catalysts. *Chem. Soc. Rev.* **1989,** *18*, 251-283.

(62) Mayernick, A. D.; Janik, M. J. Methane Activation and Oxygen Vacancy Formation Over CeO_2 and Zr, Pd Substituted CeO_2 Surfaces. *J. Phys. Chem. C* **2008,** *112*, 14955-14964.

(63) Krcha, M. D.; Mayernick, A. D.; Janik, M. J. Periodic Trends of Oxygen Vacancy Formation and C–H Bond Activation Over Transition Metal-Doped CeO_2 (111) Surfaces. *J. Catal.* **2012,** *293*, 103-115.

(64) Mayernick, A. D.; Janik, M. J. Methane oxidation on Pd–Ceria: A DFT study of the mechanism over PdxCe1−xO2, Pd, and PdO. *J. Catal.* **2011,** *278*, 16-25.

(65) Kirlin, P. S.; Gates, B. C. Activation of the C–C bond provides a molecular basis for structure sensitivity in metal catalysis. *Nature* **1987,** *325*, 38-40.

(66) Abbet, S.; Sanchez, A.; Heiz, U.; Schneider, W. D.; Ferrari, A. M.; Pacchioni, G.; Rösch, N. Acetylene Cyclotrimerization on Supported Size-Selected Pdn Clusters ($1 \leqslant n \leqslant 30$): One Atom Is Enough! *J. Am. Chem. Soc.* **2000,** *122*, 3453-3457.

(67) Fu, Q.; Saltsburg, H.; Flytzani-Stephanopoulos, M. Active Nonmetallic Au and Pt Species on Ceria-Based Water-Gas Shift Catalysts. *Science* **2003,** *301*, 935-938.

(68) Qiao, B.; Wang, A.; Yang, X.; Allard, L. F.; Jiang, Z.; Cui, Y.; Liu, J.; Li, J.; Zhang, T. Single-Atom Catalysis of CO Oxidation Using Pt_1/FeO_x. *Nat. Chem.* **2011,** *3*, 634-641.

(69) Lin, J.; Wang, A.; Qiao, B.; Liu, X.; Yang, X.; Wang, X.; Liang, J.; Li, J.; Liu, J.; Zhang, T. Remarkable Performance of Ir1/FeOx Single-Atom Catalyst in Water Gas Shift Reaction. *J. Am. Chem. Soc.* **2013,** *135*, 15314-15317.

(70) Bliem, R.; Pavelec, J.; Gamba, O.; McDermott, E.; Wang, Z.; Gerhold, S.; Wagner, M.; Osiecki, J.; Schulte, K.; Schmid, M.; Blaha, P.; Diebold, U.; Parkinson, G. S. Adsorption and incorporation of transition metals at the magnetite Fe3O4(001) surface. *Phys. Rev. B* **2015,** *92*, 075440.

(71) DeRita, L.; Dai, S.; Lopez-Zepeda, K.; Pham, N.; Graham, G. W.; Pan, X.; Christopher, P. Catalyst Architecture for Stable Single Atom Dispersion Enables Site-Specific Spectroscopic and Reactivity Measurements of CO Adsorbed to Pt Atoms, Oxidized Pt Clusters, and Metallic Pt Clusters on TiO_2. *J. Am. Chem. Soc.* **2017,** *139*, 14150-14165.

(72) Liu, P.; Zhao, Y.; Qin, R.; Mo, S.; Chen, G.; Gu, L.; Chevrier, D. M.; Zhang, P.; Guo, Q.; Zang, D.; Wu, B.; Fu, G.; Zheng, N. Photochemical Route for Synthesizing Atomically Dispersed Palladium Catalysts. *Science* **2016,** *352*, 797-801.

(73) Nie, L.; Mei, D.; Xiong, H.; Peng, B.; Ren, Z.; Hernandez, X. I. P.; DeLaRiva, A.; Wang, M.; Engelhard, M. H.; Kovarik, L.; Datye, A. K.; Wang, Y. Activation of Surface Lattice Oxygen in Single-Atom Pt/CeO_2 for Low-Temperature CO Oxidation. *Science* **2017,** *358*, 1419-1423.

(74) Zhang, J.; Wu, X.; Cheong, W.-C.; Chen, W.; Lin, R.; Li, J.; Zheng, L.; Yan, W.; Gu, L.; Chen, C.; Peng, Q.; Wang, D.; Li, Y. Cation vacancy stabilization of single-atomic-site Pt1/Ni(OH)x catalyst for diboration of alkynes and alkenes. *Nature Commun.* **2018,** *9*, 1002.

(75) Kwon, Y.; Kim, T. Y.; Kwon, G.; Yi, J.; Lee, H. Selective Activation of Methane on Single-Atom Catalyst of Rhodium Dispersed on Zirconia for Direct Conversion. *J. Am. Chem. Soc.* **2017,** *139*, 17694-17699.

(76) Zhai, Y.; Pierre, D.; Si, R.; Deng, W.; Ferrin, P.; Nilekar, A. U.; Peng, G.; Herron, J. A.; Bell, D. C.; Saltsburg, H.; Mavrikakis, M.; Flytzani-Stephanopoulos, M. Alkali-Stabilized Pt-OHx Species Catalyze Low-Temperature Water-Gas Shift Reactions. *Science* **2010,** *329*, 1633-1636.

(77) Ding, K.; Gulec, A.; Johnson, A. M.; Schweitzer, N. M.; Stucky, G. D.; Marks, L. D.; Stair, P. C. Identification of active sites in CO oxidation and water-gas shift over supported Pt catalysts. *Science* **2015,** *350*, 189-192.

(78) Peterson, E. J.; DeLaRiva, A. T.; Lin, S.; Johnson, R. S.; Guo, H.; Miller, J. T.; Hun Kwak, J.; Peden, C. H. F.; Kiefer, B.; Allard, L. F.; Ribeiro, F. H.; Datye, A. K. Low-temperature carbon monoxide oxidation catalysed by regenerable atomically dispersed palladium on alumina. *Nature Commun.* **2014,** *5*, 4885.

(79) Kwak, J. H.; Hu, J.; Mei, D.; Yi, C.-W.; Kim, D. H.; Peden, C. H. F.; Allard, L. F.; Szanyi, J. Coordinatively Unsaturated Al3+ Centers as Binding Sites for Active Catalyst Phases of Platinum on γ-Al2O3. *Science* **2009,** *325*, 1670-1673.

(80) Zhang, J.; Zhao, Y.; Guo, X.; Chen, C.; Dong, C.-L.; Liu, R.-S.; Han, C.-P.; Li, Y.; Gogotsi, Y.; Wang, G. Single platinum atoms immobilized on an MXene as an efficient catalyst for the hydrogen evolution reaction. *Nat. Catal.* **2018,** *1*, 985-992.

(81) Lin, Y.-C.; Dumcenco, D. O.; Komsa, H.-P.; Niimi, Y.; Krasheninnikov, A. V.; Huang, Y.-S.; Suenaga, K. Properties of Individual Dopant Atoms in Single-Layer MoS2: Atomic Structure, Migration, and Enhanced Reactivity. *Adv. Mater.* **2014,** *26*, 2857-2861.

(82) Liu, G.; Robertson, A. W.; Li, M. M.-J.; Kuo, W. C. H.; Darby, M. T.; Muhieddine, M. H.; Lin, Y.-C.; Suenaga, K.; Stamatakis, M.; Warner, J. H.; Tsang, S. C. E. MoS2 monolayer catalyst doped with isolated Co atoms for the hydrodeoxygenation reaction. *Nat. Chem.* **2017,** *9*, 810.

(83) Li, H.; Wang, S.; Sawada, H.; Han, G. G. D.; Samuels, T.; Allen, C. S.; Kirkland, A. I.; Grossman, J. C.; Warner, J. H. Atomic Structure and Dynamics of Single Platinum Atom Interactions with Monolayer MoS2. *ACS Nano* **2017,** *11*, 3392-3403.

(84) Yan, H.; Cheng, H.; Yi, H.; Lin, Y.; Yao, T.; Wang, C.; Li, J.; Wei, S.; Lu, J. Single-Atom Pd1/Graphene Catalyst Achieved by Atomic Layer Deposition: Remarkable Performance in Selective Hydrogenation of 1,3-Butadiene. *J. Am. Chem. Soc.* **2015,** *137*, 10484-10487.

(85) Vilé, G.; Albani, D.; Nachtegaal, M.; Chen, Z.; Dontsova, D.; Antonietti, M.; López, N.; Pérez-Ramírez, J. A Stable Single-Site Palladium Catalyst for Hydrogenations. *Angew. Chem. Int. Ed.* **2015,** *54*, 11265-11269.

(86) Greiner, M. T.; Jones, T. E.; Beeg, S.; Zwiener, L.; Scherzer, M.; Girgsdies, F.; Piccinin, S.; Armbrüster, M.; Knop-Gericke, A.; Schlögl, R. Free-atom-like d states in single-atom alloy catalysts. *Nat. Chem.* **2018,** *10*, 1008-1015.

(87) Therrien, A. J.; Hensley, A. J. R.; Marcinkowski, M. D.; Zhang, R.; Lucci, F. R.; Coughlin, B.; Schilling, A. C.; McEwen, J.-S.; Sykes, E. C. H. An atomic-scale view of single-site Pt catalysis for low-temperature CO oxidation. *Nat. Catal.* **2018,** *1*, 192-198.

(88) Giannakakis, G.; Flytzani-Stephanopoulos, M.; Sykes, E. C. H. Single-Atom Alloys as a Reductionist Approach to the Rational Design of Heterogeneous Catalysts. *Acc. Chem. Res.* **2019,** *52*, 237-247.

(89) Liu, J.; Lucci, F. R.; Yang, M.; Lee, S.; Marcinkowski, M. D.; Therrien, A. J.; Williams, C. T.; Sykes, E. C. H.; Flytzani-Stephanopoulos, M. Tackling CO Poisoning with Single-Atom Alloy Catalysts. *J. Am. Chem. Soc.* **2016,** *138*, 6396-6399.

(90) Thiel, W. Computational Catalysis—Past, Present, and Future. *Angew. Chem. Int. Ed.* **2014,** *53*, 8605-8613.

(91) Nørskov, J. K.; Abild-Pedersen, F.; Studt, F.; Bligaard, T. Density Functional Theory in Surface Chemistry and Catalysis. *Proceedings of the National Academy of Sciences* **2011,** *108*, 937-943.

(92) Jeff Greeley; Jens K. Nørskov; Mavrikakis, M. Electronic Structure and Catalysis on Metal Surfaces. *Annu. Rev. Phys. Chem.* **2002,** *53*, 319-348.

(93) Van Santen, R. A.; Neurock, M., *Molecular heterogeneous catalysis: a conceptual and computational approach*. John Wiley & Sons: 2009.

(94) Tao, F. F.; Shan, J. J.; Nguyen, L.; Wang, Z.; Zhang, S.; Zhang, L.; Wu, Z.; Huang, W.; Zeng, S.; Hu, P. Understanding Complete Oxidation of Methane on Spinel Oxides at a Molecular Level. *Nature Commun.* **2015,** *6*, 7798.

(95) Sauer, J.; Freund, H.-J. Models in Catalysis. *Catal. Lett.* **2015,** *145*, 109-125.

(96) Greeley, J. Theoretical Heterogeneous Catalysis: Scaling Relationships and Computational Catalyst Design. *Annual Review of Chemical and Biomolecular Engineering* **2016,** *7*, 605-635.

(97) Abild-Pedersen, F.; Greeley, J.; Studt, F.; Rossmeisl, J.; Munter, T.; Moses, P. G.; Skulason, E.; Bligaard, T.; Nørskov, J. K. Scaling Properties Of Adsorption Energies For Hydrogen-Containing Molecules On Transition-Metal Surfaces. *Phys. Rev. Lett.* **2007,** *99*, 016105.

(98) Calle-Vallejo, F.; Martinez, J.; García-Lastra, J. M.; Rossmeisl, J.; Koper, M. Physical and chemical nature of the scaling relations between adsorption energies of atoms on metal surfaces. *Phys. Rev. Lett.* **2012,** *108*, 116103.

(99) Montemore, M. M.; Medlin, J. W. Scaling relations between adsorption energies for computational screening and design of catalysts. *Catal. Sci. Technol.* **2014,** *4*, 3748-3761.

(100) Vojvodic, A.; Hellman, A.; Ruberto, C.; Lundqvist, B. I. From electronic structure to catalytic activity: A single descriptor for adsorption and reactivity on transition-metal carbides. *Phys. Rev. Lett.* **2009,** *103*, 146103.

(101) Vojvodic, A.; Calle-Vallejo, F.; Guo, W.; Wang, S.; Toftelund, A.; Studt, F.; Martinez, J. I.; Shen, J.; Man, I. C.; Rossmeisl, J. On the behavior of Brønsted-Evans-Polanyi relations for transition metal oxides. *J. Chem. Phys.* **2011,** *134*, 244509.

(102) Viñes, F.; Vojvodic, A.; Abild-Pedersen, F.; Illas, F. Brønsted–Evans–Polanyi relationship for transition metal carbide and transition metal oxide surfaces. *J. Phys. Chem. C* **2013,** *117*, 4168-4171.

(103) Mowbray, D.; Martinez, J. I.; Calle-Vallejo, F.; Rossmeisl, J.; Thygesen, K. S.; Jacobsen, K. W.; Nørskov, J. K. Trends in Metal Oxide Stability for Nanorods, Nanotubes, and Surfaces. *J. Phys. Chem. C* **2010,** *115*, 2244-2252.

(104) Fernández, E. M.; Moses, P. G.; Toftelund, A.; Hansen, H. A.; Martínez, J. I.; Abild-Pedersen, F.; Kleis, J.; Hinnemann, B.; Rossmeisl, J.; Bligaard, T. Scaling relationships for adsorption energies on transition metal oxide, sulfide, and nitride surfaces. *Angew. Chem.* **2008,** *120*, 4761-4764.

(105) Evans, M.; Polanyi, M. Inertia and driving force of chemical reactions. *Transactions of the Faraday Society* **1938,** *34*, 11-24.

(106) Loffreda, D.; Delbecq, F.; Vigné, F.; Sautet, P. Fast prediction of selectivity in heterogeneous catalysis from extended Brønsted–Evans–Polanyi relations: a theoretical insight. *Angew. Chem. Int. Ed.* **2009,** *48*, 8978-8980.

(107) Sutton, J. E.; Vlachos, D. G. A Theoretical and Computational Analysis of Linear Free Energy Relations for the Estimation of Activation Energies. *ACS Catal.* **2012,** *2*, 1624-1634.

(108) Bligaard, T.; Nørskov, J. K.; Dahl, S.; Matthiesen, J.; Christensen, C. H.; Sehested, J. The Brønsted–Evans–Polanyi relation and the volcano curve in heterogeneous catalysis. *J. Catal.* **2004,** *224*, 206-217.

(109) Nørskov, J. K.; Bligaard, T.; Rossmeisl, J.; Christensen, C. H. Towards the Computational Design of Solid Catalysts. *Nat. Chem.* **2009,** *1*, 37-46.

(110) Darby, M. T.; Stamatakis, M.; Michaelides, A.; Sykes, E. C. H. Lonely Atoms with Special Gifts: Breaking Linear Scaling Relationships in Heterogeneous Catalysis with Single-Atom Alloys. *J. Phys. Chem. Lett.* **2018,** *9*, 5636-5646.

(111) Sun, G.; Zhao, Z.-J.; Mu, R.; Zha, S.; Li, L.; Chen, S.; Zang, K.; Luo, J.; Li, Z.; Purdy, S. C.; Kropf, A. J.; Miller, J. T.; Zeng, L.; Gong, J. Breaking the scaling

relationship via thermally stable Pt/Cu single atom alloys for catalytic dehydrogenation. *Nature Commun.* **2018,** *9*, 4454.

(112) Hong, X.; Chan, K.; Tsai, C.; Nørskov, J. K. How Doped MoS2 Breaks Transition-Metal Scaling Relations for CO2 Electrochemical Reduction. *ACS Catal.* **2016,** *6*, 4428-4437.

(113) Michalsky, R.; Zhang, Y.-J.; Medford, A. J.; Peterson, A. A. Departures from the Adsorption Energy Scaling Relations for Metal Carbide Catalysts. *J. Phys. Chem. C* **2014,** *118*, 13026-13034.

(114) Gani, T. Z. H.; Kulik, H. J. Understanding and Breaking Scaling Relations in Single-Site Catalysis: Methane to Methanol Conversion by FeIV═O. *ACS Catal.* **2018,** *8*, 975-986.

(115) Peterson, A. A.; Nørskov, J. K. Activity Descriptors for CO2 Electroreduction to Methane on Transition-Metal Catalysts. *J. Phys. Chem. Lett.* **2012,** *3*, 251-258.

(116) Latimer, A. A.; Kakekhani, A.; Kulkarni, A. R.; Nørskov, J. K. Direct Methane to Methanol: The Selectivity–Conversion Limit and Design Strategies. *ACS Catal.* **2018,** *8*, 6894-6907.

(117) Zandkarimi, B.; Alexandrova, A. N. Dynamics of Subnanometer Pt Clusters Can Break the Scaling Relationships in Catalysis. *J. Phys. Chem. Lett.* **2019,** *10*, 460-467.

(118) Sabatier, P. Hydrogénations et deshydrogénations par catalyse. *Eur. J. Inorg. Chem.* **1911,** *44*, 1984-2001.

(119) Medford, A. J.; Vojvodic, A.; Hummelshøj, J. S.; Voss, J.; Abild-Pedersen, F.; Studt, F.; Bligaard, T.; Nilsson, A.; Nørskov, J. K. From the Sabatier principle to a predictive theory of transition-metal heterogeneous catalysis. *J. Catal.* **2015,** *328*, 36-42.

(120) Sabatier, P., *La catalyse en chimie organique*. Librairie polytechnique: Paris et Liege, 1920.

(121) Jacobsen, C. J. H.; Dahl, S.; Clausen, B. S.; Bahn, S.; Logadottir, A.; Nørskov, J. K. Catalyst Design by Interpolation in the Periodic Table: Bimetallic Ammonia Synthesis Catalysts. *J. Am. Chem. Soc.* **2001,** *123*, 8404-8405.

(122) Cheng, J.; Hu, P. Utilization of the Three-Dimensional Volcano Surface To Understand the Chemistry of Multiphase Systems in Heterogeneous Catalysis. *J. Am. Chem. Soc.* **2008,** *130*, 10868-10869.

(123) Nørskov, J. K.; Rossmeisl, J.; Logadottir, A.; Lindqvist, L.; Kitchin, J. R.; Bligaard, T.; Jonsson, H. Origin Of The Overpotential For Oxygen Reduction At A Fuel-Cell Cathode. *J. Phys. Chem. B* **2004,** *108*, 17886-17892.

(124) Stephens, I. E. L.; Bondarenko, A. S.; Perez-Alonso, F. J.; Calle-Vallejo, F.; Bech, L.; Johansson, T. P.; Jepsen, A. K.; Frydendal, R.; Knudsen, B. P.; Rossmeisl, J.; Chorkendorff, I. Tuning the Activity of Pt(111) for Oxygen Electroreduction by Subsurface Alloying. *J. Am. Chem. Soc.* **2011,** *133*, 5485-5491.

(125) Greeley, J.; Jaramillo, T. F.; Bonde, J.; Chorkendorff, I.; Nørskov, J. K. Computational high-throughput screening of electrocatalytic materials for hydrogen evolution. *Nature Mater.* **2006,** *5*, 909-913.

(126) Lendvay, G. Bond orders from ab initio calculations and a test of the principle of bond order conservation. *J. Phys. Chem.* **1989,** *93*, 4422-4429.

(127) Shustorovich, E. Chemisorption Phenomena: Analytic Modeling Based on Perturbation Theory and Bond-Order Conservation. *Surf. Sci. Rep.* **1986,** *6*, 1-63.

(128) Van Santen, R. On Shustorovich's Bond‐Order Conservation Method as Applied to Chemisorption. *Recueil des Travaux Chimiques des Pays‐Bas* **1990,** *109*, 59-63.

(129) Shustorovich, E. Activation barrier for adsorbate surface diffusion, heat of chemisorption, and adsorbate registry: theoretical interrelations. *J. Am. Chem. Soc.* **1984,** *106*, 6479-6481.

(130) Shustorovich, E. Bond making and breaking on transition-metal surfaces: Theoretical projections based on bond-order conservation. *Surf. Sci.* **1986,** *176*, L863-L872.

(131) Shustorovich, E.; Bell, A. T. Decomposition and reduction of NO on transition metal surfaces: bond order conservation Morse potential analysis. *Surf. Sci.* **1993,** *289*, 127-138.

(132) van Santen, R. A.; Tranca, I. How molecular is the chemisorptive bond? *Phys. Chem. Chem. Phys.* **2016,** *18*, 20868-20894.

(133) Nørskov, J. K. Covalent effects in the effective-medium theory of chemical binding: Hydrogen heats of solution in the 3d metals. *Phys. Rev. B* **1982,** *26*, 2875-2885.

(134) Hammer, B.; Nørskov, J. Why Gold is the Noblest of all the Metals. *Nature* **1995,** *376*, 238-240.

(135) Hammer, B.; Nørskov, J. K. Electronic factors determining the reactivity of metal surfaces. *Surf. Sci.* **1995,** *343*, 211-220.

(136) Mpourmpakis, G.; Andriotis, A. N.; Vlachos, D. G. Identification of descriptors for the CO interaction with metal nanoparticles. *Nano Lett.* **2010,** *10*, 1041-1045.

(137) Calle‐Vallejo, F.; Martínez, J. I.; García‐Lastra, J. M.; Sautet, P.; Loffreda, D. Fast Prediction of Adsorption Properties for Platinum Nanocatalysts with Generalized Coordination Numbers. *Angew. Chem. Int. Ed.* **2014,** *53*, 8316-8319.

(138) Calle-Vallejo, F.; Loffreda, D.; Koper, M. T.; Sautet, P. Introducing Structural Sensitivity Into Adsorption-Energy Scaling Relations by Means of Coordination Numbers. *Nat. Chem.* **2015,** *7*, 403-410.

(139) Ma, X.; Xin, H. Orbitalwise Coordination Number for Predicting Adsorption Properties of Metal Nanocatalysts. *Phys. Rev. Lett.* **2017,** *118*, 036101.

(140) Lee, Y.-L.; Kleis, J.; Rossmeisl, J.; Shao-Horn, Y.; Morgan, D. Prediction of Solid Oxide Fuel Cell Cathode Activity with First-Principles Descriptors. *Energy Environ. Sci.* **2011,** *4*, 3966-3970.

(141) Pavone, M.; Ritzmann, A. M.; Carter, E. A. Quantum-mechanics-based design principles for solid oxide fuel cell cathode materials. *Energy Environ. Sci.* **2011,** *4*, 4933-4937.

(142) Deml, A. M.; Stevanović, V.; Muhich, C. L.; Musgrave, C. B.; O'Hayre, R. Oxide enthalpy of formation and band gap energy as accurate descriptors of oxygen vacancy formation energetics. *Energy Environ. Sci.* **2014,** *7*, 1996-2004.

(143) van Santen, R. A.; Tranca, I.; Hensen, E. J. Theory of Surface Chemistry and Reactivity of Reducible Oxides. *Catal. Today* **2015,** *244*, 63-84.

(144) Suntivich, J.; Gasteiger, H. A.; Yabuuchi, N.; Nakanishi, H.; Goodenough, J. B.; Shao-Horn, Y. Design Principles for Oxygen-Reduction Activity on Perovskite Oxide Catalysts for Fuel Cells and Metal–Air Batteries. *Nat. Chem.* **2011,** *3*, 546-550.

(145) Hwang, J.; Rao, R. R.; Giordano, L.; Katayama, Y.; Yu, Y.; Shao-Horn, Y. Perovskites in catalysis and electrocatalysis. *Science* **2017,** *358*, 751-756.

(146) Calle-Vallejo, F.; Inoglu, N. G.; Su, H.-Y.; Martínez, J. I.; Man, I. C.; Koper, M. T.; Kitchin, J. R.; Rossmeisl, J. Number of outer electrons as descriptor for adsorption processes on transition metals and their oxides. *Chemical Science* **2013,** *4*, 1245-1249.

(147) Zeng, Z.; Calle-Vallejo, F.; Mogensen, M. B.; Rossmeisl, J. Generalized Trends in the Formation Energies of Perovskite Oxides. *Phys. Chem. Chem. Phys.* **2013,** *15*, 7526-7533.

(148) Arndtsen, B. A.; Bergman, R. G.; Mobley, T. A.; Peterson, T. H. Selective Intermolecular Carbon-Hydrogen Bond Activation by Synthetic Metal Complexes in Homogeneous Solution. *Acc. Chem. Res.* **1995,** *28*, 154-162.

(149) Wang, B.; Albarracín-Suazo, S.; Pagán-Torres, Y.; Nikolla, E. Advances in methane conversion processes. *Catal. Today* **2017,** *285*, 147-158.

(150) Ravi, M.; Ranocchiari, M.; van Bokhoven, J. A. The Direct Catalytic Oxidation of Methane to Methanol—A Critical Assessment. *Angew. Chem. Int. Ed.* **2017,** *56,* 16464-16483.

(151) Schwarz, H. Chemistry with Methane: Concepts Rather than Recipes. *Angew. Chem. Int. Ed.* **2011,** *50,* 10096-10115.

(152) Horn, R.; Schlögl, R. Methane Activation by Heterogeneous Catalysis. *Catal. Lett.* **2015,** *145,* 23-39.

(153) Bradford, M. C. J.; Vannice, M. A. CO2 Reforming of CH4. *Catalysis Reviews* **1999,** *41*, 1-42.

(154) Upham, D. C.; Agarwal, V.; Khechfe, A.; Snodgrass, Z. R.; Gordon, M. J.; Metiu, H.; McFarland, E. W. Catalytic molten metals for the direct conversion of methane to hydrogen and separable carbon. *Science* **2017,** *358*, 917-921.

(155) Moghimpour Bijani, P.; Sohrabi, M.; Sahebdelfar, S. Thermodynamic Analysis of Nonoxidative Dehydroaromatization of Methane. *Chem. Eng. Technol.* **2012,** *35,* 1825-1832.

(156) Yin, F.; Li, M.-R.; Wang, G.-C. Periodic density functional theory analysis of direct methane conversion into ethylene and aromatic hydrocarbons catalyzed by Mo4C2/ZSM-5. *Phys. Chem. Chem. Phys.* **2017,** *19*, 22243-22255.

(157) Gao, J.; Zheng, Y.; Jehng, J.-M.; Tang, Y.; Wachs, I. E.; Podkolzin, S. G. Identification of molybdenum oxide nanostructures on zeolites for natural gas conversion. *Science* **2015,** *348,* 686-690.

(158) Guo, X.; Fang, G.; Li, G.; Ma, H.; Fan, H.; Yu, L.; Ma, C.; Wu, X.; Deng, D.; Wei, M.; Tan, D.; Si, R.; Zhang, S.; Li, J.; Sun, L.; Tang, Z.; Pan, X.; Bao, X. Direct, Nonoxidative Conversion of Methane to Ethylene, Aromatics, and Hydrogen. *Science* **2014,** *344*, 616-619.

(159) Keller, G. E.; Bhasin, M. M. Synthesis of ethylene via oxidative coupling of methane: I. Determination of active catalysts. *J. Catal.* **1982,** *73*, 9-19.

(160) Zavyalova, U.; Holena, M.; Schlögl, R.; Baerns, M. Statistical Analysis of Past Catalytic Data on Oxidative Methane Coupling for New Insights into the Composition of High-Performance Catalysts. *ChemCatChem* **2011,** *3*, 1935-1947.

(161) Chin, Y.-H.; Buda, C.; Neurock, M.; Iglesia, E. Consequences of Metal–Oxide Interconversion for C–H Bond Activation during CH4 Reactions on Pd Catalysts. *J. Am. Chem. Soc.* **2013,** *135*, 15425-15442.

(162) Gambo, Y.; Jalil, A. A.; Triwahyono, S.; Abdulrasheed, A. A. Recent advances and future prospect in catalysts for oxidative coupling of methane to ethylene: A review. *Journal of Industrial and Engineering Chemistry* **2018,** *59*, 218-229.

(163) Wang, P.; Zhao, G.; Wang, Y.; Lu, Y. MnTiO3-driven low-temperature oxidative coupling of methane over TiO2-doped Mn2O3-Na2WO4/SiO2 catalyst. *Science Advances* **2017,** *3*, e1603180.

(164) Wang, P.; Zhao, G.; Liu, Y.; Lu, Y. TiO2-doped Mn2O3-Na2WO4/SiO2 catalyst for oxidative coupling of methane: Solution combustion synthesis and MnTiO3-dependent low-temperature activity improvement. *Appl. Catal., A* **2017,** *544*, 77-83.

(165) Otsuka, K.; Komatsu, T. Active catalysts in oxidative coupling of methane. *J. Chem. Soc., Chem. Commun.* **1987**, 388-389.

(166) Labinger, J. A. Oxidative coupling of methane: An inherent limit to selectivity? *Catal. Lett.* **1988,** *1*, 371-375.

(167) Zhu, Q.; Wegener, S. L.; Xie, C.; Uche, O.; Neurock, M.; Marks, T. J. Sulfur as a selective 'soft' oxidant for catalytic methane conversion probed by experiment and theory. *Nat Chem* **2013,** *5*, 104-9.

(168) Lu, Y.; Dixon, A. G.; Moser, W. R.; Hua Ma, Y. Oxidative coupling of methane in a modified γ-alumina membrane reactor. *Chem. Eng. Sci.* **2000,** *55*, 4901-4912.

(169) Farrell, B. L.; Igenegbai, V. O.; Linic, S. A Viewpoint on Direct Methane Conversion to Ethane and Ethylene Using Oxidative Coupling on Solid Catalysts. *ACS Catal.* **2016,** *6*, 4340-4346.

(170) Olivier, L.; Haag, S.; Mirodatos, C.; van Veen, A. C. Oxidative coupling of methane using catalyst modified dense perovskite membrane reactors. *Catal. Today* **2009,** *142*, 34-41.

(171) Das, A.; Xhafa, E.; Nikolla, E. Electro- and thermal-catalysis by layered, first series Ruddlesden-Popper oxides. *Catal. Today* **2016,** *277*, 214-226.

(172) Shilov, A. E.; Shul'pin, G. B. Activation of C−H Bonds by Metal Complexes. *Chem. Rev.* **1997,** *97*, 2879-2932.

(173) Periana, R. A.; Bhalla, G.; Tenn, W. J.; Young, K. J. H.; Liu, X. Y.; Mironov, O.; Jones, C. J.; Ziatdinov, V. R. Perspectives on some challenges and approaches for developing the next generation of selective, low temperature, oxidation catalysts for alkane hydroxylation based on the CH activation reaction. *J. Mol. Catal. A: Chem.* **2004,** *220*, 7-25.

(174) Periana, R. A.; Taube, D. J.; Evitt, E. R.; Löffler, D. G.; Wentrcek, P. R.; Voss, G.; Masuda, T. A Mercury-Catalyzed, High-Yield System for the Oxidation of Methane to Methanol. *Science* **1993,** *259*, 340-343.

(175) Periana, R. A.; Taube, D. J.; Gamble, S.; Taube, H.; Satoh, T.; Fujii, H. Platinum Catalysts for the High-Yield Oxidation of Methane to a Methanol Derivative. *Science* **1998,** *280*, 560-564.

(176) Ahlquist, M.; Nielsen, R. J.; Periana, R. A.; Goddard Iii, W. A. Product Protection, the Key to Developing High Performance Methane Selective Oxidation Catalysts. *J. Am. Chem. Soc.* **2009,** *131*, 17110-17115.

(177) Jones, C.; Taube, D.; Ziatdinov, V. R.; Periana, R. A.; Nielsen, R. J.; Oxgaard, J.; Goddard III, W. A. Selective Oxidation of Methane to Methanol Catalyzed, with C-H Activation, by Homogeneous, Cationic Gold. *Angew. Chem. Int. Ed.* **2004,** *43*, 4626-4629.

(178) Hakemian, A. S.; Rosenzweig, A. C. The Biochemistry of Methane Oxidation. *Annu. Rev. Biochem* **2007,** *76*, 223-241.

(179) Balasubramanian, R.; Smith, S. M.; Rawat, S.; Yatsunyk, L. A.; Stemmler, T. L.; Rosenzweig, A. C. Oxidation of methane by a biological dicopper centre. *Nature* **2010,** *465*, 115.

(180) Lieberman, R. L.; Rosenzweig, A. C. Crystal structure of a membrane-bound metalloenzyme that catalyses the biological oxidation of methane. *Nature* **2005,** *434*, 177.

(181) Park, D.; Lee, J. Biological conversion of methane to methanol. *Korean J. Chem. Eng.* **2013,** *30*, 977-987.

(182) Que Jr, L.; Tolman, W. B. Biologically inspired oxidation catalysis. *Nature* **2008,** *455*, 333.

(183) Haynes, C. A.; Gonzalez, R. Rethinking biological activation of methane and conversion to liquid fuels. *Nat. Chem. Biol.* **2014,** *10*, 331.

(184) Friedle, S.; Reisner, E.; Lippard, S. J. Current challenges of modeling diiron enzyme active sites for dioxygen activation by biomimetic synthetic complexes. *Chem. Soc. Rev.* **2010,** *39*, 2768-2779.

(185) Tinberg, C. E.; Lippard, S. J. Dioxygen Activation in Soluble Methane Monooxygenase. *Acc. Chem. Res.* **2011,** *44*, 280-288.

(186) Himes, R. A.; Barnese, K.; Karlin, K. D. One is Lonely and Three is a Crowd: Two Coppers Are for Methane Oxidation. *Angew. Chem. Int. Ed.* **2010,** *49*, 6714-6716.

(187) Groothaert, M. H.; Smeets, P. J.; Sels, B. F.; Jacobs, P. A.; Schoonheydt, R. A. Selective Oxidation of Methane by the Bis(μ-oxo)dicopper Core Stabilized on ZSM-5 and Mordenite Zeolites. *J. Am. Chem. Soc.* **2005,** *127*, 1394-1395.

(188) Woertink, J. S.; Smeets, P. J.; Groothaert, M. H.; Vance, M. A.; Sels, B. F.; Schoonheydt, R. A.; Solomon, E. I. A [Cu2O]2+ core in Cu-ZSM-5, the active site in the oxidation of methane to methanol. *Proceedings of the National Academy of Sciences* **2009,** *106*, 18908-18913.

(189) Baek, J.; Rungtaweevoranit, B.; Pei, X.; Park, M.; Fakra, S. C.; Liu, Y.-S.; Matheu, R.; Alshmimri, S. A.; Alshehri, S.; Trickett, C. A.; Somorjai, G. A.; Yaghi, O. M. Bioinspired Metal–Organic Framework Catalysts for Selective Methane Oxidation to Methanol. *J. Am. Chem. Soc.* **2018,** *140*, 18208-18216.

(190) Snyder, B. E. R.; Vanelderen, P.; Bols, M. L.; Hallaert, S. D.; Böttger, L. H.; Ungur, L.; Pierloot, K.; Schoonheydt, R. A.; Sels, B. F.; Solomon, E. I. The active site of low-temperature methane hydroxylation in iron-containing zeolites. *Nature* **2016,** *536*, 317.

(191) Hammond, C.; Forde, M. M.; Ab Rahim, M. H.; Thetford, A.; He, Q.; Jenkins, R. L.; Dimitratos, N.; Lopez-Sanchez, J. A.; Dummer, N. F.; Murphy, D. M.; Carley, A. F.; Taylor, S. H.; Willock, D. J.; Stangland, E. E.; Kang, J.; Hagen, H.; Kiely, C. J.; Hutchings, G. J. Direct Catalytic Conversion of Methane to Methanol in an Aqueous Medium by using Copper-Promoted Fe-ZSM-5. *Angew. Chem. Int. Ed.* **2012,** *51*, 5129-5133.

(192) Zhao, Z.-J.; Kulkarni, A.; Vilella, L.; Nørskov, J. K.; Studt, F. Theoretical Insights into the Selective Oxidation of Methane to Methanol in Copper-Exchanged Mordenite. *ACS Catal.* **2016,** *6*, 3760-3766.

(193) Yumura, T.; Hirose, Y.; Wakasugi, T.; Kuroda, Y.; Kobayashi, H. Roles of Water Molecules in Modulating the Reactivity of Dioxygen-Bound Cu-ZSM-5 toward Methane: A Theoretical Prediction. *ACS Catal.* **2016,** *6*, 2487-2495.

(194) Grundner, S.; Markovits, M. A. C.; Li, G.; Tromp, M.; Pidko, E. A.; Hensen, E. J. M.; Jentys, A.; Sanchez-Sanchez, M.; Lercher, J. A. Single-site trinuclear copper oxygen clusters in mordenite for selective conversion of methane to methanol. *Nature Commun.* **2015,** *6*, 7546.

(195) Vanelderen, P.; Snyder, B. E. R.; Tsai, M.-L.; Hadt, R. G.; Vancauwenbergh, J.; Coussens, O.; Schoonheydt, R. A.; Sels, B. F.; Solomon, E. I. Spectroscopic Definition of the Copper Active Sites in Mordenite: Selective Methane Oxidation. *J. Am. Chem. Soc.* **2015,** *137*, 6383-6392.

(196) Palkovits, R.; Antonietti, M.; Kuhn, P.; Thomas, A.; Schüth, F. Solid Catalysts for the Selective Low-Temperature Oxidation of Methane to Methanol. *Angew. Chem. Int. Ed.* **2009,** *48*, 6909-6912.

(197) Sattler, J. J. H. B.; Ruiz-Martinez, J.; Santillan-Jimenez, E.; Weckhuysen, B. M. Catalytic Dehydrogenation of Light Alkanes on Metals and Metal Oxides. *Chem. Rev.* **2014,** *114*, 10613-10653.

(198) Gartner, C. A.; van Veen, A. C.; Lercher, J. A. Oxidative Dehydrogenation of Ethane: Common Principles and Mechanistic Aspects. *ChemCatChem* **2013,** *5*, 3196-3217.

(199) Weaver, J. F.; Hakanoglu, C.; Antony, A.; Asthagiri, A. Alkane activation on crystalline metal oxide surfaces. *Chem. Soc. Rev.* **2014,** *43*, 7536-47.

(200) Tait, S. L.; Dohnálek, Z.; Campbell, C. T.; Kay, B. D. n-alkanes on Pt(111) and on C(0001) / Pt(111): Chain length dependence of kinetic desorption parameters. *J. Chem. Phys.* **2006,** *125*, 234308.

(201) Tait, S. L.; Dohnálek, Z.; Campbell, C. T.; Kay, B. D. n-alkanes on MgO(100). II. Chain length dependence of kinetic desorption parameters for small n-alkanes. *J. Chem. Phys.* **2005,** *122*, 164708.

(202) Weaver, J. F.; Hakanoglu, C.; Hawkins, J. M.; Asthagiri, A. Molecular Adsorption of Small Alkanes on a PdO(101) Thin Film: Evidence of Sigma-Complex Formation. *J. Chem. Phys.* **2010,** *132*, 024709.

(203) Weaver, J. F.; Carlsson, A. F.; Madix, R. J. The adsorption and reaction of low molecular weight alkanes on metallic single crystal surfaces. *Surf. Sci. Rep.* **2003,** *50*, 107-199.

(204) McNaught, A. D., *Compendium of chemical terminology*. Blackwell Science Oxford: 1997; Vol. 1669.

(205) Latimer, A. A.; Kulkarni, A. R.; Aljama, H.; Montoya, J. H.; Yoo, J. S.; Tsai, C.; Abild-Pedersen, F.; Studt, F.; Nørskov, J. K. Understanding Trends in CH Bond Activation in Heterogeneous Catalysis. *Nature Mater.* **2017,** *16*, 225-229.

(206) Kumar, G.; Lau, S. L. J.; Krcha, M. D.; Janik, M. J. Correlation of Methane Activation and Oxide Catalyst Reducibility and its Implications for Oxidative Coupling. *ACS Catal.* **2016,** *6*, 1812-1821.

(207) Tyo, E. C.; Yin, C.; Di Vece, M.; Qian, Q.; Kwon, G.; Lee, S.; Lee, B.; DeBartolo, J. E.; Seifert, S.; Winans, R. E.; Si, R.; Ricks, B.; Goergen, S.; Rutter, M.; Zugic, B.; Flytzani-Stephanopoulos, M.; Wang, Z. W.; Palmer, R. E.; Neurock, M.; Vajda, S. Oxidative dehydrogenation of cyclohexane on cobalt oxide (Co_3O_4) nanoparticles: The effect of particle size on activity and selectivity. *ACS Catal.* **2012,** *2*, 2409-2423.

(208) Latimer, A. A.; Aljama, H.; Kakekhani, A.; Yoo, J. S.; Kulkarni, A.; Tsai, C.; Garcia-Melchor, M.; Abild-Pedersen, F.; Nørskov, J. K. Mechanistic Insights Into Heterogeneous Methane Activation. *Phys. Chem. Chem. Phys.* **2017,** *19*, 3575-3581.

(209) Liu, Z.-P.; Hu, P. General Rules for Predicting Where a Catalytic Reaction Should Occur on Metal Surfaces: A Density Functional Theory Study of C−H and C−O Bond Breaking/Making on Flat, Stepped, and Kinked Metal Surfaces. *J. Am. Chem. Soc.* **2003,** *125*, 1958-1967.

(210) Antony, A.; Asthagiri, A.; Weaver, J. F. Pathways and kinetics of methane and ethane C–H bond cleavage on PdO(101). *J. Chem. Phys.* **2013,** *139*, 104702.

(211) Driscoll, D. J.; Martir, W.; Wang, J. X.; Lunsford, J. H. Formation of gas-phase methyl radicals over magnesium oxide. *J. Am. Chem. Soc.* **1985,** *107*, 58-63.

(212) Kwapien, K.; Paier, J.; Sauer, J.; Geske, M.; Zavyalova, U.; Horn, R.; Schwach, P.; Trunschke, A.; Schlögl, R. Sites for Methane Activation on Lithium-Doped Magnesium Oxide Surfaces. *Angew. Chem. Int. Ed.* **2014,** *53*, 8774-8778.

(213) Feyel, S.; Döbler, J.; Schröder, D.; Sauer, J.; Schwarz, H. Thermal activation of methane by tetranuclear [V4O10]+. *Angew. Chem. Int. Ed.* **2006,** *45*, 4681-4685.

(214) Dietl, N.; Höckendorf, R. F.; Schlangen, M.; Lerch, M.; Beyer, M. K.; Schwarz, H. Generation, Reactivity Towards Hydrocarbons, and Electronic Structure of Heteronuclear Vanadium Phosphorous Oxygen Cluster Ions. *Angew. Chem. Int. Ed.* **2011,** *50*, 1430-1434.

(215) Chen, K.; Wang, Z.-C.; Schlangen, M.; Wu, Y.-D.; Zhang, X.; Schwarz, H. Thermal Activation of Methane and Ethene by Bare MO.+ (M=Ge, Sn, and Pb): A Combined Theoretical/Experimental Study. *Chemistry – A European Journal* **2011,** *17*, 9619-9625.

(216) Feyel, S.; Döbler, J.; Höckendorf, R.; Beyer, M. K.; Sauer, J.; Schwarz, H. Activation of Methane by Oligomeric (Al2O3)x+ (x=3,4,5): The Role of Oxygen-Centered Radicals in Thermal Hydrogen-Atom Abstraction. *Angew. Chem. Int. Ed.* **2008,** *47*, 1946-1950.

(217) de Petris, G.; Troiani, A.; Rosi, M.; Angelini, G.; Ursini, O. Methane Activation by Metal-Free Radical Cations: Experimental Insight into the Reaction Intermediate. *Chemistry – A European Journal* **2009,** *15*, 4248-4252.

(218) Wu, X.-N.; Zhao, Y.-X.; Xue, W.; Wang, Z.-C.; He, S.-G.; Ding, X.-L. Active sites of stoichiometric cerium oxide cations (CemO2m+) probed by reactions with carbon monoxide and small hydrocarbon molecules. *Phys. Chem. Chem. Phys.* **2010,** *12*, 3984-3997.

(219) Dietl, N.; Schlangen, M.; Schwarz, H. Thermal Hydrogen-Atom Transfer from Methane: The Role of Radicals and Spin States in Oxo-Cluster Chemistry. *Angew. Chem. Int. Ed.* **2012,** *51*, 5544-5555.

(220) Li, J.; Zhou, S.; Zhang, J.; Schlangen, M.; Weiske, T.; Usharani, D.; Shaik, S.; Schwarz, H. Electronic Origins of the Variable Efficiency of Room-Temperature Methane Activation by Homo- and Heteronuclear Cluster Oxide Cations [XYO2]+ (X, Y = Al, Si, Mg): Competition between Proton-Coupled Electron Transfer and Hydrogen-Atom Transfer. *J. Am. Chem. Soc.* **2016,** *138*, 7973-7981.

(221) van Santen, R. A.; Neurock, M.; Shetty, S. G. Reactivity Theory of Transition-Metal Surfaces: A Brønsted− Evans− Polanyi Linear Activation Energy− Free-Energy Analysis. *Chem. Rev.* **2009,** *110*, 2005-2048.

(222) Deshlahra, P.; Iglesia, E. Reactivity and Selectivity Descriptors for the Activation of C-H Bonds in Hydrocarbons and Oxygenates on Metal Oxides. *J. Phys. Chem. C* **2016,** *120*, 16741-16760.

(223) Deshlahra, P.; Iglesia, E. Toward More Complete Descriptors of Reactivity in Catalysis by Solid Acids. *ACS Catal.* **2016,** *6*, 5386-5392.

(224) Yoo, J. S.; Khan, T. S.; Abild-Pedersen, F.; Nørskov, J. K.; Studt, F. On the role of the surface oxygen species during A–H (A = C, N, O) bond activation: a density functional theory study. *Chem. Commun.* **2015,** *51*, 2621-2624.

(225) Wang, C.-C.; Siao, S. S.; Jiang, J.-C. C–H Bond Activation of Methane via σ–d Interaction on the IrO_2 (110) Surface: Density Functional Theory Study. *J. Phys. Chem. C* **2012,** *116*, 6367-6370.

(226) Tsuji, Y.; Yoshizawa, K. Adsorption and Activation of Methane on the (110) Surface of Rutile-type Metal Dioxides. *J. Phys. Chem. C* **2018,** *122*, 15359-15381.

(227) Crabtree, R. H. Transition Metal Complexation of σ Bonds. *Angew. Chem., Int. Ed. Engl.* **1993,** *32*, 789-805.

(228) Saillard, J. Y.; Hoffmann, R. Carbon-Hydrogen and Hydrogen-Hydrogen Activation in Transition Metal Complexes and on Surfaces. *J. Am. Chem. Soc.* **1984,** *106*, 2006-2026.

(229) Wang, Z.-C.; Dietl, N.; Kretschmer, R.; Ma, J.-B.; Weiske, T.; Schlangen, M.; Schwarz, H. Direct Conversion of Methane into Formaldehyde Mediated by [Al2O3].+ at Room Temperature. *Angew. Chem. Int. Ed.* **2012,** *51*, 3703-3707.

(230) Zhou, S.; Li, J.; Schlangen, M.; Schwarz, H. The Origin of the Efficient, Thermal Chemisorption of Methane by the Heteronuclear Metal-Oxide Cluster [Al2TaO5]+. *Angew. Chem. Int. Ed.* **2016,** *55*, 14867-14871.

(231) Zhou, S.; Yue, L.; Schlangen, M.; Schwarz, H. Electronic Origin of the Competitive Mechanisms in the Thermal Activation of Methane by the Heteronuclear Cluster Oxide [Al2ZnO4].+. *Angew. Chem. Int. Ed.* **2017,** *56*, 14297-14300.

(232) Schröder, D.; Roithová, J. Low-Temperature Activation of Methane: It also Works Without a Transition Metal. *Angew. Chem. Int. Ed.* **2006,** *45*, 5705-5708.

(233) Liang, Z.; Li, T.; Kim, M.; Asthagiri, A.; Weaver, J. F. Low-Temperature Activation of Methane on the IrO_2 (110) Surface. *Science* **2017,** *356*, 299-303.

(234) Lustemberg, P. G.; Ramírez, P. J.; Liu, Z.; Gutierrez, R. A.; Grinter, D. G.; Carrasco, J.; Senanayake, S. D.; Rodriguez, J. A.; Ganduglia-Pirovano, M. V. Room-Temperature Activation of Methane and Dry Re-Forming With CO_2 On Ni-CeO_2 (111) Surfaces: Effect of Ce^{3+} Sites and Metal–Support Interactions on C–H Bond Cleavage. *ACS Catal.* **2016,** *6*, 8184-8191.

(235) Prats, H.; Gutiérrez, R. A.; Piñero, J. J.; Viñes, F.; Bromley, S. T.; Ramírez, P. J.; Rodriguez, J. A.; Illas, F. Room Temperature Methane Capture and Activation by Ni Clusters Supported on TiC(001): Effects of Metal–Carbide Interactions on the Cleavage of the C–H Bond. *J. Am. Chem. Soc.* **2019**.

(236) Su, Y.-Q.; Liu, J.-X.; Filot, I. A. W.; Zhang, L.; Hensen, E. J. M. Highly Active and Stable CH4 Oxidation by Substitution of Ce4+ by Two Pd2+ Ions in CeO2(111). *ACS Catal.* **2018,** *8*, 6552-6559.

(237) Liu, Z.; Grinter, D. C.; Lustemberg, P. G.; Nguyen-Phan, T.-D.; Zhou, Y.; Luo, S.; Waluyo, I.; Crumlin, E. J.; Stacchiola, D. J.; Zhou, J.; Carrasco, J.; Busnengo, H. F.; Ganduglia-Pirovano, M. V.; Senanayake, S. D.; Rodriguez, J. A. Dry Reforming of Methane on a Highly-Active Ni-CeO2 Catalyst: Effects of Metal-Support Interactions on C−H Bond Breaking. *Angew. Chem. Int. Ed.* **2016,** *55*, 7455-7459.

(238) Liu, Z.; Lustemberg, P.; Gutiérrez, R. A.; Carey, J. J.; Palomino, R. M.; Vorokhta, M.; Grinter, D. C.; Ramírez, P. J.; Matolín, V.; Nolan, M.; Ganduglia-Pirovano, M. V.; Senanayake, S. D.; Rodriguez, J. A. In Situ Investigation of Methane Dry Reforming on Metal/Ceria(111) Surfaces: Metal–Support Interactions and C−H Bond Activation at Low Temperature. *Angew. Chem. Int. Ed.* **2017,** *56*, 13041-13046.

2 Computational methods

2.1 Density functional theory

In this thesis we focus exclusively on 'first principles' techniques; empirical methods using reactive force fields such as reaxFF or tight binding methods such as DFTB will not be discussed, though they may be used to study heterogeneous catalysis as well. First principles, sometimes used interchangeably as *ab initio,* refers to studies from established laws without preconceptions or empirical assumptions. First principles calculations have now become a staple tool for studying surface chemistry and catalysis.

The fundamental equation for electronic structure calculations is the non-relativistic time-independent Schrödinger equation:

$$\hat{H}\psi = E\psi$$

where ψ, H, E are the wavefunction of the system, the Hamiltonian, and the total energy, respectively. This equation is further simplified by the Born-Oppenheimer approximation which splits the expression into the nuclear and electronic components due to atomic motions being several orders of magnitude slower than electrons. This allows the electronic and nuclear components to be calculated separately.

To solve the electronic structure, a number of methods have been developed. In the Hartree-Fock self-consistent field method, the total wavefunction of the system is written as the product of one-electron wavefunctions in a mean field approach. This method lacks electron-correlation effects, which must be included through additional means such as

configuration interaction methods, which involve adding unoccupied one-electron wavefunctions to include excited state contributions to the total wavefunction. Alternatively, quantum Monte Carlo methods can be used to incorporate electron correlation such as through Monte Carlo sampling to solve the many-electron wavefunction variationally from trial functions.

Density functional theory is arguably one of the most widespread and broadly applied of those methods for electronic structure calculations used today.[1] A key appeal and reason for its widespread adoption is due to the significantly lower computational scaling compared to wavefunction based methods, based on 3N coordinates for N electrons rather than three for the electron density. The basis of density functional theory is described by two theorems by Hohenberg and Kohn.[2] (1) The electron density uniquely determines the ground state properties of a system. (2) The functional of the energy of the system is a minimum for the ground state electron density (i.e. the variational principle). The functional determining the energy of the system is unknown, and the Kohn-Sham approach is used by decomposing the total energy into kinetic, Coulombic and the exchange-correlation (XC) contributions, the first two terms whose exact forms are known and computable.[3] The exact form of the XC portion remains unknown, and finding more accurate approximations to obtain the XC energy is an ongoing problem in DFT.

2.1.1 The exchange-correlation functional

As described previously, the DFT is in principle exact, and the Kohn-Sham equation leads to the exact energy if the XC functional is known. In reality, various approximate XC functionals are used in practice to describe the systems of study with varying degrees of success. Compared to wavefunction based methods, there is no clear path to improvability for DFT methods. Nevertheless, various DFT functionals can be classified on a 'Jacob's ladder' for DFT[4] The on the bottom rung of Jacob's ladder starts with the local density approximation (LDA) based on the homogenous electron gas model and depends only on the local density ρ. LDA works well, unsurprisingly, in bulk systems where electron density remains homogeneous and varies gradually, but fails in most applications to molecules and surfaces. To incorporate inhomogeneities in election density, the density gradient $\nabla\rho$ is also used in the generalized gradient approximation (GGA), of these PW91[5] and PBE[6] remain the most popular. GGAs such as PBE remain a workhorse functional in surface chemistry and catalysis due to its non-empirical nature, computational affordability and moderate accuracy across diverse systems. A further improvement of this concept is the incorporation of the second derivative information of the density, the density Laplacian $\nabla\rho^2$ and the kinetic energy density to make meta-generalized gradient approximation functionals (meta-GGA). These include the functionals such as M06-L,[7] TPSS,[8] and SCAN.[9]

To address the problem of electron self-interaction,[10] and to a limited extent strong correlation interactions,[11-12] hybrid functionals can be used, which involves the replacement of a fraction (usually 20-30%) of the local exchange functional with the

Hartree-Fock exact exchange functional.[13] Both semi-empirical hybrid functionals such as B3LYP[14] and non-empirical functionals such as PBE0[15] and HSE06[16] are commonly used. This method can also be extended to meta-GGAs to make hybrid meta-GGAs such as TPSSh.[17] For computational catalysis, hybrid functionals remain computationally prohibitive for most systems, especially where many reaction barriers and transition state search calculations are involved. In an alternative approach based on the Hubbard model,[18] DFT+U applies an on-site Coulomb interaction term U and an exchange term J on the electrons in the system (usually on the strongly correlated d and f electrons).[19-21] This method can be affordably applied to existing DFT functionals such as LDA and GGA. Unfortunately, there is no magic-bullet solution for the choice of the U parameter, which lack transferability and may even differ significantly for different applications on the same system, as many studies have found.[22-27] The problem of self-interaction remains an ongoing problem plaguing DFT predictions for surface chemistry and catalysis, especially those of metal oxides.[13, 28-30]

Finally, a variety of methods have been developed to improve the description of dispersion interactions in DFT. DFT+D is a method by Grimme et al. involving damped atom-atom empirical potentials trained on an existing functional such as PBE.[31] However, care must be taken to avoid overbinding in systems where the interactions are already overbound without the dispersion correction. Another approach involving nonlocal correlation functions can be used for dispersion interactions, involving fewer empirical parameters, such as vdW-DF2 and VV10.[32-35]

2.2 Transition state search

Transition state search is a key technique used in computational catalysis in order to provide information about reaction mechanisms and rates. Transition states are saddle points on the potential energy surface, and corresponds to the highest energy point along a minimum-energy path connecting two basins or local minima. Finding transition states via this approach allows one to study rare events with potentially high energy barriers without the need to perform brute force molecular dynamics simulations, where much of the computational effort will be wasted in simulating the system vibrating in a basin without crossing over to another. A number of approaches have been developed to find transition states, and those which rely only on first derivatives of the energy, or the forces, rather than the second derivatives are commonly used for surface chemistry. This avoids the need for a usually expensive Hessian calculation in plane wave codes, and are generally more robust and less prone to failure.

2.2.1 Nudged Elastic Band

The nudged elastic band (NEB) method can be used to find transition states given a known initial and final state, and arguably the most widely used method in the field. The initial and final states correspond to the geometry-optimized local minima of an expected elementary reaction, and several 'images' are made connecting the two geometries, usually via linear interpolation. The images are then optimized to forces perpendicular to the line connecting the images, which are kept in even spacing via additional forces between images, or imaginary 'springs.'[36] Commonly, an additional modification to the

NEB is used whereby one of the highest-energy images is further optimized along the energy path to maximize the energy to reach the saddle point.[37] This method allows for a fairly accurate approximation of the saddle point energy and reduces the number of images otherwise needed to estimate the saddle point via interpolation. Several important considerations are always present when starting a NEB calculation. First, care must be taken to ensure there are no additional local minima along the path connecting the initial or final states; for complex surfaces this may be difficult and NEB calculations may need to be restarted if such a problem arises. Second, the number of images must be chosen such that there is a sufficient resolution to find the saddle point; however too many images may end up being detrimental to convergence and significantly increase the computational cost. Finally, the choice of the initial and final state is ultimately decided by the human operator and can be biased; to avoid this bias many initial and final states should ideally be tested.

2.2.2 Dimer

For situations where the initial or final state is not known, the dimer method can be used to find the saddle point without user input or bias. Alternatively, when there is already a good guess of the transition state, the dimer method may also be used to further refine the force convergence at a cheaper cost than NEB, due to only needing two images rather than multiple. In the dimer method, two images are created from an initial geometry, spaced at a certain distance equally apart. The dimer is first rotated; minimizing the energy of the two dimers corresponds to aligning the dimer along the lowest curvature mode. The dimer is then relaxed via translation along the direction

perpendicular to the dimer axis.[38] The dimer method works best when the initial transition state guess has been pre-converged with an NEB calculation at a lower accuracy and cost. It is also highly efficient to use the dimer method when screening different systems but with the same reaction mechanism and similar transition states. Hypothetically, the dimer method should be many times faster than NEB due to the much fewer images needed; however in practice the cost savings may be somewhat moderate due to the much higher requirement for accurate forces and the increased number of steps needed which are spent rotating the images rather than translating them. Moreover, without the constraint of initial and final states, the dimer method is prone to diverging or optimizing to a different saddle point. As such, it is usually used as a second resort compared to NEB, though it can be highly effective in niche applications.

2.3 Chemical bonding analysis

To understand the fundamental chemical processes involved in catalysis, such as adsorption and bond-activation, it is arguably important to determine the chemical bonding interactions from first-principles methods. Many catalytically relevant phenomena, such as the existence of linear scaling relationships, can be traced to the similar nature of chemical interactions on surfaces observed from chemical bonding analyses (Chapter 1.2.2).

2.3.1 Charge partitioning and Bader Charge

Charge partitioning is an integral part of understanding the chemical bonding properties.[39-40] There is no universally agreed-upon or ‘correct’ method of determining

atomic charges in solids; nor is atomic charge an observable in quantum mechanics. The earliest methods include the Mulliken population analysis based on electronic orbitals.[41] Two major drawbacks are associated with such method: (1) there is a basis-set dependence on the obtained Mulliken charges and (2) such an analysis is unsuitable for studies on solids which are normally calculated with plane-wave based methods.

Bader charge instead divides charge based purely on an electron charge density ρ. This charge density is generally obtained from a quantum mechanical calculation, though it could be obtained from other means (X-ray crystallography). Bader charge divides electron density which are bounded by surfaces of zero flux where charge density is a minimum perpendicular to the surface.[39-40, 42] (Methods in which charge is partitioned into overlapping regions include the density derived electrostatic and chemical method which seeks to reproduce the electrostatic potential V(r).)[43] Bader charge partitions have been argued to be chemically meaning, and can provide an identification and analysis of chemical bonding from the charge critical points.[40, 44] In addition, the Bader charge is also used as a robust and versatile indicator of the chemical properties on the atoms.

2.3.2 Crystal Orbital Hamilton Population

Crystal Orbital Hamilton Population (COHP) is a method of partitioning band structure energy into bonding to antibonding contributions between two atoms.[45] The concept can be drawn from the earlier method of Crystal Orbital Overlap Population (COOP) which obtains bonding and antibonding contributions from multiplying the Mulliken overlap populations with the DOS or density of states.[46] This results in a COOP

curve where the amplitude at a particular energy is determined by the number of states in the interval multiplied by the overlap population. The units of this curve are in electrons and integrating this curve up to the Fermi level should result in electron population in a net (positive or negative) pairwise interaction. Analogously, in COHP, the DOS is multiplied by the Hamiltonian, which yields a COHP curve in unites of energy rather than electrons.

To apply this theory to plane wave based DFT methods, it is necessary to project the delocalized plane waves onto atomic orbitals.[47] Through this, a projected COHP can be obtained from a plane-wave output.[48-49] The efficacy of this method is highly dependent of the accuracy of the projection; some information is inevitably lost projecting the plane-wave to atomic orbitals. For practical usage, much of these methods can be accessed through a publicly-available code LOBSTER[50-51] which can read the inputs of several popular plane-wave based codes such as VASP, ABINIT and Quantum Espresso. COHP has been successfully applied to many solid-state systems as seen in these representative studies and reviews.[52-57]

2.3.3 Natural Bond Orbital

The natural bond orbital (NBO) analysis partitions the electron density into natural bond orbitals to reproduce the natural Lewis structures of the system, with the orbitals ideally containing an electron density approaching 2 electrons.[58-60] To apply this method to plane wave based methods, a projection is again needed to convert to atomic orbitals. An implementation of this projection method and NBO analysis for plane wave codes is

available by Schmidt et al.[61-62] The choice of basis set can significant improve the projection efficacy and reduce spilling; for example it has been noted that Gaussian basis sets with diffuse orbitals can cause numerical instabilities and orbitals with exponents lower than a particular threshold can be truncated. Nevertheless, periodic NBO analysis, while very effective for studying the bonding of the adsorbates, can struggle with the substrate, particularly for metallic surfaces with significant electron delocalization.

2.4 Global Optimization

Global optimization is a means of sampling and finding the lowest energy structures of a system of study. Energy is obtained either from first-principles calculations or by means of empirical potentials and more recently, from machine learning methods.[63] A number of common used global optimization schemes are used, including simulated annealing, genetic algorithm,[64] basin hopping,[65] and particle swarm approaches.[66] High efficiency is a desirable trait for a global optimization strategy, however it is impossible to prove a putative global minima is the true global minima without exhaustively sampling the complete potential energy surface. Thus, a global optimization method which can broadly sample possible configurations without bias may also be considered when choosing an optimization method. Global optimization has been highly successful in predicting structures of bulk crystals, molecular clusters and surfaces. Given the importance of structure in determining catalytic activity, global optimization should always be considered where cost is not prohibitive.

References

(1) Mardirossian, N.; Head-Gordon, M. Thirty years of density functional theory in computational chemistry: an overview and extensive assessment of 200 density functionals. *Mol. Phys.* **2017,** *115*, 2315-2372.

(2) Hohenberg, P.; Kohn, W. Inhomogeneous Electron Gas. *Physical Review* **1964,** *136*, B864-B871.

(3) Kohn, W.; Sham, L. J. Self-Consistent Equations Including Exchange and Correlation Effects. *Physical Review* **1965,** *140*, A1133-A1138.

(4) Perdew, J. P.; Ruzsinszky, A.; Tao, J.; Staroverov, V. N.; Scuseria, G. E.; Csonka, G. I. Prescription for the design and selection of density functional approximations: More constraint satisfaction with fewer fits. *J. Chem. Phys.* **2005,** *123*, 062201.

(5) Perdew, J. P.; Chevary, J. A.; Vosko, S. H.; Jackson, K. A.; Pederson, M. R.; Singh, D. J.; Fiolhais, C. Atoms, molecules, solids, and surfaces: Applications of the generalized gradient approximation for exchange and correlation. *Phys. Rev. B* **1992,** *46*, 6671-6687.

(6) Perdew, J. P.; Burke, K.; Ernzerhof, M. Generalized Gradient Approximation Made Simple. *Phys. Rev. Lett.* **1996,** *77*, 3865-3868.

(7) Zhao, Y.; Truhlar, D. G. A new local density functional for main-group thermochemistry, transition metal bonding, thermochemical kinetics, and noncovalent interactions. *J. Chem. Phys.* **2006,** *125*, 194101.

(8) Tao, J.; Perdew, J. P.; Staroverov, V. N.; Scuseria, G. E. Climbing the density functional ladder: Nonempirical meta–generalized gradient approximation designed for molecules and solids. *Phys. Rev. Lett.* **2003,** *91*, 146401.

(9) Sun, J.; Ruzsinszky, A.; Perdew, J. P. Strongly Constrained and Appropriately Normed Semilocal Density Functional. *Phys. Rev. Lett.* **2015,** *115*, 036402.

(10) Martin, R. M.; Reining, L.; Ceperley, D. M., *Interacting Electrons: Theory and Computational Approaches*. Cambridge University Press: Cambridge, 2016.

(11) Jiang, H. First-principles approaches for strongly correlated materials: A theoretical chemistry perspective. *Int. J. Quantum Chem* **2015,** *115*, 722-730.

(12) Malet, F.; Gori-Giorgi, P. Strong Correlation in Kohn-Sham Density Functional Theory. *Phys. Rev. Lett.* **2012,** *109*, 246402.

(13) Paier, J. Hybrid Density Functionals Applied to Complex Solid Catalysts: Successes, Limitations, and Prospects. *Catal. Lett.* **2016,** *146*, 861-885.

(14) Becke, A. D. Density‐functional thermochemistry. III. The role of exact exchange. *J. Chem. Phys.* **1993,** *98*, 5648-5652.

(15) Adamo, C.; Barone, V. Toward reliable density functional methods without adjustable parameters: The PBE0 model. *J. Chem. Phys.* **1999,** *110*, 6158-6170.

(16) Krukau, A. V.; Vydrov, O. A.; Izmaylov, A. F.; Scuseria, G. E. Influence of the Exchange Screening Parameter on the Performance of Screened Hybrid Functionals. *J. Chem. Phys.* **2006,** *125*, 224106.

(17) Staroverov, V. N.; Scuseria, G. E.; Tao, J.; Perdew, J. P. Comparative assessment of a new nonempirical density functional: Molecules and hydrogen-bonded complexes. *J. Chem. Phys.* **2003,** *119*, 12129-12137.

(18) Hubbard, J. Electron correlations in narrow energy bands. *Proceedings of the Royal Society of London. Series A. Mathematical and Physical Sciences* **1963,** *276*, 238-257.

(19) Anisimov, V. I.; Gunnarsson, O. Density-functional calculation of effective Coulomb interactions in metals. *Phys. Rev. B* **1991,** *43*, 7570-7574.

(20) Anisimov, V. I.; Solovyev, I. V.; Korotin, M. A.; Czyżyk, M. T.; Sawatzky, G. A. Density-functional theory and NiO photoemission spectra. *Phys. Rev. B* **1993,** *48*, 16929-16934.

(21) Dudarev, S. L.; Botton, G. A.; Savrasov, S. Y.; Humphreys, C. J.; Sutton, A. P. Electron-Energy-Loss Spectra and the Structural Stability of Nickel Oxide: An LSDA+U Study. *Phys. Rev. B* **1998,** *57*, 1505-1509.

(22) Capdevila-Cortada, M.; Łodziana, Z.; López, N. Performance of DFT+U Approaches in the Study of Catalytic Materials. *ACS Catal.* **2016,** *6*, 8370-8379.

(23) Aykol, M.; Wolverton, C. Local environment dependent GGA+U method for accurate thermochemistry of transition metal compounds. *Phys. Rev. B* **2014,** *90*, 115105.

(24) Lutfalla, S.; Shapovalov, V.; Bell, A. T. Calibration of the DFT/GGA+U Method for Determination of Reduction Energies for Transition and Rare Earth Metal Oxides of Ti, V, Mo, and Ce. *J. Chem. Theory Comput.* **2011,** *7*, 2218-2223.

(25) Getsoian, A. B.; Bell, A. T. The Influence of Functionals on Density Functional Theory Calculations of the Properties of Reducible Transition Metal Oxide Catalysts. *J. Phys. Chem. C* **2013,** *117*, 25562-25578.

(26) Curnan, M. T.; Kitchin, J. R. Investigating the Energetic Ordering of Stable and Metastable TiO2 Polymorphs Using DFT+U and Hybrid Functionals. *J. Phys. Chem. C* **2015,** *119*, 21060-21071.

(27) Zeng, Z.; Chan, M. K. Y.; Zhao, Z.-J.; Kubal, J.; Fan, D.; Greeley, J. Towards First Principles-Based Prediction of Highly Accurate Electrochemical Pourbaix Diagrams. *J. Phys. Chem. C* **2015,** *119*, 18177-18187.

(28) Ganduglia-Pirovano, M. V.; Hofmann, A.; Sauer, J. Oxygen Vacancies in Transition Metal and Rare Earth Oxides: Current State of Understanding and Remaining Challenges. *Surf. Sci. Rep.* **2007,** *62*, 219-270.

(29) Paier, J.; Penschke, C.; Sauer, J. Oxygen Defects and Surface Chemistry of Ceria: Quantum Chemical Studies Compared to Experiment. *Chem. Rev.* **2013,** *113*, 3949-3985.

(30) Pacchioni, G. Modeling doped and defective oxides in catalysis with density functional theory methods: Room for improvements. *J. Chem. Phys.* **2008,** *128*, 182505.

(31) Grimme, S.; Antony, J.; Ehrlich, S.; Krieg, H. A Consistent and Accurate ab Initio Parametrization of Density Functional Dispersion Correction (DFT-D) for the 94 Elements H-Pu. *J. Chem. Phys.* **2010,** *132*, 154104.

(32) Dion, M.; Rydberg, H.; Schröder, E.; Langreth, D. C.; Lundqvist, B. I. Van der Waals Density Functional for General Geometries. *Phys. Rev. Lett.* **2004,** *92*, 246401.

(33) Lee, K.; Murray, É. D.; Kong, L.; Lundqvist, B. I.; Langreth, D. C. Higher-accuracy van der Waals density functional. *Phys. Rev. B* **2010,** *82*, 081101.

(34) Vydrov, O. A.; Voorhis, T. V. Nonlocal van der Waals density functional: The simpler the better. *J. Chem. Phys.* **2010,** *133*, 244103.

(35) Peng, H.; Yang, Z.-H.; Perdew, J. P.; Sun, J. Versatile van der Waals Density Functional Based on a Meta-Generalized Gradient Approximation. *Physical Review X* **2016,** *6*, 041005.

(36) Mills, G.; Jónsson, H. Quantum and thermal effects in H2 dissociative adsorption: Evaluation of free energy barriers in multidimensional quantum systems. *Phys. Rev. Lett.* **1994,** *72*, 1124-1127.

(37) Henkelman, G.; Uberuaga, B. P.; Jónsson, H. A Climbing Image Nudged Elastic Band Method for Finding Saddle Points And Minimum Energy Paths. *J. Chem. Phys.* **2000,** *113*, 9901-9904.

(38) Henkelman, G.; Jónsson, H. A Dimer Method for Finding Saddle Points on High Dimensional Potential Surfaces Using Only First Derivatives. *J. Chem. Phys.* **1999,** *111*, 7010.

(39) Bader, R. F., *Atoms in Molecules: A Quantum Theory*. Clarendon Press: Oxford, U.K.: 1994.

(40) Bader, R. F. W.; Hernández-Trujillo, J.; Cortés-Guzmán, F. Chemical bonding: From Lewis to atoms in molecules. *J. Comput. Chem.* **2007,** *28*, 4-14.

(41) Mulliken, R. S. Electronic Population Analysis on LCAO–MO Molecular Wave Functions. I. *J. Chem. Phys.* **1955,** *23*, 1833-1840.

(42) Henkelman, G.; Arnaldsson, A.; Jónsson, H. A Fast and Robust Algorithm for Bader Decomposition Of Charge Density. *Comput. Mater. Sci.* **2006,** *36*, 354-360.

(43) Manz, T. A.; Sholl, D. S. Improved Atoms-in-Molecule Charge Partitioning Functional for Simultaneously Reproducing the Electrostatic Potential and Chemical States in Periodic and Nonperiodic Materials. *J. Chem. Theory Comput.* **2012,** *8*, 2844-2867.

(44) Bader, R. F. W.; MacDougall, P. J.; Lau, C. D. H. Bonded and nonbonded charge concentrations and their relation to molecular geometry and reactivity. *J. Am. Chem. Soc.* **1984,** *106*, 1594-1605.

(45) Dronskowski, R.; Bloechl, P. E. Crystal Orbital Hamilton Populations (COHP): Energy-Resolved Visualization of Chemical Bonding in Solids Based on Density-Functional Calculations. *J. Phys. Chem.* **1993,** *97*, 8617-8624.

(46) Hoffmann, R., *Solids and Surfaces: a Chemist's View of Bonding in Extended Structures*. VCH Publishers: 1988.

(47) Sanchez-Portal, D.; Artacho, E.; Soler, J. M. Projection of plane-wave calculations into atomic orbitals. *Solid State Commun.* **1995,** *95*, 685-690.

(48) Deringer, V. L.; Tchougréeff, A. L.; Dronskowski, R. Crystal Orbital Hamilton Population (COHP) Analysis as Projected from Plane-Wave Basis Sets. *J. Phys. Chem. A* **2011,** *115*, 5461-5466.

(49) Maintz, S.; Deringer, V. L.; Tchougréeff, A. L.; Dronskowski, R. Analytic projection from plane-wave and PAW wavefunctions and application to chemical-bonding analysis in solids. *J. Comput. Chem.* **2013,** *34*, 2557-2567.

(50) Maintz, S.; Deringer, V. L.; Tchougréeff, A. L.; Dronskowski, R. LOBSTER: A Tool to Extract Chemical Bonding from Plane-Wave Based DFT. *J. Comput. Chem.* **2016,** *37*, 1030-1035.

(51) http://schmeling.ac.rwth-aachen.de/cohp/.

(52) Konze, P. M.; Dronskowski, R.; Deringer, V. L. Exploring Chemical Bonding in Phase-Change Materials with Orbital-Based Indicators. *physica status solidi (RRL) – Rapid Research Letters 0*, 1800579.

(53) Steinberg, S.; Dronskowski, R. The Crystal Orbital Hamilton Population (COHP) Method as a Tool to Visualize and Analyze Chemical Bonding in Intermetallic Compounds. *Crystals* **2018,** *8*, 225.

(54) Wuttig, M.; Lüsebrink, D.; Wamwangi, D.; Wełnic, W.; Gilleßen, M.; Dronskowski, R. The role of vacancies and local distortions in the design of new phase-change materials. *Nature Mater.* **2006,** *6*, 122.

(55) Dong, X.; Oganov, A. R.; Goncharov, A. F.; Stavrou, E.; Lobanov, S.; Saleh, G.; Qian, G.-R.; Zhu, Q.; Gatti, C.; Deringer, V. L.; Dronskowski, R.; Zhou, X.-F.; Prakapenka, V. B.; Konôpková, Z.; Popov, I. A.; Boldyrev, A. I.; Wang, H.-T. A stable compound of helium and sodium at high pressure. *Nat. Chem.* **2017,** *9*, 440.

(56) Küpers, M.; Konze, P. M.; Maintz, S.; Steinberg, S.; Mio, A. M.; Cojocaru-Mirédin, O.; Zhu, M.; Müller, M.; Luysberg, M.; Mayer, J.; Wuttig, M.; Dronskowski, R. Inside Back Cover: Unexpected Ge–Ge Contacts in the Two-Dimensional Ge4Se3Te Phase and Analysis of Their Chemical Cause with the Density of Energy (DOE) Function (Angew. Chem. Int. Ed. 34/2017). *Angew. Chem. Int. Ed.* **2017,** *56*, 10247-10247.

(57) Dronskowski, R. First-Principles Approaches to Metals, Alloys, and Metallic Compounds. *Metals* **2018,** *8*, 705.

(58) Reed, A. E.; Curtiss, L. A.; Weinhold, F. Intermolecular interactions from a natural bond orbital, donor-acceptor viewpoint. *Chem. Rev.* **1988,** *88*, 899-926.

(59) Glendening, E. D.; Landis, C. R.; Weinhold, F. Natural bond orbital methods. *Wiley Interdisciplinary Reviews: Computational Molecular Science* **2012,** *2*, 1-42.

(60) Reed, A. E.; Weinstock, R. B.; Weinhold, F. Natural population analysis. *J. Chem. Phys.* **1985,** *83*, 735-746.

(61) Dunnington, B. D.; Schmidt, J. Generalization of Natural Bond Orbital Analysis to Periodic Systems: Applications to Solids and Surfaces via Plane-Wave Density Functional Theory. *J. Chem. Theory Comput.* **2012,** *8*, 1902-1911.

(62) Dunnington, B. D.; Schmidt, J. Molecular Bonding-Based Descriptors for Surface Adsorption and Reactivity. *J. Catal.* **2015,** *324*, 50-58.

(63) Behler, J. Neural network potential-energy surfaces in chemistry: a tool for large-scale simulations. *Phys. Chem. Chem. Phys.* **2011,** *13*, 17930-55.

(64) Oganov, A. R.; Glass, C. W. Crystal structure prediction using ab initio evolutionary techniques: Principles and applications. *J. Chem. Phys.* **2006,** *124*, 244704.

(65) Wales, D. J.; Doye, J. P. Global optimization by basin-hopping and the lowest energy structures of Lennard-Jones clusters containing up to 110 atoms. *J. Phys. Chem. A* **1997,** *101*, 5111-5116.

(66) Wang, Y.; Lv, J.; Zhu, L.; Ma, Y. Crystal structure prediction via particle-swarm optimization. *Phys. Rev. B* **2010,** *82*, 094116.

3 Reactions on metal oxides

3.1 Understanding oxidative dehydrogenation of ethane on Co3O4 nanorods from density functional theory

3.1.1 Abstract

Co_3O_4 is a metal oxide catalyst with weak, tunable M-O bonds promising for catalysis. Here density functional theory (DFT) is used to study the oxidative dehydrogenation (ODH) of ethane on Co_3O_4 nanorods based on the preferred surface orientation (111) from the experimental electron-microcopy image. The pathway and energetics of the full catalytic cycle including the first and second C-H bond cleavages, hydroxyl clustering, water formation, and oxygen-site regeneration are determined. We find that both lattice O and Co may participate as active sites in the dehydrogenation, with the lattice-O pathway being favored. We identify the best ethane ODH pathway based on the overall energy profiles of several routes. We identify that water formation from the lattice oxygen has the highest energy barrier and is likely a rate-determining step. This work of the complete catalytic cycle of ethane ODH will allow further study into tuning the surface chemistry of Co_3O_4 nanorods for high selectivity of alkane ODH reactions.

3.1.2 Introduction

The conversion of alkanes such as ethane and propane into olefins is an industrially and economically important process and produces a significant portion of

highly desired feedstock used in the chemical industry. Due to the high expense and energy cost of steam cracking to produce these olefins, there has been intense effort in recent years to search for more selective and energetically efficient methods.[1] Catalytic oxidative dehydrogenation (ODH) has been proposed as an attractive alternative with the advantage of being more thermodynamically favored and with the potential to have greater selectivity at lower temperatures. These qualities of the ODH pathway would significantly reduce the costs of olefin production to suit the quickly increasing global demand.[2]

A wide variety of catalytic materials have been studied for the ODH reaction: earth-abundant metal oxides[3-18] appear as a cost effective and more viable alternative to noble metal catalysts. In particular, spinel cobalt oxide (Co_3O_4) is a particularly promising candidate which has been found to be very active in many oxidation reactions including those of CO,[19] CH_4,[20] and other hydrocarbons.[21] A major factor in the catalytic activity of Co_3O_4 is the very weak M-O bond among other transition metal oxides[22] and the presence of readily generated oxygen vacancies at the surface.[20, 23] Experimental and theoretical studies have identified a number of stable surfaces on the Co_3O_4 nanoparticles and nanorods, including the (100), (110) and (111) surfaces.[19, 21, 24-32]

Of these surfaces, the high activity of the (110) facet in these studies for reactions such as CO oxidation has been widely reported; however, the (111) surface has been found to be readily formed[26, 29] and more thermodynamically stable[28] than the (110) surface. Therefore, the morphology of Co_3O_4 nanocatalysts may greatly impact their catalytic activity due to the difference in preferred surface orientations and it would be

very interesting to understand the change in the reaction mechanism on those different surfaces. DFT has been employed in many previous studies on the surface properties and catalytic activity of Co_3O_4 that is thought to proceed via the Mars-van Krevelen mechanism involving the lattice oxygen on the surface.[33-37] These active oxygen species react and desorb as products to form vacancies which must then be regenerated from gaseous molecular oxygen in order to maintain the catalytic activity of the surface.

Several recent works have shown that modifying the pure Co_3O_4 surface can improve its performance for alkane activation. These methods include doping transition metals such as Ni to facilitate the oxidation of alkanes[20] and depositing nonmetallic elements such as Si and Ge on the surface of Co_3O_4 nanorods to tune the selectivity of the catalyst towards the ethane ODH product.[38] However, the underlying mechanism of how the modification of the Co_3O_4 surface by other elements changes the activity and selectivity of the nanocatalyst for ethane ODH remains unclear.

As a first step toward understanding the roles of morphology control and surface modification in Co_3O_4 nanocatalysts for ethane ODH, herein we will present the detailed analysis of the full catalytic cycle from first principles based on the experimental determination of the preferred surface orientation of Co_3O_4 nanorods. We hope to elucidate the nature of the two C-H activations to produce ethylene, the formation of water, and the regeneration of the oxygen sites to complete the catalytic cycle. These insights will provide a better understanding of the role of the different active surface atoms on a specific surface orientation in determining selectivity and yield of the ethane ODH pathway that may allow one to design better Co_3O_4 nanocatalysts.

3.1.3 Experimental and Computational Methods

Co_3O_4 nanorods were synthesized via a previously reported method.[23, 39] Briefly, cobalt acetate tetrahydrate was dissolved in ethylene glycol and heated to 160 ^oC under N_2; then reacted with the slowly added $NaHCO_3$ aqueous solution under vigorous stirring. After centrifugation a purple precipitate was obtained, which was then dried at 50 ^oC under vacuum and calcined at 350 ^oC in air to yield the Co_3O_4 nanorods. Their crystalline form was checked with powder X-ray diffraction. Then the nanorods were imaged with the high angle annular dark field (HAADF) scanning transmission electron microscopy (STEM) on a JEOL JEM-ARM200F Transmission Electron Microscope at 200 kV. Based on the surface orientation of the Co_3O_4 nanorods from the STEM images, we then employed density functional theory (DFT) to examine the ethane ODH pathways on it.

All DFT calculations were performed using the Vienna ab initio Simulation Package (VASP).[40-41] The on-site Coulomb interaction was included using the DFT+U method by Dudarev, et al.[42] in VASP using a Hubbard parameter of U = 2 eV for Co, which yielded band gaps in good agreement with experimental results and was used to good effect in previous DFT studies of Co_3O_4 surface chemistry and catalysis.[19-20] The Perdew-Burke-Erzerhof (PBE)[43] form of the generalized-gradient approximation (GGA) was chosen for electron exchange and correlation. The electron-core interaction was described using the projector-augmented wave method (PAW).[44-45] A kinetic energy cutoff of 450 eV was used for the planewaves, and the Brillouin zone was sampled using a 3×3×1 Monkhorst-Pack scheme.[46] All calculations in this work were performed with spin polarization. The slab was created containing 11 layers with the bottom 9 layers

frozen in their bulk positions. The optimized lattice constant was found to be 8.14 Å, in very good agreement with the experimental value of 8.09 Å.[47]

The adsorption energies were defined by $E_{ads} = E_{surface+adsorbate} - (E_{surface} + E_{adsorbate})$, where the energy of the adsorbate $E_{adsorbate}$ was computed by placing an adsorbate molecule in a cubic cell of 10 Å in side length (in other words, the molecule and its nearest periodic images are separated by about 10-Å vacuum). Transition states were found via a two-step approach, using both the nudged elastic band method (NEB) and the dimer method[48] implemented in the VASP-VTST package by Henkelman et al.[49] Initial and final states of the reactions were first created and optimized, and were used to generate 8-10 equally spaced images through a linear interpolation. These images were then minimized under the NEB constraints to forces of ~0.4-0.2 eV/Å in order to generate an approximate minimum reaction energy path. The highest two energy images along the path were then used to generate a starting geometry for the dimer method, until reaching an energy convergence of 0.05 eV/Å. Selected transition states were confirmed with vibrational frequency analysis to verify the effectiveness of this method and the convergence criterion.

3.1.4 Results and discussion

3.1.4.1 Surface structure of Co3O4 nanorods

Recent work has shown that Si and Ge modified Co_3O_4 nanorods improved the selectivity and yield of ethane ODH, but the molecular-level mechanism is still unclear.[38] Here we first direct our attention to modeling the mechanism of ethane ODH on the

experimentally produced Co_3O_4 nanorods, so we can examine the role of the surface modification in the future. The synthesized Co_3O_4 nanorods were imaged via the scanning tunneling electron microscopy (STEM) (Fig. 1 A-B). The atomic-resolution HAADF-STEM image (Fig. 1B) suggests that the Co_3O_4(111) surface is preferentially exposed in this sample of Co_3O_4 nanorods. This information about the surface orientation provides a desired foundation for our DFT modeling. The Co_3O_4(111) surface as well with the Co_3O_4 (110) surface are both catalytically active and stable surfaces confirmed from both experimental and theoretical studies in previous literature.[26, 28-29] Based on the STEM images, we chose the (111) surface as a model active surface in this work.

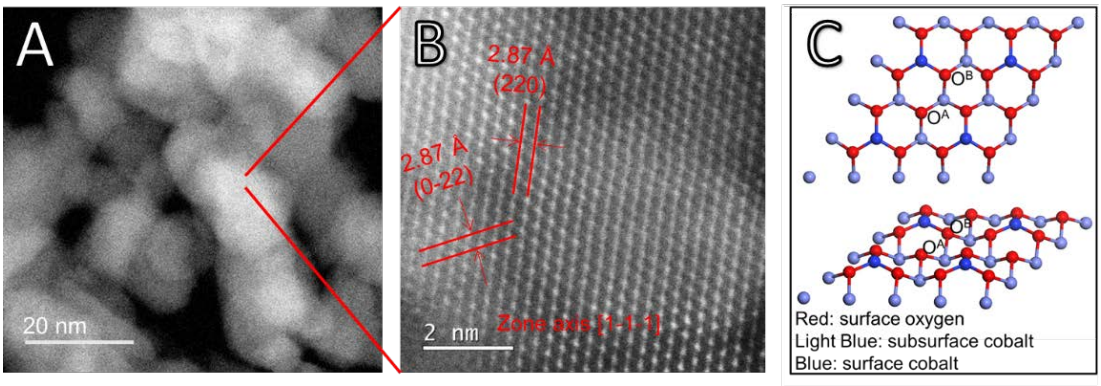

Figure 3.1.1 (A) STEM image of a large area of a Co_3O_4 nanorod sample. (B) HAADF-STEM image of a small area of the Co_3O_4 nanorod sample, marked with lattice fringes. (C) The surface model used in this DFT study for the same Co_3O_4 (111) surface: only the first three layers are shown for clarity. The two inequivalent surface lattice oxygens are labeled as O^A and O^B: O^A is coordinated with three subsurface Co^{3+} atoms (in light blue); O^B is coordinated with two subsurface Co^{3+} atoms and one surface Co^{2+} atom.

The Co_3O_4(111) surface can be terminated into six inequivalent layers; we chose the one with the lowest surface energy based on previous DFT calculations.[28] This

surface model terminates to yield tetrahedral Co^{2+} atoms and triply coordinated oxygen atoms on the surface (Fig. 1C). The surface lattice oxygens can be categorized into two types: O^A, which are triply coordinated to the subsurface cobalt (Co^{3+}); O^B, which are doubly coordinate to the subsurface Co but also singly coordinated to the surface Co (Fig. 1C). After relaxation of this Co_3O_4 (111) surface termination, the surface Co-O^B bonds shorten from 1.952 to 1.788 Å. The O^A-Co bonds shorten from 1.932 to 1.885 Å. In predicting the reactivity of the two inequivalent lattice O atoms, we find that O^A has a lower vacancy formation energy of 2.488 eV and a higher average Bader charge of -0.767 |e|. Meanwhile, the O^B has a vacancy formation energy of 2.946 eV and an average Bader charge of -0.860 |e|. The average Bader charge of the surface Co was found to be 1.298 |e|. The lower O^A vacancy formation energy suggests that the O^A oxygen is more active and more likely to react to result in a vacancy.

Both O^A and O^B vacancies lead to minimal surface rearrangement, with the O^A vacancy leading to the least change in surface bond lengths and the O^B vacancy leading to a shortening of the remaining two Co- O^B bonds from 1.788 to 1.769 Å. These results show that the Co_3O_4(111) surface can readily generate and refill oxygen vacancies without loss of surface structure, suggesting a robustness and stability consistent with experimental and theoretical findings,[26, 28, 50] and making it a good candidate as the model for the catalytic surface.

A less negative Bader charge of O^A than O^B indicates the increased ability of the O^A oxygen to further gain electrons, so O^A is more electrophilic than O^B and thus is the more favored active site for the homolytic fission of the C-H bond in the ethane ODH

reaction. The more negative Bader charge of O^B suggests that it is more nucleophilic in character and more suited in the heterolytic fission of the C-H bond as part of the metal-oxygen redox pair, where the metal cation Co^{2+} participates as the electrophile. Both the homolytic and heterolytic C-H cleavage will be examined next.

3.1.4.2 First C-H activation of ethane

In alkane oxidation reactions over metal oxides, both the full oxidation and ODH reactions proceed first via C-H activation onto the surface. Thus, we first study the activation of the ethane C-H bond by either a surface oxygen or cobalt. They can be characterized as either homolytic or heterolytic mechanisms, via the lattice oxygen or lattice cobalt, respectively.[21, 51-53] In the homolytic case, the oxygen atom abstracts a hydrogen from the alkane, forming an alkyl radical which then reacts with a nearby lattice oxygen. In the heterolytic case, the reaction occurs over the Co-O acid-base site pair with the lattice Co activating the C-H bond via σ-bond metathesis, leading to Co-C_2H_5 and O-H.

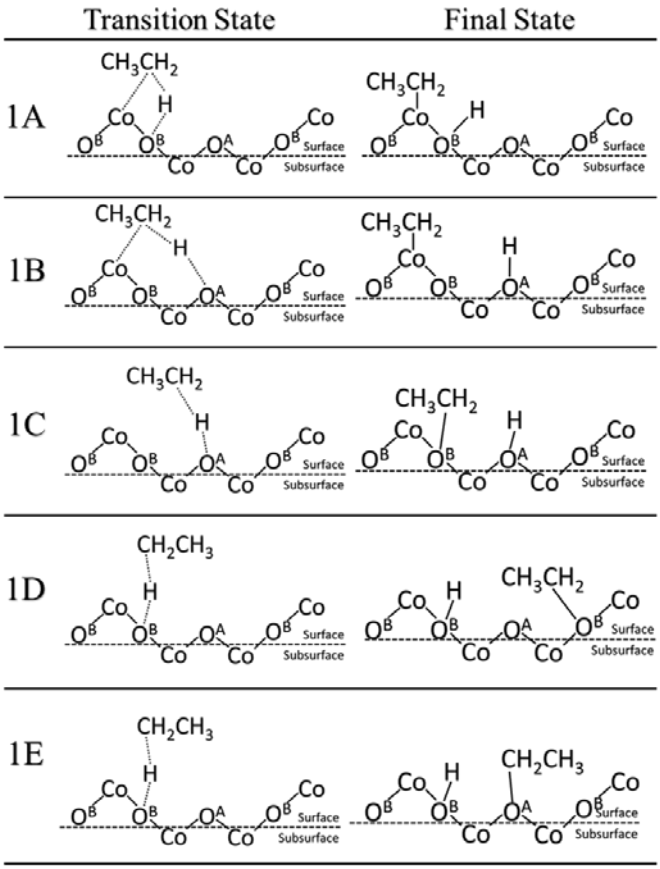

Figure 3.1.2 Transition and final states for the first C-H activation on $Co_3O_4(111)$. Reactions 1A and 1B are Co^{2+} activated heterolytic reactions. Reactions 1C-E are O activated homolytic reactions.

We examined both the heterolytic and homolytic pathways on $Co_3O_4(111)$ surface. Based on the configuration of the surface cobalt and oxygen, there should be five possible final states. Starting with a weakly physisorbed C_2H_6 on the surface, we found the minimum energy paths and transition states leading to the five final states. These transition and final states are illustrated in Fig. 2, while the energetic profiles are shown in Fig. 3. For the heterolytic activation (reactions 1A-B), the transition states were found

to form a Co-C_2H_5-H-O complex. The barrier for the pathway via O^B is 1.02 eV, lower than via O^A (1.11 eV), likely due to the fact that O^A is slightly farther from Co than O^B, which results in a less stable transition state complex. For homolytic activation (reactions 1C-E), the transition states show the formation of the CH_3CH_2--H--O complex where the C-H-O angle is almost 180 degrees, while in the final states the ethyl group attaches to another nearby lattice O. Reaction 1C is activated by the O^A oxygen with a barrier of 0.62 eV, whereas reaction 1D and 1E are both activated by the O^B oxygen with a similar barrier of 0.98 to 1.03 eV. The stronger oxidizing power of O^A than O^B, as indicated by the charge analysis, corroborates the lower activation energy of the first C-H activation on O^A.

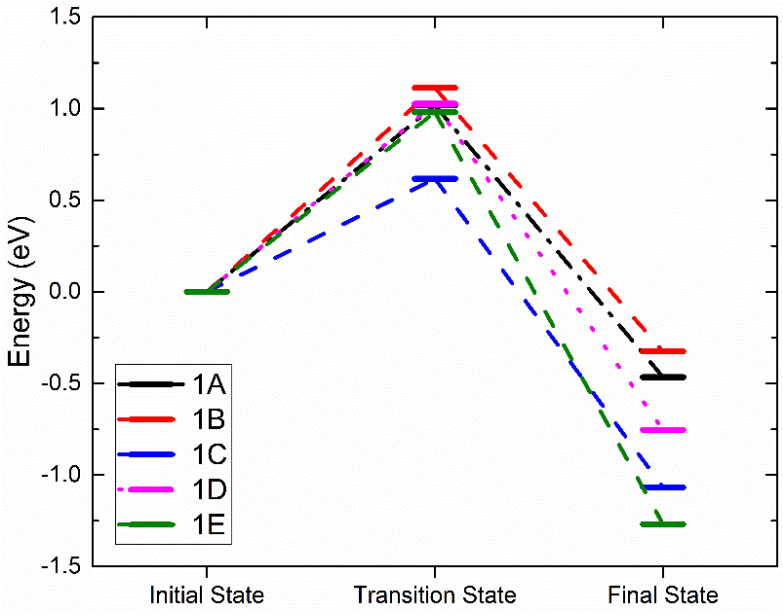

Figure 3.1.3 Energy profiles of the first C-H activation. Reactions 1A-1B are Co-activated, whereas reactions 1C-1E are O-activated.

The energy barriers (E_a) and reaction energies (ΔE) of both heterolytic and homolytic pathways of 1A-E are compared in Table 1, together with those of propane from another study.[21] We find that our calculated barriers are in very good agreement with the propane barriers for the same surface. It is apparent that the homolytic pathway is both the thermodynamically and kinetically favored reaction path due to both the overall lower barriers as well as the more negative reaction energies. The O^A-catalyzed pathway has the lowest barrier by far with a value of 0.62 eV. These results are also in good agreement with the propane DFT results and consistent with the higher bond dissociation energy of the ethane C-H bond.

Table 3.1.1 Activation energy E_a and energy of reaction ΔE of the first C-H activation of ethane. Propane E_a and ΔE in a similar study on the same Co_3O_4 (111) surface listed for comparison.

No.	Reaction Pathway	Ethane E_a (eV)	Ethane ΔE (eV)	Propane E_a (eV)[21]	Propane ΔE (eV)[21]
1A	$C_2H_6(g) \rightarrow C_2H_5\text{-}Co^{2+} + O^B\text{-}H$	1.02	-0.47	0.95	-0.71
1B	$C_2H_6(g) \rightarrow C_2H_5\text{-}Co^{2+} + O^A\text{-}H$	1.11	-0.33	N/A	N/A
1C	$C_2H_6(g) \rightarrow C_2H_5\text{-}O^B + O^A\text{-}H$	0.62	-1.07	0.41	-1.41
1D	$C_2H_6(g) \rightarrow C_2H_5\text{-}O^B + O^B\text{-}H$	1.03	-0.75	0.60	-0.80
1E	$C_2H_6(g) \rightarrow C_2H_5\text{-}O^A + O^B\text{-}H$	0.98	-1.27	N/A	N/A

3.1.4.3 Second C-H activation and C_2H_4 formation

We further examined the second C-H activation of ethane following the first C-H activation. Reactions 1A and 1C were selected as the best starting points for the second activation for the heterolytic and homolytic cases, respectively. The subsequent second

C-H pathways (transition states and final states) are illustrated in Fig. 4, while the energy profiles are shown in Fig. 5. In the heterolytic case (following 1A), the second C-H bond is activated via O^B on the CH_3 group, or the β-hydrogen elimination, (2A); via O^B on the CH_2 group, or the α-hydrogen elimination, (2B); or via O^A by the β-hydrogen elimination (2C). We find that the 2C path has the lowest barrier of only 0.39 eV (Fig. 5). In the homolytic case (following 1C), the second C-H bond is activated via either O^A by the β-hydrogen elimination (2D), O^B by the α-hydrogen elimination, (2E), or the O^A-H in the previous step by the α-hydrogen elimination (2F). We found that 2D and 2E pathways yield very similar barriers of 1.26 eV (Fig. 5). The 2F pathway has a much higher barrier of 2.46 eV, because the presence of a preexisting adsorbed hydrogen on the lattice O severely deactivates it from further C-H activation.

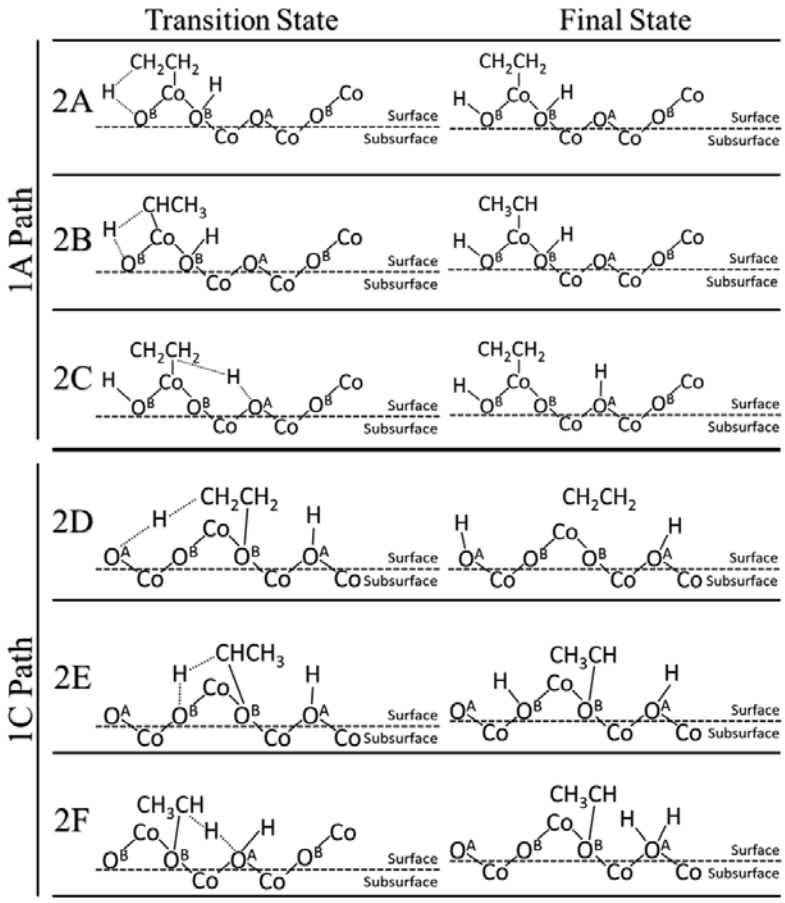

Figure 3.1.4 Initial, intermediate and final states for the second C-H activation of ethane. Reactions 2A-2C continue from the previous heterolytic reaction 1A. Reactions 2D-2F continue from the previous homolytic reaction 1C.

The barriers and reaction energies of the second C-H activation are compared in Table 2. Most notably, the second C-H activation following the heterolytic pathway (1A then 2C) appears to have lower barriers than following the homolytic pathway (1C then 2D or 2E). This result is also consistent with the DFT study of propane on the Co_3O_4 (110) surface.[21] Reactions via β-hydrogen elimination, 2A, 2C, and 2D all lead to ethylene formation. In the case of 2A and 2C, we found that desorption of C_2H_4 is uphill

by about 1.0 eV, while in the case of 2D, C_2H_4 was found to spontaneously go to the gas phase. Reactions 2B, 2E, and 2F via α-hydrogen elimination generate CH_3CH which were found to bind very strongly to the surface Co or O with a strength greater than 2 eV. We expect that the CH_3CH intermediate is unlikely to result in ethylene production and more likely to be part of the further oxidation pathways.

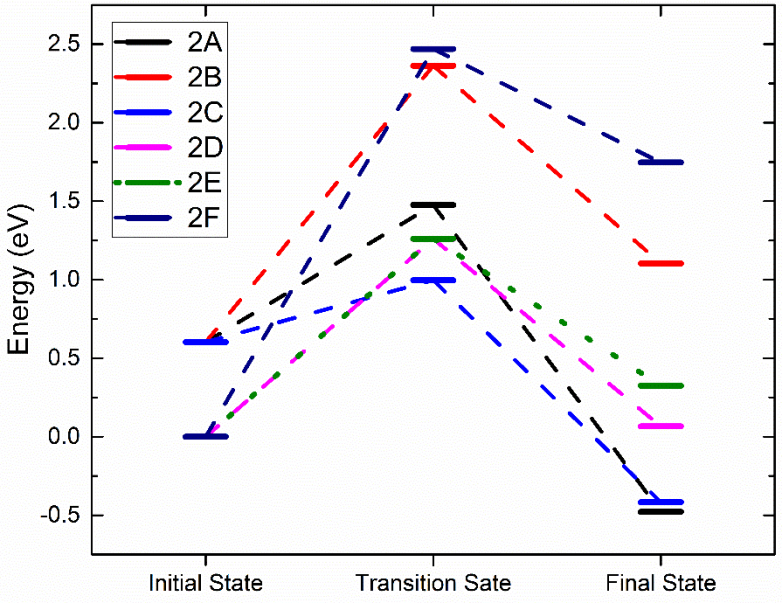

Figure 3.1.5 Energy profiles of the second C-H activation. Reactions 2A-2C follow the 1A path. Reactions 2D-2E follow the 1C path.

Table 3.1.2 Activation energy (E_a) and reaction energy (ΔE) of the second C-H activation of ethane, starting from the most favored Co-activated path (1A) and O-activated path (1C) from the first C-H activation.

No.	Reaction Pathway	E_a (eV)	ΔE (eV)
2A	$C_2H_5\text{-}Co^{2+} + O^B\text{-}H \rightarrow CH_2CH_2\text{-}Co^{2+} + 2O^B\text{-}H$	0.87	-1.08
2B	$C_2H_5\text{-}Co^{2+} + O^B\text{-}H \rightarrow CH_3CH\text{-}Co^{2+} + 2O^B\text{-}H$	1.76	0.50
2C	$C_2H_5\text{-}Co^{2+} + O^B\text{-}H \rightarrow CH_2CH_2\text{-}Co^{2+} + O^A\text{-}H + O^B\text{-}H$	0.39	-1.02
2D	$C_2H_5\text{-}O^B + O^A\text{-}H \rightarrow CH_2CH_2\text{-}O^B + 2O^A\text{-}H$	1.26	0.07
2E	$C_2H_5\text{-}O^B + O^A\text{-}H \rightarrow CH_3CH\text{-}O^B + O^A\text{-}H + O^B\text{-}H$	1.26	0.33
2F	$C_2H_5\text{-}O^B + O^A\text{-}H \rightarrow CH_3CH\text{-}O^B + H\text{-}O^A\text{-}H$	2.47	2.34

3.1.4.4 Hydroxyl clustering, water formation, and water desorption

Following the second C-H activation, ethylene will desorb in the ODH reaction, leaving two lattice O sites with adsorbed hydrogen, that is, formation of hydroxyls. Previous experimental isotopic studies have thoroughly shown that the oxidation and ODH reactions result in the formation of water containing the lattice oxygen.[20] Therefore, these surface hydroxyls will come closer (clustering), then form water, and desorb from the surface, in order for the catalytic cycle to proceed. This simplistic path for hydroxyl clustering is via diffusion of the hydrogen atom from a surface hydroxyl to a neighboring lattice oxygen. With two hydroxyl groups nearby, then one hydrogen of a hydroxyl can

combine with the neighboring hydroxyl to form water. The barrier for a representative H diffusion from O^A to O^B on the Co_3O_4(111) surface was found to be 1.35 eV (Fig. 6A). Next, we examined the water formation from two neighboring hydroxyl groups (Fig. 6B) and the barrier increases to 2.02 eV.

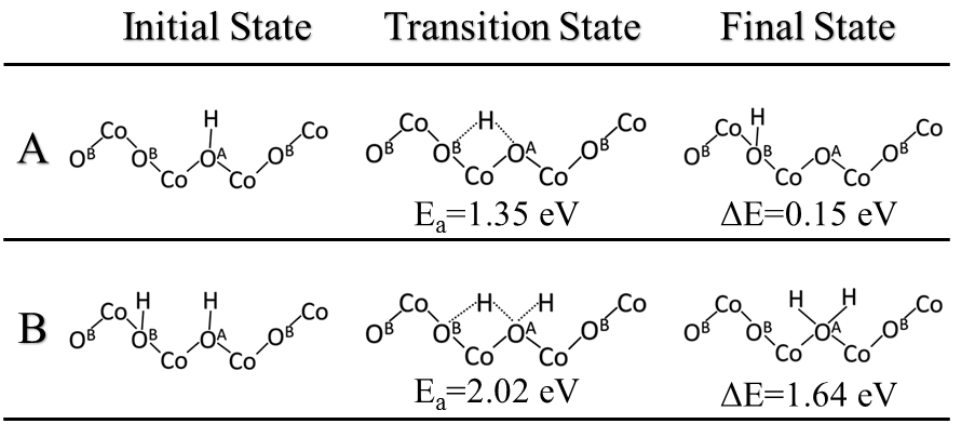

Figure 3.1.6 Initial, transition, and final states of hydrogen diffusion across the Co_3O_4 (111) surface: A, diffusion of hydrogen from O^A to O^B; B, diffusion of hydrogen from O^B to a O^A-H hydroxyl group.

After the H-O-H species is formed on the surface (Fig. 6B), it can then desorb to the gas phase. This desorption energy was found to be 0.581 eV, much lower than the lattice-oxygen vacancy formation energy (2.488 eV for the O^A atom). Indeed, the addition of two hydrogen atoms on the lattice oxygen destabilizes the system and lengthening the Co-O bonds. Oxygen vacancies are then formed following the desorption of water.

3.1.4.5 Regeneration of lattice oxygen sites

The oxygen vacancies left from water desorption can react with gas phase O_2 to regenerate the lattice oxygen sites. A very likely scenario would be that one gaseous O_2 molecule refills at a double oxygen vacancy site. We found that O_2 first binds vertically on one of the vacancies and then one oxygen atom of O_2 then dissociates to the neighboring vacancy site. We calculated the barrier of this process and found that it occurs via a barrier of only 0.51 eV and a reaction energy of -4.24 eV (Fig. 7A). These double vacancies may be generated through the process of continued water formation/desorption reactions on the surface during the catalytic cycle, or through vacancy diffusion across the surface. The diffusion of these oxygen vacancies were also studied and found to have a barrier of 1.63 eV for a diffusion from a vacancy at O^A to O^B (Fig. 7B). This double-vacancy regeneration model with very low barriers is also consistent with previous theoretical works on the $Co_3O_4(110)$ surface.[19, 21] Thus, we can conclude that regeneration of the lattice oxygen sites is highly facile in oxygen rich environments and unlikely to be a rate-determining step in the overall catalytic cycle.

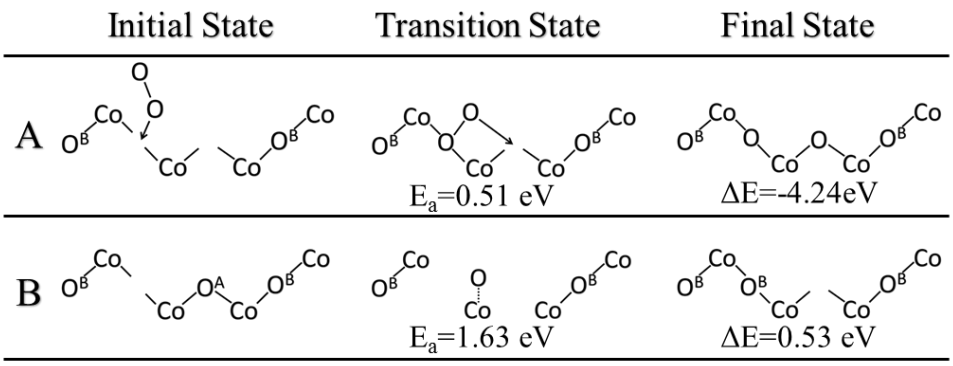

Figure 3.1.7 (A) Regeneration of lattice oxygen on Co_3O_4(111) via reaction of double oxygen vacancies with gaseous molecular oxygen. (B) Vacancy diffusion on the on Co_3O_4(111) surface from O^B site to O^A site.

3.1.4.6 Overall energy profile

Fig. 8 shows the overall energy profile including the first and second C-H activations, hydroxyl clustering via hydrogen diffusion, and water formation and desorption. We select the 1C-2D reaction path as the most representative ODH pathway through consideration of both activation energies, reaction energies, and product desorption. We omit the vacancy regeneration portion of the cycle for simplicity as well as the fact that its barriers are quite low in comparison. Fig. 8 shows that the water formation step is the least energetically favored step and a possible rate-determining step in the overall catalytic cycle. Alternative to the 1C-2D path, we also considered a competitive path via the 1A-2C channel where the first C-H activation is via Co^{2+} and the second C-H activation is via O^A. We found that again the water formation is the rate-determining step (RDS) in this mechanism.

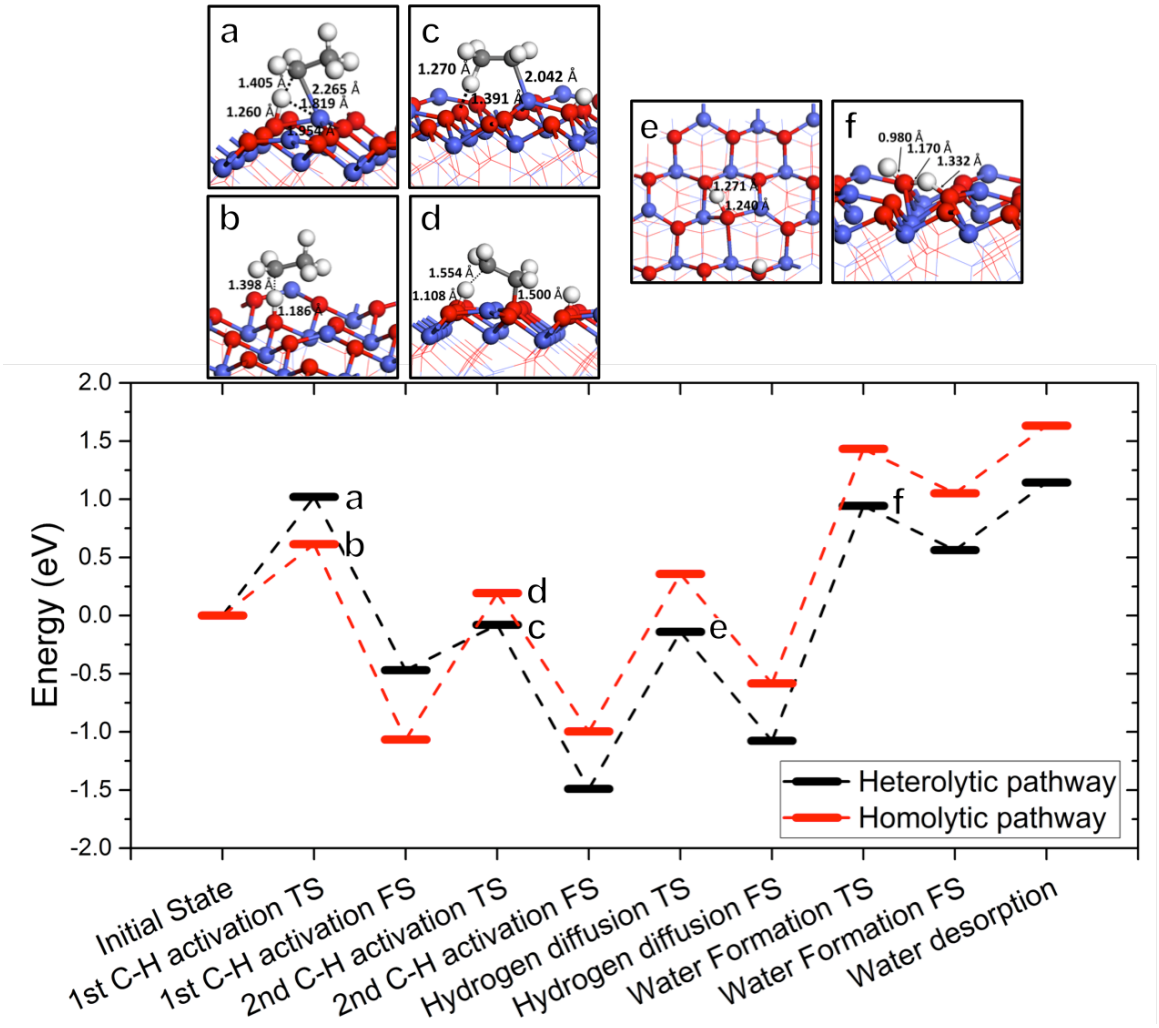

Figure 3.1.8 The overall energy profile of ODH of ethane to ethylene on $Co_3O_4(111)$. The C-H cleavages follow the 1C-2D path in red and the 1A-2C path in black (Fig. 2 and Fig. 4), while hydrogen diffusion and water formation energies are from Fig. 6.

A schematic drawing of the complete catalytic cycle for the homolytic path is shown in Fig. 9, composed of the first and second C-H activations, hydrogen diffusion, water formation, and lattice-oxygen regeneration. It starts with C_2H_6 adsorption, followed by the first C-H cleavage on lattice O^A. Then, the second C-H cleavage takes place on

another lattice O^A, leading to formation and desorption of C_2H_4. Next, hydroxyl clusters via hydrogen diffusion and water forms from nearby hydroxyl groups. Water desorbs and leaves lattice-oxygen vacancy, which is refilled by molecular oxygen. The cycle repeats.

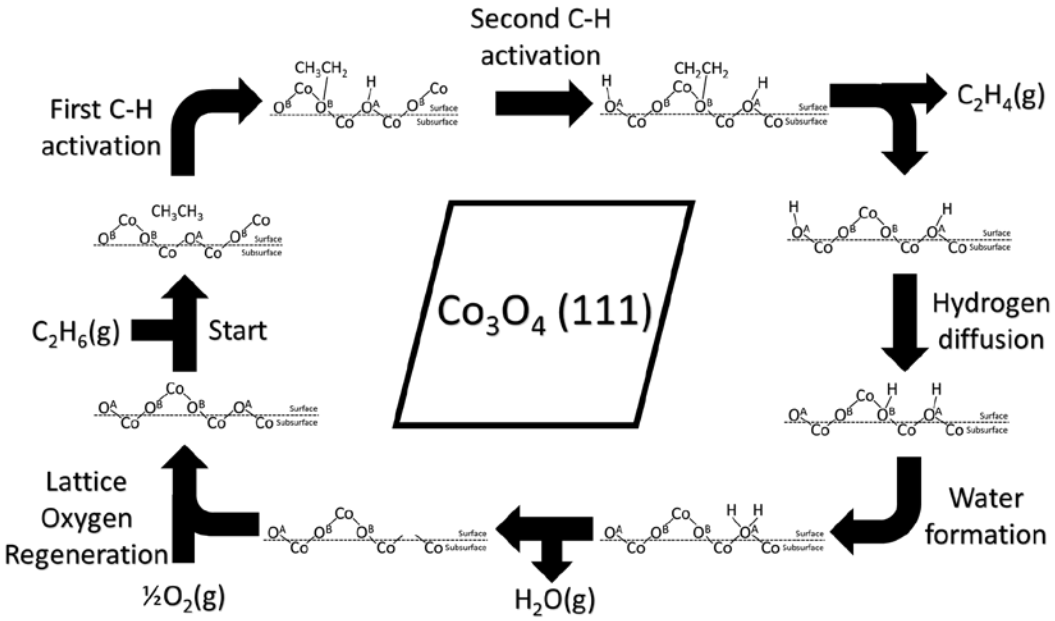

Figure 3.1.9 Schematic drawing of the complete catalytic cycle of ethane ODH on the Co_3O_4 (111) surface.

3.1.4.7 Implications of the present DFT results

Our present DFT study of ethane ODH on the Co_3O_4 (111) surface presents several interesting perspectives regarding the reaction characteristics. First, we find that for ethane, the first step of the reaction occurs via the activation of its C-H bond over either the Co^{2+} or the O^A / O^B atoms. While the first C-H activation is strongly favored towards the O-activated homolytic pathway, the second C-H activation is in fact more

favored towards the heterolytic pathway. In reality, it is likely for both pathways to participate in the formation of ethylene; however, without further kinetic analysis it would be very difficult to quantify their respective contributions towards forming the ODH product.

Next, we have found that the vacancy formation energy and Bader charge of the lattice oxygen to be a good descriptor of the catalytic activity of the lattice oxygen. We were able to predict the O^A oxygen to have lower barriers for C-H activation than the O^B oxygen. We would expect this trend to hold for lattice oxygen atoms of different Co_3O_4 surfaces, such as (110), (100), and (112), which could be important of Co_3O_4 nanocatalysts with different morphologies.

We find that the water formation step of the catalytic cycle on the pure (111) surface appears to be the RDS, while experiments shows that changing the alkane will change the overall barriers,[54] thus suggesting that the C-H activation barrier is significant to the overall rates. Based on preliminary DFT results, we believe that the hydroxylation of the surface will affect the energy profile by increasing the barriers of C-H activation and reducing the barriers of H_2O formation. In this model, we can then expect that the actual experimental energy profile will have the C-H activation and water formation barriers approach in energy at a steady-state hydrogen coverage of the surface. Thus, varying C-H bond strength would in fact affect the rates of the overall ODH reaction.

Experimental findings have indeed shown that surface hydroxylation occurs on the surfaces of metal oxides as the dominant species during and after a reaction.[55-56] In

addition, water formation, and consequently water concentration were found to affect the rates of the ODH/oxidation reactions on many studied metal oxides.[55, 57-59] This phenomenon occurs for CO and CH_4 oxidation on Co_3O_4 as well.[56, 60-61] These experimental findings support our conclusion that the water formation is an important step of the ethane ODH on Co_3O_4(111). This phenomenon is notably absent in CO oxidation, which is consistent with experimental observations of CO oxidations having much lower barriers and reaction temperatures than alkane oxidation. The coverage effect of surface hydroxyl groups on the catalytic pathways thus warrants further studies.

The experimental work of ethane ODH on Co_3O_4 nanorods[20, 38] have focused on ethylene/CO_2 selectivity and ethylene yield as a function of surface modification by Si and Ge oxides. Detailed kinetic data such as reaction rates and apparent activation energy on the unmodified Co_3O_4 nanorods are still not available for a direct comparison. To compare with the experimental ethylene/CO_2 selectivity, the complete pathway of ethane combustion has to be mapped out, which requires substantial more work and is beyond the scope of the present work. A joint experimental and computational study is expected for the near future to directly compare the computational results and the experimental data.

The present DFT study focuses on the (111) surface based on the STEM images of our Co_3O_4 nanorod sample (Fig. 1), but other facets may also exist such as the (100) and (110) surfaces depending upon preparation methods and calcination temperature. The different facets can affect the energetics of the elementary steps because the oxygen reactivity can be different. For example, the (110)-B surface of Co_3O_4 has a twofold-

coordinate oxygen site, in contrast with the threefold-coordinate oxygen sites on the (111) surface. How this twofold-coordinate oxygen site on the (110)-B surface would change the energetics of ethane ODH steps is a question that we intend to find out in a future study.

3.1.5 Conclusions

We have studied the oxidative dehydrogenation (ODH) of ethane to ethylene on the Co_3O_4(111) surface with DFT+U, in order to understand the mechanism on Co_3O_4 nanorods. The more reactive lattice oxygen (O^A) was found to yield the lowest barriers for the first C-H activation, consistent with our predictions based on vacancy formation energy and Bader charges. Overall, we found the barriers for the first C-H activation to be lower for the homolytic pathway (~0.62 eV), but the barriers for the second C-H activation to be lower for the heterolytic pathway. The cleaved hydrogen from C_2H_6 forms hydroxyl groups on Co_3O_4(111), which can cluster via hydrogen diffusion. Water formation from nearby hydroxyl groups and desorption to leave oxygen vacancy on the surface were found to have a large activation energy (2.02 eV) and is likely to be the rate-determining step. These vacancies can readily react with oxygen molecules in gas phase to regenerate the lattice oxygen sites. These insights will help understand the role of the surface orientation of the Co_3O_4 nanocatalysts in improving the selectivity and yield of alkane to alkene conversion through ODH.

References

(1) Cavani, F.; Ballarini, N.; Cericola, A. Oxidative dehydrogenation of ethane and propane: How far from commercial implementation? *Catal. Today* **2007,** *127*, 113-131.

(2) Tullo, A. H. PETROCHEMICALS. *C&EN* **2001,** *79*, 18.

(3) Heracleous, E.; Machli, M.; Lemonidou, A. A.; Vasalos, I. A. Oxidative dehydrogenation of ethane and propane over vanadia and molybdena supported catalysts. *J. Mol. Catal. A: Chem.* **2005,** *232*, 29-39.

(4) Dai, G.-L.; Liu, Z.-P.; Wang, W.-N.; Lu, J.; Fan, K.-N. Oxidative Dehydrogenation of Ethane Over V_2O_5 (001): A Periodic Density Functional Theory Study. *J. Phys. Chem. C* **2008,** *112*, 3719-3725.

(5) Fu, H.; Liu, Z.-P.; Li, Z.-H.; Wang, W.-N.; Fan, K.-N. Periodic Density Functional Theory Study of Propane Oxidative Dehydrogenation Over V_2O_5(001) Surface. *J. Am. Chem. Soc.* **2006,** *128*, 11114-11123.

(6) Lezanska, M.; Szymanski, G. S.; Pietrzyk, P.; Sojka, Z.; Lercher, J. A. Characterization of Cr-MCM-41 and Al, Cr-MCM-41 mesoporous catalysts for gas-phase oxidative dehydrogenation of cyclohexane. *J. Phys. Chem. C* **2007,** *111*, 1830-1839.

(7) Thorsteinson, E.; Wilson, T.; Young, F.; Kasai, P. The oxidative dehydrogenation of ethane over catalysts containing mixed oxides of molybdenum and vanadium. *J. Catal.* **1978,** *52*, 116-132.

(8) Botella, P.; Garcıa-González, E.; Dejoz, A.; Nieto, J. L.; Vázquez, M.; González-Calbet, J. Selective oxidative dehydrogenation of ethane on MoVTeNbO mixed metal oxide catalysts. *J. Catal.* **2004,** *225*, 428-438.

(9) Chen, K.; Bell, A. T.; Iglesia, E. The relationship between the electronic and redox properties of dispersed metal oxides and their turnover rates in oxidative dehydrogenation reactions. *J. Catal.* **2002,** *209*, 35-42.

(10) Heracleous, E.; Lemonidou, A. Ni–Me–O mixed metal oxides for the effective oxidative dehydrogenation of ethane to ethylene–Effect of promoting metal Me. *J. Catal.* **2010,** *270*, 67-75.

(11) Sun, X.; Li, B.; Metiu, H. Ethane Activation by Nb-Doped NiO. *J. Phys. Chem. C* **2013,** *117*, 23597-23608.

(12) Gartner, C. A.; van Veen, A. C.; Lercher, J. A. Oxidative Dehydrogenation of Ethane: Common Principles and Mechanistic Aspects. *ChemCatChem* **2013,** *5*, 3196-3217.

(13) Qiao, A.; Kalevaru, V. N.; Radnik, J.; Duvel, A.; Heitjans, P.; Kumar, A. S. H.; Prasad, P. S. S.; Lingaiah, N.; Martin, A. Oxidative Dehydrogenation of Ethane to Ethylene over V_2O_5/Al_2O_3 Catalysts: Effect of Source of Alumina on the Catalytic Performance. *Ind. Eng. Chem. Res.* **2014,** *53*, 18711-18721.

(14) Gartner, C. A.; van Veen, A. C.; Lercher, J. A. Oxidative Dehydrogenation of Ethane on Dynamically Rearranging Supported Chloride Catalysts. *J. Am. Chem. Soc.* **2014,** *136*, 12691-12701.

(15) Kristoffersen, H. H.; Metiu, H. Molten LiCl Layer Supported on MgO: Its Possible Role in Enhancing the Oxidative Dehydrogenation of Ethane. *J. Phys. Chem. C* **2015,** *119*, 8681-8691.

(16) Zhu, H. B.; Rosenfeld, D. C.; Anjum, D. H.; Sangaru, S. S.; Saih, Y.; Ould-Chikh, S.; Basset, J. M. Ni-Ta-O mixed oxide catalysts for the low temperature oxidative dehydrogenation of ethane to ethylene. *J. Catal.* **2015,** *329*, 291-306.

(17) Chen, X.; Yang, Q. L.; Chu, B. Z.; An, H.; Cheng, Y. Valence variation of phase-pure M1 MoVNbTe oxide by plasma treatment for improved catalytic performance in oxidative dehydrogenation of ethane. *Rsc Adv* **2015,** *5*, 91295-91301.

(18) Smolakova, L.; Kout, M.; Koudelkova, E.; Capek, L. Effect of Calcination Temperature on the Structure and Catalytic Performance of the Ni/Al2O3 and Ni-Ce/Al2O3 Catalysts in Oxidative Dehydrogenation of Ethane. *Ind. Eng. Chem. Res.* **2015,** *54*, 12730-12740.

(19) Jiang, D. E.; Dai, S. The role of low-coordinate oxygen on Co_3O_4(110) in catalytic CO oxidation. *Phys. Chem. Chem. Phys.* **2011,** *13*, 978-84.

(20) Tao, F. F.; Shan, J. J.; Nguyen, L.; Wang, Z.; Zhang, S.; Zhang, L.; Wu, Z.; Huang, W.; Zeng, S.; Hu, P. Understanding Complete Oxidation of Methane on Spinel Oxides at a Molecular Level. *Nature Commun.* **2015,** *6*, 7798.

(21) Tyo, E. C.; Yin, C.; Di Vece, M.; Qian, Q.; Kwon, G.; Lee, S.; Lee, B.; DeBartolo, J. E.; Seifert, S.; Winans, R. E.; Si, R.; Ricks, B.; Goergen, S.; Rutter, M.; Zugic, B.; Flytzani-Stephanopoulos, M.; Wang, Z. W.; Palmer, R. E.; Neurock, M.; Vajda, S. Oxidative dehydrogenation of cyclohexane on cobalt oxide (Co_3O_4) nanoparticles: The effect of particle size on activity and selectivity. *ACS Catal.* **2012,** *2*, 2409-2423.

(22) Zhang, S.; Shan, J.-j.; Zhu, Y.; Frenkel, A. I.; Patlolla, A.; Huang, W.; Yoon, S. J.; Wang, L.; Yoshida, H.; Takeda, S.; Tao, F. WGS Catalysis and In Situ Studies of CoO1-x, PtCon/Co3O4, and PtmCom '/CoO1-x Nanorod Catalysts. *J. Am. Chem. Soc.* **2013,** *135*, 8283-8293.

(23) Xie, X. W.; Li, Y.; Liu, Z. Q.; Haruta, M.; Shen, W. J. Low-temperature oxidation of CO catalysed by Co3O4 nanorods. *Nature* **2009,** *458*, 746-749.

(24) Liu, X.; Qiu, G.; Li, X. Shape-controlled synthesis and properties of uniform spinel cobalt oxide nanocubes. *Nanotechnology* **2005,** *16*, 3035-3040.

(25) Zasada, F.; Gryboś, J.; Indyka, P.; Piskorz, W.; Kaczmarczyk, J.; Sojka, Z. Surface Structure and Morphology of M[CoM′]O4(M = Mg, Zn, Fe, Co and M′ = Ni, Al, Mn, Co) Spinel Nanocrystals—DFT+U and TEM Screening Investigations. *J. Phys. Chem. C* **2014,** *118*, 19085-19097.

(26) Meyer, W.; Biedermann, K.; Gubo, M.; Hammer, L.; Heinz, K. Surface structure of polar Co(3)O(4)(111) films grown epitaxially on Ir(100)-(1 x 1). *J Phys Condens Matter* **2008,** *20*, 265011.

(27) Chen, J.; Selloni, A. Electronic states and magnetic structure at the Co 3 O 4 (110) surface: A first-principles study. *Phys. Rev. B* **2012,** *85*, 085306.

(28) Xu, X.-L.; Chen, Z.-H.; Li, Y.; Chen, W.-K.; Li, J.-Q. Bulk and surface properties of spinel Co3O4 by density functional calculations. *Surf. Sci.* **2009,** *603*, 653-658.

(29) Ferstl, P.; Mehl, S.; Arman, M. A.; Schuler, M.; Toghan, A.; Laszlo, B.; Lykhach, Y.; Brummel, O.; Lundgren, E.; Knudsen, J.; Hammer, L.; Schneider, M. A.; Libuda, J. Adsorption and Activation of CO on Co3O4(111) Thin Films. *J. Phys. Chem. C* **2015,** *119*, 16688-16699.

(30) Li, Y.; Tan, B.; Wu, Y. Freestanding mesoporous quasi-single-crystalline Co3O4 nanowire arrays. *J. Am. Chem. Soc.* **2006,** *128*, 14258-14259.

(31) Zasada, F.; Piskorz, W.; Janas, J.; Gryboś, J.; Indyka, P.; Sojka, Z. Reactive Oxygen Species on the (100) Facet of Cobalt Spinel Nanocatalyst and their Relevance in16O2/18O2Isotopic Exchange,deN2O, anddeCH4Processes—A Theoretical and Experimental Account. *ACS Catal.* **2015,** *5*, 6879-6892.

(32) Biedermann, K.; Gubo, M.; Hammer, L.; Heinz, K. Phases and phase transitions of hexagonal cobalt oxide films on Ir (100)-(1× 1). *J. Phys.: Condens. Matter* **2009,** *21*, 185003.

(33) Doornkamp, C.; Ponec, V. The universal character of the Mars and Van Krevelen mechanism. *J. Mol. Catal. A: Chem.* **2000,** *162*, 19-32.

(34) Broqvist, P. A DFT Study on CO Oxidation over Co3O4. *J. Catal.* **2002,** *210*, 198-206.

(35) Pang, X. Y.; Liu, C.; Li, D. C.; Lv, C. Q.; Wang, G. C. Structure sensitivity of CO oxidation on Co3O4: a DFT study. *ChemPhysChem* **2013,** *14*, 204-12.

(36) Xu, X.-L.; Yang, E.; Li, J.-Q.; Li, Y.; Chen, W.-K. A DFT Study of CO Catalytic Oxidation by N2O or O2on the Co3O4(110) Surface. *ChemCatChem* **2009,** *1*, 384-392.

(37) Pestman, R.; Koster, R.; Pieterse, J.; Ponec, V. Reactions of carboxylic acids on oxides: 1. Selective hydrogenation of acetic acid to acetaldehyde. *J. Catal.* **1997,** *168*, 255-264.

(38) Tao, F. Promoting catalytic selectivity through surface faceting of oxide for oxidative dehydrogenation.

(39) Xie, X. W.; Shang, P. J.; Liu, Z. Q.; Lv, Y. G.; Li, Y.; Shen, W. J. Synthesis of Nanorod-Shaped Cobalt Hydroxycarbonate and Oxide with the Mediation of Ethylene Glycol. *J. Phys. Chem. C* **2010,** *114*, 2116-2123.

(40) Kresse, G.; Furthmuller, J. Efficiency of Ab-Initio Total Energy Calculations for Metals and Semiconductors Using a Plane-Wave Basis Set. *Comput. Mater. Sci.* **1996,** *6*, 15-50.

(41) Kresse, G.; Furthmuller, J. Efficient Iterative Schemes for Ab Initio Total-Energy Calculations Using a Plane-Wave Basis Set. *Phys. Rev. B* **1996,** *54*, 11169-11186.

(42) Dudarev, S. L.; Botton, G. A.; Savrasov, S. Y.; Humphreys, C. J.; Sutton, A. P. Electron-Energy-Loss Spectra and the Structural Stability of Nickel Oxide: An LSDA+U Study. *Phys. Rev. B* **1998,** *57*, 1505-1509.

(43) Perdew, J. P.; Burke, K.; Ernzerhof, M. Generalized Gradient Approximation Made Simple. *Phys. Rev. Lett.* **1996,** *77*, 3865-3868.

(44) Kresse, G.; Joubert, D. From Ultrasoft Pseudopotentials to the Projector Augmented-Wave Method. *Phys. Rev. B* **1999,** *59*, 1758.

(45) Blöchl, P. E. Projector Augmented-Wave Method. *Phys. Rev. B* **1994,** *50*, 17953-17979.

(46) Monkhorst, H. J.; Pack, J. D. Special Points for Brillouin-Zone Integrations. *Phys. Rev. B* **1976,** *13*, 5188-5192.

(47) Dutta, P.; Seehra, M. S.; Thota, S.; Kumar, J. A comparative study of the magnetic properties of bulk and nanocrystalline Co3O4. *J. Phys.: Condens. Matter* **2008,** *20*, 015218.

(48) Henkelman, G.; Jónsson, H. A Dimer Method for Finding Saddle Points on High Dimensional Potential Surfaces Using Only First Derivatives. *J. Chem. Phys.* **1999,** *111*, 7010.

(49) http://theory.cm.utexas.edu/vtsttools/.

(50) Hu, L.; Peng, Q.; Li, Y. Selective synthesis of Co_3O_4 nanocrystal with different shape and crystal plane effect on catalytic property for methane combustion. *J. Am. Chem. Soc.* **2008,** *130*, 16136-16137.

(51) Martin, G.; Mirodatos, C. Surface chemistry in the oxidative coupling of methane. *Fuel Process. Technol.* **1995,** *42*, 179-215.

(52) Fu, G.; Xu, X.; Lu, X.; Wan, H. Mechanisms of Methane Activation and Transformation on Molybdenum Oxide Based Catalysts. *J. Am. Chem. Soc.* **2005,** *127*, 3989-3996.

(53) Holthausen, M. C.; Koch, W. A theoretical view on Co+-mediated CC and CH bond activations in ethane. *J. Am. Chem. Soc.* **1996,** *118*, 9932-9940.

(54) Tian, Z.; Bahlawane, N.; Qi, F.; Kohse-Höinghaus, K. Catalytic oxidation of hydrocarbons over Co3O4 catalyst prepared by CVD. *Catal. Commun.* **2009,** *11*, 118-122.

(55) Argyle, M. D.; Chen, K.; Bell, A. T.; Iglesia, E. Ethane oxidative dehydrogenation pathways on vanadium oxide catalysts. *J. Phys. Chem. B* **2002,** *106*, 5421-5427.

(56) Hoflund, G. B.; Li, Z. Surface characterization study of a Pd/Co3O4 methane oxidation catalyst. *Appl. Surf. Sci.* **2006,** *253*, 2830-2834.

(57) Argyle, M. D.; Chen, K.; Bell, A. T.; Iglesia, E. Effect of catalyst structure on oxidative dehydrogenation of ethane and propane on alumina-supported vanadia. *J. Catal.* **2002,** *208*, 139-149.

(58) Chen, K.; Bell, A. T.; Iglesia, E. Kinetics and mechanism of oxidative dehydrogenation of propane on vanadium, molybdenum, and tungsten oxides. *J. Phys. Chem. B* **2000,** *104*, 1292-1299.

(59) Kilos, B.; Bell, A. T.; Iglesia, E. Mechanism and Site Requirements for Ethanol Oxidation on Vanadium Oxide Domains. *J. Phys. Chem. C* **2009,** *113*, 2830-2836.

(60) Yu, Y.; Takei, T.; Ohashi, H.; He, H.; Zhang, X.; Haruta, M. Pretreatments of Co3O4 at moderate temperature for CO oxidation at −80°C. *J. Catal.* **2009,** *267*, 121-128.

(61) Grillo, F.; Natile, M. M.; Glisenti, A. Low temperature oxidation of carbon monoxide: the influence of water and oxygen on the reactivity of a Co 3 O 4 powder surface. *Appl. Catal., B* **2004,** *48*, 267-274.

3.2 Trends of Alkane Activation on Doped Co_3O_4 from First Principles

3.2.1 Abstract

Surface doping of a metal oxide can tune its catalytic performance, but it remains unclear how the tuning depends on the dopant type and the surface facet. Herein we study doped Co_3O_4 (111) and (311) surface facets using first principles density functional theory to obtain general descriptors of oxygen reactivity (including vacancy formation energy and hydrogen adsorption energy) and correlate them to ethane C-H activation as a measure of the catalytic performance. The periodic trends of the dopants are investigated for a total of twenty dopants, including the elements from K to Ge. We find strong linear correlations between the oxygen reactivity descriptors and the computed energy barriers. We also discover a strong surface facet sensitivity among certain dopants such that different surface orientations and sites have different or even opposing dopant performance. This work provides a useful guide of dopant performance in ethane activation on the two very different Co_3O_4 surfaces.

3.2.2 Introduction

Metal oxides have been extensively studied for their catalytic ability for reactions such as the oxidative coupling and dehydrogenation of alkanes. These catalysts have been found to be effective in activating the otherwise chemically inert C-H bonds, allowing for the further conversion of the reactants. For many of these oxides, the activation occurs over

the active lattice oxygen via the homolytic cleavage of the C-H bond,[1-4] and the resulting radicals are adsorbed onto the surface for further reaction.

As a further dimension in catalyst design, doped metal oxides have been shown to be a promising direction in tuning catalytic reactivity. Most commonly seen are the substitutional dopants which replace the framework metal cation and alter the electronic structure of the neighboring atoms and thus their catalytic reactivity. Many theoretical works in the literature have studied the effects of doping and its effect on the reactivity of lattice oxygen. For example, Metiu et al.[5] concluded that lower valence dopants increase the reactivity of the oxygen, and hence the reactivity of the surface via the Mars-van Krevelen (MvK) mechanism. Meanwhile, higher valence dopants are harder to characterize, depending on the reducibility of the oxide and the nature of the dopant.[5]

It is well known that metal oxides with different surface facets contain oxygen sites with very different activities, and must be considered when predicting the catalytic performance of a metal oxide. For example, Co_3O_4 has been shown to be active and stable for alkane oxidation and oxidative dehydrogenation under high temperatures.[4, 6-9] Depending on the synthesis and treatment method, Co_3O_4 nanoparticles of different, exposed, surface facet orientations can be observed, with different reactivities.[8, 10-14] Additionally, Co_3O_4 has been doped in experimental studies in attempts to tune its reactivity and selectivity towards the desired products.[7, 15-22] Therefore, it is a suitable system to study and a useful starting point for our understanding of dopant sensitivity to surface orientation.

Despite the previous work, the exact impact that different surface orientations have on dopant efficacy is not well studied experimentally or theoretically. It is often convenient to assume a dopant which creates enhanced reactivity on one surface facet will do so for another on the same oxide. But the general applicability of this assumption needs to be examined. By using Co_3O_4 as an example, this work aims to systematically study the effect of a wide range of dopants on a metal oxide from first principles, as well as to demonstrate the significance of different surface facets on determining the dopant's effect of increasing or decreasing reactivity of the metal oxide for ethane activation.

3.2.3 Computational Method

The density functional theory (DFT) calculations in this work were carried out using the Vienna ab initio Simulation Package (VASP).[23-24] The on-site Coulomb interaction was included using the DFT+U method by Dudarev, et al.[25] in VASP using a Hubbard parameter U = 2 eV for the Co atom, which comprises the bulk of the slab atoms, as used in previous studies.[6, 26-27] Theoretical studies have shown that changing the U value does not disturb the linear relationships studied in this work.[28] The Perdew-Burke-Ernzerhof (PBE)[29] form of the generalized-gradient approximation (GGA) was used for electron exchange and correlation energies. All calculations were performed with spin polarization. The projector-augmented wave method was used to describe the electron-core interaction.[23, 30] The kinetic energy cutoff was set to be 450 eV for the planewave basis set. For the studied surface slabs, a 3×3×1 sampling of Brillouin zone using a Monkhorst-Pack scheme was used.[31] A vacuum layer of 15 Å was created for the surface slabs. The top two layers of the slabs were allowed to relax in the calculations. Vacancy formation energy

(E_{vac}) is calculated with the equation $E_{vac}=E_{vacancy\text{-}surface} + 1/2E_{O2} - E_{perfect\text{-}surface}$, where $E_{vacancy\text{-}surface}$ is the energy of the surface slab with the oxygen atom removed and $E_{perfect\text{-}surface}$ is the energy of the vacancy-free surface, while E_{O2} is the energy of an isolated O_2 molecule. The hydrogen adsorption energy (E_{Hads}) is calculated with the equation $E_{Hads} = E_{surface+H} - (E_{perfect\text{-}surface} + E_H)$, where $E_{surface+H}$ is the energy of the surface with a hydrogen adsorbed on the oxygen atom and E_H is the energy of an isolated H atom. The energies of E_{O2} and E_H were computed by placing the adsorbate in a cubic cell with a 10 Å wide vacuum in each direction. Transition states (TS) were found with the dimer method[32] implemented in the VASP-VTST package by Henkelman et al. using a force convergence criterion of 0.05 eV/Å.

3.2.4 Results and Discussion

3.2.4.1 Two facets of Co_3O_4 and localization of dopant effects

We examined both a flat surface, (111), and a rough surface, (311), of Co_3O_4. Their surface models are shown in Figure 1. The dopant replaces the Co atom at the location labeled “Site”. We found no significant local structural change on either facet after doping, probably due to the comparatively low dopant concentration used. The oxygen coordination number of the metal is three on the (111) site and is five on the (311) site. The doping is expected to change the activities of these oxygen atoms. A simple descriptor of their activity is the oxygen-vacancy formation energy, E_{vac}.

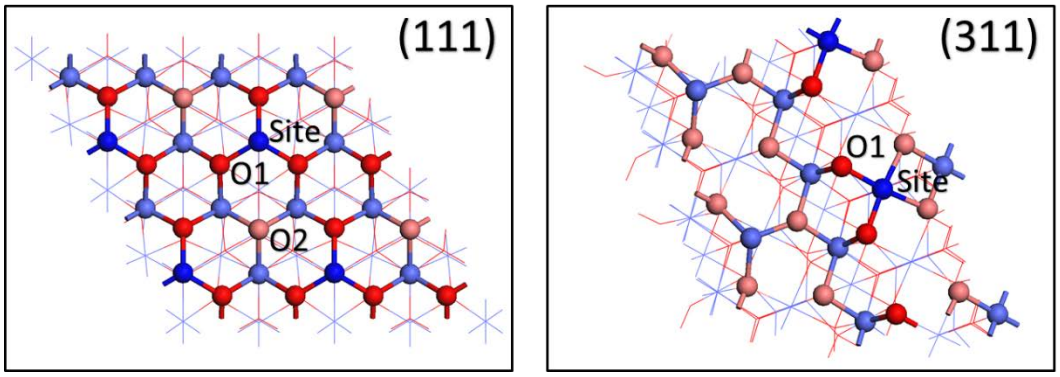

Figure 3.2.1 Surface models for the (111) surface (left) and the (311) surface (right) of Co_3O_4, showing the upper layer atoms as circles and the sublayer atoms as lines. The blue atoms denote Co and the red atoms denote O. The dark blue atoms are the exposed Co sites, and one is replaced by a dopant at the location labeled 'Site'. The nearest neighbor oxygen atom studied is labeled O1, and the second nearest neighbor is labeled O2.

We obtained E_{vac} on the first neighbors O1 and second neighbors O2 on the (111) surface and found that changes in O1 E_{vac} can be significant among dopants, while the O2 E_{vac} energies remain largely unchanged (Figure 2). In other words, the effect of doping is rather local and limited to the nearest-neighbor oxygen atoms, and the impact on the oxygen atoms beyond the first coordination shell is very weak. This is largely consistent with an earlier theoretical work on the CeO_2 surface.[33] Consequently, we focus on studying the nearest-neighbor oxygen (O1).

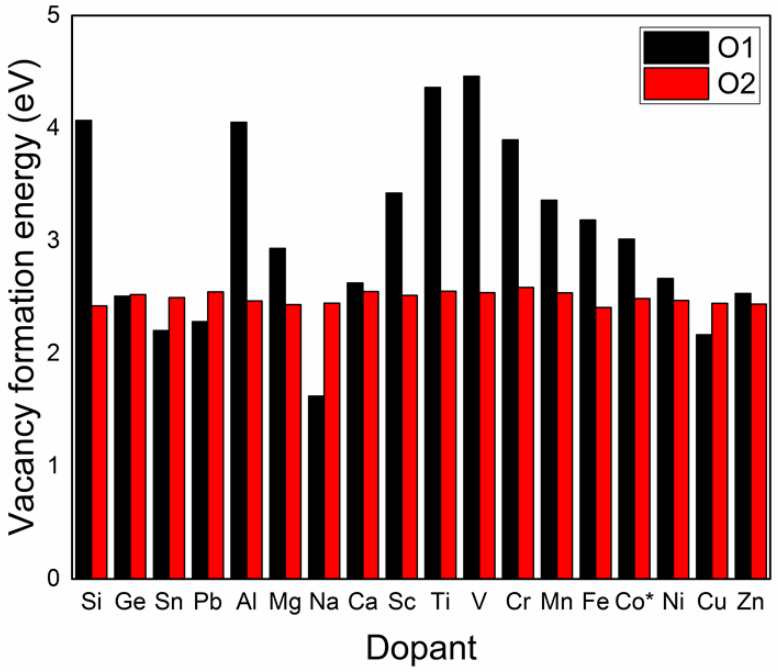

Figure 3.2.2 Vacancy formation energies of oxygen atoms on the doped Co_3O_4(111) surface. Co* denotes the undoped surface. O1 represents the oxygen first neighbors, O2 represents the oxygen second neighbors (see Figure 1).

3.2.4.2 Charge transfer between dopant and oxygen

From the perspective of electronic structure, we can track the partial transfer of electrons from the metal to the neighboring oxygen atoms using Bader charges. Figure 3 plots the dopant Bader charge versus the oxygen Bader charge for both the (111) and (311) facets. One can see the strong linear correlation between the electron loss of the lattice metal or dopant and the electron gain of the lattice oxygen, regardless of the identity of the metal dopant used. Furthermore, it suggests that the change in the lattice oxygen charge is directly due to changing the identity of the dopant used, and not as a result of geometric reconstruction or the forming of new coordination following doping, which would result

in large deviations from the linear correlation. In Figure 3 we can also distinguish the correlation of charge transfer as two distinct lines corresponding to the (111) and (311) surface. This can be explained by the difference in oxygen coordination of the dopant site on (111) and (311), namely, three and five, respectively. Consequently, the electron transfer for the dopant on (311) is further dispersed among two extra oxygen atoms, which would shift the line to the right and generate a larger slope.

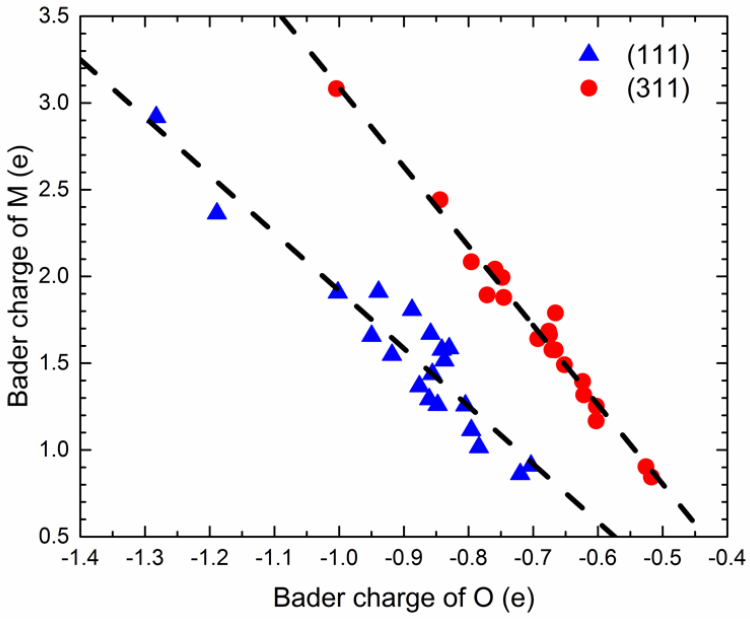

Figure 3.2.3 The Bader charge of the dopant M vs the Bader charge of the nearest neighbor O. The blue triangles and red circles denote points from the (111) and (311) surfaces of Co_3O_4, respectively. Black dashed lines represent linear best fit lines for the two surfaces.

3.2.4.3 Descriptors and trends of oxygen reactivity for the doped surfaces

A number of descriptors have been proposed as possible descriptors of oxygen reactivity in metal oxides, including the energetic quantities E_{Hads}[28, 34-38] and $E_{vac,}$[6, 34, 39-41]

as well as electronic ones such as Bader charge[26, 42] and work function[28]. Figure 4 shows that E_{Hads} and E_{vac} show strong linear correlations, with a low mean absolute error (MAE) of 0.16 eV and R value of 0.93. This is consistent with the general observation that the correlation between E_{Hads} and E_{vac} is independent of changing the identity of the metal in the metal oxide, or its surface orientation, and can be applied generally, because both are energetic descriptors to predict the oxygen site's reactivity. Below we will base our analysis of oxygen reactivity on both E_{Hads} and E_{vac} as descriptors.

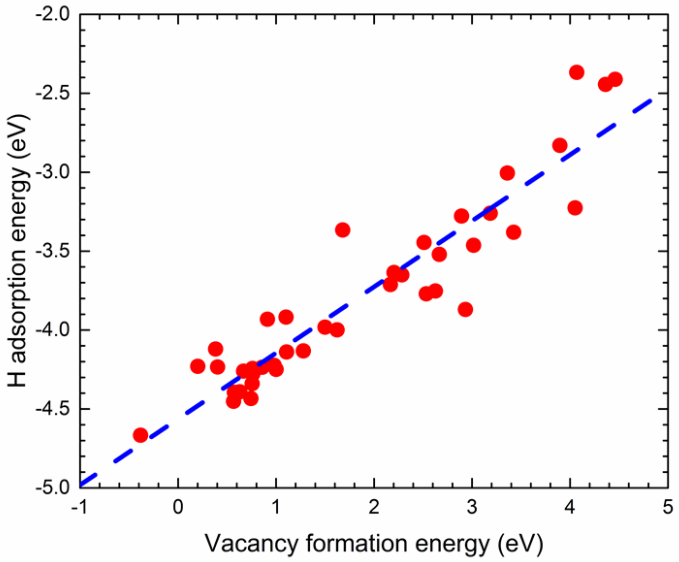

Figure 3.2.4 Correlation between H adsorption energy and vacancy formation energy for the oxygen sites closest to the dopant sites on the Co_3O_4 surfaces. The blue dashed line represents the linear best fit line.

We examine the dopant periodic trends on the oxygen reactivity descriptors and C-H activation energy for a series of elements in the same period. These trends are displayed in Figure 5 for both E_{Hads} and E_{vac}. Overall, it appears that the oxygen reactivity is the highest

(that is, most negative E_{Hads} or smallest E_{vac}) for group 1 (with potassium as the dopant) for both surfaces, and decreases sequentially to a peak at V for (111) or Cr for (311), before increasing in activity again until Zn. Oxygen reactivity decreases again at Ga, though the dopant effect is mixed for Ge for different surfaces. It is important to note that the peaks in oxygen reactivity differ in location between the two surfaces, indicating that the surfaces on which the dopants reside in may have an important role on its reactivity. This phenomenon is further explored below. A volcano trend can be observed in Figure 5, with peaks at Ti/V for (111) and Cr for (311). From left to right, the oxidation state of the elements increases, which corresponds to stronger M-O bonds, leading to more positive E_{Hads} and $E_{vac.}$ As the dopant occupies the tetrahedral +2 site on (111) and the octahedral +3 site on (311), the peak of the volcano for (311) is shifted to the right. To the right of the volcano, E_{Hads} and E_{vac} become more negative as the oxidation states decrease to Zn, and increase again for Ga and Ge.

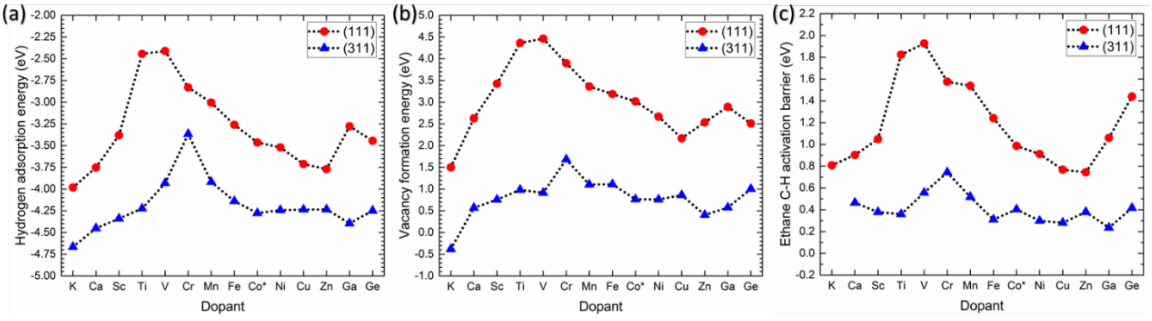

Figure 3.2.5 The periodic trends of oxygen reactivity on the M-doped Co_3O_4 surfaces: (a) H adsorption energy; (b) vacancy formation energy; (c) C-H activation energy. Co* denotes the undoped surface.

3.2.4.4 C-H activation on doped surfaces

It is generally found that for Co_3O_4, and other oxides in general, the first step of the catalytic reaction involves C-H activation, regardless of the subsequent pathways through oxidative dehydrogenation or complete combustion. While both homolytic and heterolytic bond cleavage mechanisms are possible, studies have found that the homolytic pathway is often the pathway with the lowest barriers on Co_3O_4,[8, 26] involving H abstraction and cleavage of the C-H bond over a lattice oxygen. It is this pathway which allows for easy prediction of C-H barriers through *Brønsted*-Evans-Polanyi (BEP) relations. Furthermore, it has been shown that the activation barriers of alkanes and alcohols of different chemical compositions can be linearly related to one another simply as a function of the C-H bond strength;[35] therefore, it can be possible to extrapolate results from a single alkane to the entire class of compounds. Herein we focus our efforts on the homolytic C-H activation, using ethane as our probe molecule.

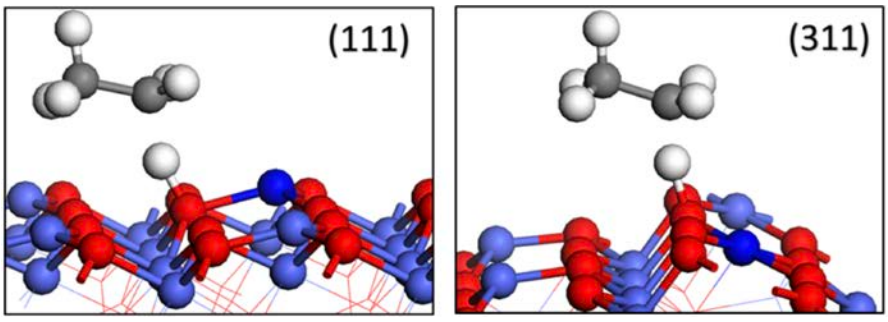

Figure 3.2.6 The transition state geometries of ethane C-H activation via H abstraction for the (111) surface and the (311) surface.

Figure 6 shows representative transition state (TS) geometries for the homolytic C-H activation over the two undoped (111) surface and the (311) surface. The TS takes the form of an ethane molecule with an elongated C-H bond with the hydrogen situated in between the carbon and the lattice oxygen. Both exhibit similar geometries, and differ mainly in the TS O*-H and C-H distances and their corresponding E_a. The bond distances for the transition states are accordingly plotted against E_{Hads} in Figure 7. The distance trends are apparent, showing that as E_{Hads} becomes more negative (that is, stronger) and the lattice oxygen becomes more reactive, the TS O*-H distance increases and the TS C-H distance decreases. This observation is consistent with the BEP relationship, in terms of the TS of H abstraction being the overlap between the potential energy surfaces C-H bond dissolution and O-H bond formation. In our case (Figure 6), the strength of the C-H bond is roughly constant, while the strength of the O-H bond is varied via the different dopants. When the oxygen reactivity is high, the TS is early, so the C-H bond is short and the O-H bond is long; when the oxygen reactivity is low, the TS is late, so the C-H bond is long and the O-H bond is short. This phenomenon, in the context of C-H bond activation on metal oxides, has been brought up in a previous theoretical study,[36] but can now be verified in terms of a general linear scaling relationship in Figure 7.

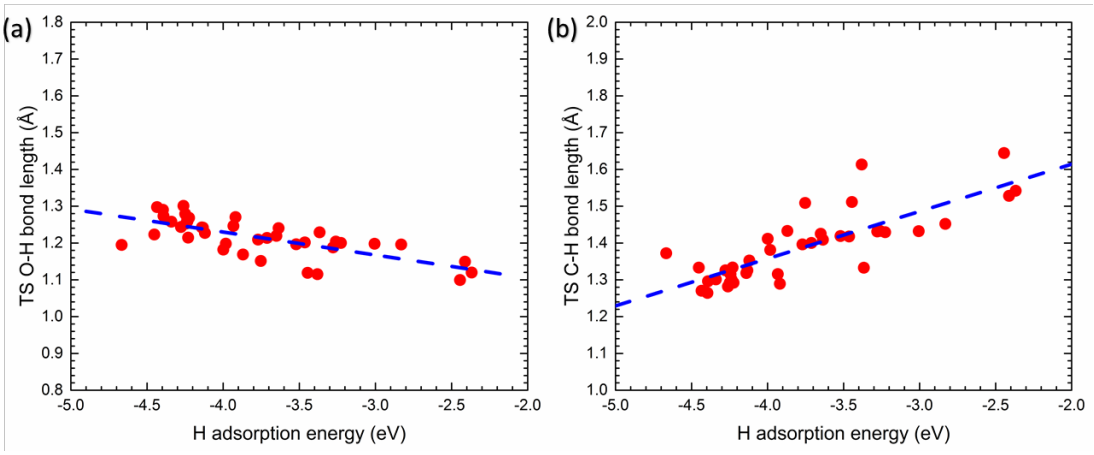

Figure 3.2.7 Correlation of the transition-state (TS) geometry of ethane C-H activation with H adsorption energy on doped Co_3O_4 surfaces: (a) O-H bond length; (b) C-H bond length. The blue dashed lines represent the linear best fit for the points.

3.2.4.5 Correlation between C-H activation and oxygen descriptors

Many recent theoretical works[34-35, 43] have demonstrated the validity of oxygen descriptors such as vacancy formation and H adsorption towards predicting C-H activation barriers. Figure 5c shows the trend of the ethane C-H activation energy (E_a) across the periodic table for both doped Co_3O_4 (111) and (311) facets. One can see that the overall trends of E_{Hads}, E_{vac}, and E_a across the different dopants are similar. Figure 8 shows that indeed E_a has very strong linear correlations with both E_{Hads} and E_{vac}, with mean average error (MAE) at 0.15 and 0.11 eV, respectively. These small MAEs suggest that it is promising to use these oxygen reactivity descriptors as a method of screening dopants prior to expensive transition state search calculations. We can refer to the BEP-relationship to provide an explanation for this correlation from the perspective of E_{Hads}.

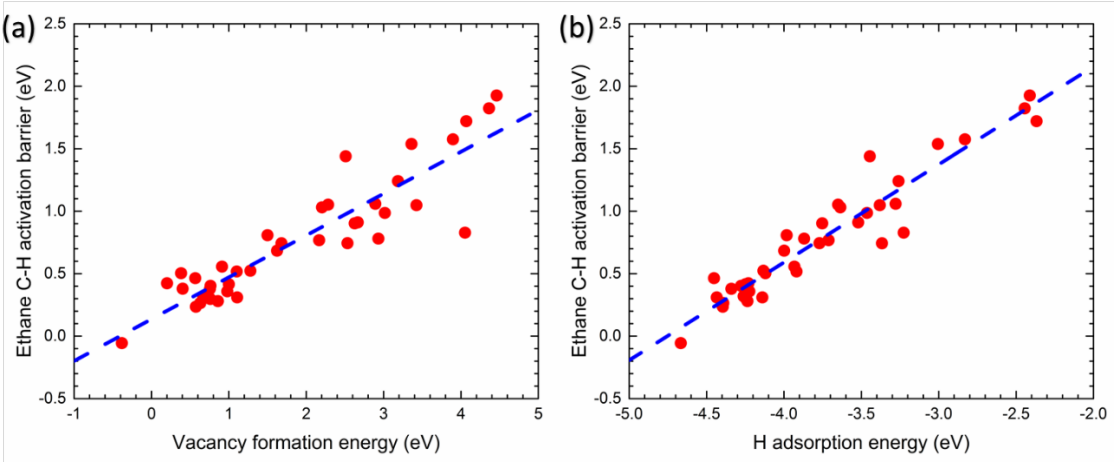

Figure 3.2.8 Correlation of the ethane C-H activation energy with: (a) vacancy formation energy; (b) H adsorption energy. The blue dashed lines represent the linear best fit for the points.

3.2.4.6 Surface facet sensitivity of different dopants

Figure 9 shows the C-H activation-energy difference between (111) and (311) surfaces for the different dopants. Overall, both undoped and doped (311) surfaces are more reactive than the corresponding (111) surfaces for C-H activation of ethane. More specifically, one can see that Ti, V and Si show the highest sensitivity to the facets, having $\Delta E_a \sim 1.3$ to 1.4 eV. If one uses the undoped Co_3O_4 surfaces as a reference, K, Cr, Mn, Fe, Ga, and Fe also display significantly higher sensitivity to the facets.

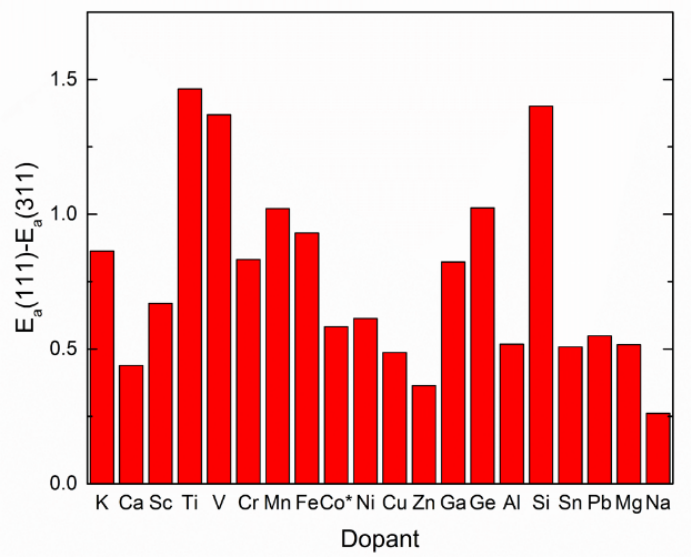

Figure 3.2.9 The difference in ethane C-H activation energy between the (111) and (311) facets for the different dopants.

3.2.4.7 Implications of present results

In this work, we have focused our study on comparing two surfaces, a low index (111) surface with exposed tetrahedral Co^{2+}, and a high index (311) surface with exposed octahedral Co^{3+}, which is sufficient to qualitatively demonstrate large differences in dopant effects between the two. It is very probable that this phenomenon will extend to metal oxides in general, beyond Co_3O_4 as studied in this work. Further systematic studies on other metal oxides can be useful in developing a sufficiently comprehensive understanding linking the geometric and electronic structure of the dopant site to the oxygen reactivity through sampling and studying a larger number of surface facets and corresponding substitution sites. The importance of surface orientation in determining dopant performance has significant implications towards the prediction of catalytic properties of

doped oxides. As different experimental synthesis techniques can invariably lead to nanoparticles with various exposed surfaces, the role of a dopant can be complicated by the surface-facet sensitivity.

The present work considered a fixed dopant concentration. We expect that the scaling relation between the computed barriers and the descriptors would remain for different dopant concentrations, but testing this hypothesis would require substantial more calculations. Further studies are warranted.

3.2.5 Conclusions

The effects of doping Co_3O_4 on oxygen reactivity and C-H activation barriers were investigated for a range of dopants on two different surfaces, (111) and (311). We found the dopant effects to be limited to the nearest-neighbor oxygen atoms, with no significant changes to oxygen reactivity at or beyond the second coordination shell. The periodic trends of doping on oxygen reactivity were examined by comparing oxygen-vacancy formation, H adsorption energy on oxygen, and homolytic C-H activation of ethane. The oxygen reactivity descriptors (vacancy formation H adsorption energy) were linked to the C-H activation energies and the transition-state geometry. It was further shown that the surface orientation can have a significant impact on dopant efficacy. This work demonstrates that oxygen-activity descriptors can be used to predict dopant performance on transition-metal oxide surfaces and that doping and the surface orientation can be combined together to tune the transition-metal oxide's reactivity.

References

(1) Lunsford, J. H. The Catalytic Oxidative Coupling of Methane. *Angew. Chem. Int. Ed.* **1995,** *34*, 970-980.

(2) Schwarz, H. Chemistry with Methane: Concepts Rather than Recipes. *Angew. Chem. Int. Ed.* **2011,** *50*, 10096-10115.

(3) Feyel, S.; Döbler, J.; Schröder, D.; Sauer, J.; Schwarz, H. Thermal activation of methane by tetranuclear [V4O10]+. *Angew. Chem. Int. Ed.* **2006,** *45*, 4681-4685.

(4) Hu, W.; Lan, J.; Guo, Y.; Cao, X.-M.; Hu, P. Origin of efficient catalytic combustion of methane over Co_3O_4 (110): active low-coordination lattice oxygen and cooperation of multiple active sites. *ACS Catal.* **2016,** *6*, 5508-5519.

(5) McFarland, E. W.; Metiu, H. Catalysis by Doped Oxides. *Chem. Rev.* **2013,** *113*, 4391-4427.

(6) Liu, J. J.; Zhang, S. R.; Zhou, Y.; Fung, V.; Nguyen, L.; Jiang, D. E.; Shen, W. J.; Fan, J.; Tao, F. F. Tuning Catalytic Selectivity of Oxidative Catalysis through Deposition of Nonmetallic Atoms in Surface Lattice of Metal Oxide. *ACS Catal.* **2016,** *6*, 4218-4228.

(7) Tao, F. F.; Shan, J. J.; Nguyen, L.; Wang, Z.; Zhang, S.; Zhang, L.; Wu, Z.; Huang, W.; Zeng, S.; Hu, P. Understanding Complete Oxidation of Methane on Spinel Oxides at a Molecular Level. *Nature Commun.* **2015,** *6*, 7798.

(8) Tyo, E. C.; Yin, C.; Di Vece, M.; Qian, Q.; Kwon, G.; Lee, S.; Lee, B.; DeBartolo, J. E.; Seifert, S.; Winans, R. E.; Si, R.; Ricks, B.; Goergen, S.; Rutter, M.; Zugic, B.; Flytzani-Stephanopoulos, M.; Wang, Z. W.; Palmer, R. E.; Neurock, M.; Vajda, S. Oxidative dehydrogenation of cyclohexane on cobalt oxide (Co_3O_4) nanoparticles: The effect of particle size on activity and selectivity. *ACS Catal.* **2012,** *2*, 2409-2423.

(9) Wang, H.-F.; Wang, D.; Liu, X.; Guo, Y.-L.; Lu, G.-Z.; Hu, P. Unexpected C–C Bond Cleavage Mechanism in Ethylene Combustion at Low Temperature: Origin and Implications. *ACS Catal.* **2016,** *6*, 5393-5398.

(10) Hu, L.; Peng, Q.; Li, Y. Selective synthesis of Co_3O_4 nanocrystal with different shape and crystal plane effect on catalytic property for methane combustion. *J. Am. Chem. Soc.* **2008,** *130*, 16136-16137.

(11) Chen, Z.; Kronawitter, C. X.; Koel, B. E. Facet-dependent activity and stability of Co_3O_4 nanocrystals towards the oxygen evolution reaction. *Phys. Chem. Chem. Phys.* **2015,** *17*, 29387-29393.

(12) Sun, H.; Ang, H. M.; Tadé, M. O.; Wang, S. Co_3O_4 nanocrystals with predominantly exposed facets: synthesis, environmental and energy applications. *J. Mater. Chem. A* **2013,** *1*, 14427-14442.

(13) Sun, Y. N.; Liu, J. W.; Song, J. J.; Huang, S. S.; Yang, N. T.; Zhang, J.; Sun, Y. H.; Zhu, Y. Exploring the Effect of Co_3O_4 Nanocatalysts with Different Dimensional Architectures on Methane Combustion. *ChemCatChem* **2016,** *8*, 540-545.

(14) Fung, V.; Tao, F. F.; Jiang, D. E. General Structure-Reactivity Relationship for Oxygen on Transition-Metal Oxides. *J. Phys. Chem. Lett.* **2017,** *8*, 2206-2211.

(15) Zhou, M.; Cai, L.; Bajdich, M.; García-Melchor, M.; Li, H.; He, J.; Wilcox, J.; Wu, W.; Vojvodic, A.; Zheng, X. Enhancing catalytic CO oxidation over Co_3O_4 nanowires by substituting Co^{2+} with Cu^{2+}. *ACS Catal.* **2015,** *5*, 4485-4491.

(16) Hamdani, M.; Singh, R.; Chartier, P. Co3O4 and Co-based spinel oxides bifunctional oxygen electrodes. *Int. J. Electrochem. Sci* **2010,** *5*, 556.

(17) Ohnishi, C.; Asano, K.; Iwamoto, S.; Chikama, K.; Inoue, M. Alkali-doped Co 3 O 4 catalysts for direct decomposition of N 2 O in the presence of oxygen. *Catal. Today* **2007,** *120*, 145-150.

(18) Asano, K.; Ohnishi, C.; Iwamoto, S.; Shioya, Y.; Inoue, M. Potassium-doped Co 3 O 4 catalyst for direct decomposition of N 2 O. *Appl. Catal., B* **2008,** *78*, 242-249.

(19) Shang, Z.; Sun, M.; Chang, S.; Che, X.; Cao, X.; Wang, L.; Guo, Y.; Zhan, W.; Guo, Y.; Lu, G. Activity and stability of Co 3 O 4-based catalysts for soot oxidation: The enhanced effect of Bi 2 O 3 on activation and transfer of oxygen. *Appl. Catal., B* **2017,** *209*, 33-44.

(20) Zhu, Z.; Lu, G.; Zhang, Z.; Guo, Y.; Guo, Y.; Wang, Y. Highly Active and Stable Co3O4/ZSM-5 Catalyst for Propane Oxidation: Effect of the Preparation Method. *ACS Catal.* **2013,** *3*, 1154-1164.

(21) Lou, Y.; Wang, L.; Zhao, Z.; Zhang, Y.; Zhang, Z.; Lu, G.; Guo, Y.; Guo, Y. Low-temperature CO oxidation over Co 3 O 4-based catalysts: Significant promoting effect of Bi 2 O 3 on Co 3 O 4 catalyst. *Appl. Catal., B* **2014,** *146*, 43-49.

(22) Lou, Y.; Cao, X.-M.; Lan, J.; Wang, L.; Dai, Q.; Guo, Y.; Ma, J.; Zhao, Z.; Guo, Y.; Hu, P. Ultralow-temperature CO oxidation on an In 2 O 3–Co 3 O 4 catalyst: a strategy to tune CO adsorption strength and oxygen activation simultaneously. *Chem. Commun.* **2014,** *50*, 6835-6838.

(23) Kresse, G.; Furthmuller, J. Efficiency of Ab-Initio Total Energy Calculations for Metals and Semiconductors Using a Plane-Wave Basis Set. *Comput. Mater. Sci.* **1996,** *6*, 15-50.

(24) Kresse, G.; Furthmuller, J. Efficient Iterative Schemes for Ab Initio Total-Energy Calculations Using a Plane-Wave Basis Set. *Phys. Rev. B* **1996,** *54*, 11169-11186.

(25) Dudarev, S. L.; Botton, G. A.; Savrasov, S. Y.; Humphreys, C. J.; Sutton, A. P. Electron-Energy-Loss Spectra and the Structural Stability of Nickel Oxide: An LSDA+U Study. *Phys. Rev. B* **1998,** *57*, 1505-1509.

(26) Fung, V.; Tao, F.; Jiang, D. E. Understanding oxidative dehydrogenation of ethane on Co3O4 nanorods from density functional theory. *Catal. Sci. Technol.* **2016,** *6*, 6861-6869.

(27) Jiang, D. E.; Dai, S. The role of low-coordinate oxygen on Co_3O_4(110) in catalytic CO oxidation. *Phys. Chem. Chem. Phys.* **2011,** *13*, 978-84.

(28) Kumar, G.; Lau, S. L. J.; Krcha, M. D.; Janik, M. J. Correlation of Methane Activation and Oxide Catalyst Reducibility and its Implications for Oxidative Coupling. *ACS Catal.* **2016,** *6*, 1812-1821.

(29) Perdew, J. P.; Burke, K.; Ernzerhof, M. Generalized Gradient Approximation Made Simple. *Phys. Rev. Lett.* **1996,** *77*, 3865-3868.

(30) Blöchl, P. E. Projector Augmented-Wave Method. *Phys. Rev. B* **1994,** *50*, 17953-17979.

(31) Monkhorst, H. J.; Pack, J. D. Special Points for Brillouin-Zone Integrations. *Phys. Rev. B* **1976,** *13*, 5188-5192.

(32) Henkelman, G.; Jónsson, H. A Dimer Method for Finding Saddle Points on High Dimensional Potential Surfaces Using Only First Derivatives. *J. Chem. Phys.* **1999,** *111*, 7010.

(33) Hu, Z.; Metiu, H. Effect of dopants on the energy of oxygen-vacancy formation at the surface of ceria: Local or global? *J. Phys. Chem. C* **2011,** *115*, 17898-17909.

(34) Krcha, M. D.; Mayernick, A. D.; Janik, M. J. Periodic Trends of Oxygen Vacancy Formation and C–H Bond Activation Over Transition Metal-Doped CeO_2 (111) Surfaces. *J. Catal.* **2012,** *293*, 103-115.

(35) Latimer, A. A.; Kulkarni, A. R.; Aljama, H.; Montoya, J. H.; Yoo, J. S.; Tsai, C.; Abild-Pedersen, F.; Studt, F.; Norskov, J. K. Understanding trends in C-H bond activation in heterogeneous catalysis. *Nature Mater.* **2016,** *advance online publication*.

(36) Deshlahra, P.; Iglesia, E. Reactivity and Selectivity Descriptors for the Activation of C-H Bonds in Hydrocarbons and Oxygenates on Metal Oxides. *J. Phys. Chem. C* **2016,** *120*, 16741-16760.

(37) Deshlahra, P.; Iglesia, E. Toward More Complete Descriptors of Reactivity in Catalysis by Solid Acids. *ACS Catal.* **2016,** *6*, 5386-5392.

(38) van Santen, R. A.; Neurock, M.; Shetty, S. G. Reactivity Theory of Transition-Metal Surfaces: A Brønsted− Evans− Polanyi Linear Activation Energy− Free-Energy Analysis. *Chem. Rev.* **2009,** *110*, 2005-2048.

(39) Harth, M.; Mitdank, R.; Habel, D.; Görke, O.; Tovar, M.; Winter, H.; Schubert, H. Thermally activated redox-processes in V_2O_5-x under high oxygen partial pressures investigated by means of impedance spectroscopy and Rutherford backscattering. *Int. J. Mater. Res.* **2012,** *104*, 657-665.

(40) Li, B.; Metiu, H. DFT Studies of Oxygen Vacancies on Undoped and Doped La_2O_3 Surfaces. *J. Phys. Chem. C* **2010,** *114*, 12234-12244.

(41) Derk, A. R.; Li, B.; Sharma, S.; Moore, G. M.; McFarland, E. W.; Metiu, H. Methane Oxidation by Lanthanum Oxide Doped with Cu, Zn, Mg, Fe, Nb, Ti, Zr, or Ta: the Connection Between the Activation Energy and the Energy of Oxygen-Vacancy Formation. *Catal. Lett.* **2013,** *143*, 406-410.

(42) Dai, G.-L.; Liu, Z.-P.; Wang, W.-N.; Lu, J.; Fan, K.-N. Oxidative Dehydrogenation of Ethane Over V_2O_5 (001): A Periodic Density Functional Theory Study. *J. Phys. Chem. C* **2008,** *112*, 3719-3725.

(43) Krcha, M. D.; Janik, M. J. Catalytic Propane Reforming Mechanism Over Zr-Doped CeO_2(111). *Catal. Sci. Technol.* **2014,** *4*, 3278.

4 Descriptors for metal oxides

4.1 General Structure-Reactivity Relationship for Oxygen on Transition Metal Oxides

4.1.1 Abstract

Despite many recent developments in designing and screening catalysts for improved performance, transition-metal oxides continue to prove challenging due to the myriad inherent complexities of the systems and the possible morphologies that it can exhibit. Herein we propose a structural descriptor, the adjusted coordination number (ACN), which can generalize the reactivity of the oxygen sites over the many possible surface facets and defects of a transition-metal oxide. We demonstrate the strong correlation of this geometric descriptor with the electronic and energetic properties of the active sites on five facets of four transition-metal oxides. We then use the structural descriptor to predict C-H activation energies, to show the great potential of using ACN for the prediction of catalytic performance. This study presents a first look into quantifying the relation between active site structure and reactivity of transition-metal-oxide catalysts.

4.1.2 Introduction

The widespread adoption of density functional theory (DFT) has opened up new avenues in the use of computational methods to model and predict the structure-activity relationship of promising catalysts. Unfortunately, due to the inherent computational cost of fully ab-initio techniques and the sheer number and complexity of possible catalytic

materials and pathways to study, there has been much interest in developing approximate but fast methods of predicting catalytic activity based on DFT results. This "descriptor" approach based on adsorption energy, dissociation energy, d-band center and width, etc., has been employed successfully to transition metal catalysts.[1-3] Subsequent recent works have further demonstrated the concept of "structural" descriptors as a geometric based method of catalyst screening and design for transition metals[4-7] which can be further extended to an 'orbitalwise' description of coordination.[8]

Transition-metal (TM) oxides are another class of materials of considerable interest and potential for heterogeneous catalysis. The complexity of TM oxide surfaces can be up to several orders of magnitude greater than transition metals due to the multiple oxidation states, high density of surface defects, and complex electronic and spin structures. The inherent complexity of TM oxides coupled with their industrial importance provides a strong impetus towards the development of broadly applicable and quantitative descriptors of their catalytic activity. In this work, we propose a structural descriptor to provide a first look into structure-reactivity relationships for the active oxygen sites of TM oxides, corroborated by DFT calculations (see the Supporting Information for computational details).

Two commonly studied quantities to describe the oxygen reactivity on metal oxides are vacancy formation energy[9-18] and H adsorption energy.[1, 14, 19-22] Vacancy formation energy measures the energy required to remove a lattice oxygen from the surface and has been suggested as a descriptor of catalytic performance.[12, 18, 23] H adsorption has also been used in the correlations with the activation energies of C-H bond dissociation via the

BEP relationship.[19-21, 24] Besides the energetic descriptors, the electronic properties of solid catalysts in relation to their energetic properties or reactivity have been well demonstrated for transition metals and other transition metal based materials.[18, 25-30]

In search of a structural descriptor for TM oxides, we were inspired by a recent success for such a descriptor for transition metals. Calle-Vallejo et al. used coordination number and "generalized coordination number" as structural descriptors for transition metals to describe the structural and electronic environment of the adsorption site and its nearest neighbors,[4-6] and correlated them to the d-band center. Inspired by their work, we think that the coordination number of the oxygen atom (CN_O) on TM oxide surfaces can be used as a structural descriptor. However, for metal oxides, the relevant CN_O rarely goes beyond one to four at the surface and cannot provide the same level of sensitivity and predictive ability as coordination in transition metals. Therefore, we propose to include not only the coordination number of the surface oxygen site but also the coordination numbers of its neighboring *metal* atoms as a sum ($\sum CN_M$). Take the O-M-O*-M-O bonding motif as an example, with O* being the oxygen in question and M being a metal. The coordination number of O*, CN_O, is 2 in this case, while the sum of the coordination numbers of the coordinating M atoms, $\sum CN_M$, is 2 + 2 = 4.

4.1.3 Results and Discussion

To correlate these coordination numbers to the electronic structure and reactivity of a metal oxide surface, a logical approach is to examine how they relate to the partial charge on the oxygen site, which is a good indication of reducibility. Indeed we found

strong linear correlation of Bader charge[31] with vacancy formation energy and H adsorption energy associated with a surface oxygen site on various surfaces [(100), (110), (111), (211), and (311)] and types of TM oxides (V_2O_3, Cr_2O_3, Co_3O_4, and NiO), as shown in Figure S1 and Table S1 in SI. So we only need to find a structural descriptor that is a function of CN_O and CN_M and at the same time correlates well with the O Bader charge. Intuitively, increasing CN_O will make the O Bader charge more negative by providing additional sources of electron density, i.e., the metal cations. Meanwhile, increasing $\sum CN_M$ decreases Bader charge because the oxygen atoms in the second shell will withdraw electron density from the metal cations, leaving less to be transferred to the oxygen site.

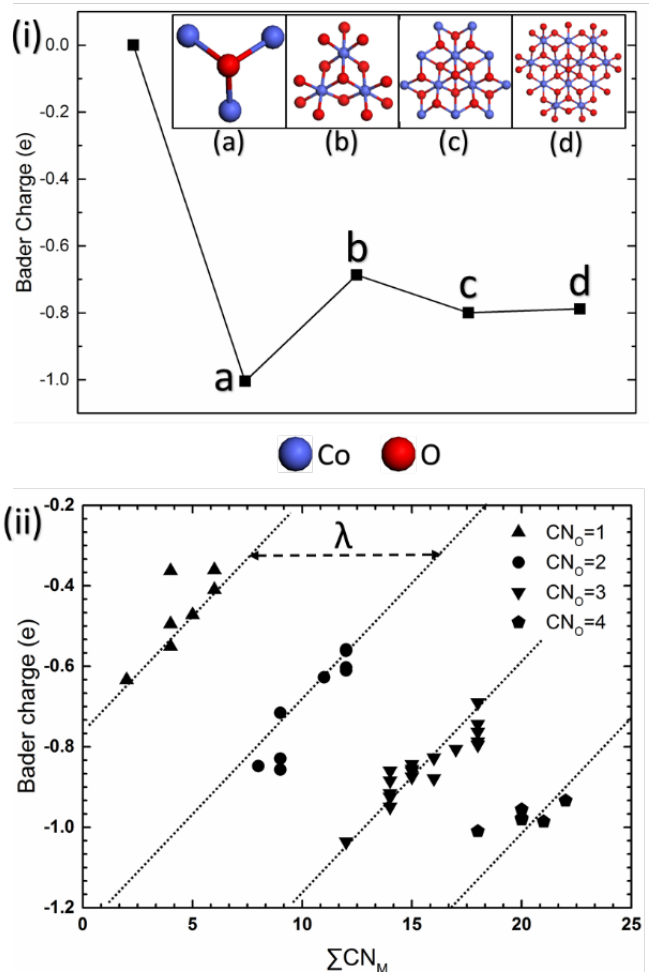

Figure 4.1.1 (i) The electron-donating and electron-withdrawing effect of the cobalt and oxygen shells in Co_3O_4 in a cluster model. The first point at the Bader charge of zero is represented by a single gas phase O (red) atom. Points a-d represent adding successive 'shells' of alternating cobalt (blue) and oxygen (red) to the central oxygen. The cluster model represents the coordination environment of a typical O site on Co_3O_4 (111). (ii) The coordination effect of the oxygen CN_O on shifting the CN_M relations versus Bader charge on Co_3O_4. A near constant separation between each CN_O is denoted by λ.

We demonstrate the metal-oxygen electron transfer model with successively larger clusters of Co_xO_y: the alternating electron donating and withdrawing effect of the successive neighboring oxygen and cobalt atoms can be seen in the Bader charge trend in

Figure 1(i). This leads to the oscillating Bader charges as each successive cobalt shell donates charge and oxygen shell withdraws charge until finally converging as it approaches the characteristics of a periodic surface. In theory, one can further refine this model by counting the coordination of further successively bonded atoms; the improvement to accuracy should rapidly converge as the difference in the subsequent coordination shells will vary less and less the further away from the oxygen atoms in question. So we will focus only on the first cobalt and oxygen shells here.

To identify a structural descriptor that is a function of both CN_O and CN_M, we need to examine the relationship between CN_O and $\sum CN_M$. As an example, here we use oxygen atoms on the Co_3O_4 faces where CN_O can vary from 1 to 4. In plotting Bader charge versus $\sum CN_M$ in Figure 1(ii), we can see that these two quantities exhibit a strong linear relationship, i.e. by increasing $\sum CN_M$ one will make the O Bader charge more positive. More interestingly, we see the existence of multiple, parallel scaling lines in the figure, distinguished by the CN_O of the surface oxygen sites. For an increasing value of CN_O, the line becomes more and more right-shifted, corresponding to a region of more negative Bader charge; the lines shift by an approximately constant value, labeled as λ. Therefore, we can formulate an "adjusted coordination number" (ACN) where we off-shift, or adjust, the offset of CN_O in relation to $\sum CN_M$; thus the ACN becomes a function of CN_O and $\sum CN_M$ and the data points in Figure 1(ii) can fall into one line. A straightforward construction of ACN can take the form of

$$ACN = CN_O * \lambda - \sum CN_M, \quad (1)$$

where λ is a single parameter that fits the linear offset to Bader charge and is fixed for a specific oxide once its bulk structure is given. The quantities CN_O *and* $\sum CN_M$ are then subtracted from each other due to the opposing effects that they have on the Bader charge of the lattice oxygen in question. λ can be obtained by optimizing the value to maximize the linear correlation constant between ACN and Bader charge (see Table S2 for λ values; Figure S2 and Table S3 for the linear correlation between oxygen ACN and Bader charge).

The strength of ACN lies in giving an extremely fast, zeroth-order approximation of the local electronic structure of the lattice oxygen in question through its correlation with the Bader charge, which then correlates to reactivity. Through this, a general prediction of the oxygen site reducibility through its structural properties becomes clear. Figure 2 shows the calculation of ACN on two Co_3O_4 sites from different facets. Both have a low CN_O of 2, suggesting high reactivity, but a different coordination of its neighboring metal atoms, leading to a different $\sum CN_M$. ACN for the (311) site calculated with Equation 1 is 7.59, lower than that for the (110) site (10.59), correctly predicting the stronger H adsorption energy (E_H) on the (311) site.

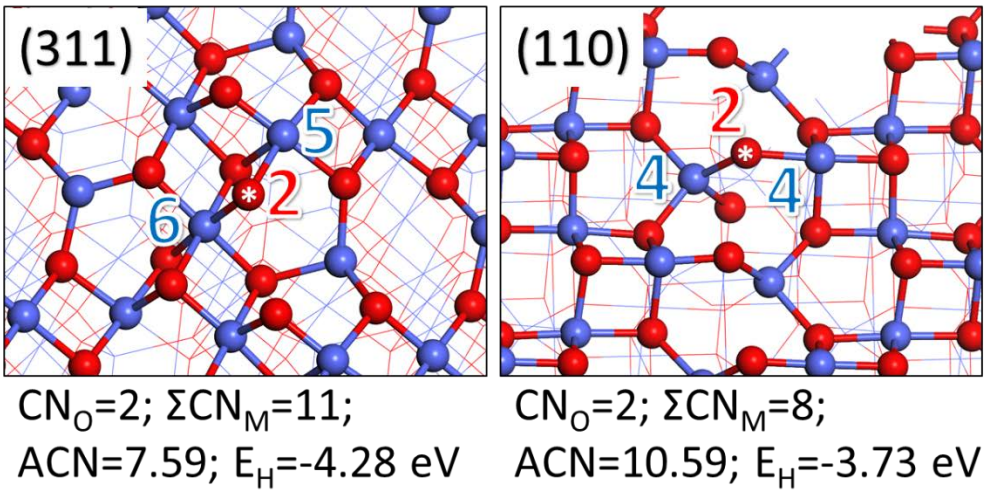

Figure 4.1.2 Coordination and reactivity of two different oxygen sites (labeled by an asterisk) on two Co_3O_4 surfaces: CN_O, $\sum CN_M$, ACN (adjusted coordination number), and E_H (H adsorption energy) are shown at the bottom. In the structures, the red numbers denote CN_O and the blue numbers denote CN_M. Co, blue; O, red.

Figure 3 demonstrates the strong correlation of ACN with H adsorption energy and vacancy formation energy, two commonly used energetic descriptors. One can see that ACN applies to a wide range of TM oxides with different stoichiometry, bulk structure, and metal oxidation states, exemplified by V_2O_3, Cr_2O_3, Co_3O_4, and NiO. In addition to perfect surfaces (Figure S3) including (100), (110), (111), (211), and (311), defected facets and oxygen adatoms were also considered (Figure S4). The strength of the linear correlation for all studied metal oxides is surprisingly evident given the simplicity of the ACN model. Although noise in the correlation is to be expected, the deviations were found to be reasonably low (Table S3). Therefore, we can conclude that in general oxygen with a lower ACN are more reducible and have higher reactivity for the relevant catalytic reactions.

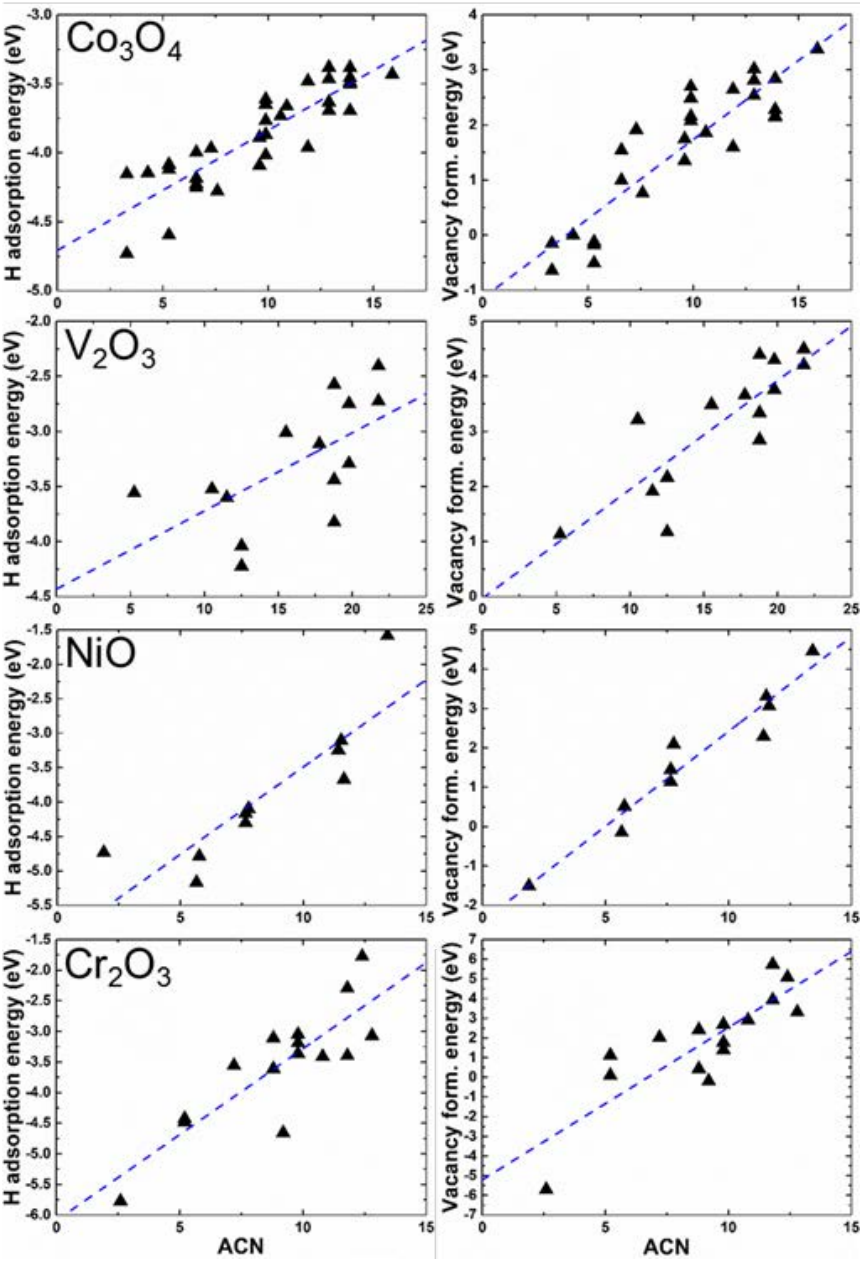

Figure 4.1.3 Linear correlation of ACN with H adsorption energy (left) and vacancy formation energy (right) for V_2O_3, Cr_2O_3, Co_3O_4, and NiO. Each individual point denotes a unique individual oxygen site present on the surface of the metal oxide. λ values and linear-fit (dashed line) parameters are provided in Table S2 and S3, respectively, in SI.

Using Co_3O_4 as a system well studied both experimentally[16, 32-34] and theoretically[15-16, 20, 35-36] for alkane activation and combustion, we apply ACN towards the prediction of C-H activation energies. Figure 4 shows the correlation between the first C-H activation energy of ethane on different Co_3O_4 surfaces and ACN, via a radical-forming reaction mechanism[15, 20, 22] (transition states in Figure S5). A clear linear correlation can be seen whereby a lower ACN value correlates to a lower C-H activation energy with an RMSD of 0.13 eV, or within the range of DFT error. This demonstrates the first usage of a structural descriptor towards directly predicting the otherwise computationally expensive DFT-obtained energy barriers.

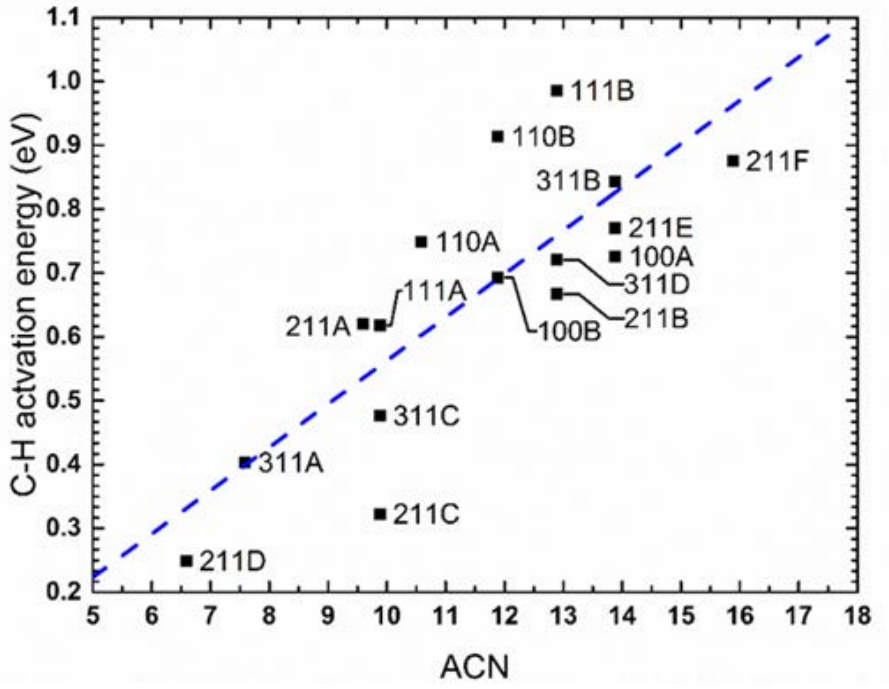

Figure 4.1.4 Correlation between the C-H activation energy and adjusted coordination number (ACN). Linear best fit (blue line) and fitting parameters are given in Table S4 in SI.

The correlation between active site structure and energy barriers might be applicable towards the prediction of actual catalytic performance. For example, the morphology of Co_3O_4 has been shown to be controllable through the synthesis and treatment method, yielding exposed surfaces with different crystal facets and performance.[33, 37-40] For methane combustion, a reaction dependent on the same C-H activation energy trends, it has been shown experimentally in the literature that the reactivity trend follows the relation (211) > (110) > (100)[33] from Co_3O_4 nanoparticles synthesized with different shapes. In terms of ACN, the most active oxygen of the three surfaces have values of 7.6, 10.6, and 11.9 respectively, which is consistent with the experimental trend. Methane combustion is a complex process, and more rigorous experimental and theoretical studies will be needed to firmly establish the correlation between the facet activity and the ACN descriptor.

In addition to the case of C-H activation on Co_3O_4, we further extend the generality of ACN as a predictor of oxygen reactivity by studying its scaling relation with the adsorption of other important intermediates such as CH_3, NH_2, and OH. These adsorbates form on the surface in a variety of important reactions including hydrogen evolution, oxygen evolution and reduction, alkane activation and combustion, and nitrogen reduction, among others, and can be used as descriptors of catalytic activity.[1, 41] Similarly, strong linear correlations can be observed for these adsorbates in Figure 5. This result is promising in that it demonstrates the broad applicability of a single oxygen reactivity descriptor such as ACN as valid for the prediction of adsorption properties over

a wide range of different atomic/molecular adsorbates, allowing for the screening of catalytic performance on a general level, rather than on a case by case basis.

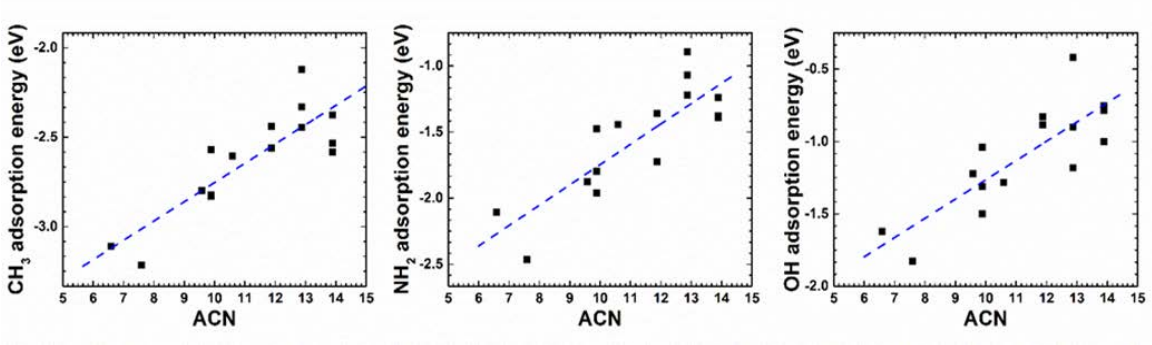

Figure 4.1.5 Correlation between CH_3 (left), NH_2 (middle), and OH (right) adsorption energies on the Co_3O_4 surfaces with ACN. Linear best fits (blue lines) and fitting parameters are given in Table S5 in SI.

Herein we have proposed ACN as an approximate descriptor for the oxygen site which we believe incorporates the major contributions of structure to oxygen reactivity. ACN is shown to be effective within the same oxide and bulk geometry, but does not seem be directly comparable across different oxides, as Figure 3 shows that different H adsorption and vacancy formation energies will be obtained for the four TMOs at the same ACN. Nevertheless, on the basis of ACN, the path to subsequent refinements toward structure-reactivity relations becomes much clearer. In addition, ACN provides a structural basis for catalyst design by quantitatively identifying the effect of changing CN_O and CN_M to tune the oxygen selectivity to a desired state. In essence, ACN can greatly reduce the structural search space by boiling down the oxygen site geometry to just two parameters (CN_O and $\sum CN_M$).

Recent experimental and theoretical studies on gas-phase metal-oxide clusters and their reactivity[42-44] identified different oxygen sites such as terminal M=O, bridging M-O-M, oxygen radical M-O*, superoxide, and peroxide on the clusters. It will be interesting to see if the ACN descriptor can be applied to describe the reactivity of those oxygen sites as well. In addition, the effect of the spin states on reactivity is more pronounced in clusters,[45-46] while its effect in our extended surfaces is indirectly taken into account in the ACN descriptor via the correlation with the Bader charge that is derived from spin-polarized calculations.

4.1.4 Conclusion

In conclusion, we proposed a structural descriptor for transition-metal oxides called adjusted coordination number (ACN), on the physical basis of oxygen partial charge, which captures the charge-transfer effect through the surface oxygen's metal coordination and the second-shell oxygen coordination. We demonstrated the strong correlation between ACN and the conventional descriptors of oxygen reactivity. Most importantly, we further applied the scaling relationships to reaction barriers for C-H activation, showing for the first time that a structural descriptor can have predictive power towards catalytic barriers. Finally, we have applied ACN to a number of other adsorbates, including CH_3, NH_2, and OH, and found that the same scaling relationships exist. These results demonstrate that ACN is a promising first step towards rigorously quantifying active site structural sensitivity to reactivity form transition-metal oxides. Subsequent

fundamental studies corroborating theoretical predictions through ACN and experimental results in the future will help further validate structural descriptors as a practical tool for catalytic prediction.

References

(1) Nørskov, J. K.; Bligaard, T.; Rossmeisl, J.; Christensen, C. H. Towards the Computational Design of Solid Catalysts. *Nat. Chem.* **2009,** *1*, 37-46.

(2) Norskov, J. K.; Abild-Pedersen, F.; Studt, F.; Bligaard, T. Density functional theory in surface chemistry and catalysis. *Proc. Natl. Acad. Sci. U. S. A.* **2011,** *108*, 937-43.

(3) Medford, A. J.; Vojvodic, A.; Hummelshøj, J. S.; Voss, J.; Abild-Pedersen, F.; Studt, F.; Bligaard, T.; Nilsson, A.; Nørskov, J. K. From the Sabatier principle to a predictive theory of transition-metal heterogeneous catalysis. *J. Catal.* **2015,** *328*, 36-42.

(4) Calle-Vallejo, F.; Loffreda, D.; Koper, M. T.; Sautet, P. Introducing Structural Sensitivity Into Adsorption-Energy Scaling Relations by Means of Coordination Numbers. *Nat. Chem.* **2015,** *7*, 403-410.

(5) Calle‐Vallejo, F.; Martínez, J. I.; García‐Lastra, J. M.; Sautet, P.; Loffreda, D. Fast Prediction of Adsorption Properties for Platinum Nanocatalysts with Generalized Coordination Numbers. *Angew. Chem. Int. Ed.* **2014,** *53*, 8316-8319.

(6) Calle-Vallejo, F.; Tymoczko, J.; Colic, V.; Vu, Q. H.; Pohl, M. D.; Morgenstern, K.; Loffreda, D.; Sautet, P.; Schuhmann, W.; Bandarenka, A. S. Finding optimal surface sites on heterogeneous catalysts by counting nearest neighbors. *Science* **2015,** *350*, 185-189.

(7) Mpourmpakis, G.; Andriotis, A. N.; Vlachos, D. G. Identification of descriptors for the CO interaction with metal nanoparticles. *Nano Lett.* **2010,** *10*, 1041-1045.

(8) Ma, X.; Xin, H. Orbitalwise Coordination Number for Predicting Adsorption Properties of Metal Nanocatalysts. *Phys. Rev. Lett.* **2017,** *118*, 036101.

(9) Ganduglia-Pirovano, M. V.; Hofmann, A.; Sauer, J. Oxygen Vacancies in Transition Metal and Rare Earth Oxides: Current State of Understanding and Remaining Challenges. *Surf. Sci. Rep.* **2007,** *62*, 219-270.

(10) Derk, A. R.; Li, B.; Sharma, S.; Moore, G. M.; McFarland, E. W.; Metiu, H. Methane Oxidation by Lanthanum Oxide Doped with Cu, Zn, Mg, Fe, Nb, Ti, Zr, or Ta: the Connection Between the Activation Energy and the Energy of Oxygen-Vacancy Formation. *Catal. Lett.* **2013,** *143*, 406-410.

(11) Hu, Z.; Metiu, H. Effect of dopants on the energy of oxygen-vacancy formation at the surface of ceria: Local or global? *J. Phys. Chem. C* **2011,** *115*, 17898-17909.

(12) Beck, B.; Harth, M.; Hamilton, N. G.; Carrero, C.; Uhlrich, J. J.; Trunschke, A.; Shaikhutdinov, S.; Schubert, H.; Freund, H.-J.; Schlögl, R. Partial oxidation of ethanol on vanadia catalysts on supporting oxides with different redox properties compared to propane. *J. Catal.* **2012,** *296*, 120-131.

(13) Zhou, M.; Cai, L.; Bajdich, M.; García-Melchor, M.; Li, H.; He, J.; Wilcox, J.; Wu, W.; Vojvodic, A.; Zheng, X. Enhancing catalytic CO oxidation over Co_3O_4 nanowires by substituting Co^{2+} with Cu^{2+}. *ACS Catal.* **2015,** *5*, 4485-4491.

(14) Zhu, Q.; Wegener, S. L.; Xie, C.; Uche, O.; Neurock, M.; Marks, T. J. Sulfur as a selective 'soft' oxidant for catalytic methane conversion probed by experiment and theory. *Nature Chem.* **2013,** *5*, 104-9.

(15) Fung, V.; Tao, F.; Jiang, D. E. Understanding oxidative dehydrogenation of ethane on Co3O4 nanorods from density functional theory. *Catal. Sci. Technol.* **2016,** *6*, 6861-6869.

(16) Liu, J. J.; Zhang, S. R.; Zhou, Y.; Fung, V.; Nguyen, L.; Jiang, D. E.; Shen, W. J.; Fan, J.; Tao, F. F. Tuning Catalytic Selectivity of Oxidative Catalysis through Deposition of Nonmetallic Atoms in Surface Lattice of Metal Oxide. *ACS Catal.* **2016,** *6*, 4218-4228.

(17) Li, B.; Metiu, H. DFT Studies of Oxygen Vacancies on Undoped and Doped La_2O_3 Surfaces. *J. Phys. Chem. C* **2010,** *114*, 12234-12244.

(18) Kumar, G.; Lau, S. L. J.; Krcha, M. D.; Janik, M. J. Correlation of Methane Activation and Oxide Catalyst Reducibility and its Implications for Oxidative Coupling. *ACS Catal.* **2016,** *6*, 1812-1821.

(19) Deshlahra, P.; Iglesia, E. Reactivity and Selectivity Descriptors for the Activation of C-H Bonds in Hydrocarbons and Oxygenates on Metal Oxides. *J. Phys. Chem. C* **2016,** *120*, 16741-16760.

(20) Tyo, E. C.; Yin, C.; Di Vece, M.; Qian, Q.; Kwon, G.; Lee, S.; Lee, B.; DeBartolo, J. E.; Seifert, S.; Winans, R. E.; Si, R.; Ricks, B.; Goergen, S.; Rutter, M.; Zugic, B.; Flytzani-Stephanopoulos, M.; Wang, Z. W.; Palmer, R. E.; Neurock, M.; Vajda, S. Oxidative dehydrogenation of cyclohexane on cobalt oxide (Co_3O_4) nanoparticles: The effect of particle size on activity and selectivity. *ACS Catal.* **2012,** *2*, 2409-2423.

(21) Deshlahra, P.; Iglesia, E. Toward More Complete Descriptors of Reactivity in Catalysis by Solid Acids. *ACS Catal.* **2016,** *6*, 5386-5392.

(22) Latimer, A. A.; Kulkarni, A. R.; Aljama, H.; Montoya, J. H.; Yoo, J. S.; Tsai, C.; Abild-Pedersen, F.; Studt, F.; Nørskov, J. K. Understanding Trends in CH Bond Activation in Heterogeneous Catalysis. *Nature Mater.* **2017,** *16*, 225-229.

(23) Krcha, M. D.; Mayernick, A. D.; Janik, M. J. Periodic Trends of Oxygen Vacancy Formation and C–H Bond Activation Over Transition Metal-Doped CeO_2 (111) Surfaces. *J. Catal.* **2012,** *293*, 103-115.

(24) van Santen, R. A.; Neurock, M.; Shetty, S. G. Reactivity Theory of Transition-Metal Surfaces: A Brønsted− Evans− Polanyi Linear Activation Energy− Free-Energy Analysis. *Chem. Rev.* **2009,** *110*, 2005-2048.

(25) Vojvodic, A.; Hellman, A.; Ruberto, C.; Lundqvist, B. I. From electronic structure to catalytic activity: A single descriptor for adsorption and reactivity on transition-metal carbides. *Phys. Rev. Lett.* **2009,** *103*, 146103.

(26) Calle-Vallejo, F.; Martinez, J.; García-Lastra, J. M.; Rossmeisl, J.; Koper, M. Physical and chemical nature of the scaling relations between adsorption energies of atoms on metal surfaces. *Phys. Rev. Lett.* **2012,** *108*, 116103.

(27) Abild-Pedersen, F.; Greeley, J.; Studt, F.; Rossmeisl, J.; Munter, T.; Moses, P. G.; Skulason, E.; Bligaard, T.; Nørskov, J. K. Scaling Properties Of Adsorption Energies For Hydrogen-Containing Molecules On Transition-Metal Surfaces. *Phys. Rev. Lett.* **2007,** *99*, 016105.

(28) Lee, Y.-L.; Kleis, J.; Rossmeisl, J.; Shao-Horn, Y.; Morgan, D. Prediction of Solid Oxide Fuel Cell Cathode Activity with First-Principles Descriptors. *Energy Environ. Sci.* **2011,** *4*, 3966-3970.

(29) Calle-Vallejo, F.; Díaz-Morales, O. A.; Kolb, M. J.; Koper, M. T. Why Is Bulk Thermochemistry a Good Descriptor for the Electrocatalytic Activity of Transition Metal Oxides? *ACS Catal.* **2015,** *5*, 869-873.

(30) Calle-Vallejo, F.; Inoglu, N. G.; Su, H.-Y.; Martínez, J. I.; Man, I. C.; Koper, M. T.; Kitchin, J. R.; Rossmeisl, J. Number of outer electrons as descriptor for adsorption processes on transition metals and their oxides. *Chemical Science* **2013,** *4*, 1245-1249.

(31) Bader, R. F., *Atoms in Molecules: A Quantum Theory*. Clarendon Press: Oxford, U.K.: 1994.

(32) Tao, F. F.; Shan, J. J.; Nguyen, L.; Wang, Z.; Zhang, S.; Zhang, L.; Wu, Z.; Huang, W.; Zeng, S.; Hu, P. Understanding Complete Oxidation of Methane on Spinel Oxides at a Molecular Level. *Nature Commun.* **2015,** *6*, 7798.

(33) Hu, L.; Peng, Q.; Li, Y. Selective synthesis of Co_3O_4 nanocrystal with different shape and crystal plane effect on catalytic property for methane combustion. *J. Am. Chem. Soc.* **2008,** *130*, 16136-16137.

(34) Ren, Z.; Botu, V.; Wang, S.; Meng, Y.; Song, W.; Guo, Y.; Ramprasad, R.; Suib, S. L.; Gao, P. X. Monolithically integrated spinel $MxCo_{3-x}O_4$ (M= Co, Ni, Zn) nanoarray catalysts: scalable synthesis and cation manipulation for tunable low-temperature CH_4 and CO oxidation. *Angew. Chem. Int. Ed.* **2014,** *53*, 7223-7227.

(35) Jiang, D. E.; Dai, S. The role of low-coordinate oxygen on Co_3O_4(110) in catalytic CO oxidation. *Phys. Chem. Chem. Phys.* **2011,** *13*, 978-84.

(36) Hu, W.; Lan, J.; Guo, Y.; Cao, X.-M.; Hu, P. Origin of efficient catalytic combustion of methane over Co_3O_4 (110): active low-coordination lattice oxygen and cooperation of multiple active sites. *ACS Catal.* **2016,** *6*, 5508-5519.

(37) Chen, Z.; Kronawitter, C. X.; Koel, B. E. Facet-dependent activity and stability of Co_3O_4 nanocrystals towards the oxygen evolution reaction. *Phys. Chem. Chem. Phys.* **2015,** *17*, 29387-29393.

(38) Gao, R.; Zhu, J.; Xiao, X.; Hu, Z.; Liu, J.; Liu, X. Facet-Dependent Electrocatalytic Performance of Co_3O_4 for Rechargeable Li–O2 Battery. *J. Phys. Chem. C* **2015,** *119*, 4516-4523.

(39) Sun, H.; Ang, H. M.; Tadé, M. O.; Wang, S. Co_3O_4 nanocrystals with predominantly exposed facets: synthesis, environmental and energy applications. *J. Mater. Chem. A* **2013,** *1*, 14427-14442.

(40) Sun, Y. N.; Liu, J. W.; Song, J. J.; Huang, S. S.; Yang, N. T.; Zhang, J.; Sun, Y. H.; Zhu, Y. Exploring the Effect of Co_3O_4 Nanocatalysts with Different Dimensional Architectures on Methane Combustion. *ChemCatChem* **2016,** *8*, 540-545.

(41) Man, I. C.; Su, H. Y.; Calle‐Vallejo, F.; Hansen, H. A.; Martínez, J. I.; Inoglu, N. G.; Kitchin, J.; Jaramillo, T. F.; Nørskov, J. K.; Rossmeisl, J. Universality in oxygen evolution electrocatalysis on oxide surfaces. *ChemCatChem* **2011,** *3*, 1159-1165.

(42) Tyo, E. C.; Nossler, M.; Harmon, C. L.; Mitrić, R.; Bonačić-Koutecký, V.; Castleman Jr, A. Investigating Reactive Superoxide Units Bound to Zirconium Oxide Cations. *J. Phys. Chem. C* **2011,** *115*, 21559-21566.

(43) Johnson, G. E.; Mitric, R.; Nössler, M.; Tyo, E. C.; Bonacic-Koutecky, V.; Castleman Jr, A. Influence of charge state on catalytic oxidation reactions at metal oxide clusters containing radical oxygen centers. *J. Am. Chem. Soc.* **2009,** *131*, 5460-5470.

(44) Zhao, Y.-X.; Wu, X.-N.; Ma, J.-B.; He, S.-G.; Ding, X.-L. Characterization and reactivity of oxygen-centred radicals over transition metal oxide clusters. *Phys. Chem. Chem. Phys.* **2011,** *13*, 1925-1938.

(45) Dietl, N.; Schlangen, M.; Schwarz, H. Thermal Hydrogen‐Atom Transfer from Methane: The Role of Radicals and Spin States in Oxo‐Cluster Chemistry. *Angew. Chem. Int. Ed.* **2012,** *51*, 5544-5555.

(46) Reveles, J. U.; Johnson, G. E.; Khanna, S. N.; Castleman Jr, A. Reactivity trends in the oxidation of CO by anionic transition metal oxide clusters. *J. Phys. Chem. C* **2009,** *114*, 5438-5446.

Supplementary Information

1. Computational details

All DFT calculations were performed using the Vienna ab initio Simulation Package (VASP).[1-2] The on-site Coulomb interaction was included using the DFT+U method by Dudarev, et al.[3] in VASP using a Hubbard parameter U. Following previous existing studies using DFT+U in the literature, we use a U value of 2, 4, 5.3, and 5 eV for Co_3O_4[4-6], V_2O_3[7], NiO[8-9], and Cr_2O_3[10-11], respectively. The Perdew-Burke-Erzerhof (PBE)[12] form of the generalized-gradient approximation (GGA) was chosen for electron exchange and correlation. All calculations in this work were performed with spin polarization. The electron-core interaction was described using the projector-augmented wave method (PAW).[13-14] A kinetic energy cutoff of 450 eV was used for the planewave basis set, and the Brillouin zone was sampled using a 3×3×1 Monkhorst-Pack scheme.[15] For the studied slabs, the top two layers were generally allowed to relax, and the bottom layers were fixed in the optimizations. A vacuum slab of 18 Å is used.

Vacancy formation energy, sometimes known as defect formation energy, or alternatively as a measure of M-O bond strength, is calculated in this paper as the direct energy difference between the defect and pure surface with reference to half the molecular oxygen gas energy, in the form, $E_{vac}=E_{defect}+1/2E_{O2}-E_{pure}$. The absorption energies are defined as $E_{ads} = E_{surface+adsorbate} - (E_{surface} + E_{adsorbate})$, where $E_{adsorbate}$ was computed by placing the adsorbate in a 10 Å wide cubic cell to prevent intermolecular interactions from the periodic boundary conditions. Transition states were found via using both the nudged

elastic band method (NEB) and the dimer method[16] implemented in the VASP-VTST package by Henkelman et al. Initial and final states of the reactions were first created and optimized, and were used to generate 8-10 equally spaced images through a linear interpolation. These images were then minimized under the NEB constraints to generate an approximate minimum reaction energy path. The highest two energy images along the path were then used to generate a starting geometry for the dimer method, which is then used to converge to a saddle point until reaching an energy convergence of 0.05 eV/Å.

2. Correlation between descriptors of oxygen reducibility

The three descriptors from the main text are cross correlated here in Figure S1. Bader charge measures the partial charge of the atomic oxygen in the extended periodic slab, and provides an approximate measure of oxygen reducibility, and explains the seemingly strong correlation between H adsorption and vacancy formation, which are both result in the reduction of the active site. Oxygens which are less negatively charged are more reducible and more reactive, which corresponds with general chemical intuition. It is important to note that on metal oxide surfaces, the metal cations can also play a major role in the reducibility of the surface. For example, the formation of a vacancy can lead to the metal cation to be reduced and adopt a lower oxidation state. Thus, the Bader charge of O is an approximate model where the reducibility of M is approximated to be roughly equal for each oxygen site and thus neglected for simplicity.

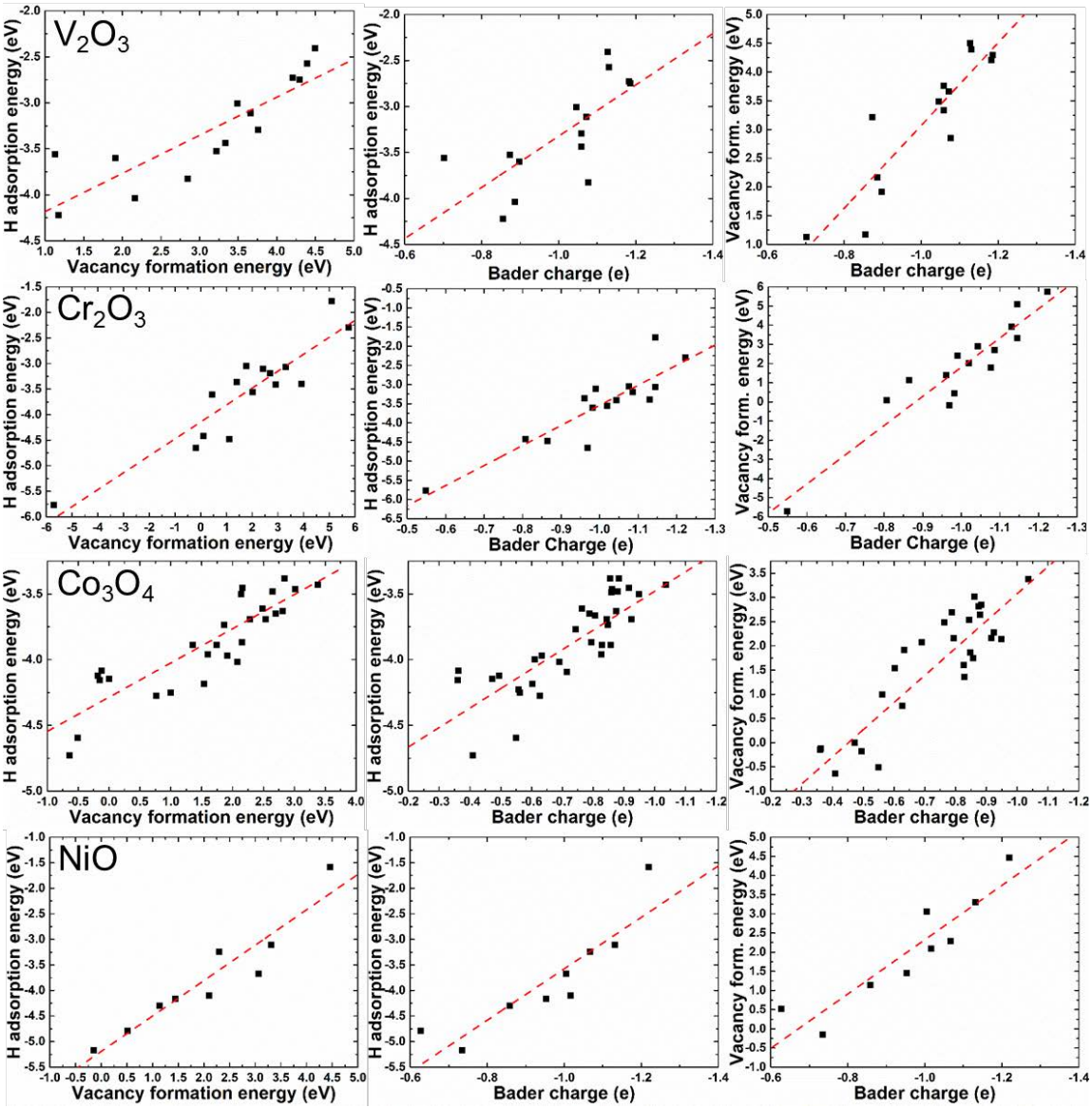

Figure S4.1.1 Correlation between Bader charge, H adsorption energy and vacancy formation energy associated with oxygen sites on V_2O_3, Cr_2O_3, Co_3O_4, and NiO. The red lines are the linear best fits of the points, and the parameters and the root-mean-square deviation **(**RMSD) are given in Table S1.

Table S4.1.1: Calculated slopes, intercepts and RMSD's of the linear best fits for Figure S1

metal oxide		slope	intercept	RMSD	R
Co_3O_4	H adsorption vs Vacancy form.	0.26036	-4.28483	0.16925	0.89479
	H adsorption vs Bader charge	-1.48179	-4.96031	0.21433	0.82480
	Vacancy form. vs Bader Charge	-5.61538	-2.53904	0.54157	0.90949
V_2O_3	H adsorption vs Vacancy form.	0.41447	-4.59607	0.29357	0.86030
	H adsorption vs Bader charge	-2.78457	-6.10641	0.39778	0.72311
	Vacancy form. vs Bader Charge	-7.20043	-4.13140	0.51896	0.81151
NiO	H adsorption vs Vacancy form.	0.69284	-5.19120	0.37007	0.94551
	H adsorption vs Bader charge	-5.03302	-8.60770	0.51169	0.89293
	Vacancy form. vs Bader Charge	-7.07833	-4.75316	0.60715	0.92021
Cr_2O_3	H adsorption vs Vacancy form.	0.33150	-4.14216	0.41799	0.91140
	H adsorption vs Bader charge	-5.23763	-8.77851	0.46559	0.88876
	Vacancy form. vs Bader Charge	-15.23311	-13.41956	0.95140	0.94018

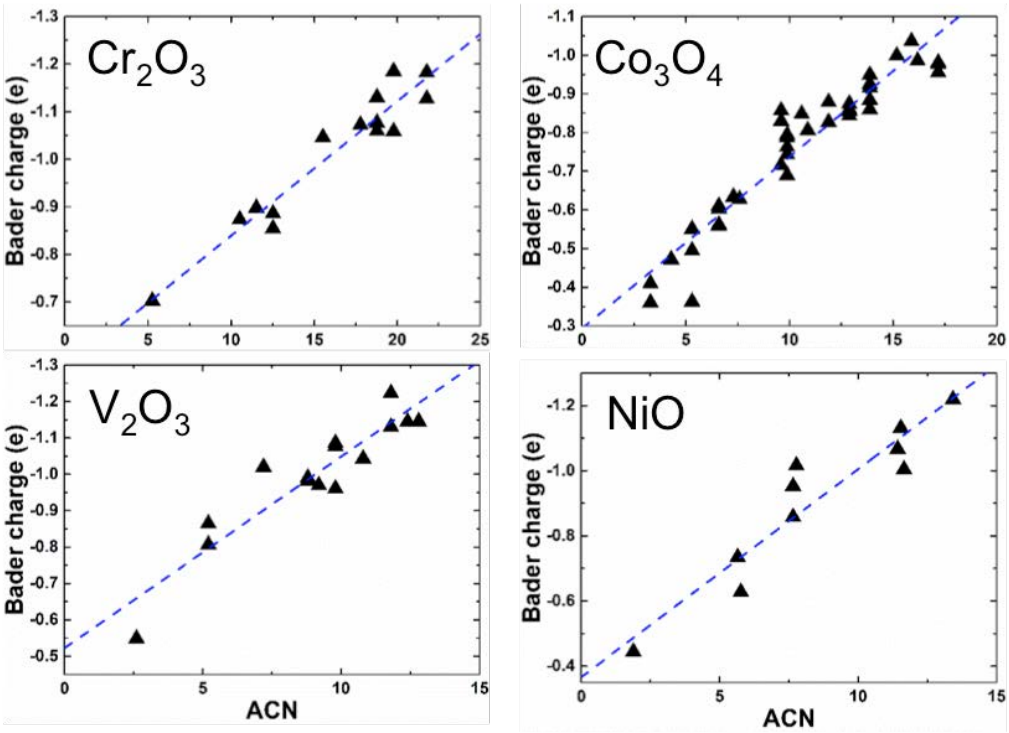

Figure S4.1.2 Correlation between adjusted coordination number (ACN) and Bader charge associated with oxygen sites on V_2O_3, Cr_2O_3, Co_3O_4, and NiO. The dashed lines are the linear best fits of the points, and the parameters and the root-mean-square deviation **(**RMSD) are given in Table S3.

Table S4.1.2: The fitted λ parameter for the studied metal oxides

metal oxide	λ
Co_3O_4	9.294335
V_2O_3	11.25841
NiO	7.885177
Cr_2O_3	8.600026

Table S4.1.3: Calculated slopes, intercepts and RMSD's of the linear best fits for Figure 3 in the text and Figure S2 in SI.

metal oxide		slope	intercept	RMSD	R
Co_3O_4	Bader charge vs ACN	-0.04437	-0.29344	0.05742	0.95269
	H adsorption vs ACN	0.08699	-4.70686	0.16968	0.87472
	Vacancy form. vs ACN	0.28794	-1.14347	0.54617	0.89132
V_2O_3	Bader charge vs ACN	-0.02824	-0.55715	0.04086	0.96195
	H adsorption vs ACN	0.07095	-4.43147	0.44833	0.62764
	Vacancy form. vs ACN	0.19767	-0.02868	0.64404	0.84244
NiO	Bader charge vs ACN	-0.06383	-0.36677	0.08618	0.94123
	H adsorption vs ACN	0.25357	-6.02653	0.56542	0.86027
	Vacancy form. vs ACN	0.48200	-2.40209	0.46325	0.96889
Cr_2O_3	Bader charge vs ACN	-0.05257	-0.52282	0.06480	0.92664
	H adsorption vs ACN	0.28081	-6.08950	0.55138	0.83984
	Vacancy form. vs ACN	0.77331	-5.20539	1.50997	0.84122

3. Model surfaces and example calculations for CAN

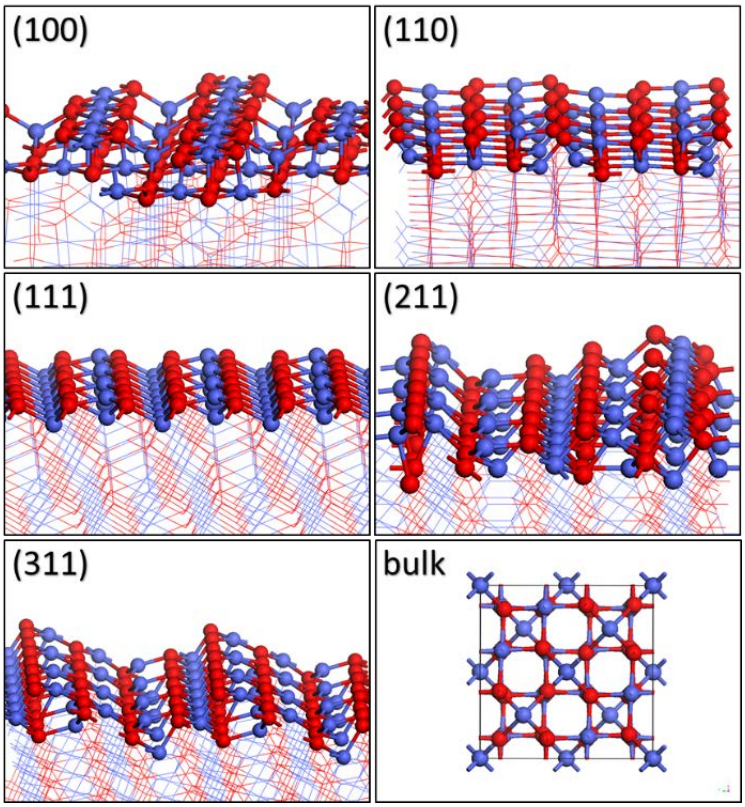

Figure S4.1.3 Surface facet structure of Co_3O_4. The studied surface facets (100), (110), (111), (211), (311), and the bulk spinel structure of Co_3O_4. Co atoms are in blue and O atoms are in red. All surfaces are shown as a 2x2 supercell except (211), which is shown as a 1x2 supercell.

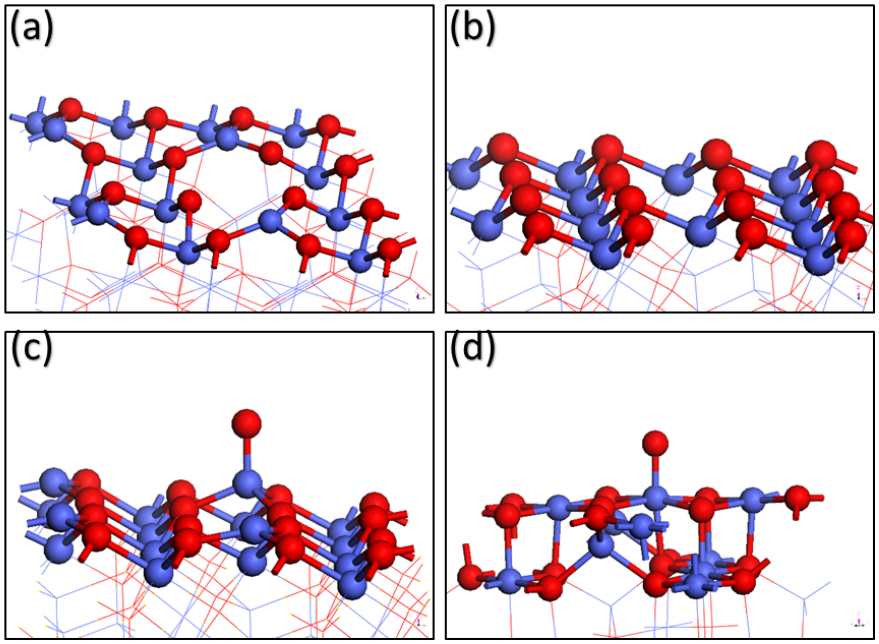

Figure S4.1.4 Example defect surfaces of Co_3O_4. (a) The (111) surface with a subsurface Co defect; (b) The (111) surface with an alternate termination; (c-d) The (111) and (100) surfaces with oxygen adatoms on the surface Co.

4. Example transition states for C_2H_6 C-H activation

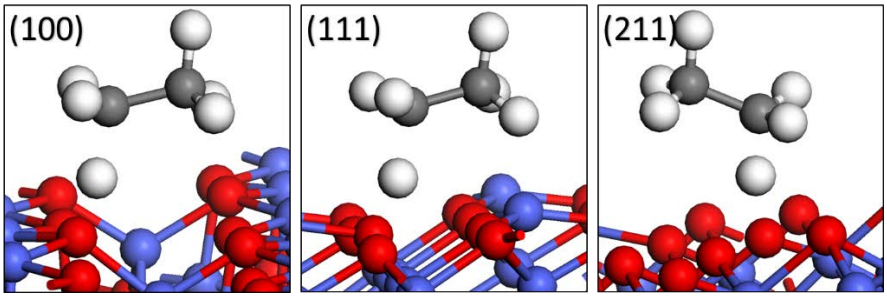

Figure S4.1.5 Example transition states of ethane C-H activation. Transition states for the first C-H activation of ethane on several Co_3O_4 surfaces. White atoms represent H and grey atoms represent C.

Example transition states for C-H activation are shown in Figure S6, representing the homolytic H-abstraction pathway, which is found to have the lowest barriers for many metal oxide systems[4, 17-19]. The transition states structures are similar throughout the different surface facets, differing only slightly in the C-H and O-H bond lengths. No prior chemisorption of the ethane onto the surface was found on any of the studied metal oxides. The C-H activation through this pathway results in an adsorbed H on the surface oxygen and a ethyl radical which can undergo gas phase reactions or adsorb strongly to the surface, usually on a nearby lattice O.

Table S4.1.4: Calculated slopes, intercepts and RMSD's of the linear best fits for Figure 4 in the text.

	slope	intercept	RMSD	R
C-H activation vs ACN	0.06789	-0.11618	0.12870	0.80713

Table S4.1.5: Calculated slopes, intercepts and RMSD's of the linear best fits for Figure 5 in the text.

	slope	intercept	RMSD	R
ACN vs CH_3 ads.	0.10782	-3.83138	0.15815	0.85110
ACN vs NH_2 ads.	0.15378	-3.28383	0.24048	0.83552
ACN vs OH ads.	0.13309	-2.59549	0.21696	0.82478

5. DFT+U effect on scaling relations

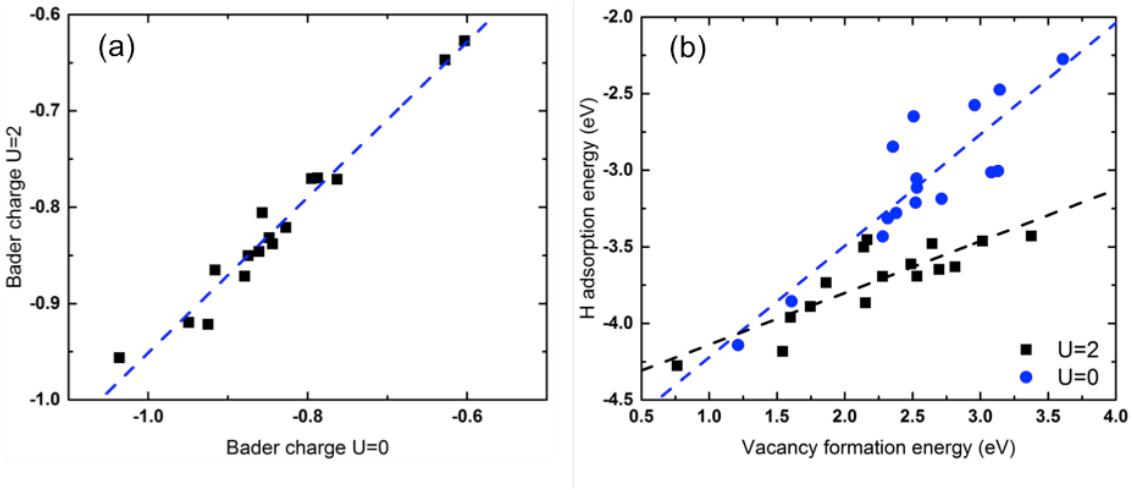

Figure S4.1.6 The comparison of DFT-GGA (U=0) and DFT-GGA+U (U=2 eV). a, Bader charge at U=2 eV vs. Bader charge at U=0 eV for Co_3O_4. b, correlation between H-adsorption energy and vacancy-formation energy Co_3O_4 for U=2 eV and U=0.

References

(1) Kresse, G.; Furthmuller, J. Efficiency of Ab-Initio Total Energy Calculations for Metals and Semiconductors Using a Plane-Wave Basis Set. *Comput. Mater. Sci.* **1996,** *6*, 15-50.

(2) Kresse, G.; Furthmuller, J. Efficient Iterative Schemes for Ab Initio Total-Energy Calculations Using a Plane-Wave Basis Set. *Phys. Rev. B* **1996,** *54*, 11169-11186.

(3) Dudarev, S. L.; Botton, G. A.; Savrasov, S. Y.; Humphreys, C. J.; Sutton, A. P. Electron-Energy-Loss Spectra and the Structural Stability of Nickel Oxide: An LSDA+U Study. *Phys. Rev. B* **1998,** *57*, 1505-1509.

(4) Fung, V.; Tao, F.; Jiang, D. E. Understanding oxidative dehydrogenation of ethane on Co3O4 nanorods from density functional theory. *Catal. Sci. Technol.* **2016,** *6*, 6861-6869.

(5) Jiang, D. E.; Dai, S. The role of low-coordinate oxygen on Co_3O_4(110) in catalytic CO oxidation. *Phys. Chem. Chem. Phys.* **2011,** *13*, 978-84.

(6) Tao, F. F.; Shan, J. J.; Nguyen, L.; Wang, Z.; Zhang, S.; Zhang, L.; Wu, Z.; Huang, W.; Zeng, S.; Hu, P. Understanding Complete Oxidation of Methane on Spinel Oxides at a Molecular Level. *Nature Commun.* **2015,** *6*, 7798.

(7) Scanlon, D. O.; Walsh, A.; Morgan, B. J.; Watson, G. W. An ab initio Study of Reduction of V2O5 through the Formation of Oxygen Vacancies and Li Intercalation. *J. Phys. Chem. C* **2008,** *112*, 9903-9911.

(8) Rohrbach, A.; Hafner, J.; Kresse, G. Molecular adsorption on the surface of strongly correlated transition-metal oxides: A case study for CO/NiO (100). *Phys. Rev. B* **2004,** *69*, 075413.

(9) Zhang, W.-B.; Hu, Y.-L.; Han, K.-L.; Tang, B.-Y. Structural distortion and electronic properties of NiO under high pressure: an ab initio GGA+ U study. *J. Phys.: Condens. Matter* **2006,** *18*, 9691.

(10) Rohrbach, A.; Hafner, J.; Kresse, G. Ab initio study of the (0001) surfaces of hematite and chromia: Influence of strong electronic correlations. *Phys. Rev. B* **2004,** *70*, 125426.

(11) Lebreau, F. o.; Islam, M. M.; Diawara, B.; Marcus, P. Structural, Magnetic, Electronic, Defect, and Diffusion Properties of Cr2O3: A DFT+ U Study. *J. Phys. Chem. C* **2014,** *118*, 18133-18145.

(12) Perdew, J. P.; Burke, K.; Ernzerhof, M. Generalized Gradient Approximation Made Simple. *Phys. Rev. Lett.* **1996,** *77*, 3865-3868.

(13) Kresse, G.; Joubert, D. From Ultrasoft Pseudopotentials to the Projector Augmented-Wave Method. *Phys. Rev. B* **1999,** *59*, 1758.

(14) Blöchl, P. E. Projector Augmented-Wave Method. *Phys. Rev. B* **1994,** *50*, 17953-17979.

(15) Monkhorst, H. J.; Pack, J. D. Special Points for Brillouin-Zone Integrations. *Phys. Rev. B* **1976,** *13*, 5188-5192.

(16) Henkelman, G.; Jónsson, H. A Dimer Method for Finding Saddle Points on High Dimensional Potential Surfaces Using Only First Derivatives. *J. Chem. Phys.* **1999,** *111*, 7010.

(17) Tyo, E. C.; Vajda, S. Catalysis by clusters with precise numbers of atoms. *Nat. Nanotechnol.* **2015,** *10*, 577-588.

(18) Kumar, G.; Lau, S. L. J.; Krcha, M. D.; Janik, M. J. Correlation of Methane Activation and Oxide Catalyst Reducibility and its Implications for Oxidative Coupling. *ACS Catal.* **2016,** *6*, 1812-1821.

(19) Latimer, A. A.; Kulkarni, A. R.; Aljama, H.; Montoya, J. H.; Yoo, J. S.; Tsai, C.; Abild-Pedersen, F.; Studt, F.; Nørskov, J. K. Understanding Trends in CH Bond Activation in Heterogeneous Catalysis. *Nature Mater.* **2017,** *16*, 225-229.

4.2 Exploring perovskites for methane activation from first principles

4.2.4 Abstract

Diversity of perovskites offers many opportunities for catalysis, but an overall trend has been elusive. Using density functional theory, we studied a large set of perovskite compositions in the ABO_3 formula via descriptors of oxygen reactivity such as vacancy formation energy, hydrogen adsorption energy, and first C-H activation energy of methane. It was found that changing the identity of B within a period increases oxygen reactivity from the early to late transition metals, while changing A within a group has a much smaller effect on oxygen reactivity. Within the same group, B in the 3d period has the most reactive lattice oxygen than in the 4d or 5d period. Some perovskites display large differences in reactivity for different terminations. Further examination of second C-H bond breaking on these perovskites revealed that larger A cations and non-transition metal B cations have higher activation energies, which is conductive to formation of coupling productions instead of oxidation to CO_x. Balance of first C-H bond breaking and methyl desorption suggests a just right oxygen reactivity as described by hydrogen adsorption energy. These insights may help design of better perovskite catalysts for methane activation.

4.2.5 Introduction

Perovskites are a prominent class of mixed-metal oxides with a wide range of possible compositions and corresponding physical and chemical properties. Following the general formula of ABO_3, the 12-fold coordinated A and 6-fold coordinated B metal

cations can be sourced from the majority of the metallic elements in the periodic table, so long as the ionic radii of the comprising elements are suitable for the formation of the cubic perovskite structure, which can be estimated from calculating the Goldschmidt tolerance factor.[1] Deviations from the ideal structural tolerance factor of one may lead to distorted lattices with orthorhombic and rhombohedral structures. As a further level of compositional diversity, the A and B cations can be substituted with additional elements, leading to non-stoichiometric perovskites with cationic or anionic deficiencies. From this wide diversity of possible configurations, a significant portion have been found to have good thermal stability and promising catalytic activity for a wide range of industrially important reactions.[2-8] It is highly desirable to predict many important catalytic properties of a perovskite from first principles.[9-10]

Perovskites are extensively studied in photocatalysis, and can also be a potential replacement to expensive noble metals for heterogeneous and electrocatalysis.[2-6, 11-12] Hydrogen adsorption and vacancy formation energies have been shown to be viable 'descriptors' of catalytic activity.[10, 13-19] Experimentally, catalysts with high oxygen mobility and low vacancy formation energies are often reactive for a wide range of reactions, because the lattice oxygen often plays a critical role in the catalysis reaction via the Mars van-Krevelen mechanism. Similarly, hydrogen adsorption energy is important since it can be linked to the energy barrier of C-H activation via a homolytic mechanism. Being able to estimate the energy barrier for C-H activation and relate it to experimental rates is crucial for elucidating favored reaction pathways on metal oxides.[20]

CH_4 utilization has received renewed interest in recent years due to the increase in shale gas production. Perovskite catalysts have shown excellent thermal stability (up to 1000 °C), resistance to sintering of substituted metals and high oxygen mobility, which offers great potential for methane combustion and oxidative coupling reaction.[3, 5, 21-24] These routes for the conversion of methane[21, 25-28] to methanol or ethylene have wide ranging implications for the fuel and chemical industry. For the catalytic reaction of hydrocarbons on metal oxides, C-H bond activation is generally the first step in the reaction.[13, 26, 29-30] Following C-H activation, the products adsorb to form methyl and hydroxyl groups on the surface lattice oxygens. The methyl groups can couple on the surface or in the gas phase to form C_2 products, or can further oxidize to form combustion products such as CO and CO_2.

For perovskites, the (001) surface facet is the stable and experimentally observed[31-34] facet, though other orientations can exist in high-surface-area or mesoporous structures. To isolate the effect of compositional changes on catalytic activity, this study will focus on the most commonly exposed (001) surface facet. Two possible terminations exist for this facet: the 'A' surface with the AO layer at the termination, and the 'B' surface with the BO_2 layer. Experimentally, it is possible to control the surface termination through various treatments, which has been demonstrated to lead to different catalytic activity and selectivity for reactions.[34]

The present work aims to understand the catalytic activity of perovskites for methane activation. Taking advantage of the well-defined structure of cubic perovskites, and the diversity of possible compositions, we screen a large set of promising perovskites

for low C-H activation energies. We first demonstrate the validity of the H-adsorption-energy (HAE) and vacancy-formation-energy (VFE) descriptors, in correlating to C-H activation energies, and use these to identify the most plausible active perovskites. Finally, we study whether or not it would be possible to further improve performance by selecting perovskites which disfavor the subsequent alkane oxidation steps on the surface.

4.2.6 Methods

Density functional theory calculations were performed with the Vienna ab initio Simulation Package (VASP).[35-36] The Perdew-Burke-Ernzerhof (PBE)[37] form of the generalized-gradient approximation (GGA) was used for electron exchange and correlation energies. All calculations were performed with spin polarization. The projector-augmented wave method was used to describe the electron-core interaction,[35, 38] and the kinetic energy cutoff was set to be 450 eV. For the studied surface slabs, a 3×3×1 sampling of Brillouin zone with a Monkhorst-Pack scheme was used.[39] The D3 correction method by Grimme et al. was applied for the van der Waals energy.[40] The surface slabs of the studied ABO_3 perovskites were created containing three AO layers and three BO_2 layers, for a total of six, with a 15 Å vacuum layer. A 2×2 supercell of the unit slab was used in subsequent calculations. The top two layers of the slabs were allowed to relax in all calculations. Vacancy formation energy (E_{vac}) was calculated with the equation $E_{vac}=E_{defect\text{-}surface} + ½\ E_{O2} - E_{surface}$. The hydrogen absorption energy (E_{Hads}) was calculated with the equation $E_{Hads} = E_{surface+H} - (E_{surface} + E_H)$. The energies of E_{O2} and E_H were computed by placing the adsorbate in a cubic cell with a 15 Å wide vacuum in each direction. Transition states (TS)

were found with the dimer method[41] and the climbing-image nudged elastic band method[42] with a force convergence of 0.05 eV/Å.

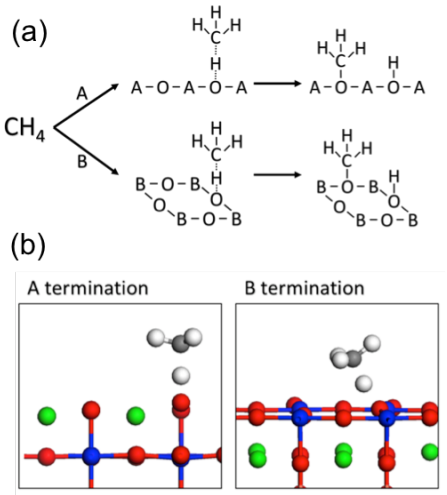

Figure 4.2.1 CH_4 activation on the perovskite (001) A and B terminations: (a) the homolytic C-H pathway; (b) the typical transition states (A, green; B, blue; O, red; C, grey; H, white).

4.2.7 Results and discussion

4.2.7.1 Descriptors of oxygen reactivity

The cubic perovskite (001) surface can have both the 'A' and 'B' terminations (Fig. 1). On each model termination, there is one possible lattice oxygen site for catalysis. On the 'A' surface, the oxygen is fourfold-coordinated to the surface A cation, and onefold-coordinated to the subsurface B cation. On the 'B' surface, the oxygen is twofold-coordinated to the surface B cation, and twofold-coordinated to the subsurface A cation.

We are interested in these oxygen sites' activity for alkane activation. The first C-H bond breaking is regarded to be rate limiting in many cases of alkane activation;[25-26] therefore, the C-H activation energy can be a useful quantity to predict the overall ability of a surface to react with methane. Furthermore, conclusions regarding relative reactivity for methane activation can be transferred to other similar C-H activation energies for other alkanes.[13] On metal oxides, the reactive lattice oxygen activates the molecule via a homolytic cleavage of the C-H bond (illustrated in Fig. 1a), and the perovskite (001) surfaces follow the same mechanism. H adsorption energy (HAE) and O vacancy formation energy (OVFE) are the commonly used energetic descriptors for oxygen reactivity, so we explored their correlation with the C-H activation energy for the A- and B- terminations of many cubic ABO_3 perovskites. Fig. 2 shows the correlation between OVFE and C-H E_a (R=0.97, MAE=0.19 eV) and between HAE and C-H E_a (R=0.99, MAE=0.10 eV). Example geometries for the C-H activation transition states can be found in Fig. 1b. The good linear correlations suggest that one can use either HAE or OVFE as a descriptor to predict E_a: the stronger the H adsorption on the lattice oxygen or the easier the formation of an oxygen vacancy at the lattice-oxygen site, the lower the C-H activation energy of methane.

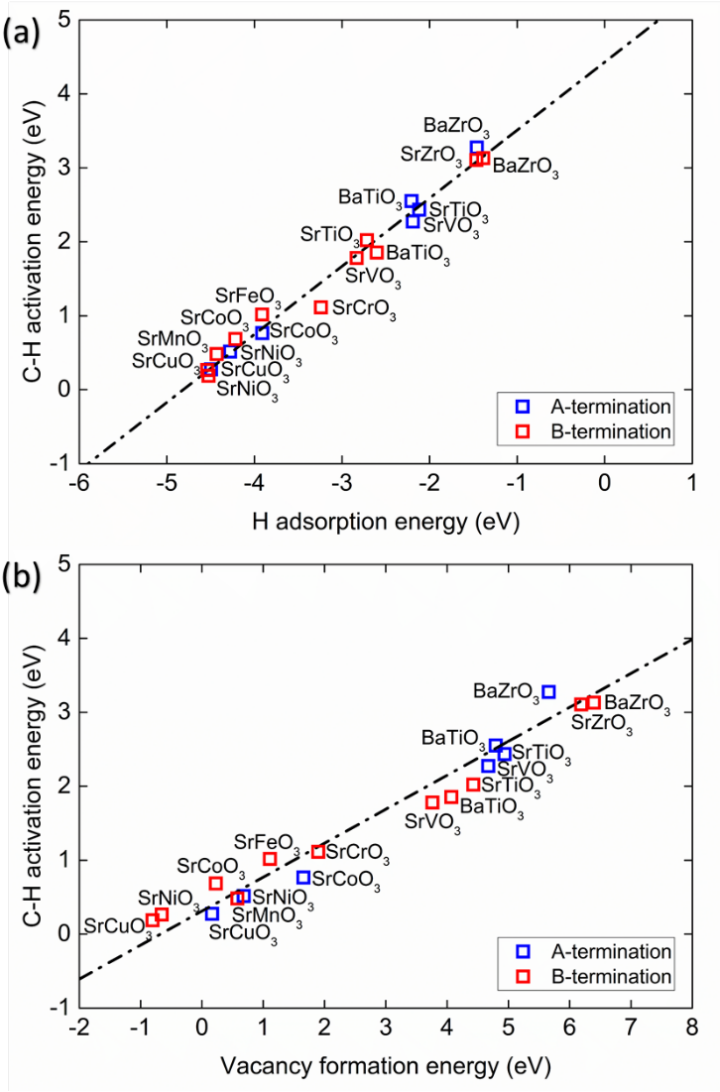

Figure 4.2.2 Correlation between homolytic C-H activation energy of CH_4 with hydrogen adsorption energy (a) and oxygen vacancy formation energy (b). The lines represent the linear best fit.

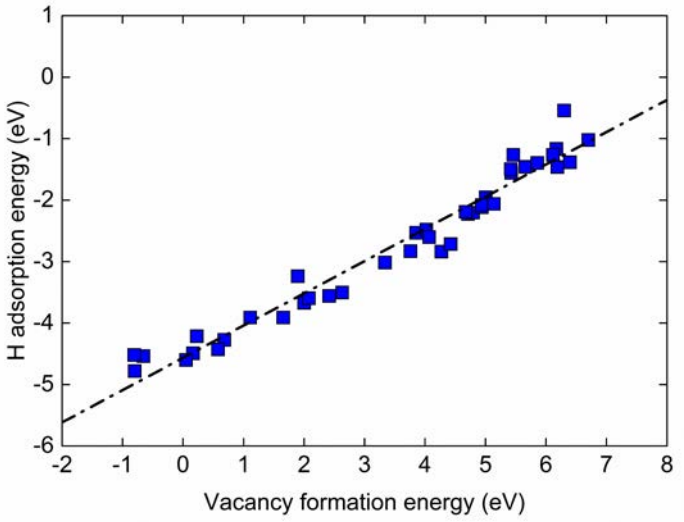

Figure 4.2.3 Correlation between hydrogen adsorption and vacancy formation energy of the lattice oxygen. The black dotted line represents the linear best fit.

The activity of the lattice oxygen can also play an additional role beyond the direct activation of the C-H such as oxygen transport and recombination.[43-44] In particular, the existing descriptor OVFE could possibly relate to the activity of oxygen for these processes. OVFE directly correlates to the thermodynamic barrier for the removal of oxygen lattice and by extension the strength of the M-O bond. Furthermore, the formation of vacancies can have an important role in controlling the rate of oxygen activation on the surface.[45] Unsurprisingly, as both HAE and OVFE relate well to C-H activation, we can find a strong linear correlation between HAE and OVFE as shown in Fig. 3. Therefore, we can reduce the ability of C-H activation and oxygen vacancy formation on the surface to a single parameter. Below we analyze in detail the trend of the oxygen reactivity from the perspectives of A cations, B cations, and terminations.

4.2.7.2 Impact of the A cation on oxygen reactivity

Fig. 4 shows that changing the identity of the A cation within the same group (Ca to Sr) has a negligible impact (~ 0.1 eV) on HAE. This is true regardless of the termination of the surface. For comparison, the HAE on the pure alkali earth oxides varies by about 0.8 eV among CaO, BaO, and SrO. In other words, even though the A termination exposes only the alkali earth metal and O ions, the reactivity is still dictated by the B transition metal. Another common A cation in perovskites is lanthanum[6] which has charge of +3 instead of +2. Correspondingly, the oxidation state of the B cation becomes +3 instead of +4, which has a significant impact on the bonding with oxygen. This results in both strengthening of the B-O bond and diminishing the reducibility of the B atom, leading to a lower HAE (Fig. 4). Therefore, selecting a suitable A cation should be driven by oxidation states rather than by the size of the ions, provided that they are sufficient to form a stable perovskite.

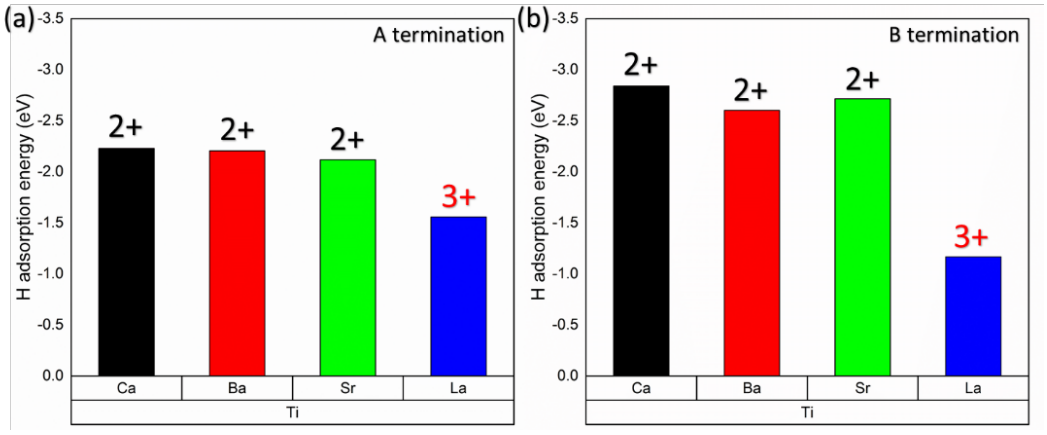

Figure 4.2.4 Hydrogen adsorption energy for perovskites with different A cations: (a) A termination; (b) B termination. The numbers at the top of the bars show the oxidation states of the A cations.

4.2.7.3 Impact of the B cation on oxygen reactivity

Fig. 5a shows that within one period, the difference in HAE between $SrTiO_3$ and $SrCuO_3$ is over 2 eV for the A termination and about 1.5 eV for the B termination. In other words, the oxygen reactivity on both terminations increases from Ti to Cu. One can understand this trend from the B-O bond strength across the period: as the number of d-electrons increases along the same period, the weakening of the B-O bond occurs from the filling of the anti-bonding orbitals, leading to higher oxygen reactivity. Within a group, the HAE decreases or the oxygen reactivity decreases going down the period table, such as from Ti to Zr to Hf (Fig. 5b), which corresponds to decreasing electronegativity or increasing metallicity from Ti (1.54) to Zr (1.33) and Hf (1.30). In other words, oxygen becomes more ionic and less reactive toward atomic hydrogen.

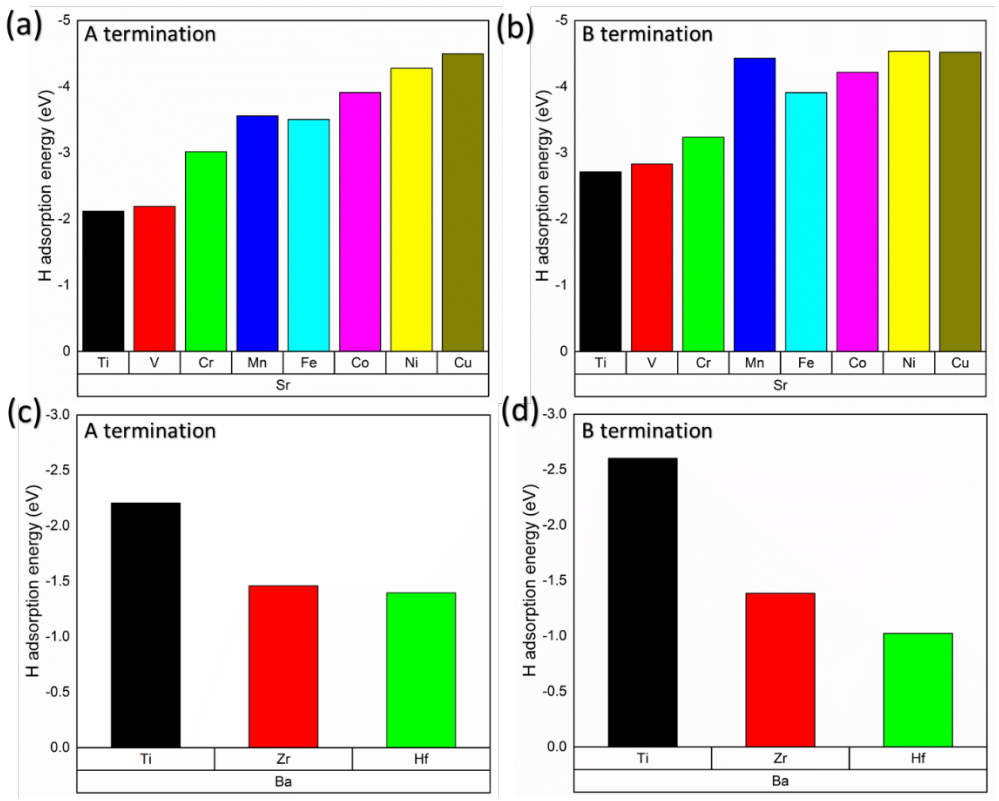

Figure 4.2.5 Hydrogen adsorption energy for perovskites with different B cations: (a) across the period for the A termination; (b) across the period for the B termination; (c) down in the same group for the A termination; (d) down in the same group for the B termination.

The strong influence of the B cation over the A cation on HAE and hence oxygen reactivity demonstrates the primary role of the transition metal B cations in controlling perovskite reducibility. On reducible metal oxides, the formation of a vacancy or the adsorption of the hydrogen results in the donation of electrons to the neighboring metal.[15, 17] For comparatively irreducible oxides such as alkali earth oxides, the electron(s) is instead delocalized over the system.[14] In the perovskite, the extra electrons will reduce the B cation much like in reducible metal oxide cases. Meanwhile, the A cations (with the same

oxidation state) will have very little impact on the reducibility of the surface as the electron will not become delocalized like in the pure alkali metal oxide when there is a reducible center which is more favorable in energetic stability. Furthermore, the O-B bond distance is always shorter than the O-A bond distance,[46] which provides a much more viable channel for electron transfer. This can explain why changing the A cation from Ca to Sr to Ba has very little impact on the surface reducibility, while changing the B cation has a much greater effect.

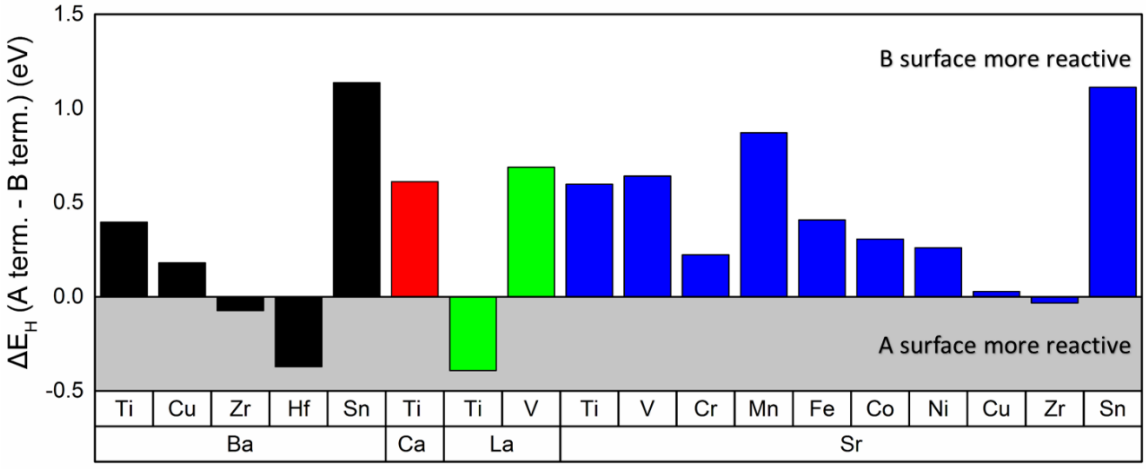

Figure 4.2.6 Difference in hydrogen adsorption energy between the A and B terminations of the (001) facet.

4.2.7.4 Impact of termination on oxygen reactivity

To compare the two terminations of the same facet, we plotted the difference in HAE between A and B terminations. Fig. 6 shows that for most of the perovskites examined, the B termination is more active. The reason can be traced to the different coordination environment of the lattice oxygen atoms. The oxygen is doubly coordinated to the B cation

on the B termination but only singly coordinated on the A termination. Given that the nearby B cations are reduction centers, the presence of an addition O-B coordination can aid the reducibility of the oxygen. This is also consistent with our finding that the reducibility of the surface is primarily directed by the B cation. In particular, $ASnO_3$, $ATiO_3$, AVO_3, $AMnO_3$ show significant differences in oxygen reactivity on the two terminations, with the largest difference being on the order of over 1 eV for $ASnO_3$. A difference of this magnitude suggests that experimentally altering the termination can provide another dimension of controlling catalyst activity. For $LaTiO_3$, $BaZrO_3$ and $BaHfO_3$, oxygen on the A termination is more reactive. In the case of $LaTiO_3$, the more reducible La (A-termination) replaces Ti (B-termination) as the reduction center on the surface. Similarly, ZrO_2 and HfO_2 are highly irreducible oxides[47] and even more irreducible than the alkali earth metals, resulting in less reducible B termination surfaces as well.

4.2.7.5 Second C-H activation or oxidative coupling on perovskites

Further oxidation of adsorbed methyl to the CO_x products proceeds via the further cleavage of C-H bonds. We examined the cleavage of H-CH_2O*, as this step is generally irreversible and will proceed down to CO_x. As seen from Fig. 7, the transition states for CH_4 and H-CH_2O* cleavage are fundamentally different. The CH_4 → CH_3 transition state (Fig. 1b) involves only the oxygen site, whereas the H-CH_2O* → H* + CH_2-O* transition state shows close proximity of the adsorbate species with the metal cations. Unlike the highly linear correlation between the 1st C-H activation and HAE (Fig. 2a), the correlation between the 2nd C-H activation and HAE (Fig. 8) shows a general trend (blue line) with

certain deviations. First, some perovskites and facets have higher than expected 2nd C-H activation energies, such as the A termination of $BaBO_3$ (B=Ti, Zr, and Hf) and non-transition metal B cations such as $ASnO_3$ (A=Sr, Ba). The large Ba cation will sterically hinder C-H activation of the methoxide to the nearby oxygen, which straddles between two Ba cations on the A termination. The Sn cation performs worse than transition metal B cations in stabilizing the methoxide C-H activation on the B termination.

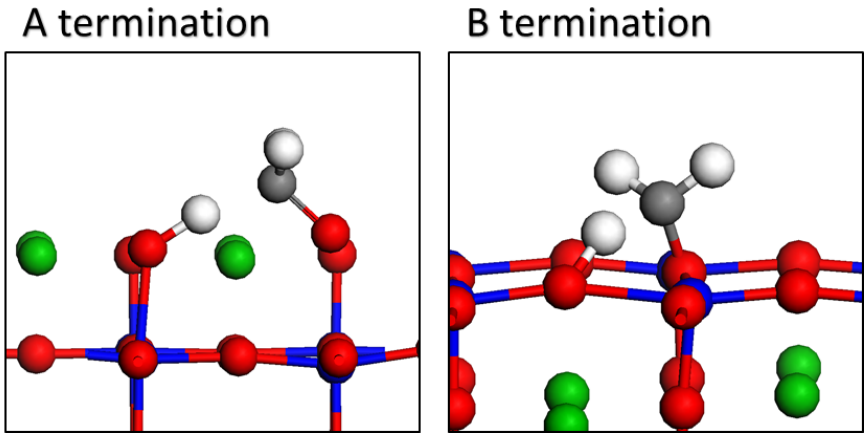

Figure 4.2.7 Typical transition states for the 2nd C-H activation of methane ($H\text{-}CH_2O^* \rightarrow H^* + CH_2\text{-}O^*$) on A termination and B termination of a perovskite (001) surface.

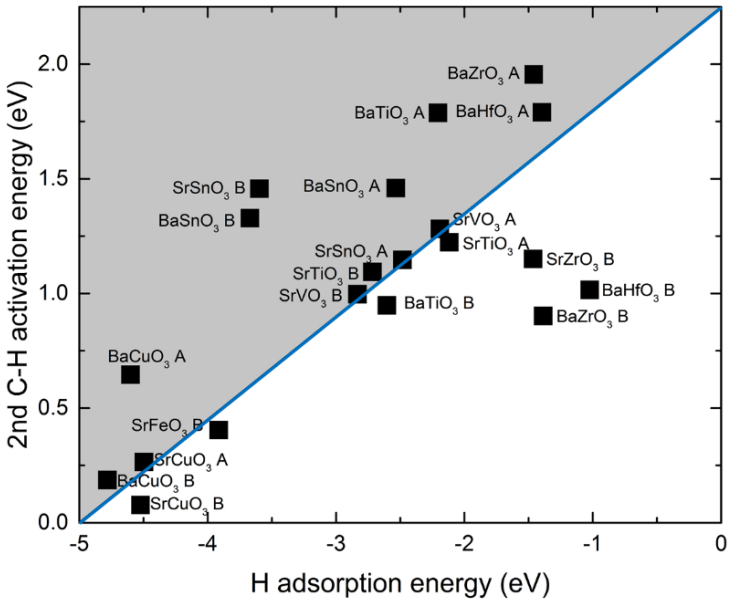

Figure 4.2.8 Correlation between 2nd C-H activation energy of methane (H-CH_2O* → H* + CH_2-O*) and H adsorption energy. The blue line is a visual aid for a linear correlation between the two quantities.

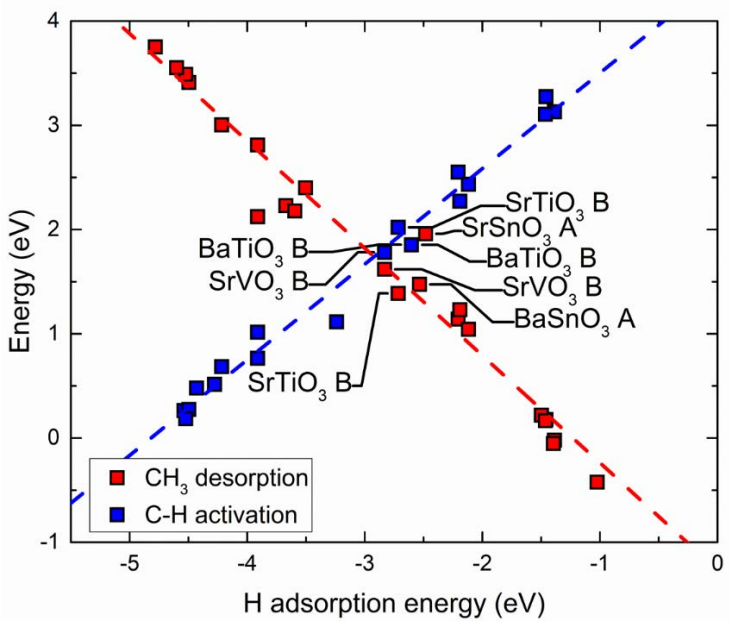

Figure 4.2.9 Correlation between CH_3 desorption energy (red) with hydrogen adsorption energy. For comparison, correlation between C-H activation energy (blue) with hydrogen adsorption energy is also shown. The dotted line(s) represent the linear best fits.

Instead of second C-H activation, the CH_3 groups can desorb from the surface oxygen site and couple in the gas phase to form C_2 products.[25] Interestingly, we found that CH_3 desorption energy also linearly correlates with hydrogen adsorption energy (HAE) for both A and B terminations, as seen in Fig. 9. This means that the termination sensitivity found in Fig. 6 (as reflected in the difference in HAE between A and B terminations) also applies to CH_3 desorption energy. Fig. 9 shows that very negative HAE correlates to very positive CH_3 desorption energy. In other words, while stronger H adsorption leads to easier first C-H activation, it also causes more difficult methyl desorption. As a result, the perovskites at the intersect between the two scaling lines offer a good balance between first C-H activation and methyl desorption, which is more conductive towards the coupling products.

4.2.7.6 Implications

Due to the diversity of possible perovskite compositions, it is imperative to obtain useful design principles in order to identify the most promising perovskite compositions for targeted experimental preparation and characterization. The descriptor-based approach is useful in quickly obtaining general and reliable catalyst properties from first principles. Descriptors for metal oxides have only recently begun gaining general attention,[13] given the inherent electronic and structural complexity of the system compared to transition metals.

In this study, we have found hydrogen adsorption energy (HAE) to be a central descriptor for several catalytically relevant properties of the perovskites. There are several important implications from the present work. In the very negative HAE limit, C-H activation is extremely facile, but will result in low OVFE, so formation of high amounts of defects in both the surface and the bulk, especially at elevated temperatures, can have a detrimental effect on its catalytic activity by reducing the fraction of available active sites[13] and affecting its structural stability. Very negative HAE also leads to difficult CH_3 desorption which is detrimental for formation of C_2 products in the gas phase. At the limit of very weak H adsorption, C-H activation becomes difficult, but the catalyst surface is expected to be more stable and desorption of the methyl groups is favorable. These observations suggest the Sabatier principle[10, 48-49] at work: surfaces which are neither too reactive nor too inert (too high or too low hydrogen adsorption) offer the optimal performance.

It is desirable to compare our prediction here with previous experimental studies of perovskites for methane activation. We predict that perovskites with B = Mn to Cu are the most active for homolytic C-H activation, which is supported by some experimental results.[2-3, 5, 50-51] On the other hand, we predict perovskites with B in group 5 or lower (such as Ti, Zr, Hf) to be less active for C-H activation, though experimental results show that catalysts such as $SrTiO_3$ are still active for methane combustion.[52-53] One explanation is that in our model we considered only the (100) surface with perfect A or B termination (instead of other facets and mixed terminations). In addition, we only examined the initial steps of methane activation instead of the whole catalytic pathways. Further work is

warranted to improve our modeling. Nevertheless, we have demonstrated that HAE can be a valuable litmus test of perovskite activity in its various linear scaling relationships.

4.2.8 Conclusions

We have correlated oxygen reactivity descriptors such as oxygen vacancy formation energy and hydrogen adsorption energy with methane C-H activation energy among a large set of perovskite compositions. Within the same group, the A cation has a negligible effect on oxygen reactivity, but becomes significant when changing between different oxidation states. Meanwhile, the reducibility and by extension the redox reactivity of the lattice oxygen is largely driven by the B cation, and can vary significantly within a period; perovskites with late transition metals have the most reactive oxygen. For the same reason, the activity of the B termination is higher than the A terminations in most cases. To select perovskites for high 2^{nd} C-H activation energies to avoid combustion to CO and CO_2, we found that larger A cations and non-transition metal B cations (with $BaSnO_3$ as a promising example) may lead to higher selectivity and yields for C_2 products. The tradeoff between first C-H bond breaking and methyl desorption suggests a sweat-spot oxygen reactivity for oxidative methane coupling. This study presents an initial attempt toward addressing the compositional diversity of perovskites in the context of energetic descriptors as well as methane activation.

References

(1) Goldschmidt, V. M. Die gesetze der krystallochemie. *Naturwissenschaften* **1926,** *14*, 477-485.

(2) Arai, H.; Yamada, T.; Eguchi, K.; Seiyama, T. Catalytic combustion of methane over various perovskite-type oxides. *Appl. Catal.* **1986,** *26*, 265-276.

(3) Pena, M.; Fierro, J. Chemical structures and performance of perovskite oxides. *Chem. Rev.* **2001,** *101*, 1981-2018.

(4) Zhu, J.; Li, H.; Zhong, L.; Xiao, P.; Xu, X.; Yang, X.; Zhao, Z.; Li, J. Perovskite oxides: preparation, characterizations, and applications in heterogeneous catalysis. *ACS Catal.* **2014,** *4*, 2917-2940.

(5) Royer, S.; Duprez, D.; Can, F.; Courtois, X.; Batiot-Dupeyrat, C.; Laassiri, S.; Alamdari, H. Perovskites as substitutes of noble metals for heterogeneous catalysis: dream or reality. *Chem. Rev.* **2014,** *114*, 10292-10368.

(6) Zhu, H.; Zhang, P.; Dai, S. Recent advances of lanthanum-based perovskite oxides for catalysis. *ACS Catal.* **2015,** *5*, 6370-6385.

(7) Labhasetwar, N.; Saravanan, G.; Megarajan, S. K.; Manwar, N.; Khobragade, R.; Doggali, P.; Grasset, F. Perovskite-type catalytic materials for environmental applications. *Sci. Tech. Adv. Mater.* **2015,** *16*, 036002.

(8) Wang, W.; Tadé, M. O.; Shao, Z. Research progress of perovskite materials in photocatalysis-and photovoltaics-related energy conversion and environmental treatment. *Chem. Soc. Rev.* **2015,** *44*, 5371-5408.

(9) Norskov, J. K.; Abild-Pedersen, F.; Studt, F.; Bligaard, T. Density functional theory in surface chemistry and catalysis. *Proc. Natl. Acad. Sci. U. S. A.* **2011,** *108*, 937-43.

(10) Nørskov, J. K.; Bligaard, T.; Rossmeisl, J.; Christensen, C. H. Towards the Computational Design of Solid Catalysts. *Nat. Chem.* **2009,** *1*, 37-46.

(11) Suntivich, J.; Gasteiger, H. A.; Yabuuchi, N.; Nakanishi, H.; Goodenough, J. B.; Shao-Horn, Y. Design Principles for Oxygen-Reduction Activity on Perovskite Oxide Catalysts for Fuel Cells and Metal–Air Batteries. *Nat. Chem.* **2011,** *3*, 546-550.

(12) Foo, G. S.; Polo Garzon, F.; Fung, V.; Jiang, D.-e.; Overbury, S. H.; Wu, Z. Acid-Base Reactivity of Perovskite Catalysts Probed via Conversion of 2-Propanol over Titanates and Zirconates. *ACS Catal.* **2017**.

(13) Latimer, A. A.; Kulkarni, A. R.; Aljama, H.; Montoya, J. H.; Yoo, J. S.; Tsai, C.; Abild-Pedersen, F.; Studt, F.; Nørskov, J. K. Understanding Trends in CH Bond Activation in Heterogeneous Catalysis. *Nature Mater.* **2017,** *16*, 225-229.

(14) Kumar, G.; Lau, S. L. J.; Krcha, M. D.; Janik, M. J. Correlation of Methane Activation and Oxide Catalyst Reducibility and its Implications for Oxidative Coupling. *ACS Catal.* **2016,** *6*, 1812-1821.

(15) Krcha, M. D.; Mayernick, A. D.; Janik, M. J. Periodic Trends of Oxygen Vacancy Formation and C–H Bond Activation Over Transition Metal-Doped CeO_2 (111) Surfaces. *J. Catal.* **2012,** *293*, 103-115.

(16) Liu, J. J.; Zhang, S. R.; Zhou, Y.; Fung, V.; Nguyen, L.; Jiang, D. E.; Shen, W. J.; Fan, J.; Tao, F. F. Tuning Catalytic Selectivity of Oxidative Catalysis through Deposition of Nonmetallic Atoms in Surface Lattice of Metal Oxide. *ACS Catal.* **2016,** *6*, 4218-4228.

(17) Mayernick, A. D.; Janik, M. J. Methane Activation and Oxygen Vacancy Formation Over CeO_2 and Zr, Pd Substituted CeO_2 Surfaces. *J. Phys. Chem. C* **2008,** *112*, 14955-14964.

(18) Beck, B.; Harth, M.; Hamilton, N. G.; Carrero, C.; Uhlrich, J. J.; Trunschke, A.; Shaikhutdinov, S.; Schubert, H.; Freund, H.-J.; Schlögl, R. Partial oxidation of ethanol on vanadia catalysts on supporting oxides with different redox properties compared to propane. *J. Catal.* **2012,** *296*, 120-131.

(19) Derk, A. R.; Li, B.; Sharma, S.; Moore, G. M.; McFarland, E. W.; Metiu, H. Methane Oxidation by Lanthanum Oxide Doped with Cu, Zn, Mg, Fe, Nb, Ti, Zr, or Ta: the Connection Between the Activation Energy and the Energy of Oxygen-Vacancy Formation. *Catal. Lett.* **2013,** *143*, 406-410.

(20) Schwach, P.; Pan, X.; Bao, X. Direct Conversion of Methane to Value-Added Chemicals over Heterogeneous Catalysts: Challenges and Prospects. *Chem. Rev.* **2017,** *117*, 8497-8520.

(21) Amenomiya, Y.; Birss, V. I.; Goledzinowski, M.; Galuszka, J.; Sanger, A. R. Conversion of methane by oxidative coupling. *Cat. Rev. - Sci. Eng.* **1990,** *32*, 163-227.

(22) Choudhary, T.; Banerjee, S.; Choudhary, V. Catalysts for combustion of methane and lower alkanes. *Appl. Catal., A* **2002,** *234*, 1-23.

(23) Pakhare, D.; Spivey, J. A review of dry (CO_2) reforming of methane over noble metal catalysts. *Chem. Soc. Rev.* **2014,** *43*, 7813-7837.

(24) Chen, J.; Arandiyan, H.; Gao, X.; Li, J. Recent Advances in Catalysts for Methane Combustion. *Catal. Surv. Asia* **2015,** *19*, 140-171.

(25) Lunsford, J. H. The Catalytic Oxidative Coupling of Methane. *Angew. Chem. Int. Ed.* **1995,** *34*, 970-980.

(26) Schwarz, H. Chemistry with Methane: Concepts Rather than Recipes. *Angew. Chem. Int. Ed.* **2011,** *50*, 10096-10115.

(27) Horn, R.; Schlögl, R. Methane Activation By Heterogeneous Catalysis. *Catal. Lett.* **2015,** *145*, 23-39.

(28) Coperet, C. C− H bond activation and organometallic intermediates on isolated metal centers on oxide surfaces. *Chem. Rev.* **2009,** *110*, 656-680.

(29) Tyo, E. C.; Yin, C.; Di Vece, M.; Qian, Q.; Kwon, G.; Lee, S.; Lee, B.; DeBartolo, J. E.; Seifert, S.; Winans, R. E.; Si, R.; Ricks, B.; Goergen, S.; Rutter, M.; Zugic, B.; Flytzani-Stephanopoulos, M.; Wang, Z. W.; Palmer, R. E.; Neurock, M.; Vajda, S. Oxidative dehydrogenation of cyclohexane on cobalt oxide (Co_3O_4) nanoparticles: The effect of particle size on activity and selectivity. *ACS Catal.* **2012,** *2*, 2409-2423.

(30) Fung, V.; Tao, F.; Jiang, D. E. Understanding oxidative dehydrogenation of ethane on Co3O4 nanorods from density functional theory. *Catal. Sci. Technol.* **2016,** *6*, 6861-6869.

(31) Zheng, H.; Zhan, Q.; Zavaliche, F.; Sherburne, M.; Straub, F.; Cruz, M. P.; Chen, L.-Q.; Dahmen, U.; Ramesh, R. Controlling self-assembled perovskite− spinel nanostructures. *Nano Lett.* **2006,** *6*, 1401-1407.

(32) Tanaka, H.; Tabata, H.; Kawai, T. Probing the surface forces of atomic layered $SrTiO_3$ films by atomic force microscopy. *Thin Solid Films* **1999,** *342*, 4-7.

(33) Erdman, N.; Poeppelmeier, K. R.; Asta, M.; Warschkow, O.; Ellis, D. E.; Marks, L. D. The structure and chemistry of the TiO_2-rich surface of $SrTiO_3$ (001). *Nature* **2002,** *419*, 55-58.

(34) Polo-Garzon, F.; Yang, S.-Z.; Fung, V.; Foo, G. S.; Bickel, E. E.; Chisholm, M. F.; Jiang, D.-e.; Wu, Z. Controlling Reaction Selectivity via Surface Termination of Perovskite Catalysts. *Angew. Chem.* **2017**.

(35) Kresse, G.; Furthmuller, J. Efficiency of Ab-Initio Total Energy Calculations for Metals and Semiconductors Using a Plane-Wave Basis Set. *Comput. Mater. Sci.* **1996,** *6*, 15-50.

(36) Kresse, G.; Furthmuller, J. Efficient Iterative Schemes for Ab Initio Total-Energy Calculations Using a Plane-Wave Basis Set. *Phys. Rev. B* **1996,** *54*, 11169-11186.

(37) Perdew, J. P.; Burke, K.; Ernzerhof, M. Generalized Gradient Approximation Made Simple. *Phys. Rev. Lett.* **1996,** *77*, 3865-3868.

(38) Blöchl, P. E. Projector Augmented-Wave Method. *Phys. Rev. B* **1994,** *50*, 17953-17979.

(39) Monkhorst, H. J.; Pack, J. D. Special Points for Brillouin-Zone Integrations. *Phys. Rev. B* **1976,** *13*, 5188-5192.

(40) Grimme, S.; Antony, J.; Ehrlich, S.; Krieg, H. A Consistent and Accurate ab Initio Parametrization of Density Functional Dispersion Correction (DFT-D) for the 94 Elements H-Pu. *J. Chem. Phys.* **2010,** *132*, 154104.

(41) Henkelman, G.; Jónsson, H. A Dimer Method for Finding Saddle Points on High Dimensional Potential Surfaces Using Only First Derivatives. *J. Chem. Phys.* **1999,** *111*, 7010.

(42) Henkelman, G.; Uberuaga, B. P.; Jónsson, H. A Climbing Image Nudged Elastic Band Method for Finding Saddle Points And Minimum Energy Paths. *J. Chem. Phys.* **2000,** *113*, 9901-9904.

(43) Rossetti, I.; Allieta, M.; Biffi, C.; Scavini, M. Oxygen transport in nanostructured lanthanum manganites. *Phys. Chem. Chem. Phys.* **2013,** *15*, 16779-16787.

(44) Rossetti, I.; Biffi, C.; Forni, L. Oxygen non-stoichiometry in perovskitic catalysts: Impact on activity for the flameless combustion of methane. *Chem. Eng. J.* **2010,** *162*, 768-775.

(45) Staykov, A.; Téllez, H.; Akbay, T.; Druce, J.; Ishihara, T.; Kilner, J. Oxygen Activation and Dissociation on Transition Metal Free Perovskite Surfaces. *Chem. Mater.* **2015,** *27*, 8273-8281.

(46) Zeng, Z.; Calle-Vallejo, F.; Mogensen, M. B.; Rossmeisl, J. Generalized Trends in the Formation Energies of Perovskite Oxides. *Phys. Chem. Chem. Phys.* **2013,** *15*, 7526-7533.

(47) McTaggart, F. Reduction of zirconium and hafnium oxides. *Nature* **1961,** *191*, 1192-1192.

(48) Medford, A. J.; Vojvodic, A.; Hummelshøj, J. S.; Voss, J.; Abild-Pedersen, F.; Studt, F.; Bligaard, T.; Nilsson, A.; Nørskov, J. K. From the Sabatier principle to a predictive theory of transition-metal heterogeneous catalysis. *J. Catal.* **2015,** *328*, 36-42.

(49) Sabatier, P. Hydrogénations et deshydrogénations par catalyse. *Eur. J. Inorg. Chem.* **1911,** *44*, 1984-2001.

(50) Tascon, J.; Tejuca, L. G. Catalytic activity of perovskite-type oxides $LaMeO_3$. *React. Kinet. Catal. Lett.* **1980,** *15*, 185-191.

(51) Voorhoeve, R. J.; Remeika, J.; Freeland, P.; Matthias, B. Rare-earth oxides of manganese and cobalt rival platinum for the treatment of carbon monoxide in auto exhaust. *Science* **1972,** *177*, 353-354.

(52) Oliva, C.; Cappelli, S.; Rossetti, I.; Kryukov, A.; Bonoldi, L.; Forni, L. Effect of M ion oxidation state in Sr 1− x M x TiO 3±δ perovskites in methane catalytic flameless combustion. *J. Mol. Catal. A: Chem.* **2006,** *245*, 55-61.

(53) Oliva, C.; Bonoldi, L.; Cappelli, S.; Fabbrini, L.; Rossetti, I.; Forni, L. Effect of preparation parameters on SrTiO 3±δ catalyst for the flameless combustion of methane. *J. Mol. Catal. A: Chem.* **2005,** *226*, 33-40.

4.3 New Bonding Model of Radical Adsorbate on Lattice Oxygen of Perovskites

4.3.4 Abstract

A new model of bonding between radical adsorbates and lattice oxygens is proposed that considers both the adsorbate-oxygen bonding and the weakening of the metal-oxygen bonds. Density-functional calculations of $SrMO_3$ perovskites for M being 3d, 4d, and 5d transitions metals are used to correlate the bulk electronic structure with the surface-oxygen reactivity. Occupation of the metal-oxygen antibonding states, examined via the crystal orbital Hamilton population (COHP), is found to be a useful bulk descriptor that correlates with the vacancy formation energy of the lattice oxygen and its hydrogen adsorption energy. Analysis of density-of-states and COHP indicates that H adsorption energy is a combined result of formation of the O-H bond and the weakening of the surface metal-oxygen bond due to occupation of the metal-oxygen antibonding states by the electron from H. This insight will be useful in understanding the trends in surface reactivity of perovskites and transition-metal oxides in general.

4.3.5 Introduction

Metal oxides are ubiquitous in the study of surface chemistry and catalysis. A better physical and chemical understanding of these materials is consequently warranted to meet the increased interest and pace of development. For transition metals, widely applicable and elegant models have been developed, such as the d-band center[1-3] and the coordination number,[4-5] as descriptors of adsorption and catalytic properties. However, metal oxides

remain a challenge to accurately characterize due to the significantly increased complexity in electronic, magnetic, and surface structures.

Catalytic reactivity descriptors for metal oxides are frequently found to be linked to stability. From a computational standpoint, these reactivity descriptors are generally adsorption energies of relevant reactants or intermediates on the metal and O sites of the surface. For example, in electrocatalytic oxygen evolution and oxygen reduction reactions, the main descriptors involve the adsorption energies of oxygen-containing species (O, OH, OOH)[6-7] and oxygen molecule (O_2)[8], respectively. In the homolytic C-H activation, hydrogen adsorption energy (HAE) on the oxygen site is a very good descriptor for the first C-H activation energy.[9-11] Meanwhile, stability descriptors are used to characterize metal oxides, including bulk formation energy[6, 12-13] and oxygen vacancy formation energy (VFE).[10, 14-19] It has been observed that HAE and VFE have a persistent correlation,[9-10, 20-21] but an electronic understanding of the underlying relation remains unclear.

In this paper, we attempt to unravel the nature of oxygen-adsorbate (O-X) bonding, whereby a radical group, as a result of dissociative adsorption or activation by surface sites, forms a strong σ-bond with a surface oxygen of a transition-metal oxide (TMO). As the adsorption strength of these species is a prime descriptor for an oxide's catalytic activity, establishing an energetic model for the oxygen-adsorbate interaction is a necessary step towards rational catalyst design.

Because the energetics of formation of the surface O-X bond is intrinsically linked to the electronic structure of the TMO, we begin our study first on the metal-oxygen bond in the TMO. TMOs can be characterized as having polar covalent M-O bonds from the

mixing of M d states and O 2p states.[16, 22] We focus our efforts here on cubic perovskites which prove to be computationally convenient systems with a fixed ABO_3 stoichiometry and a well-defined crystal structure. The A cation is chosen here to be Sr^{2+}, which is ionically bonded to the oxygen, while the B cation varies from the transition metals in the periodic table of different orbital occupations. The varying d-electron count of cation B will allow us to explore the trends in the B-O bonding and its relation to the O-X bonding from the density functional theory (DFT) calculations of the changing electronic structure and surface energetics.

4.3.6 Computational Method

Our DFT study was based on the Perdew-Burke-Ernzerhof (PBE) functional[23] within the generalized gradient approximation (GGA). Although band gaps are usually underestimated with GGA, it has nevertheless proven to be robust in sufficiently replicating energetic quantities such as formation energy,[13, 24-25] to reveal the relative trends. HSE06[26] was used to validate the PBE results, confirming the linear trends from PBE (Figure S1). An important concept utilized in this work is the crystal orbital Hamilton population (COHP),[27] which is a product of the density of states (DOS) and the overlap Hamiltonian element, an improvement[28] over the classic crystal orbital overlap population (COOP). With COHP, the chemistry of bonding-antibonding interactions can be revealed from the solid state. Further computational details can be found in the SI and relaxed geometries were used for all computed energetics. While the basic principle for bonding on surfaces,[22, 29] particularly molecular adsorbates on metals via back donation,[30-31] has been proposed for many years, to date there is no explicit ab-initio work done to study bonding trends on

metal oxides from the perspective of the bonding and antibonding contributions. In this work we try to tackle the problem using COHP and the perovskite model system, and by drawing trends from screening a large number of elemental compositions.

4.3.7 Results and Discussion

Figure 1a shows the integrated crystal orbital Hamilton population (ICOHP) of the M-O bond in the bulk $SrMO_3$ perovskite that provides a useful, relative quantification of the metal-oxygen bonding. One can see a clear trend between ICOHP and the d-electron count for each of the three periods of 3d to 5d TMs: ICOHP increases with the number of d-electrons in M, consistent with the weakening of the M-O bond from group 3 to 12, implying that the M-O covalent contributions are more significant than the polar ones. The corresponding COHP plots are shown for several 3d perovskites (Figure 1b). For M=Ti, all states above the Fermi level are antibonding (positive COHP or negative -COHP). Moving to Zn, the antibonding states become progressively more occupied. The downward shift of the antibonding states relative to the Fermi level from additional d-electrons thereby leads to increasing ICOHP (Figure 1a). In conjunction with the increasing positive COHP states, the net bonding states also decrease from the overall destabilization of the M-O bond.

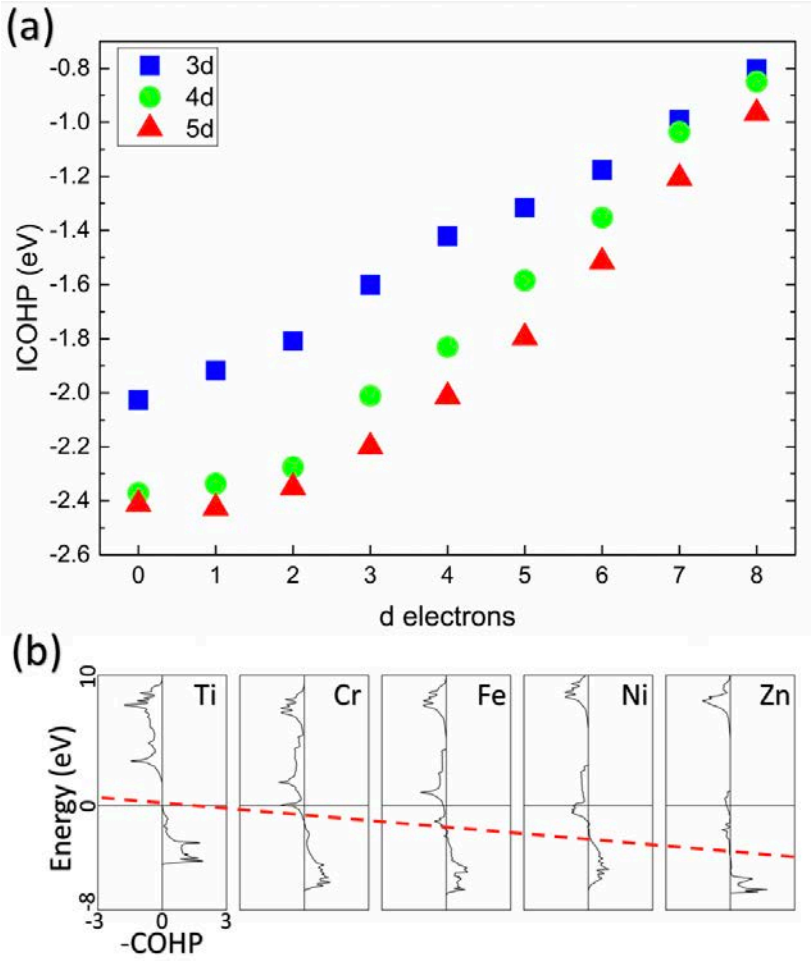

Figure 4.3.1 (a) Averaged integrated crystal orbital Hamilton populations (ICOHP) of the metal-oxygen (M-O) bonds as a function of the number of d-electrons in the bulk perovskite, $SrMO_3$, with M being 3d, 4d, and 5d transition metals. (b) Crystal-orbital Hamilton population (COHP) versus energy for several 3d metals; note that -COHP is used as the a-axis. The dashed line in (b) illustrates the downshift of the separation point between the antibonding (negative) and bonding (positive) states as more antibonding states are populated across a period.

More interestingly, we find that ICOHP correlates well with the VFE of surface lattice oxygen for M being all the 3d-5d metal in $SrMO_3$ (Figure 2a). This suggests that ICOHP is a useful bulk descriptor for the surface oxygen's reactivity, since the VFE of surface lattice oxygen correlates well with the surface reactivity such as HAE and the Bader

charges on the O atom (Figure 3). This correlation is further confirmed between the bulk M-O ICOHP and HAE (Figure 2b). To rule out the bond-distance effect, we plotted the M-O and O-H bond distances and found that they vary little with the number of d electrons (Figure S2). Given the destabilizing impact of increasing d-electron count on the M-O covalent bonding as manifested by the ICOHP, the correlation between ICOHP and HAE therefore suggests that adsorbate bonding can also impact the M-O covalent bonding, as we analyze next.

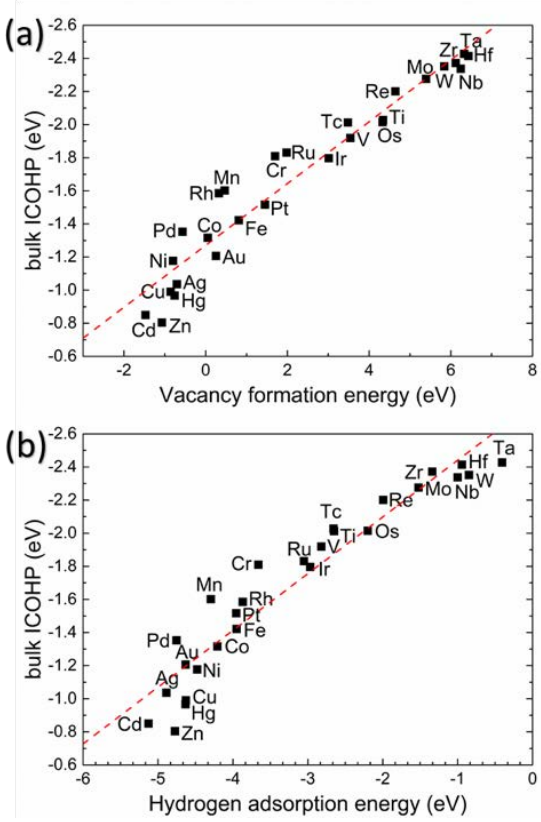

Figure 4.3.2 Correlation plots for perovskite $SrMO_3$(100) M-terminated surfaces with M being the transition metals denoted: (a) between bulk integrated crystal orbital Hamilton population (ICOHP) and vacancy formation energy of the lattice oxygen; (b) between bulk ICOHP and hydrogen adsorption energy on the lattice oxygen. The dashed red line corresponds to the linear best fit with R^2=0.94 for (a) and 0.91 for (b).

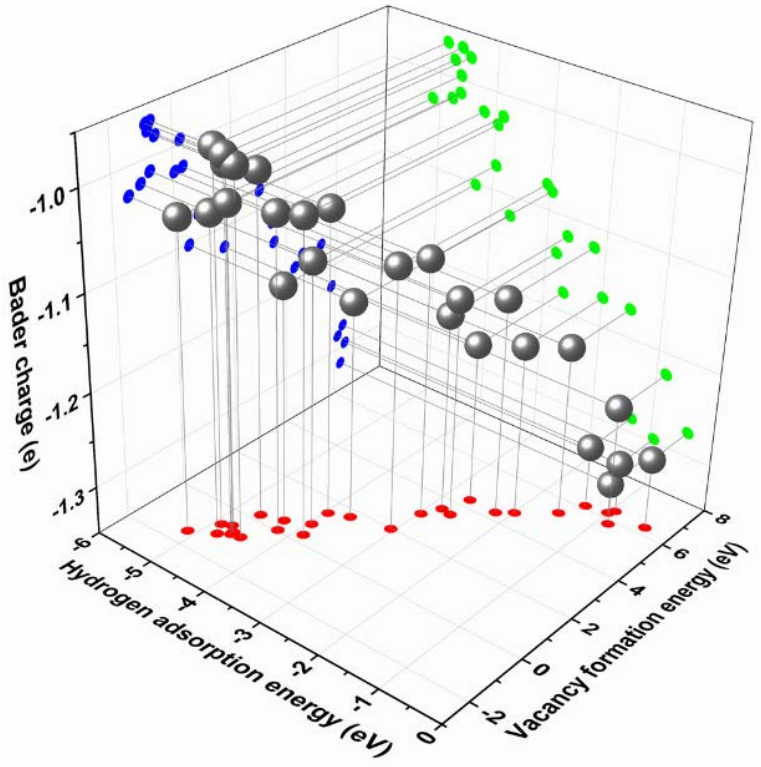

Figure 4.3.3 3D scatterplot of hydrogen adsorption energy (HAE), vacancy formation energy (VFE), and Bader charge of the lattice oxygen on the (100) surface of the $SrMO_3$ perovskite with varying M. Surface relaxation was taken into account for both HAE and VFE calculations.

In an oxide surface, oxygen has a formal charge of -2 and its 2p states are situated below the Fermi level. Since the O-H antibonding state is far above the Fermi level, the electron from H will end up occupying the lower lying states in the conduction band, as schematically shown in Figure 4. For a TM oxide, as we have shown from COHP (Figure 1), the conduction band corresponds to the antibonding M-O states. Using M=Ti as a case study, the filling of the conduction band primarily onto the Ti 3d states (Figure 5a) can be seen when H is adsorbed to O. COHP plots confirm that the filling of the conduction band corresponds to an increase in occupancy in the M-O antibonding orbitals (Figure 5b).

Similar reports for the phenomenon of M-O antibonding occupancy from reduction have also been observed in the case of metal clusters.[32] We find a significant decrease in ICOHP for the Ti-O bond from -1.86 eV to -1.11 eV after H adsorption. In other words, the Ti-O bond is significantly weakened after H adsorption. Furthermore, the O-H ICOHP (Figure S3) is found to stay roughly constant with respect to the different HAEs, demonstrating that the change in HAE on different perovskites must be linked to the extent of weakening of the M-O bond from reduction.

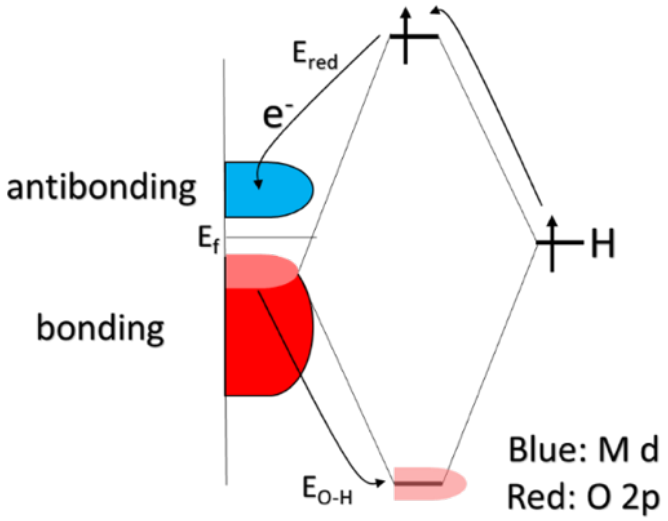

Figure 4.3.4 Diagram of the O-H bonding involving O 2p nonbonding states (pink) and one-electron reduction into the M-O antibonding states (blue).

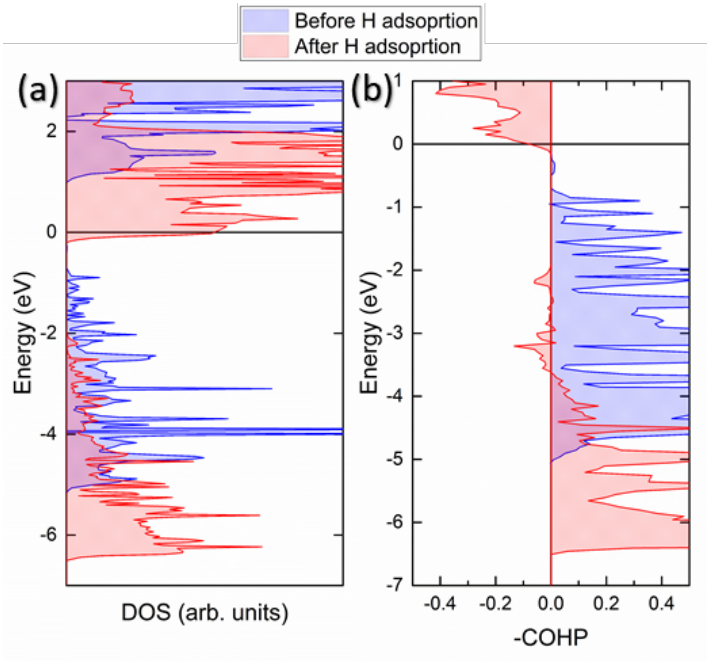

Figure 4.3.5 (a) Ti 3d partial density of states before and after hydrogen adsorption on the lattice oxygen of $SrTiO_3$. (b) -COHP plot of the local Ti-O bond before and after hydrogen adsorption.

Traditionally, as a radical adsorbate (X) approaches a surface, a bond is drawn between O and X, and the neighboring metal center is reduced by one electron (Figure 6a). Our present findings suggest that such a picture may be over simplified. Indeed, Bader charge analysis shows that the electron transfer from hydrogen to the neighboring metal sites is significantly lower than expected from the traditional bonding scheme (Table S1). Instead, we propose a revised model (Figure 6b) where the reduction by the electron takes place mainly at the M-O bonds. Hence the oxygen charge, the M-O bonding states, and the M site reducibility all contribute to the surface reactivity of the oxide. The qualitative cross-correlation between properties such as VFE and O Bader charge with HAE (Figure 3) can thereby be explained. The stronger the M-O bonds, the more positive the VFE and the more negative the O charge; consequently, the extent of destabilization from the occupation of

the M-O antibonding states is greater which leads to a less negative HAE or weaker adsorption for H. Conversely, the weaker the M-O bonds, the smaller the VFE and the less negative the O charge; in this case, the already weakened M-O bond leaves the O atom with more free valence to react with H, leading to more negative HAE or stronger adsorption.

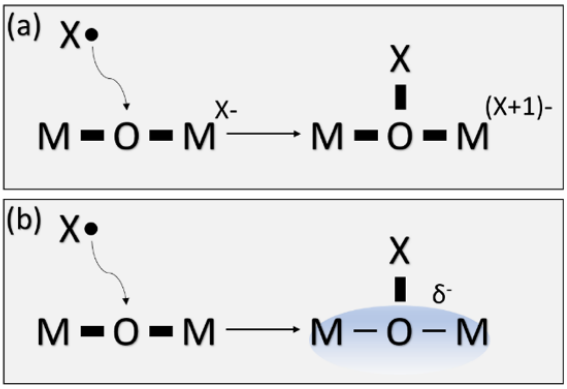

Figure 4.3.6 Two different models for O-X bonding on an oxide: (a) Conventional picture involving the one-electron reduction of a neighboring metal center; (b) New model proposed in this work showing delocalization of reducing electron into nearby surface states centered on O and partially on M, as well as weakening of M-O bonds.

The proposed O-X bonding model can be generalized beyond hydrogen adsorption to other radical species such as CH_3, NH_2, and SH, which can also covalently bond with oxygen and reduce the surface. We found that the adsorption energies of these adsorbates on the lattice oxygen have close linear relationships with HAE (R^2 values close to one; Figure S4), indicating that they will follow the same ICOHP trends and surface reduction mechanisms. Deviations from the linear correlations can be attributed to the different spin states, especially for the 3d transition metals. Further and full analysis on the spin distributions is warranted in the future.

4.3.8 Conclusion

In conclusion, analysis of crystal orbital Hamilton population (ICOHP) from density functional theory calculations of $SrMO_3$ perovskites (M being all 3d, 4d, and 5d transitions metals) shows that reductive adsorption on oxygen sites of perovskite surfaces is best described as a compromise between the energetic stabilization of forming a strong O-X bonding and the destabilizing effect of electron transfer into the surface M-O antibonding states. On the same oxygen site, metals with strong M-O bonds become destabilized to a greater extent from electron transfer, and subsequently the formation of O-X bonds becomes more *energetically disfavored* compared to those with weak M-O bonds. Hence one can understand why hydrogen adsorption energy is a universal descriptor for any radical adsorption on perovskite surfaces and transition metal oxides in general. With our model, the deliberate tuning of oxygen charge, M-O bond strength, and M sites can be rationalized in understanding adsorption properties on lattice oxygen of metal oxide catalysts.[33-34]

References

(1) Nørskov, J. K.; Abild-Pedersen, F.; Studt, F.; Bligaard, T. Density Functional Theory in Surface Chemistry and Catalysis. *Proc. Natl. Acad. Sci. U. S. A.* **2011,** *108*, 937-43.

(2) Nørskov, J. K.; Bligaard, T.; Rossmeisl, J.; Christensen, C. H. Towards the Computational Design of Solid Catalysts. *Nat. Chem.* **2009,** *1*, 37-46.

(3) Hammer, B.; Nørskov, J. Why Gold is the Noblest of all the Metals. *Nature* **1995,** *376*, 238-240.

(4) Calle‐Vallejo, F.; Martínez, J. I.; García‐Lastra, J. M.; Sautet, P.; Loffreda, D. Fast Prediction of Adsorption Properties for Platinum Nanocatalysts with Generalized Coordination Numbers. *Angew. Chem. Int. Ed.* **2014,** *53*, 8316-8319.

(5) Calle-Vallejo, F.; Loffreda, D.; Koper, M. T.; Sautet, P. Introducing Structural Sensitivity Into Adsorption-Energy Scaling Relations by Means of Coordination Numbers. *Nat. Chem.* **2015,** *7*, 403-410.

(6) Calle-Vallejo, F.; Díaz-Morales, O. A.; Kolb, M. J.; Koper, M. T. Why Is Bulk Thermochemistry a Good Descriptor for the Electrocatalytic Activity of Transition Metal Oxides? *ACS Catal.* **2015,** *5*, 869-873.

(7) Rossmeisl, J.; Qu, Z.-W.; Zhu, H.; Kroes, G.-J.; Nørskov, J. K. Electrolysis of Water on Oxide Surfaces. *J. Electroanal. Chem.* **2007,** *607*, 83-89.

(8) Suntivich, J.; Gasteiger, H. A.; Yabuuchi, N.; Nakanishi, H.; Goodenough, J. B.; Shao-Horn, Y. Design Principles for Oxygen-Reduction Activity on Perovskite Oxide Catalysts for Fuel Cells and Metal–Air Batteries. *Nat. Chem.* **2011,** *3*, 546-550.

(9) Latimer, A. A.; Kulkarni, A. R.; Aljama, H.; Montoya, J. H.; Yoo, J. S.; Tsai, C.; Abild-Pedersen, F.; Studt, F.; Nørskov, J. K. Understanding Trends in CH Bond Activation in Heterogeneous Catalysis. *Nature Mater.* **2017,** *16*, 225-229.

(10) Fung, V.; Tao, F. F.; Jiang, D. E. General Structure-Reactivity Relationship for Oxygen on Transition-Metal Oxides. *J. Phys. Chem. Lett.* **2017,** *8*, 2206-2211.

(11) Deshlahra, P.; Iglesia, E. Reactivity and Selectivity Descriptors for the Activation of C-H Bonds in Hydrocarbons and Oxygenates on Metal Oxides. *J. Phys. Chem. C* **2016,** *120*, 16741-16760.

(12) Zeng, Z.; Calle-Vallejo, F.; Mogensen, M. B.; Rossmeisl, J. Generalized Trends in the Formation Energies of Perovskite Oxides. *Phys. Chem. Chem. Phys.* **2013,** *15*, 7526-7533.

(13) Calle-Vallejo, F.; Martínez, J. I.; García-Lastra, J. M.; Mogensen, M.; Rossmeisl, J. Trends in Stability of Perovskite Oxides. *Angew. Chem. Int. Ed.* **2010,** *49*, 7699-7701.

(14) Lee, Y.-L.; Kleis, J.; Rossmeisl, J.; Shao-Horn, Y.; Morgan, D. Prediction of Solid Oxide Fuel Cell Cathode Activity with First-Principles Descriptors. *Energy Environ. Sci.* **2011,** *4*, 3966-3970.

(15) Ganduglia-Pirovano, M. V.; Hofmann, A.; Sauer, J. Oxygen Vacancies in Transition Metal and Rare Earth Oxides: Current State of Understanding and Remaining Challenges. *Surf. Sci. Rep.* **2007,** *62*, 219-270.

(16) van Santen, R. A.; Tranca, I.; Hensen, E. J. Theory of Surface Chemistry and Reactivity of Reducible Oxides. *Catal. Today* **2015,** *244*, 63-84.

(17) Kumar, G.; Lau, S. L. J.; Krcha, M. D.; Janik, M. J. Correlation of Methane Activation and Oxide Catalyst Reducibility and its Implications for Oxidative Coupling. *ACS Catal.* **2016,** *6*, 1812-1821.

(18) Krcha, M. D.; Mayernick, A. D.; Janik, M. J. Periodic Trends of Oxygen Vacancy Formation and C–H Bond Activation Over Transition Metal-Doped CeO_2 (111) Surfaces. *J. Catal.* **2012,** *293*, 103-115.

(19) Derk, A. R.; Li, B.; Sharma, S.; Moore, G. M.; McFarland, E. W.; Metiu, H. Methane Oxidation by Lanthanum Oxide Doped with Cu, Zn, Mg, Fe, Nb, Ti, Zr, or Ta: the Connection Between the Activation Energy and the Energy of Oxygen-Vacancy Formation. *Catal. Lett.* **2013,** *143*, 406-410.

(20) Fung, V.; Tao, F. F.; Jiang, D.-e. Trends of Alkane Activation on Doped Cobalt (II, III) Oxide from First Principles. *ChemCatChem* **2018,** *10*, 244-249.

(21) Fung, V.; Polo-Garzon, F.; Wu, Z.; Jiang, D.-e. Exploring Perovskites for Methane Activation from First Principles. *Catal. Sci. Technol.* **2018,** *8*, 702-709.

(22) Hoffmann, R., *Solids and Surfaces: a Chemist's View of Bonding in Extended Structures*. VCH Publishers: 1988.

(23) Perdew, J. P.; Burke, K.; Ernzerhof, M. Generalized Gradient Approximation Made Simple. *Phys. Rev. Lett.* **1996,** *77*, 3865-3868.

(24) Mowbray, D.; Martinez, J. I.; Calle-Vallejo, F.; Rossmeisl, J.; Thygesen, K. S.; Jacobsen, K. W.; Nørskov, J. K. Trends in Metal Oxide Stability for Nanorods, Nanotubes, and Surfaces. *J. Phys. Chem. C* **2010,** *115*, 2244-2252.

(25) Martinez, J. I.; Hansen, H. A.; Rossmeisl, J.; Nørskov, J. K. Formation Energies of Rutile Metal Dioxides Using Density Functional Theory. *Phys. Rev. B* **2009,** *79*, 045120.

(26) Krukau, A. V.; Vydrov, O. A.; Izmaylov, A. F.; Scuseria, G. E. Influence of the Exchange Screening Parameter on the Performance of Screened Hybrid Functionals. *J. Chem. Phys.* **2006,** *125*, 224106.

(27) Dronskowski, R.; Bloechl, P. E. Crystal Orbital Hamilton Populations (COHP): Energy-Resolved Visualization of Chemical Bonding in Solids Based on Density-Functional Calculations. *J. Phys. Chem.* **1993,** *97*, 8617-8624.

(28) Glassey, W. V.; Hoffmann, R. A Comparative Study of Hamilton and Overlap Population Methods for the Analysis of Chemical Bonding. *J. Chem. Phys.* **2000,** *113*, 1698-1704.

(29) Hoffmann, R. A Chemical and Theoretical Way to Look at Bonding on Surfaces. *Rev. Mod. Phys.* **1988,** *60*, 601-628.

(30) Shustorovich, E. Chemisorption Phenomena: Analytic Modeling Based on Perturbation Theory and Bond-Order Conservation. *Surf. Sci. Rep.* **1986,** *6*, 1-63.

(31) Van Santen, R. On Shustorovich's Bond-Order Conservation Method as Applied to Chemisorption. *Recueil des Travaux Chimiques des Pays-Bas* **1990,** *109*, 59-63.

(32) Nishimoto, Y.; Yokogawa, D.; Yoshikawa, H.; Awaga, K.; Irle, S. Super-Reduced Polyoxometalates: Excellent Molecular Cluster Battery Components and Semipermeable Molecular Capacitors. *J. Am. Chem. Soc.* **2014,** *136*, 9042-9052.

Supplementary Information

1. Computational details

The density functional theory (DFT) calculations were performed with the Vienna ab initio Simulation Package (VASP).[1-2] The Perdew-Burke-Ernzerhof (PBE)[3] functional form of generalized-gradient approximation (GGA) was used for electron exchange and correlation energies. The PBE functional is chosen instead of the PBE+U approach because the U parameters would bring large uncertainty to the overall trend. We further point-checked the ICOHP trend using the Heyd-Scuseria-Ernzerhof (HSE)[4] hybrid functional based on PBE-optimized geometries for three systems, $SrZnO_3$, $SrFeO_3$, and $SrTiO_3$. Figure S1 confirms the linear trends of ICOPH against the number of d-electrons and H adsorption energy. All calculations were performed with spin polarization. The projector-augmented wave method was used to describe the electron-core interaction[1, 5] with a kinetic energy cutoff of 450 eV for the surface calculations. A 3×3×1 sampling of Brillouin zone using a Monkhorst-Pack scheme was used for the kpoints.[6] A vacuum layer of 15 Å was created for the surface slabs. The top two layers of the surface slab were relaxed in the calculations. Atomic charges were obtained from Bader's method of separating charge density.[7-8] Charge densities and isosurfaces were visualized using the VESTA program.[9]

Adsorption energies (O-X; X=H) were calculated with the equation $E_{ads} = E_{surface+adsorbate} - (E_{perfect\text{-}surface} + E_{adsorbate})$ where $E_{surface+adsorbate}$ is the energy of the surface slab with a adsorbate. The energies of $E_{adsorbate}$ were computed by placing the adsorbate in

a cubic cell with a 15 Å wide vacuum in each direction. Vacancy formation energy was calculated with the equation $E_{VFE} = E_{defect\_surface} - (E_{perfect\text{-}surface} + 0.5*E_{O2})$. Adsorption energies were calculated on the most stable (100) facet of the $SrMO_3$ perovskites on the M termination, with a six-layered slab model. For completeness, all transition metals are used for M, though some elements may not form stable perovskites in standard conditions. Calculations involving crystal overlap Hamilton populations (COHP) were performed with the LOBSTER program[10-12] read from VASP outputs. In order for the COHP comparisons to hold for the different studied systems, the M-O and O-H bonds should remain the same. Figure S2 shows the M-O and O-H distances as a function of d-electrons, showing minor changes across the period. Furthermore, the O-H COHP is shown stay roughly constant within the range of 3.8 ± 0.1 eV, demonstrating the change in hydrogen adsorption energy must be due to the electron reduction contribution.

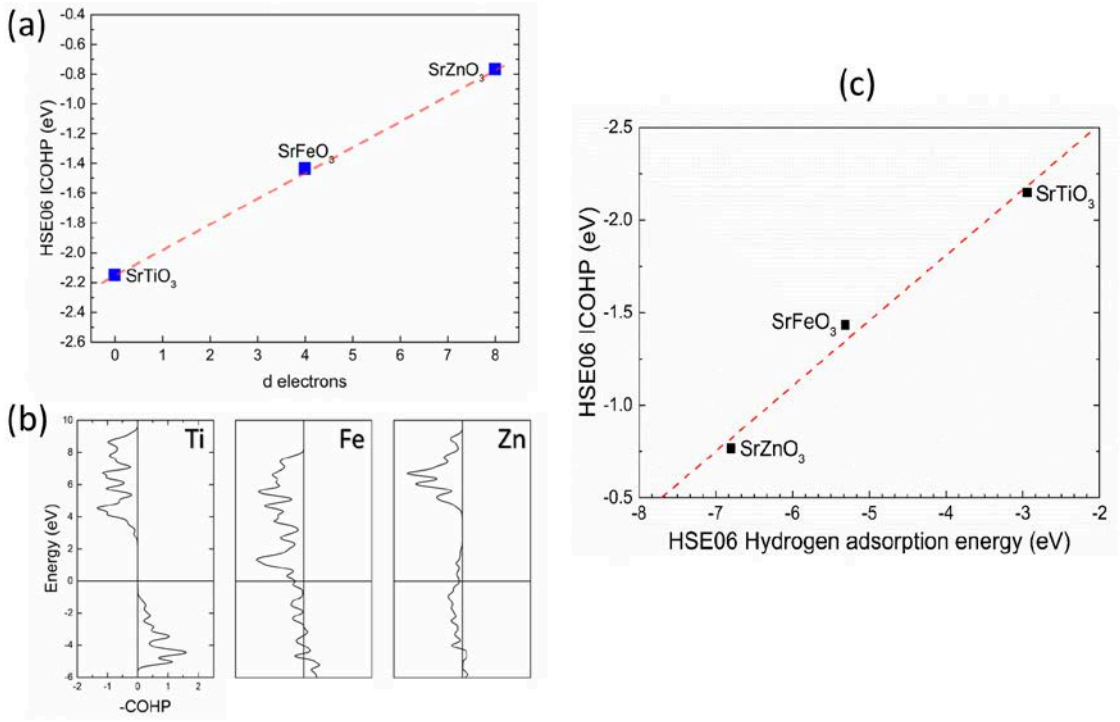

Figure S4.3.1: DFT-HSE06 results for $SrZnO_3$, $SrFeO_3$, and $SrTiO_3$: (a) averaged integrated crystal orbital Hamilton populations (ICOHP) of the metal-oxygen (M-O) bonds as a function of the number of d-electrons; (b) crystal-orbital Hamilton population (COHP) versus energy; (c) correlation between bulk ICOHP and hydrogen adsorption energy on the lattice oxygen.

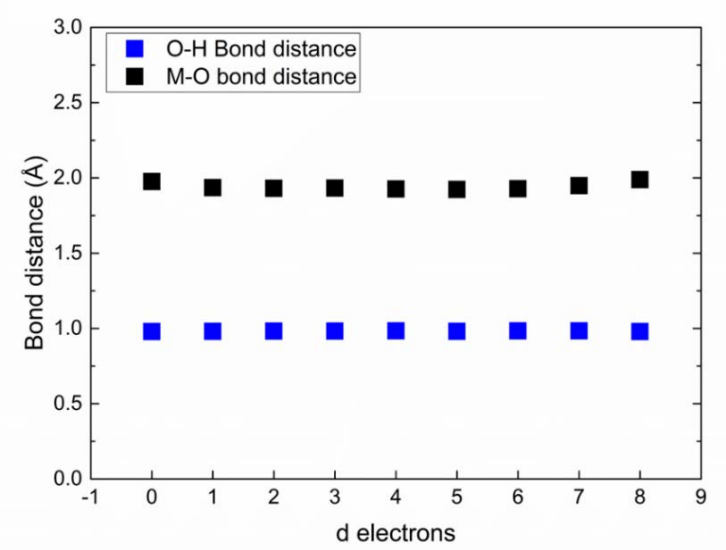

Figure S4.3.2: M-O and O-H distances as a function of d electrons in $SrMO_3$(100) for M being 3d transition metals. M-O from the clean relaxed (100) surface before H adsorption; O-H from the relaxed structure after adsorption.

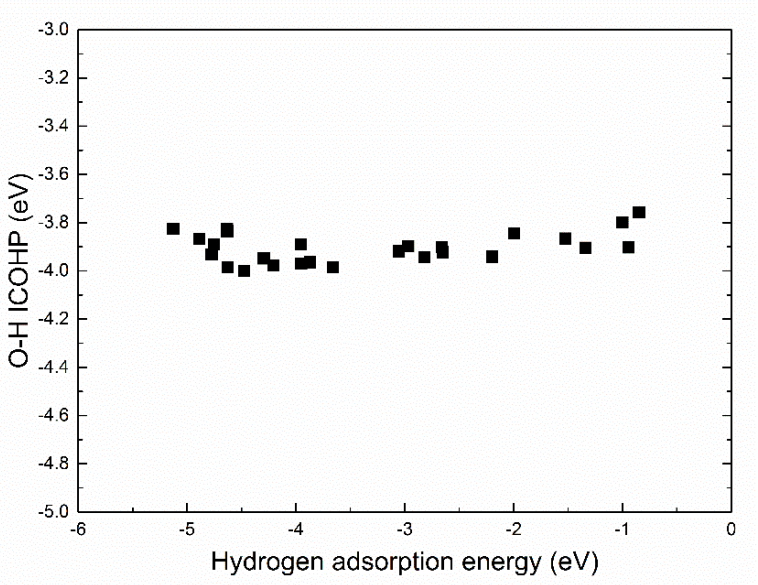

Figure S4.3.3: Scatterplot of O-H ICOHP versus hydrogen adsorption energy.

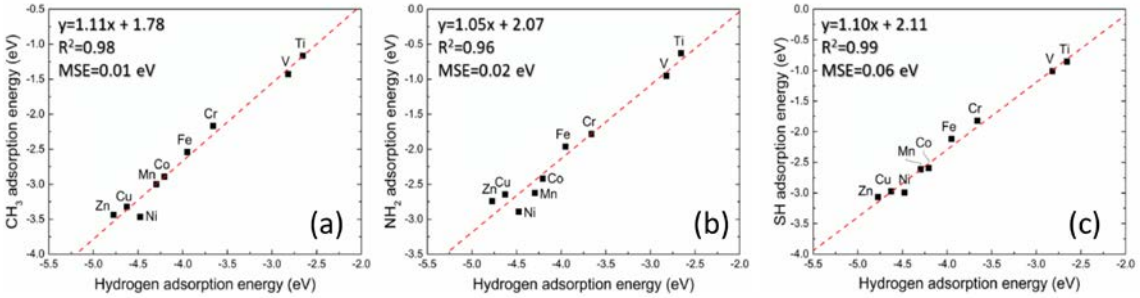

Figure S4.3.4: Linear correlations between adsorption energies of other radical adsorbates and hydrogen adsorption energy on the $SrMO_3$(100)-B termination surfaces: (a) CH_3; (b) NH_2; (c) SH. The red dotted lines denote the linear best-fit lines.

Table S4.3.1. Bader charge distribution from hydrogen adsorption on selected $SrMO_3$(100) surfaces

Surface	H charge	e^- transferred to O	e^- transferred to M
$SrTiO_3$	+0.608	0.112	0.027
$SrFeO_3$	+0.610	0.197	0.017
$SrZnO_3$	+0.591	0.285	0.011

References

(1) Kresse, G.; Furthmuller, J. Efficiency of Ab-Initio Total Energy Calculations for Metals and Semiconductors Using a Plane-Wave Basis Set. *Comput. Mater. Sci.* **1996,** *6*, 15-50.

(2) Kresse, G.; Furthmuller, J. Efficient Iterative Schemes for Ab Initio Total-Energy Calculations Using a Plane-Wave Basis Set. *Phys. Rev. B* **1996,** *54*, 11169-11186.

(3) Perdew, J. P.; Burke, K.; Ernzerhof, M. Generalized Gradient Approximation Made Simple. *Phys. Rev. Lett.* **1996,** *77*, 3865-3868.

(4) Krukau, A. V.; Vydrov, O. A.; Izmaylov, A. F.; Scuseria, G. E. Influence of the Exchange Screening Parameter on the Performance of Screened Hybrid Functionals. *J. Chem. Phys.* **2006,** *125*, 224106.

(5) Blöchl, P. E. Projector Augmented-Wave Method. *Phys. Rev. B* **1994,** *50*, 17953-17979.

(6) Monkhorst, H. J.; Pack, J. D. Special Points for Brillouin-Zone Integrations. *Phys. Rev. B* **1976,** *13*, 5188-5192.

(7) Bader, R. F., *Atoms in Molecules: A Quantum Theory*. Clarendon Press: Oxford, U.K.: 1994.

(8) Henkelman, G.; Arnaldsson, A.; Jónsson, H. A Fast and Robust Algorithm for Bader Decomposition Of Charge Density. *Comput. Mater. Sci.* **2006,** *36*, 354-360.

(9) Momma, K.; Izumi, F. VESTA 3 for Three-Dimensional Visualization of Crystal, Volumetric and Morphology Data. *J. Appl. Crystallogr.* **2011,** *44*, 1272-1276.

(10) Deringer, V. L.; Tchougréeff, A. L.; Dronskowski, R. Crystal Orbital Hamilton Population (COHP) Analysis as Projected from Plane-Wave Basis Sets. *J. Phys. Chem. A* **2011,** *115*, 5461-5466.

(11) Dronskowski, R.; Bloechl, P. E. Crystal Orbital Hamilton Populations (COHP): Energy-Resolved Visualization of Chemical Bonding in Solids Based on Density-Functional Calculations. *J. Phys. Chem.* **1993,** *97*, 8617-8624.

(12) Maintz, S.; Deringer, V. L.; Tchougréeff, A. L.; Dronskowski, R. LOBSTER: A Tool to Extract Chemical Bonding from Plane‐Wave Based DFT. *J. Comput. Chem.* **2016,** *37*, 1030-1035.

5 Metal clusters

5.1 Exploring Structural Diversity and Fluxionality of Ptn (n=10-13) Clusters from First Principles

5.1.1 Abstract

Subnanometer transition metal clusters have been shown to possess catalytic activity that is size-dependent. It has been suggested that the fluxionality of these small clusters may be closely related to their catalytic activity. Here, we use basin-hopping global optimization with density functional theory (DFT) to study the energy landscape of Pt_n (n=10-13) clusters. We analyze a large set of local minima obtained from the DFT-based global optimization. We find that Pt_{10} is unique with respect to the other studied sizes in its structural landscape, which shows a single, distinct structural motif corresponding to a tetrahedral global minimum. In contrast, Pt_{11-13} all display characteristics of high fluxionality with the presence of multiple significantly differing structural features in the low-energy region, as characterized by coordination number, interatomic distances, and shape. These observations demonstrate the structural diversity and fluxionality of the subnanometer Pt clusters that will have important implications for catalysis.

5.1.2 Introduction

Subnanometer transition metal clusters are of considerable research interest in chemistry. These clusters often possess electronic, magnetic, and catalytic properties very different from those of the bulk. In particular, platinum surfaces and clusters are an industrially important catalyst for a wide variety of reactions, from electrochemistry such

as hydrogen evolution reaction (HER) and oxygen reduction reaction (ORR)[1-4] to catalytic activation of alkanes.[5] Recent shift from Pt surfaces to nanosystems focuses on 5-30 atoms, which show significantly increased activity.[1, 4-10]

For clusters in this size regime, small changes in the coordination and morphology can have a significant impact on properties such as molecular adsorption.[11-12] It is therefore necessary to explore the energy landscape of these small-sized clusters. Structure prediction through global optimization is one such method to obtain the global minimum structures through theoretical modeling. Many examples of global optimization algorithms exist in use today, including genetic algorithms, particle swarm optimization, and basin hopping.[13-15]

Key to the global optimization scheme is the method to evaluate energy and forces of the sampled structures for geometry optimization. Since global optimization needs to sample a significant number of possible structures, the evaluation of cluster energy can be expensive. While semi-empirical potentials are a popular and relatively inexpensive method, they are in general not accurate enough to describe the energy landscape of transition-metal nanoclusters. This necessitates the use of a more accurate method such as density functional theory (DFT).

Small Pt clusters of size 10 to 13 sit near the peak of catalytic activity for some reactions[5, 8-9, 16] and are of special interest because they are more amenable to DFT-based global minimization than the larger sizes. While locating stable Pt clusters in this size regime has been pursued before,[17-19] a detailed analysis of the structure diversity and its

correlation with the energy has not been demonstrated. Herein we will use DFT local minimization with basin hopping to explore the energy landscape of Pt subnanometer clusters. More importantly, we will take advantage of the large number of local minima obtained to investigate structure-energy relationships for these Pt clusters, thereby giving us a more fundamental understanding of their properties than the global minima alone.

5.1.3 Computational Method

First principles local optimization with DFT is used in conjunction with the global minimum search using basin hopping (BH).[20] The general scheme of basin-hopping global minima search for clusters has been described by Wales et al. with Lennard-Jones potentials,[15] and later applied using first principles methods such as DFT for a variety of transition metals.[13-14] Basin hopping is a Monte Carlo method which transforms the potential-energy landscape into steps of local minima: starting with an initial local minimum (E_0), all atoms are randomly displaced off their equilibrium positions and then the structure is locally optimized (E_1). A Metropolis sampling is then performed: the new structure is accepted when a randomly generated number, *n*, between 0 and 1 is less than the Boltzmann factor, $e^{-\Delta E/kT}$, where T is an artificial temperature to control the importance of $\Delta E = E_1 - E_0$. Then the sequence of random move, local minimization, and Metropolis sampling is repeated. In this work, the BH algorithm was used at a temperature of 7500 K for the Metropolis sampling, and the step size dynamically updated to maintain an acceptance ratio of 50%. A total of around 20000 Monte Carlo (MC) steps were performed, including five long parallel runs of 1000 steps each using different starting configurations

for each cluster size. For each MC step, the optimized configurations were then analyzed by calculating a variety of its structural properties.

The local optimization at each Monte Carlo step was interfaced with the Vienna Ab Initio Simulation Package (VASP)[21-22] using DFT in a cubic cell of 18 Å on each side. The Perdew-Burke-Erznerhof (PBE)[23] form of the generalized-gradient approximation (GGA) was chosen for electron exchange and correlation. The electron-core interaction was described using the projector-augmented wave method (PAW).[24-25] The Brillouin zone was sampled using the Γ point only. All calculations in this work were performed with spin polarization. After the putative global minimum was found, accurate calculations were performed using a higher energy cutoff of 400 eV for optimizations.

The binding energy of a cluster is calculated with the formula $E_b(n) = -[E(Pt_n)-nE(Pt_1)]/n$ where $E(Pt_n)$ is the energy of the cluster and $E(Pt_1)$ is the energy of the isolated Pt atom. Using DFT-PBE, we found the E_b of the Pt-Pt dimer to be 1.86 eV and the Pt-Pt distance to be 2.33 Å, in good agreement with previous theoretical[18, 26] and experimental[27] works. Prolateness/oblateness parameter η *is obtained from the formula* $\eta = (2I_b-I_a-I_c)/I_a$, where $I_a \geq I_b \geq I_c$ are the principal moments of inertia obtained by diagonalizing the moment of inertia tensor in Cartesian coordinates.[28] A negative value corresponds to an oblate spheroid and a positive value corresponds to a prolate spheroid; in a perfect sphere, $\eta = 0$. The variance of the cluster is simply $\sigma^2 = \Sigma(x_i-x_{com})^2/n$, where x_i is the coordinate of the i_{th} atom in the cluster and x_{com} is the position of the center of mass.

5.1.4 Results and discussion

5.1.4.1 Basin-hopping global optimization of Pt clusters.

Figure 1 shows an example of a DFT-BH run for Pt_{13}, starting from an icosahedral initial structure (Figure 1a) obtained from the Cambridge cluster database.[29] The global minimum (Figure 1b) was found surprisingly quickly in this particular run in only 20 steps, despite the structural difference between the initial and the global optimum. Other low-lying isomers are also displayed, including one at step 717 (Figure 1c) and step 803 (Figure 1d).

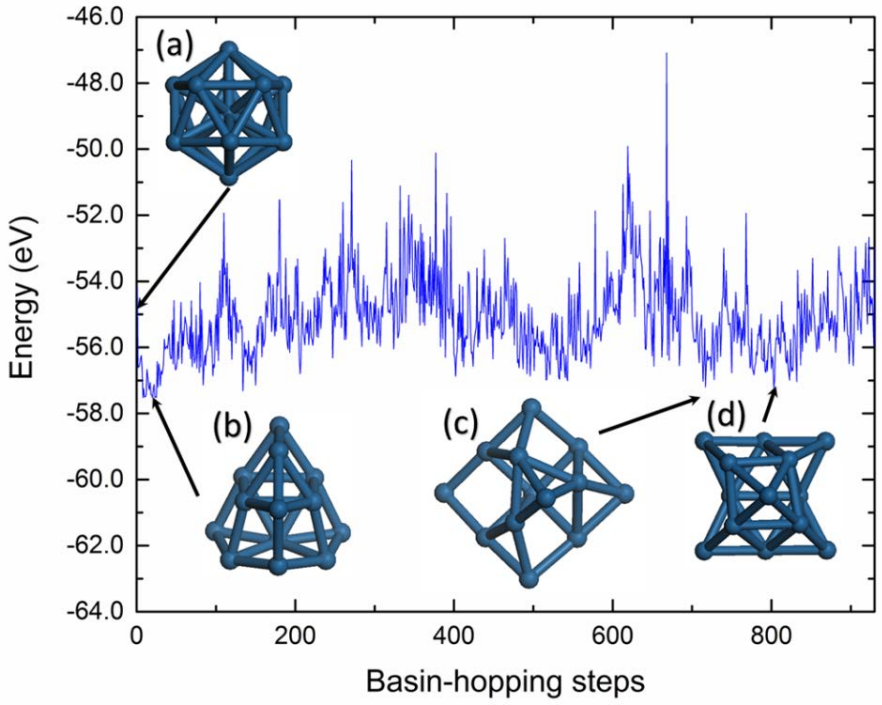

Figure 5.1.1 A DFT basin-hopping run for $Pt_{13.}$ The Pt_{13} icosahedron (a) was used as the starting structure for this example, and the global minimum was found in structure (b). Other low energy structures in this run (c and d) are also shown.

Similar DFT-BH runs were performed for all clusters from Pt_{10} to Pt_{13}, with each cluster size containing around 5000 Monte-Carlo steps. In all the cluster sizes, the global minimum was found in at least two separate parallel DFT-BH runs starting from different initial configurations. The structures of the putative global minima are shown in Figure 2. One can see that Pt_{10} has the highest symmetry with a tetrahedral geometry, and Pt_{11} has the lowest symmetry. Pt_{12} and Pt_{13} have similar geometry, with Pt_{13} having an additional atom attached to the side of the Pt_{12} structure. The features of these putative global minima are compared in Table 1.

It is evident that Pt_{10} is unique and can be considered a "magic cluster", given its high symmetry. This structure has been previously found by both semi-empirical methods and by other means of global optimization.[18-19] Furthermore, experimentally it has been suggested that Pt_{10} is a magic cluster[19, 30] with a significantly lower reactivity[30-32] than other clusters in this size regime. Meanwhile, we did not find any evidence that the n=11-13 sizes contained magic clusters. The putative global minimum structure for Pt_{13} was significantly lower in energy than the icosahedral geometry, and is in agreement with a recent structure search[26] which found the same global minimum structure in comparison with previously examined structural models.[26, 33-35] Same global minimum was also found for Pt_{12}.[26] Including spin-orbit coupling was found to have a minor impact (~ 0.01 eV) on the relative energy between low energy structures,[26, 36] so we did not consider it in the present work. The putative global minimum for Pt_{11} as a highly disordered geometry (Figure 2b) is, however, dissimilar from other proposed structures in the literature.[18-19]

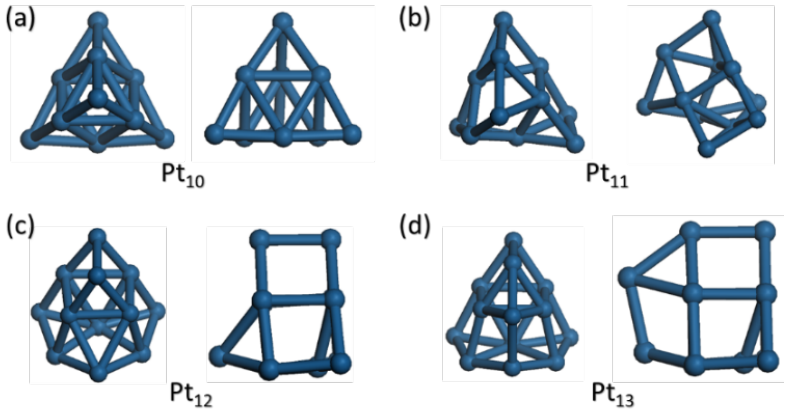

Figure 5.1.2 Putative global minima from DFT basin-hopping runs: (a) Pt_{10}; (b) Pt_{11}; (c) Pt_{12}; (d) Pt_{13}. Two different views are shown for each structure.

Table 5.1.1 Binding energy (E_b), minimum Pt-Pt distance (min. Pt-Pt), maximum Pt-Pt distance (max. Pt-Pt), average coordination number (avg. C.N.; Pt-Pt distance cutoff at 2.900 Å), Oblateness/Prolateness (O/P), and magnetic moment (mag. mom.) of the global minima of Pt_n (n=10-13).

Cluster Size	E_b (eV)	Min. Pt-Pt (Å)	Max. Pt-Pt (Å)	Avg. C.N.	O/P	Mag. Mom. (μ_B)
10	-3.70	2.534	5.08	4.80	-0.0020	8
11	-3.71	2.509	5.81	3.82	0.0931	2
12	-3.76	2.506	5.77	4.17	0.1028	2
13	-3.83	2.509	6.10	4.15	-0.0478	2

5.1.4.2 Coordination-energy correlation.

Although the global minima are important, it is equally interesting to examine the structure diversity of the isomers, especially those whose energies are close to that of the

global minimum. To analyze these structures, we first examined the coordination-energy correlation of the Pt clusters by looking at the average coordination number (that is, averaging the coordination numbers of all atoms in a cluster structure) for all the isomers explored along the DFT-BH steps. One would expect that a cluster with a higher average coordination number to be more stable, due to the greater number of stabilizing Pt-Pt interactions which would lower the energy of the cluster.

Figure 3 shows that there is a clear trend of decreasing energy or increasing stability with coordination, especially for n=10, suggesting that a higher coordination number indeed corresponds to more stable structures. However, when reaching the low energy region (right side of each panel in Figure 3), there is also a significant spread in the average coordination of up to one for the n=11-13 cases. In fact, the structure with the highest average coordination number is not necessarily the lowest energy structure. For example, while the highest average coordination number of the structures in the low energy region can reach over 5, the average coordination number of the lowest energy structures with the exception of n=10 is much lower than that (4.15 ~ 4.18 for n=11-13). This result has two important implications. First, it clearly shows that there is a general trend where a higher coordination number roughly corresponds to a lower energy structure, especially for Pt_{10} whose global minimum is highly symmetric and can be considered a magic cluster. Second, for clusters whose global minima are less symmetric (for example, n=11-13 in this study), low lying isomers near the global minimum can be very different in structure, given their large variation in the average coordination number. We will see further evidence for the fluxionality of these clusters in the following sections.

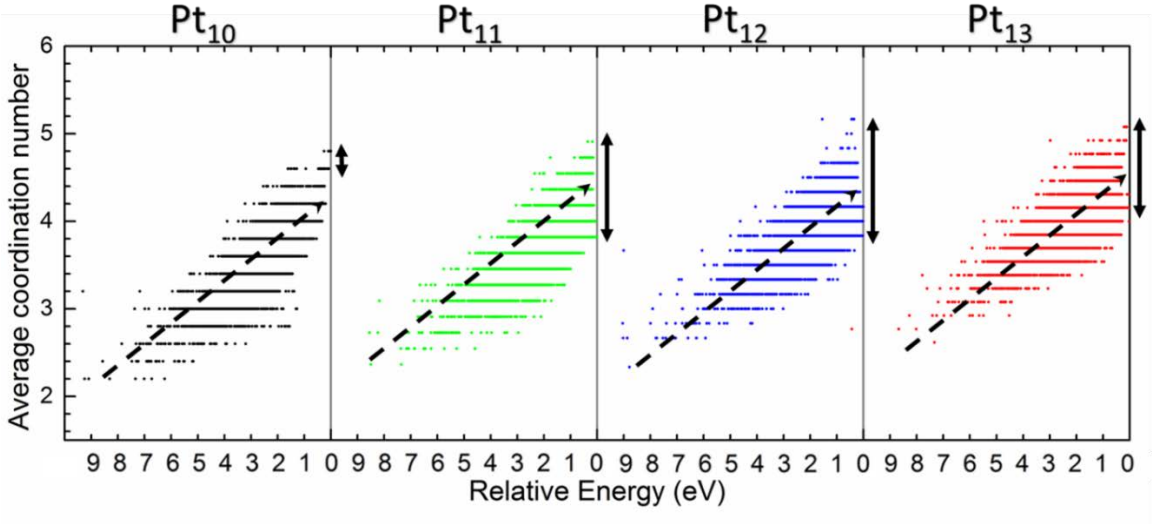

Figure 5.1.3 Average coordination number vs. energy for all local minima from the DFT basin-hopping run for each cluster size. The vertical line at zero relative energy on the right side of each panel denotes the lowest energy structure. Each dot represents a local minimum.

5.1.4.3 Distance-energy correlation.

Whereas coordination contains some chemical property by only selecting interactions that are within a bonding range, interatomic distances are a more geometric and fundamental parameter of a cluster. Figure 4 shows how Pt-Pt distance and energy are correlated. We find a rough correlation between higher minimum (or nearest neighbor) Pt-Pt distance and lower energy, where the distance increases towards the bulk value. We also find a correlation between lower maximum Pt-Pt distance and lower energy. So, low-energy structures tend to have geometries with high minimum Pt-Pt distance and low maximum Pt-Pt distance. The intuitive reasons behind this trend can be explained as follows. Clusters with a high minimum Pt-Pt distance tend to also have high coordination, as the Pt-Pt bond elongates from a Pt-Pt dimer with a single bond of around 2.3 Å to the

bulk length of 2.8 Å. Thus, it should follow that clusters with properties closer to the bulk should have a lower energy, with the bulk energy being the lowest. Meanwhile, clusters with a low maximum interatomic distance tend to describe more compact and better coordinated clusters, which should also be lower in energy than more diffuse and disorganized clusters.

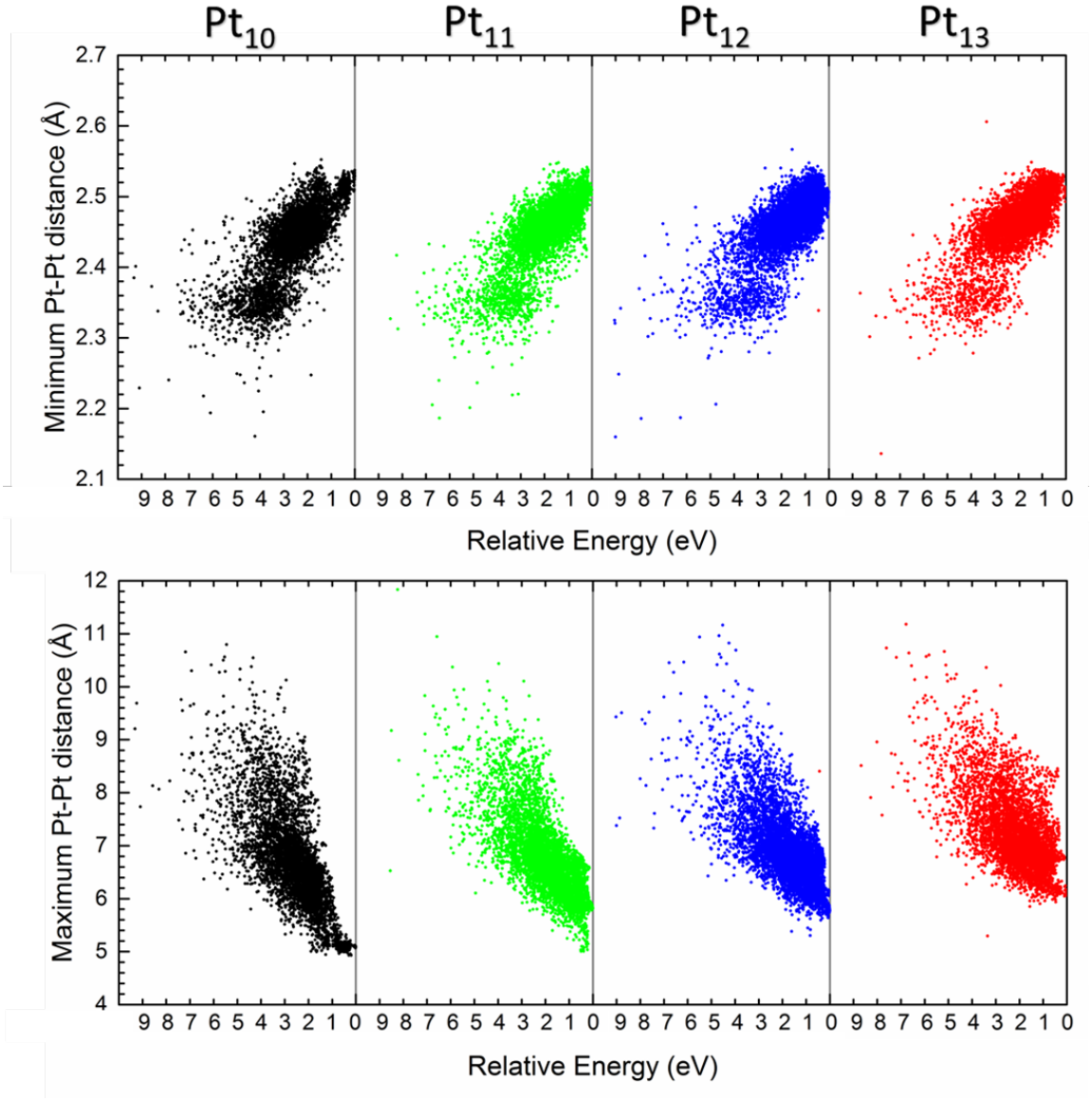

Figure 5.1.4 Upper panel: Minimum Pt-Pt distance vs energy for all local minima of Pt_n (n=10-14) from the DFT basin-hopping runs. Lower panel: Maximum Pt-Pt distance vs energy for all local minima of Pt_n (n=10-14) the DFT basin-hopping runs. Each dot represents a local minimum.

Examining the low-lying structures (those close to the zero-energy line on the right of each panel in Figure 4), we found that the fluxionality of the non-magic clusters (Pt_{11-13})

versus the magic Pt_{10} cluster is remarkably pronounced. For both the minimum and maximum interatomic distances, Pt_{10} has a much narrower spread, with the low energy structures confined to minimum Pt-Pt distances of 2.52-2.54 Å and maximum Pt-Pt distances of 5.0-5.2 Å, whereas the other size clusters have a much larger spread and multiple points nearly intersecting the global minimum energy (the vertical lines) in Figure 4; this is especially pronounced for the maximum Pt-Pt distance which shows a spread over 2 Å for Pt_{13}. Hence, the difference in structural diversity of the magic clusters and the fluxional non-magic clusters becomes visually obvious.

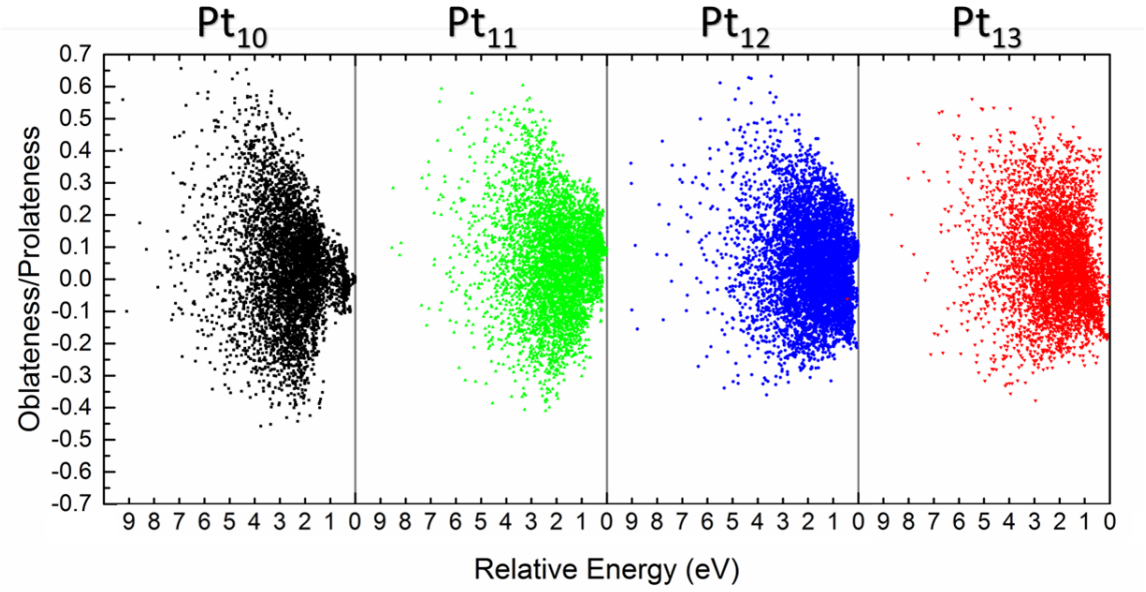

Figure 5.1.5 Oblateness/Prolateness (O/P or η) vs energy for all local minima of Pt_n (n=10-14) from the DFT basin-hopping runs. Positive η, oblate; negative η, prolate; η=0, spherical like. The vertical line at zero relative energy on the right side of each panel denotes the lowest energy structures. Each dot represents a local minimum.

5.1.4.4 Shape-energy correlation.

To further differentiate the shapes of these clusters, we can look at η, a measure of the prolateness/oblateness of the cluster spheroid in Figure 5. Clusters that differ in η can be expected to be structurally inequivalent. We can clearly see that the low-lying isomers of Pt_{10} have very similar shapes close to the global minimum, with an η of close to zero, and the spread in cluster shape sharply decreasing toward the vertical line at zero relative energy. Whereas for n=11-13, we can see points nearly intersecting the zero-relative-energy line at multiple points on the graph, sometimes with significantly with different η values. This is further evidence for the fluxionality of non-magic Pt clusters (Pt_{11-13}) where there may exist many different structural conformations of a cluster with similarly low energies.

5.1.4.5 Structure analysis of Pt_{12}

We take an in-depth look at the low-lying isomers by selecting the non-magic Pt_{12} as a case study. Unlike Pt_{10}, Pt_{12} is an experimentally reactive cluster[8, 31] whose fluxionality may explain the significantly different catalytic performance when compared to Pt_{10}. In Figure 6a, we can see multiple motifs with similarly low energies by selecting structures with different η (Oblateness/Prolateness). These different low-energy structures can be symmetric or asymmetric, and are structurally unique. In Figure 6b, we see that both structures with high and low average coordination number can be low in energy, but the lowest energy structure falls somewhere in between the two displayed structures. In Figure 6c, we look at the variance of the cluster, calculated as the variance of the atomic distance

from the center of mass of the cluster. This descriptor can be understood as a combined effect of the minimum and maximum Pt-Pt distances shown in Figure 4. A high variance corresponds to a diffuse cluster with atoms spaced out from each other, whereas a low variance corresponds to a cluster whose atoms are very tightly bound, so variance offers a useful single value to describe the diffuseness of the structure. We see that lower energy clusters tend towards the lower variance structures, where the cluster is closer to the center of mass and is correspondingly less diffuse. However, we can also discern an “island” of stability as highlighted by Figure 6c(ii) where the structure is flatter and has a correspondingly higher variance, but is only 0.21 eV higher in energy than the global minimum.

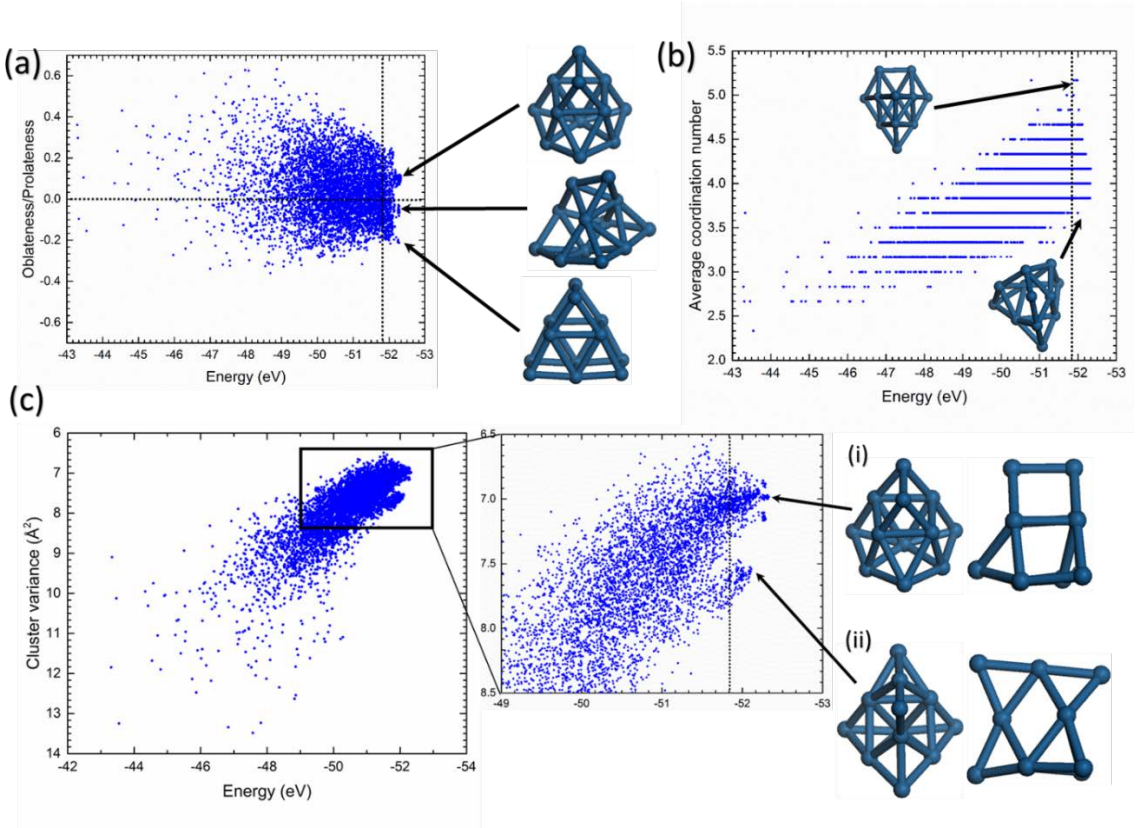

Figure 5.1.6 An in-depth look of the structural fluxionality of Pt_{12}: (a) Oblateness/Prolateness (O/P) vs energy; (b) average coordination number vs energy; (c) cluster variance vs energy. The dashed vertical lines separate clusters within 0.5 eV from the global minimum. Each dot represents a local minimum.

5.1.4.6 Implications.

This work represents an in-depth investigation into the structure-energy relationships of subnanometer Pt clusters by taking advantage of the large number of basin-hopping local minima in the configuration space from DFT local minimization**.** In the study of metal clusters, especially ones which exhibit high degrees of fluxionality, it is often not sufficient to only study several putative global minima, but a much broader configurational

region is needed to have a better view of the energy landscape**.** We found a high degree of fluxionality for the Pt_{11-13} clusters from the large spread in values of the structural descriptors of the sampled low-energy structures from bond distances to coordination to shape. This high degree of fluxionality may provide insights into the high catalytic activity of small Pt clusters for a variety of reactions. The high fluxionality and low symmetry of these clusters may allow for the better bonding and accommodation of adsorbates to the surface. This study also highlights the importance of sufficiently sampling the configuration space of low energy structures for energetically relevant configurations that may still be structurally diverse, instead of a single global minimum.

Pt_{10} is much less fluxional than the other sizes due to its magic nature. This is probably also true for Pd_{10} and Au_{10}, but not for Ag_{10}, since Ag_{10} has been found not to be a magic cluster,[37] while Au_{10} has a planar geometry.[38] The clear differences in fluxionality in the studied Pt clusters are a promising result towards the future investigation of larger cluster sizes, including the possible Pt magic clusters of n=14 and n=20 which have been prepared in a dendrimer recently.[10] While we have studied the thermodynamic stability of the global and low-lying minima for Pt clusters, the kinetics of the system are still relatively uncharacterized. Future work regarding the kinetics of cluster fluxionality can be carried out by mapping out transition states connecting different minima or using molecular dynamics to explore the atomistic processes of basin hopping under realistic temperatures.

5.1.5 Conclusion

Using DFT-based basin hopping for global minimization, we explored both the most stable structures and the structure diversity of Pt_n (n=10-13) clusters. We confirmed that Pt_{10} is a magic cluster with a global minimum of tetrahedral geometry, but found that the other clusters have less symmetric global minima. By analyzing all the local-minimum structures from the basin-hopping searches, we examined the relationships between coordination number, interatomic distances, and cluster shape versus cluster energy. While in general qualitative trends could be drawn from these relationships, we found a significant spread in these geometric quantities with respect to energy. In particular, many low-lying isomers could be found for Pt_{11-13} which are structurally distinct but energetically similar, suggesting a high degree of fluxionality for clusters of this size. This fluxionality could be important in catalysis by subnanometer Pt clusters.

References

(1) Yamamoto, K.; Imaoka, T.; Chun, W. J.; Enoki, O.; Katoh, H.; Takenaga, M.; Sonoi, A. Size-specific catalytic activity of platinum clusters enhances oxygen reduction reactions. *Nature Chem.* **2009,** *1*, 397-402.

(2) Guo, S.; Zhang, S.; Sun, S. Tuning nanoparticle catalysis for the oxygen reduction reaction. *Angew. Chem. Int. Ed.* **2013,** *52*, 8526-8544.

(3) Schweinberger, F. F.; Berr, M. J.; Döblinger, M.; Wolff, C.; Sanwald, K. E.; Crampton, A. S.; Ridge, C. J.; Jäckel, F.; Feldmann, J.; Tschurl, M. Cluster size effects in the photocatalytic hydrogen evolution reaction. *J. Am. Chem. Soc.* **2013,** *135*, 13262-13265.

(4) Nesselberger, M.; Roefzaad, M.; Hamou, R. F.; Biedermann, P. U.; Schweinberger, F. F.; Kunz, S.; Schloegl, K.; Wiberg, G. K.; Ashton, S.; Heiz, U. The effect of particle proximity on the oxygen reduction rate of size-selected platinum clusters. *Nature Mater.* **2013,** *12*, 919-924.

(5) Vajda, S.; Pellin, M. J.; Greeley, J. P.; Marshall, C. L.; Curtiss, L. A.; Ballentine, G. A.; Elam, J. W.; Catillon-Mucherie, S.; Redfern, P. C.; Mehmood, F.; Zapol, P. Subnanometre platinum clusters as highly active and selective catalysts for the oxidative dehydrogenation of propane. *Nature Mater.* **2009,** *8*, 213-6.

(6) Tyo, E. C.; Vajda, S. Catalysis by clusters with precise numbers of atoms. *Nat. Nanotechnol.* **2015,** *10*, 577-588.

(7) Vajda, S.; White, M. G. Catalysis Applications of Size-Selected Cluster Deposition. *ACS Catal.* **2015,** *5*, 7152-7176.

(8) Imaoka, T.; Kitazawa, H.; Chun, W.-J.; Omura, S.; Albrecht, K.; Yamamoto, K. Magic number Pt_{13} and misshapen Pt_{12} clusters: which one is the better catalyst? *J. Am. Chem. Soc.* **2013,** *135*, 13089-13095.

(9) Heiz, U.; Sanchez, A.; Abbet, S.; Schneider, W.-D. Catalytic oxidation of carbon monoxide on monodispersed platinum clusters: each atom counts. *J. Am. Chem. Soc.* **1999,** *121*, 3214-3217.

(10) Imaoka, T.; Kitazawa, H.; Chun, W. J.; Yamamoto, K. Finding the Most Catalytically Active Platinum Clusters With Low Atomicity. *Angew. Chem. Int. Ed.* **2015,** *54*, 9810-9815.

(11) Calle-Vallejo, F.; Martínez, J. I.; García-Lastra, J. M.; Sautet, P.; Loffreda, D. Fast Prediction of Adsorption Properties for Platinum Nanocatalysts with Generalized Coordination Numbers. *Angew. Chem. Int. Ed.* **2014,** *53*, 8316-8319.

(12) Calle-Vallejo, F.; Tymoczko, J.; Colic, V.; Vu, Q. H.; Pohl, M. D.; Morgenstern, K.; Loffreda, D.; Sautet, P.; Schuhmann, W.; Bandarenka, A. S. Finding optimal surface sites on heterogeneous catalysts by counting nearest neighbors. *Science* **2015,** *350*, 185-189.

(13) Jiang, D.-e.; Walter, M. Au_{40}: A large tetrahedral magic cluster. *Phys. Rev. B* **2011,** *84*, 193402.

(14) Priest, C.; Tang, Q.; Jiang, D.-e. Structural Evolution of Tc_n (n= 4–20) Clusters from First-Principles Global Minimization. *J. Phys. Chem. A* **2015,** *119*, 8892-8897.

(15) Wales, D. J.; Doye, J. P. Global optimization by basin-hopping and the lowest energy structures of Lennard-Jones clusters containing up to 110 atoms. *J. Phys. Chem. A* **1997,** *101*, 5111-5116.

(16) Watanabe, Y.; Wu, X.; Hirata, H.; Isomura, N. Size-dependent catalytic activity and geometries of size-selected Pt clusters on TiO_2 (110) surfaces. *Catal. Sci. Technol.* **2011,** *1*, 1490-1495.

(17) Nie, A.; Wu, J.; Zhou, C.; Yao, S.; Luo, C.; Forrey, R. C.; Cheng, H. Structural evolution of subnano platinum clusters. *Int. J. Quantum Chem* **2007,** *107*, 219-224.

(18) Kumar, V.; Kawazoe, Y. Evolution of atomic and electronic structure of Pt clusters: planar, layered, pyramidal, cage, cubic, and octahedral growth. *Phys. Rev. B* **2008,** *77*, 205418.

(19) Chaves, A. S.; Rondina, G. G.; Piotrowski, M. J.; Tereshchuk, P.; Da Silva, J. L. The role of charge states in the atomic structure of Cu_n and Pt_n (n= 2–14 atoms) clusters: A DFT investigation. *J. Phys. Chem. A* **2014,** *118*, 10813-10821.

(20) Jiang, D. e.; Walter, M.; Dai, S. Gold Sulfide Nanoclusters: A Unique Core-In-Cage Structure. *Chemistry–A European Journal* **2010,** *16*, 4999-5003.

(21) Kresse, G.; Furthmuller, J. Efficient Iterative Schemes for Ab Initio Total-Energy Calculations Using a Plane-Wave Basis Set. *Phys. Rev. B* **1996,** *54*, 11169-11186.

(22) Kresse, G.; Furthmuller, J. Efficiency of Ab-Initio Total Energy Calculations for Metals and Semiconductors Using a Plane-Wave Basis Set. *Comput. Mater. Sci.* **1996,** *6*, 15-50.

(23) Perdew, J. P.; Burke, K.; Ernzerhof, M. Generalized Gradient Approximation Made Simple. *Phys. Rev. Lett.* **1996,** *77*, 3865-3868.

(24) Kresse, G.; Joubert, D. From Ultrasoft Pseudopotentials to the Projector Augmented-Wave Method. *Phys. Rev. B* **1999,** *59*, 1758.

(25) Blöchl, P. E. Projector Augmented-Wave Method. *Phys. Rev. B* **1994,** *50*, 17953-17979.

(26) Rodríguez-Kessler, P.; Rodríguez-Domínguez, A. Size and structure effects of PtN (N= 12− 13) clusters for the oxygen reduction reaction: First-principles calculations. *J. Chem. Phys.* **2015,** *143*, 184312.

(27) Gupta, S. K.; Nappi, B. M.; Gingerich, K. A. Mass spectrometric study of the stabilities of the gaseous molecules diatomic platinum and platinum-yttrium. *Inorg. Chem.* **1981,** *20*, 966-969.

(28) Cheng, J.; Fournier, R. Structural optimization of atomic clusters by tabu search in descriptor space. *Theor. Chem. Acc.* **2004,** *112*, 7-15.

(29) D. J. Wales, J. P. K. D., A. Dullweber, M. P. Hodges, F. Y. Naumkin F. Calvo, J. Hernández-Rojas and T. F. Middleton The Cambridge Cluster Database. http://www-wales.ch.cam.ac.uk/CCD.html.

(30) Adlhart, C.; Uggerud, E. Reactions of platinum clusters $Pt_n^{\pm}$, n= 1–21, with CH_4: to react or not to react. *Chem. Commun.* **2006**, 2581-2582.

(31) Trevor, D.; Cox, D.; Kaldor, A. Methane activation on unsupported platinum clusters. *J. Am. Chem. Soc.* **1990,** *112*, 3742-3749.

(32) Balteanu, I.; Balaj, O. P.; Beyer, M. K.; Bondybey, V. E. Reactions of platinum clusters 195 $Pt_n^{\pm}$, n= 1–24, with N_2O studied with isotopically enriched platinum. *Phys. Chem. Chem. Phys.* **2004,** *6*, 2910-2913.

(33) Piotrowski, M. J.; Piquini, P.; Da Silva, J. L. Density functional theory investigation of 3 d, 4 d, and 5 d 13-atom metal clusters. *Phys. Rev. B* **2010,** *81*, 155446.

(34) Chou, J. P.; Hsing, C. R.; Wei, C. M.; Cheng, C.; Chang, C. M. Ab initio random structure search for 13-atom clusters of fcc elements. *J Phys Condens Matter* **2013,** *25*, 125305.

(35) Bunău, O.; Bartolomé, J.; Bartolomé, F.; Garcia, L. Large orbital magnetic moment in Pt_{13} clusters. *J. Phys.: Condens. Matter* **2014,** *26*, 196006.

(36) Błoński, P.; Hafner, J. Magneto-structural properties and magnetic anisotropy of small transition-metal clusters: a first-principles study. *J. Phys.: Condens. Matter* **2011,** *23*, 136001.

(37) Pereiro, M.; Baldomir, D.; Arias, J. Unexpected magnetism of small silver clusters. *Phys. Rev. A* **2007,** *75*, 063204.

(38) Häkkinen, H.; Yoon, B.; Landman, U.; Li, X.; Zhai, H.-J.; Wang, L.-S. On the Electronic and Atomic Structures of Small Au N-(N= 4-14) Clusters: A Photoelectron Spectroscopy and Density-Functional Study. *J. Phys. Chem. A* **2003,** *107,* 6168-6175.

Supplementary Information

Coordinates for the putative global minimum in Figure 5.2.2:

10
Pt10
Pt 8.001540 9.226260 10.649520
Pt 8.456759 10.497420 6.323580
Pt 7.332660 8.952120 7.996861
Pt 10.679399 9.073979 10.016640
Pt 9.997560 8.752501 7.349580
Pt 8.929620 7.059240 9.249300
Pt 9.077220 10.941120 8.755380
Pt 6.467040 7.376400 9.785521
Pt 11.384460 7.061940 8.642879
Pt 9.673920 11.059020 11.230740

11
Pt11
Pt 9.279000 8.035740 10.140659
Pt 11.822399 10.585259 9.102600
Pt 10.109879 10.263420 11.015460
Pt 7.764480 9.426061 11.724300
Pt 10.783620 8.474401 8.126100
Pt 8.277480 6.004800 9.037260
Pt 7.800660 8.250480 7.889940
Pt 7.407900 10.558260 6.912000
Pt 6.924240 10.116540 9.418320
Pt 9.553141 6.609780 6.962760
Pt 9.277200 10.675260 8.670240

12
Pt12
Pt 8.665560 7.763220 6.090660
Pt 8.291700 6.464340 10.941481
Pt 10.095480 8.301781 11.283300
Pt 8.614440 6.972120 8.485200
Pt 7.422300 9.347940 7.603380
Pt 7.838460 8.927999 10.348921
Pt 8.568720 11.324880 10.118880
Pt 10.866600 8.938260 6.382440
Pt 11.026800 10.568340 10.454220
Pt 10.757880 8.291340 8.851680
Pt 9.674100 10.469521 8.039340
Pt 6.177960 10.630080 9.400320

13

Pt13
Pt 11.948580 9.295560 8.847900
Pt 7.190820 6.237720 8.161560
Pt 7.169400 8.522280 9.368820
Pt 11.463840 7.495380 10.596241
Pt 9.408239 6.745680 9.282060
Pt 9.809460 10.431900 9.519300
Pt 8.190900 10.914660 7.113060
Pt 7.362180 11.028780 9.550260
Pt 9.294479 8.673480 11.250540
Pt 10.827180 10.998000 7.147080
Pt 7.481520 8.452260 6.858180
Pt 9.871740 8.569800 7.622640
Pt 6.981660 9.634501 11.682361

6. Reactions on single atoms

6.1 Low-temperature activation of methane on anchored single atoms: descriptor and prediction

6.1.1 Abstract

Catalytic transformation of methane under mild conditions remains a grand challenge. Fundamental understanding of C-H activation of methane is crucial for designing catalyst for utilization of methane at low temperature. Recent experiments show that strong methane chemisorption on oxides of precious metals leads to facile C-H activation. However, only very few such oxides are capable (for example, IrO_2 and PdO). Here we show for the first time that strong methane chemisorption and facile C-H activation can be accomplished by single transition-metal atoms anchored on TiO_2, some of which are even better than IrO_2. Using methane adsorption energy as a descriptor, we screened over 30 transition-metal single atoms doped on TiO_2 for chemisorption of methane by replacing a surface Ti atom with a single atom of a transition metal. It is found that the adsorption energies of methane on single atom of Pd, Rh, Os, Ir, and Pt doped on rutile TiO_2(110) are higher than or similar to rutile IrO_2(110), a benchmark for chemisorption of methane on transition oxides. Electronic structure analysis uncovered orbital overlap and mixing between methane and the single atom, as well as significant localization of charge between the molecule and the surface, demonstrating chemical bonding of CH_4 to doped single atoms. Facile C-H dissociation has been found on the

single-atom sites with the transition state energies lower than desorption energies. Our computational studies predict that Pd, Rh, Os, Ir, and Pt single atoms on rutile TiO_2(110) can activate C-H of methane at a temperature lower than 25 ^oC.

6.1.2 Introduction

Methane is an inexpensive energy resource. Hydraulic fracturing supplies much of this earth-abundant source from shale, which makes conversion of methane to easily transportable, value-added chemicals or fuels is of particular economic and scientific significance.[1-3] The existing catalytic processes in industry employ mainly partial oxidation by O_2 and reforming through CO_2 or H_2O, which are performed at high temperatures. From a thermodynamic point of view, it is feasible to activate methane and transform it to chemical and fuel feedstock at relatively low temperature (< 200^oC). A kinetically favorable activation of C-H of methane is important for the realization of the catalytic transformation of methane at relatively low temperature. Hutchings et al. have pioneered the experimental exploration of anchored cations in zeolite and demonstrated activation of C-H on Cu and Fe anchored in microporous aluminosilicate.[4-5]

Transition metal oxides have been extensively explored for catalytic methane conversion. There are two primary pathways for the cleavage of the C-H bond on metal oxides:[6-9] the heterolytic pathway by which the C-H bond is cleaved over a metal-oxygen pair and methyl is stabilized on a metal site; the homolytic pathway by which the C-H bond is cleaved directly over a surface oxygen to form a radical-like intermediate.[10-11] The homolytic H abstraction pathway is predicted to occur with lower barriers for redox-facile oxides,[7, 12] consistent with density functional theory (DFT) calculations.[13-16] Further use of

easily computable quantities such as lattice oxygen coordination[17] and hydrogen adsorption energy[17-20] as descriptors enables quick screening of metal-oxide active sites for the best homolytic C-H activation ability.

Instead of homolytic cleavage which usually occurs at high temperature, the heterolytic pathway has recently gained interest for the chemisorption and low-temperature activation of methane. Ni and Co supported on CeO_2[21-23] have been demonstrated to be promising methane activation and dry reforming catalysts via the low C-H activation barriers from a chemisorbed methane complex. Weaver et al. reported the first case of experimentally observed low-temperature methane C-H activation on rutile IrO_2 at 150K,[24] supported by earlier DFT calculations showing methane chemisorption and an lower activation energy for surface C-H dissociation than methane desorption.[25]

Single-atom catalysts have attracted great attention recently and can be potentially useful for methane activation. They usually comprise noble-metal single atoms on an oxide support.[26-28] TiO_2 has been used as a support to anchor single atom and played a significant role in single atom catalysis, particularly in photocatalysis and CO oxidation.[29-32] Unmodified TiO_2 is not active for methane activation, and methane only weakly interacts to it.[33] Surface doping of guest cation could dramatically change electronic state of the guest cations since doping typically provides a different chemical and coordination environment for guest cations.[19, 34-37] Depending on the dopant and the synthesis method, the dopant may prefer to be situated in the cationic vacancies.[26, 38-39]

The capability of IrO_2 to activate methane at low temperatures and the idea of using single-atom catalysts for methane activation inspired us to propose the use of methane

adsorption energy as a descriptor to screen single-atom systems that have similar local surface structures to IrO_2. To this end, we use first principles density functional theory to test all d-block single atoms substitutionally situated in a common oxide support, TiO_2 (especially the rutile phase in analogue to IrO_2), and then examine and analyze their propensity for methane adsorption and dissociation.

6.1.3 Methods

The density functional theory (DFT) calculations were performed with the Vienna ab initio Simulation Package (VASP).[40-41] The on-site Coulomb interaction was included with the DFT+U method by Dudarev, et al.[42] in VASP using a Hubbard parameter U = 3 eV for the Ti atom, as demonstrated to perform well in previous studies of TiO_2.[43-44] The Perdew-Burke-Ernzerhof (PBE)[45] functional form of generalized-gradient approximation (GGA) was used for electron exchange and correlation energies. Additional validation at the PBE-D3, SCAN, and HSE06 levels was also performed as described in the main text. All calculations were performed with spin polarization. The projector-augmented wave method was used to describe the electron-core interaction.[40, 46] A kinetic energy cutoff of 450 eV was used for the plane waves. The Brillouin zone was sampled with the Monkhorst-Pack scheme of a 3×2×1 k-point mesh.[47] A vacuum layer of 15 Å was added for the surface slabs along the z-direction; the slab contains a total of four layers, with the bottom two layers fixed in their bulk positions.

The methane absorption energy (E_{ads}) is calculated with the equation $E_{ads} = E_{surface+CH4} - (E_{perfect\text{-}surface} + E_{CH4})$ where $E_{surface+CH4}$ is the energy of the surface slab with a methane. The energies of E_{CH4} was computed by placing the adsorbate in a cubic cell with a 15 Å

wide vacuum in each direction. Transition states (TS) were found with the nudged elastic band (NEB)[48] and the dimer method[49] implemented in the VASP-VTST package using a force convergence criterion of 0.05 eV/Å. To compute the free energy for the profile of methane activation on Pt-TiO_2, the zero-point energy (ZPE) and entropy of the adsorbed species were obtained from DFT vibrational frequencies, while the JANAF tables were referenced for gas phase methane. The change in ZPE for Pt-TiO_2 for adsorption was found to be less than 0.04 eV and omitted for the other screened elements. Charge densities and isosurfaces were visualized using the VESTA program.[50]

To calculate the occupancies of the molecular bonds of methane, the periodic natural bond orbital (NBO) analysis implemented by Schmidt et al. was used.[51] The plane wave basis from VASP is projected onto slightly modified Gaussian-type def2-SVP basis sets.[52] To avoid numerical instabilities due to diffuse orbitals in the Gaussian basis sets,[53] orbitals with exponents lower than 0.1 were simply truncated for the metals; despite this, the atomic orbitals of the methane molecule remained well represented.

6.1.4 Results and Discussion

6.1.4.1 Geometry and energies of chemisorbed methane on M-TiO_2

We chose TiO_2 anatase (101) and rutile (110), the two most commonly studied facets of TiO_2, to study the effect of single-atom sites on methane adsorption. First, the popular DFT-PBE method was used, while validation with more advanced functionals will be discussed later. On both surfaces, the surface single-atom or M_1 site is coordinated to four surface oxygen and one subsurface oxygen. Binding energies for select dopants to the Ti

vacancy can be found in Table S1, which are lower in energy than for adsorption in the O vacancy and ontop the pristine surface (Figure S1). Furthermore, the diffusion of the metal dopant out of the cationic vacancy shows high barriers and is endothermic in energy (Figure S2). We screened single atoms of all transition metal elements doped on TiO_2 and found that methane adsorption is stronger on the single-atom site on the rutile (110) surface than on the anatase (101) surface (see Figure S3 and Table S2 in Electronic Supplementary Information for the comparison). More important, we have identified guest metal elements whose cations exhibit strong chemisorption of methane on M_1-rutile-TiO_2 (110) systems, which is the focus of the present work. Figure 1 shows the local coordination of the M_1-rutile-TiO_2 (110) system and a typical geometry of a chemisorbed CH_4 on it. One can see that CH_4 is located above the single atom (M_1) and between two bridging oxygen sites (O_a and O_b). The molecule slightly tilts on one side, with one H atom pointing more downwards (denoted as H_a).

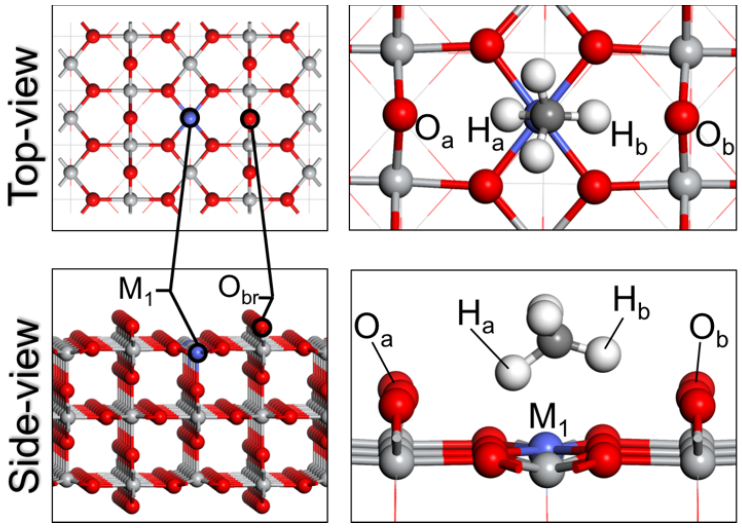

Figure 6.1.1 Structural representations of the single-atom site, M_1 (blue), doped on rutile TiO_2 (110) surface (left) and CH_4 adsorption on the site (right). Ti, grey; O, red; C, dark grey; H, white.

Figure 2 shows adsorption energy of CH_4 for all the d-block transition metal single atoms on the rutile TiO_2(110) surface (a heatmap on the periodic table is provided in Figure S4 and the values are given in Table S3). One can see that 3d metals all have weak CH_4 adsorption, because their d orbitals are too contracted; among the 4d metals, Pd and Rh have the strongest adsorption; among the 5d metals, Re, Os, Ir, and Pt have larger adsorption energy than Pd and Rh. If one uses methane adsorption on rutile IrO_2 (110) as a benchmark (-0.36 eV; green line in Figure 2), one can see that Os, Ir and Pt single atoms on rutile TiO_2(110) have even stronger CH_4 adsorption. Especially, Pt_1-rutile-TiO_2(110), shortened as Pt_1-TiO_2 below, is predicted to have the adsorption energy at -0.62 eV at the DFT-PBE level, the strongest methane adsorption on an undecorated solid surface reported to date.[54-55] For comparison, CH_4 adsorption energy is -0.10 eV on the Ti site of the perfect rutile TiO_2(110) surface, while CH_4 adsorption on isolated gas-phase single atoms is also weak (Table S4; E_{ad} ranging from -0.01 to -0.23 eV). It is evident the coordination to the

rutile TiO_2 surface has modified the electronic structure of the site for chemisorption. Below we analyze in-depth how CH_4 interacts with the Pt_1-TiO_2 surface chemically.

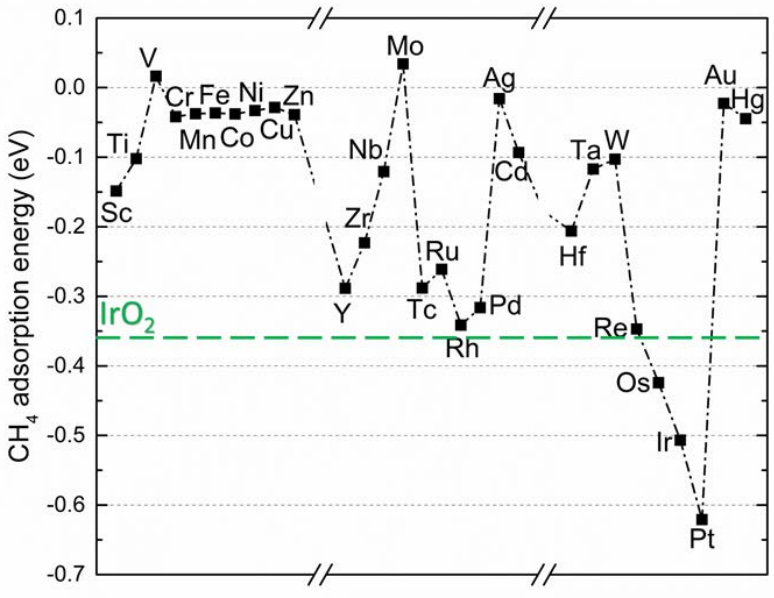

Figure 6.1.2 Adsorption energies of methane on the M_1 (single-atom) site on rutile TiO_2 110) with M being 3d, 4d, and 5d transition metals, in comparison with that on rutile IrO_2(110) (green line).

6.1.4.2 Electronic structure of the methane σ complex

Chemisorption of methane is hypothesized to involve formation of an alkane σ complex.[55-57] Figure 3A-B shows the electronic-density-difference plots for CH_4 adsorption on Pt_1-TiO_2. The transfer of electron density from the C-H bonds and the Pt atom to the region between the C-H_a bond and Pt is clearly seen. The charge depletion on Pt is likely the result of the back-bonding into CH_4 antibonding orbitals. Slight charge accumulation is found on O_a and O_b, due to the hydrogen-bond interaction between the C-H and O, which is made possible by the significant polarization of the C-H bond and the loss of charge density on H_a and H_b. Bader charge analysis shows a net increase in electron

density on the carbon and a net decrease in electron density on H_b and to a lesser extent on H_a (Table S5), with a slight net loss in electron density on CH_4. Similar charge-transfer pattern is also found for CH_4 adsorption on Ir_1-TiO_2 (Figures S5 and S6). Local density-of-states plots (Figure S7) show mixing of CH_4 orbitals and dopant d states. More specifically, the electron donation occurs from the C-H bond into the metal d_{z2} orbital, and back-donation occurs from the metal d_{xy} orbital into the C-H σ* orbital, as illustrated in a schematic (Figure 3C) using the d^6 configuration of Pt^{4+}. Less or more d electrons (Figure S8) lead to weakening interaction with CH_4.

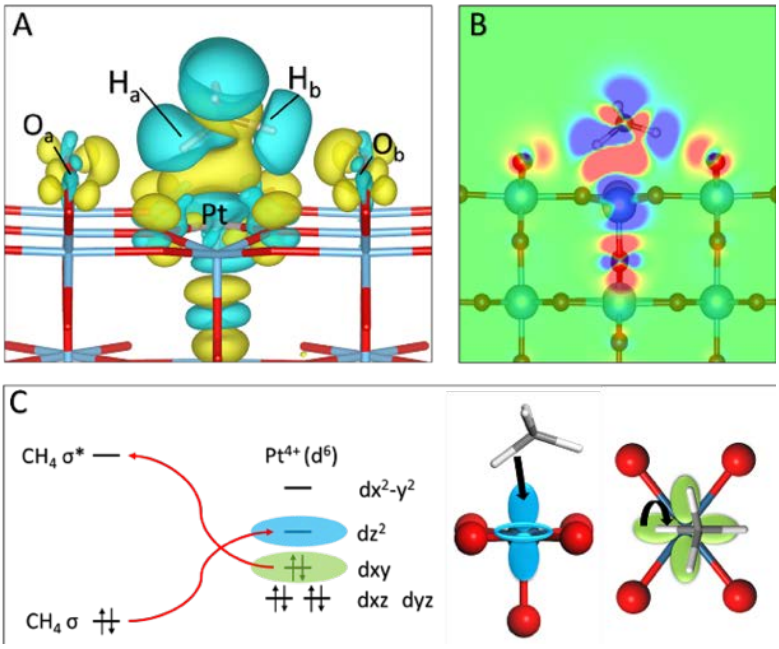

Figure 6.1.3 (**A**) Isosurface plot of the charge density difference from CH_4 adsorption on Pt_1-rutile-TiO_2 (110): yellow, charge accumulation; cyan, charge depletion. (**B**) 2-D charge density plot on the H_a-C-H_b plane: red, charge accumulation; blue, charge depletion. (**C**) Schematic of orbital interactions between CH_4 and Pt^{4+}.

To reveal the extent of the weakening of the C-H_a bond, we used the natural bond orbital (NBO) analysis to determine the effective σ occupancy, i.e., the difference in

occupancy between σ and σ*.[53] Figure 4 shows a linear correlation between C-H_a σ-σ* occupancy and CH_4 adsorption energy, confirming that the greatest weakening of the C-H_a bond takes place on Pt_1-TiO_2 as suggested by the chemisorption model in Figure 3C. The weakening of the C-H_a bond and the polarization of the CH_4 molecule are further reflected in the linear correlations of the C-H_a bond length and the C-M (single atom) distance with CH_4 adsorption energy (Figure S9).

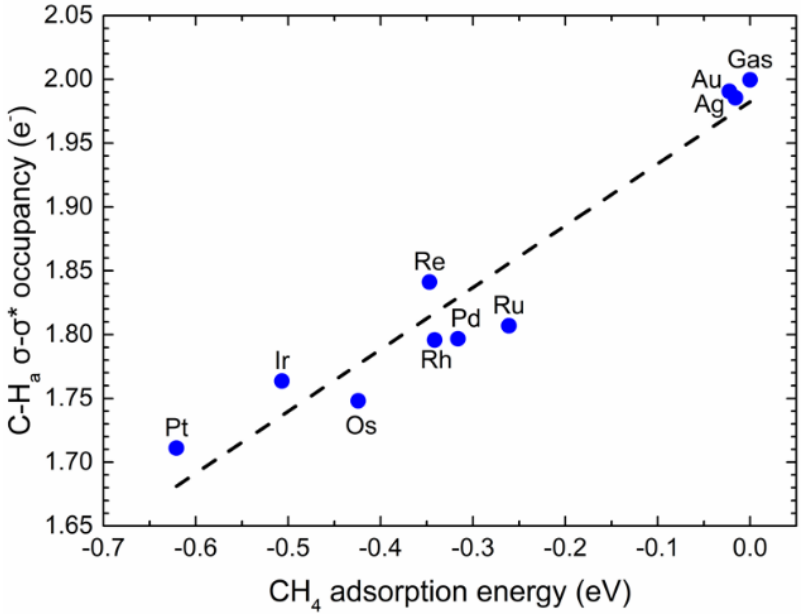

Figure 6.1.4 Linear correlation between methane C-H_a σ-σ* occupancy and adsorption energy on M_1 (single-atom) site on rutile TiO_2 (110) with M being various transition metals.

6.1.4.3 Methane C-H activation barriers and linear scaling descriptors

For single-atom sites yielding the strongest chemisorption of CH_4, the heterolytic C-H activation on them are expected to be facile as well. Transition states are obtained for these single-atom sites on rutile TiO_2(110). Of all the single atoms, Pt_1 and Pd_1 have the lowest methane dissociation barriers of only 0.15 and 0.13 eV, respectively. Figure 5 illustrates

the minimum free-energy path for CH_4 dissociation on Pt_1-TiO_2, characterized by a lengthening of the C-H_a bond and the shortening of the C-Pt distance, which eventually results in a hydroxyl group on the O_{br} site and a methyl group coordinated to Pt. One can see from Figure 5 that facile C-H activation is predicted on Pt_1-TiO_2 below room temperature instead of desorption, due to the strong adsorption of CH_4.

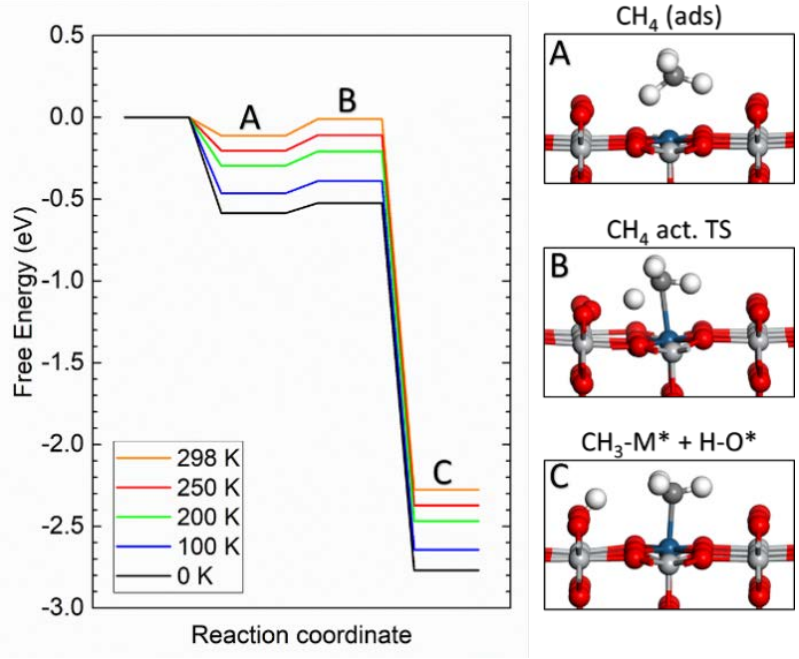

Figure 6.1.5 Free energy profile of CH_4 activation on Pt_1-rutile-TiO_2 (110) for a range of temperatures from 0 to 298 K. The structures for the initial state (A), transition state (B), and final state (C) are shown on the right. The free energies are obtained by including the zero point and vibrational contributions to the enthalpy. The vibrational frequencies are obtained from the DFT calculations.

We further explored methane dissociation on other single atoms on rutile TiO_2(110). Interestingly, we found that the first C-H activation energy and dissociation energy of CH_4 on the chemisorbing surface sites (blue circles in Figure 6A) follow the Bronsted-Evans-Polanyi (BEP) relationship (R^2=0.99).[58-60] The BEP α value is 0.27, suggesting an early

transition state with a major influence from *both* the reactant chemisorption and the product (dissociation) energies. Furthermore, the obtained linear correlation for the methane-chemisorbing single atoms lies beneath physisorbing ones (brown triangles in Figure 6A), attesting to the stabilizing and energy-lowering effect of chemisorption on transition state energies.

For low-temperature methane activation to occur, the energy of the transition state of C-H activation (E_a) must be lower than the energy of desorption (E_d, the opposite of the adsorption E_{ads}) of the reactant CH_4 molecule to the gas phase. The shaded area in Figure 6B where $E_a - E_d = E_a + E_{ads} < 0$ therefore denotes the region where low-temperature activation is most likely. One can see that these include the Pd, Rh, Os, Ir, and Pt single atoms. The elements Re and Ru lie close to the boundary and are also possible to activate CH_4 at low temperature on rutile TiO_2 (110).

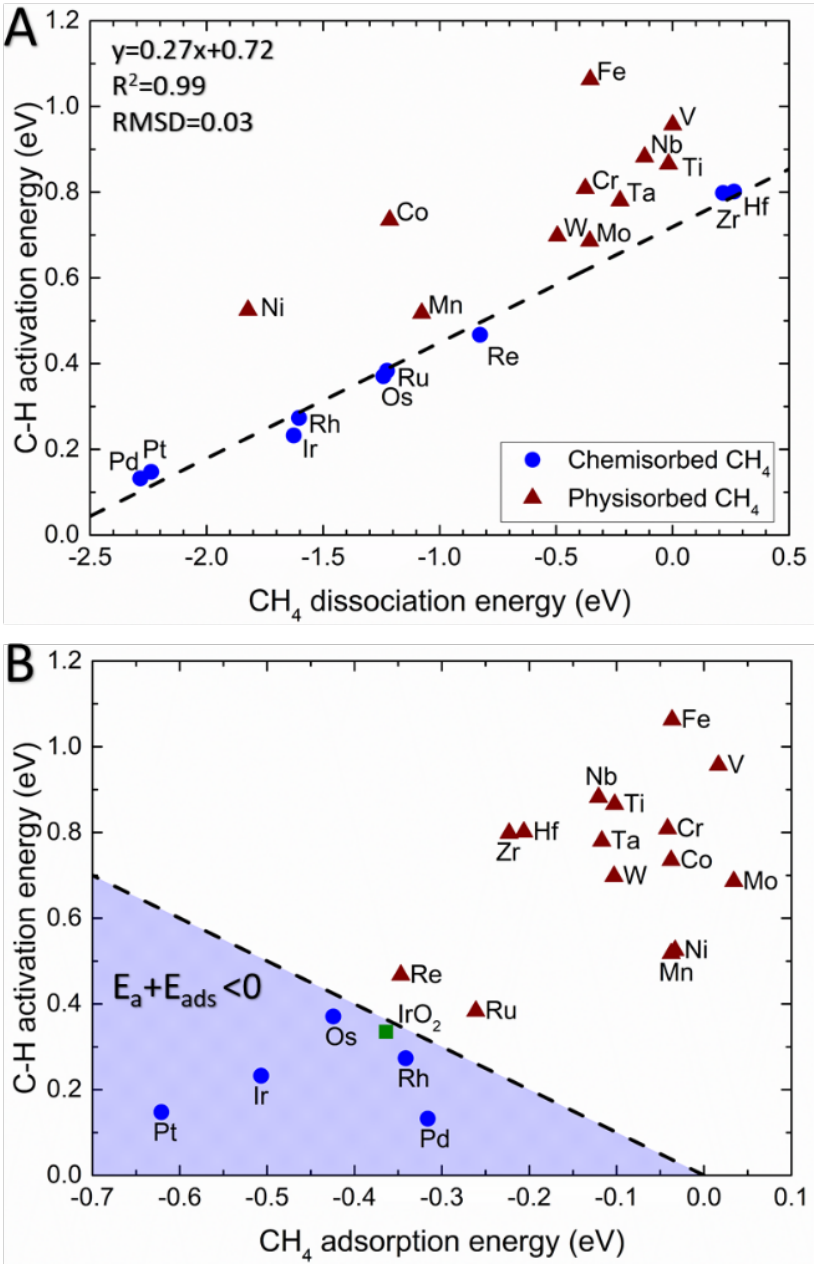

Figure 6.1.6 (**A**) Correlation between C-H activation energy and dissociation energy of CH_4 on the M_1 site on rutile TiO_2 (110) with M being various transition metals. A linear correlation plot is drawn for the chemisorbing dopants (blue circles) and fitting parameters shown in the top left. (**B**) C-H activation energy (E_a) vs adsorption energy of CH_4 (E_{ads}) on the M_1 site on rutile TiO_2 (110) with M being various transition metals, in comparison with rutile IrO_2(110); in the shaded region, low-temperature activation of CH_4 is most likely. The point labeled 'Ti' denotes the pure TiO_2 surface.

6.1.4.4 Validation and comparison of functionals

To be able to compare with previous works,[24-25, 55, 61] we have used the DFT-PBE functional to describe CH_4 adsorption and activation on M_1-TiO_2 sites. To confirm our main findings above based on the GGA-PBE energies, further calculations were performed using PBE-D3 to include dispersion interaction,[62] a recent meta-GGA (SCAN[63]), a hybrid functional (HSE06),[64] and a van der Waals density functional (optPBE-vdW).[66] As shown in Table S6, the different functionals give slight variations in CH_4 adsorption energies and the transition state energies. Despite these variations, the main conclusions remain the same in all cases that the single-atom sites such as Ir and Pt on rutile TiO_2(110) are most promising for low temperature CH_4 activation, due to strong CH_4 chemisorption and low C-H activation energy.

6.1.4.5 Implications

Our results above indicate that CH_4 activation on a site such as on Pt_1-TiO_2 would be facile. To our knowledge, there has been no experimental report on this reaction so far. So we look forward to the experimental realization. After the first C-H activation step, one possible follow-up route is via the oxidative coupling process to form ethylene. Figure 5 suggests that the binding of CH_3 and H on Pt_1-TiO_2 is strong, given the very negative energy change. This may impede subsequent reactions. But a recent DFT study on IrO_2 has shown that the coupling barriers can be very low despite similarly strong metal-CH_x bonds.[67] We expect that a similar process can be catalyzed by Pt_1-TiO_2.

Methane chemisorption energy seems to be a good descriptor for identifying M_1-TiO_2 sites that activate C-H facilely. We expect that this descriptor can be extended to other oxides and oxide-supported single-atom sites. In contrast, on pure metal surfaces, the descriptor used is generally the methane dissociation energy.[68]

6.1.5 Conclusions

In sum, we screened single atoms of all 3d, 4d, and 5d transition-metal elements doped on TiO_2 surfaces for chemisorption of CH_4 and heterolytic C-H activation from first principles. DFT-PBE identified chemisorption of CH_4 and predicted that Rh, Pd, Os, Pt and Ir single atoms on rutile TiO_2(110) would chemisorb CH_4 equally to or even stronger than IrO_2(110). Detailed electronic structure analysis and correlations show that CH_4 is polarized by the single atom's extended d orbitals through the σ-complex formation as well as by the surface oxygen atoms on the rutile TiO_2(110) surface. Further studies confirmed that CH_4 can be activated by these single-atom site facilely from the chemisorption configuration following a heterolytic pathway. Our work suggests a very promising approach to realize low-temperature transformation of methane on precious metal single-atom sites doped on rutile TiO_2. To our knowledge, this is the first time that such an M_1-TiO_2 system has been predicted to activate CH_4 based on strong chemisorption.

References

(1) Schwach, P.; Pan, X.; Bao, X. Direct Conversion of Methane to Value-Added Chemicals over Heterogeneous Catalysts: Challenges and Prospects. *Chem. Rev.* **2017,** *117*, 8497-8520.

(2) Horn, R.; Schlögl, R. Methane Activation By Heterogeneous Catalysis. *Catal. Lett.* **2015,** *145*, 23-39.

(3) Taifan, W.; Baltrusaitis, J. CH_4 Conversion to Value Added Products: Potential, Limitations and Extensions of a Single Step Heterogeneous Catalysis. *Appl. Catal., B* **2016,** *198*, 525-547.

(4) Hammond, C.; Forde, M. M.; Rahim, A.; Hasbi, M.; Thetford, A.; He, Q.; Jenkins, R. L.; Dimitratos, N.; Lopez-Sanchez, J. A.; Dummer, N. F. Direct Catalytic Conversion of Methane to Methanol in an Aqueous Medium by using Copper-Promoted Fe-ZSM-5. *Angew. Chem. Int. Ed.* **2012,** *51*, 5129-5133.

(5) Forde, M. M.; Armstrong, R. D.; Hammond, C.; He, Q.; Jenkins, R. L.; Kondrat, S. A.; Dimitratos, N.; Lopez-Sanchez, J. A.; Taylor, S. H.; Willock, D.; Kiely, C. J.; Hutchings, G. J. Partial Oxidation of Ethane to Oxygenates Using Fe- and Cu-Containing ZSM-5. *J. Am. Chem. Soc.* **2013,** *135*, 11087-11099.

(6) Nørskov, J. K.; Abild-Pedersen, F.; Studt, F.; Bligaard, T. Density Functional Theory in Surface Chemistry and Catalysis. *Proc. Natl. Acad. Sci. U. S. A.* **2011,** *108*, 937-43.

(7) Schwarz, H. Chemistry with Methane: Concepts Rather than Recipes. *Angew. Chem. Int. Ed.* **2011,** *50*, 10096-10115.

(8) Dietl, N.; Schlangen, M.; Schwarz, H. Thermal Hydrogen-Atom Transfer from Methane: The Role of Radicals and Spin States in Oxo-Cluster Chemistry. *Angew. Chem. Int. Ed.* **2012,** *51*, 5544-5555.

(9) Tao, F. F.; Shan, J. J.; Nguyen, L.; Wang, Z.; Zhang, S.; Zhang, L.; Wu, Z.; Huang, W.; Zeng, S.; Hu, P. Understanding Complete Oxidation of Methane on Spinel Oxides at a Molecular Level. *Nature Commun.* **2015,** *6*, 7798.

(10) Hibbitts, D.; Neurock, M. Promotional effects of chemisorbed oxygen and hydroxide in the activation of C–H and O–H bonds over transition metal surfaces. *Surf. Sci.* **2016,** *650*, 210-220.

(11) Xing, B.; Pang, X.-Y.; Wang, G.-C. C–H bond activation of methane on clean and oxygen pre-covered metals: A systematic theoretical study. *J. Catal.* **2011,** *282*, 74-82.

(12) Lunsford, J. H. The Catalytic Oxidative Coupling of Methane. *Angew. Chem. Int. Ed.* **1995,** *34*, 970-980.

(13) Fung, V.; Tao, F.; Jiang, D. E. Understanding oxidative dehydrogenation of ethane on Co3O4 nanorods from density functional theory. *Catal. Sci. Technol.* **2016,** *6*, 6861-6869.

(14) Kwapien, K.; Paier, J.; Sauer, J.; Geske, M.; Zavyalova, U.; Horn, R.; Schwach, P.; Trunschke, A.; Schlögl, R. Sites for Methane Activation on Lithium-Doped Magnesium Oxide Surfaces. *Angew. Chem. Int. Ed.* **2014,** *53*, 8774-8778.

(15) Fu, H.; Liu, Z.-P.; Li, Z.-H.; Wang, W.-N.; Fan, K.-N. Periodic Density Functional Theory Study of Propane Oxidative Dehydrogenation Over V_2O_5(001) Surface. *J. Am. Chem. Soc.* **2006,** *128*, 11114-11123.

(16) Krcha, M. D.; Mayernick, A. D.; Janik, M. J. Periodic Trends of Oxygen Vacancy Formation and C–H Bond Activation Over Transition Metal-Doped CeO_2 (111) Surfaces. *J. Catal.* **2012,** *293*, 103-115.

(17) Fung, V.; Tao, F. F.; Jiang, D. E. General Structure-Reactivity Relationship for Oxygen on Transition-Metal Oxides. *J. Phys. Chem. Lett.* **2017,** *8*, 2206-2211.

(18) Latimer, A. A.; Kulkarni, A. R.; Aljama, H.; Montoya, J. H.; Yoo, J. S.; Tsai, C.; Abild-Pedersen, F.; Studt, F.; Nørskov, J. K. Understanding Trends in CH Bond Activation in Heterogeneous Catalysis. *Nature Mater.* **2017,** *16*, 225-229.

(19) Kumar, G.; Lau, S. L. J.; Krcha, M. D.; Janik, M. J. Correlation of Methane Activation and Oxide Catalyst Reducibility and its Implications for Oxidative Coupling. *ACS Catal.* **2016,** *6*, 1812-1821.

(20) Deshlahra, P.; Iglesia, E. Reactivity and Selectivity Descriptors for the Activation of C-H Bonds in Hydrocarbons and Oxygenates on Metal Oxides. *J. Phys. Chem. C* **2016,** *120*, 16741-16760.

(21) Liu, Z.; Grinter, D. C.; Lustemberg, P. G.; Nguyen-Phan, T. D.; Zhou, Y.; Luo, S.; Waluyo, I.; Crumlin, E. J.; Stacchiola, D. J.; Zhou, J. Dry Reforming of Methane on a Highly-Active Ni-CeO_2 Catalyst: Effects of Metal-Support Interactions on C−H Bond Breaking. *Angew. Chem. Int. Ed.* **2016,** *55*, 7455-7459.

(22) Liu, Z.; Lustemberg, P.; Gutiérrez, R. A.; Carey, J. J.; Palomino, R. M.; Vorokhta, M.; Grinter, D. C.; Ramírez, P. J.; Matolín, V.; Nolan, M. In Situ Investigation of Methane Dry Reforming on Metal/Ceria (111) Surfaces: Metal–Support Interactions and C−H Bond Activation at Low Temperature. *Angew. Chem. Int. Ed.* **2017,** *56*, 13041-13046.

(23) Lustemberg, P. G.; Ramírez, P. J.; Liu, Z.; Gutierrez, R. A.; Grinter, D. G.; Carrasco, J.; Senanayake, S. D.; Rodriguez, J. A.; Ganduglia-Pirovano, M. V. Room-Temperature Activation of Methane and Dry Re-Forming With CO_2 On Ni-CeO_2 (111) Surfaces: Effect of Ce^{3+} Sites and Metal–Support Interactions on C–H Bond Cleavage. *ACS Catal.* **2016,** *6*, 8184-8191.

(24) Liang, Z.; Li, T.; Kim, M.; Asthagiri, A.; Weaver, J. F. Low-Temperature Activation of Methane on the IrO_2 (110) Surface. *Science* **2017,** *356*, 299-303.

(25) Wang, C.-C.; Siao, S. S.; Jiang, J.-C. C–H Bond Activation of Methane via σ–d Interaction on the IrO_2 (110) Surface: Density Functional Theory Study. *J. Phys. Chem. C* **2012,** *116*, 6367-6370.

(26) Qiao, B.; Wang, A.; Yang, X.; Allard, L. F.; Jiang, Z.; Cui, Y.; Liu, J.; Li, J.; Zhang, T. Single-Atom Catalysis of CO Oxidation Using Pt_1/FeO_x. *Nat. Chem.* **2011,** *3*, 634-641.

(27) Nie, L.; Mei, D.; Xiong, H.; Peng, B.; Ren, Z.; Hernandez, X. I. P.; DeLaRiva, A.; Wang, M.; Engelhard, M. H.; Kovarik, L.; Datye, A. K.; Wang, Y. Activation of Surface Lattice Oxygen in Single-Atom Pt/CeO_2 for Low-Temperature CO Oxidation. *Science* **2017,** *358*, 1419-1423.

(28) DeRita, L.; Dai, S.; Lopez-Zepeda, K.; Pham, N.; Graham, G. W.; Pan, X.; Christopher, P. Catalyst Architecture for Stable Single Atom Dispersion Enables Site-Specific Spectroscopic and Reactivity Measurements of CO Adsorbed to Pt Atoms, Oxidized Pt Clusters, and Metallic Pt Clusters on TiO_2. *J. Am. Chem. Soc.* **2017,** *139*, 14150-14165.

(29) Liu, P.; Zhao, Y.; Qin, R.; Mo, S.; Chen, G.; Gu, L.; Chevrier, D. M.; Zhang, P.; Guo, Q.; Zang, D.; Wu, B.; Fu, G.; Zheng, N. Photochemical Route for Synthesizing Atomically Dispersed Palladium Catalysts. *Science* **2016,** *352*, 797-801.

(30) Li, S.; Zhao, X.; Shi, J.; Jia, Y.; Guo, Z.; Cho, J.-H.; Gao, Y.; Zhang, Z. Interplay Between the Spin-Selection Rule and Frontier Orbital Theory in O_2 Activation and CO Oxidation by Single-Atom-Sized Catalysts on TiO_2(110). *Phys. Chem. Chem. Phys.* **2016,** *18*, 24872-24879.

(31) Shi, J.; Zhao, X.; Zhang, L.; Xue, X.; Guo, Z.; Gao, Y.; Li, S. An Oxidized Magnetic Au Single Atom on Doped TiO_2 (110) Becomes a High Performance CO Oxidation Catalyst Due to the Charge Effect. *J. Mater. Chem. A* **2017,** *5*, 19316-19322.

(32) Sui, Y.; Liu, S.; Li, T.; Liu, Q.; Jiang, T.; Guo, Y.; Luo, J.-L. Atomically Dispersed Pt on Specific TiO_2 Facets for Photocatalytic H_2 Evolution. *J. Catal.* **2017,** *353*, 250-255.

(33) Chen, L.; Smith, R. S.; Kay, B. D.; Dohnalek, Z. Adsorption of Small Hydrocarbons on Rutile TiO_2 (110). *Surf. Sci.* **2016,** *650*, 83-92.

(34) McFarland, E. W.; Metiu, H. Catalysis by Doped Oxides. *Chem. Rev.* **2013,** *113*, 4391-4427.

(35) Li, B.; Metiu, H. DFT Studies of Oxygen Vacancies on Undoped and Doped La_2O_3 Surfaces. *J. Phys. Chem. C* **2010,** *114*, 12234-12244.

(36) Sun, X.; Li, B.; Metiu, H. Methane Dissociation on Li-, Na-, K-, and Cu-Doped Flat and Stepped CaO (001). *J. Phys. Chem. C* **2013,** *117*, 7114-7122.

(37) Fung, V.; Tao, F. F.; Jiang, D.-e. Trends of Alkane Activation on Doped Cobalt (II, III) Oxide from First Principles. *ChemCatChem* **2018,** *10*, 244-249.

(38) Bliem, R.; Pavelec, J.; Gamba, O.; McDermott, E.; Wang, Z.; Gerhold, S.; Wagner, M.; Osiecki, J.; Schulte, K.; Schmid, M.; Blaha, P.; Diebold, U.; Parkinson, G. S. Adsorption and incorporation of transition metals at the magnetite Fe3O4(001) surface. *Phys. Rev. B* **2015,** *92*, 075440.

(39) Qiao, B.; Liu, J.; Wang, Y.-G.; Lin, Q.; Liu, X.; Wang, A.; Li, J.; Zhang, T.; Liu, J. Highly Efficient Catalysis of Preferential Oxidation of CO in H2-Rich Stream by Gold Single-Atom Catalysts. *ACS Catal.* **2015,** *5*, 6249-6254.

(40) Kresse, G.; Furthmuller, J. Efficiency of Ab-Initio Total Energy Calculations for Metals and Semiconductors Using a Plane-Wave Basis Set. *Comput. Mater. Sci.* **1996,** *6*, 15-50.

(41) Kresse, G.; Furthmuller, J. Efficient Iterative Schemes for Ab Initio Total-Energy Calculations Using a Plane-Wave Basis Set. *Phys. Rev. B* **1996,** *54*, 11169-11186.

(42) Dudarev, S. L.; Botton, G. A.; Savrasov, S. Y.; Humphreys, C. J.; Sutton, A. P. Electron-Energy-Loss Spectra and the Structural Stability of Nickel Oxide: An LSDA+U Study. *Phys. Rev. B* **1998,** *57*, 1505-1509.

(43) Hu, Z.; Metiu, H. Choice of U for DFT+U Calculations for Titanium Oxides. *J. Phys. Chem. C* **2011,** *115*, 5841-5845.

(44) Finazzi, E.; Di Valentin, C.; Pacchioni, G.; Selloni, A. Excess Electron States in Reduced Bulk Anatase TiO_2: Comparison of Standard GGA, GGA+U, and Hybrid DFT Calculations. *J. Chem. Phys.* **2008,** *129*, 154113.

(45) Perdew, J. P.; Burke, K.; Ernzerhof, M. Generalized Gradient Approximation Made Simple. *Phys. Rev. Lett.* **1996,** *77*, 3865-3868.

(46) Blöchl, P. E. Projector Augmented-Wave Method. *Phys. Rev. B* **1994,** *50*, 17953-17979.

(47) Monkhorst, H. J.; Pack, J. D. Special Points for Brillouin-Zone Integrations. *Phys. Rev. B* **1976,** *13*, 5188-5192.

(48) Henkelman, G.; Uberuaga, B. P.; Jónsson, H. A Climbing Image Nudged Elastic Band Method for Finding Saddle Points And Minimum Energy Paths. *J. Chem. Phys.* **2000,** *113*, 9901-9904.

(49) Henkelman, G.; Jónsson, H. A Dimer Method for Finding Saddle Points on High Dimensional Potential Surfaces Using Only First Derivatives. *J. Chem. Phys.* **1999,** *111*, 7010.

(50) Momma, K.; Izumi, F. VESTA 3 for Three-Dimensional Visualization of Crystal, Volumetric and Morphology Data. *J. Appl. Crystallogr.* **2011,** *44*, 1272-1276.

(51) Dunnington, B. D.; Schmidt, J. Generalization of Natural Bond Orbital Analysis to Periodic Systems: Applications to Solids and Surfaces via Plane-Wave Density Functional Theory. *J. Chem. Theory Comput.* **2012,** *8*, 1902-1911.

(52) Weigend, F.; Ahlrichs, R. Balanced Basis Sets Of Split Valence, Triple Zeta Valence and Quadruple Zeta Valence Quality for H to Rn: Design and Assessment of Accuracy. *Phys. Chem. Chem. Phys.* **2005,** *7*, 3297-3305.

(53) Dunnington, B. D.; Schmidt, J. Molecular Bonding-Based Descriptors for Surface Adsorption and Reactivity. *J. Catal.* **2015,** *324*, 50-58.

(54) Weaver, J. F. Surface Chemistry Of Late Transition Metal Oxides. *Chem. Rev.* **2013,** *113*, 4164-4215.

(55) Weaver, J. F.; Hakanoglu, C.; Antony, A.; Asthagiri, A. Alkane activation on crystalline metal oxide surfaces. *Chem. Soc. Rev.* **2014,** *43*, 7536-47.

(56) Hall, C.; Perutz, R. N. Transition Metal Alkane Complexes. *Chem. Rev.* **1996,** *96*, 3125-3146.

(57) Saillard, J. Y.; Hoffmann, R. Carbon-Hydrogen and Hydrogen-Hydrogen Activation in Transition Metal Complexes and on Surfaces. *J. Am. Chem. Soc.* **1984,** *106*, 2006-2026.

(58) Latimer, A. A.; Aljama, H.; Kakekhani, A.; Yoo, J. S.; Kulkarni, A.; Tsai, C.; Garcia-Melchor, M.; Abild-Pedersen, F.; Nørskov, J. K. Mechanistic Insights Into Heterogeneous Methane Activation. *Phys. Chem. Chem. Phys.* **2017,** *19*, 3575-3581.

(59) van Santen, R. A.; Neurock, M.; Shetty, S. G. Reactivity Theory of Transition-Metal Surfaces: A Brønsted− Evans− Polanyi Linear Activation Energy− Free-Energy Analysis. *Chem. Rev.* **2009,** *110*, 2005-2048.

(60) Li, H.-Y.; Guo, Y.-L.; Guo, Y.; Lu, G.-Z.; Hu, P. C–H Bond Activation over Metal Oxides: A New Insight into the Dissociation Kinetics from Density Functional Theory. *J. Chem. Phys.* **2008,** *128*, 051101.

(61) Weaver, J. F.; Hakanoglu, C.; Hawkins, J. M.; Asthagiri, A. Molecular Adsorption of Small Alkanes on a PdO(101) Thin Film: Evidence of Sigma-Complex Formation. *J. Chem. Phys.* **2010,** *132*, 024709.

(62) Grimme, S.; Antony, J.; Ehrlich, S.; Krieg, H. A Consistent and Accurate ab Initio Parametrization of Density Functional Dispersion Correction (DFT-D) for the 94 Elements H-Pu. *J. Chem. Phys.* **2010,** *132*, 154104.

(63) Sun, J.; Remsing, R. C.; Zhang, Y.; Sun, Z.; Ruzsinszky, A.; Peng, H.; Yang, Z.; Paul, A.; Waghmare, U.; Wu, X. Accurate First-Principles Structures and Energies of Diversely Bonded Systems from an Efficient Density Functional. *Nat. Chem.* **2016,** *8*, 831-836.

(64) Krukau, A. V.; Vydrov, O. A.; Izmaylov, A. F.; Scuseria, G. E. Influence of the Exchange Screening Parameter on the Performance of Screened Hybrid Functionals. *J. Chem. Phys.* **2006,** *125*, 224106.

Supplementary Information

Figure S6.1.1 Binding energies of Pt on oxygen vacancy and pristine TiO_2 surfaces.

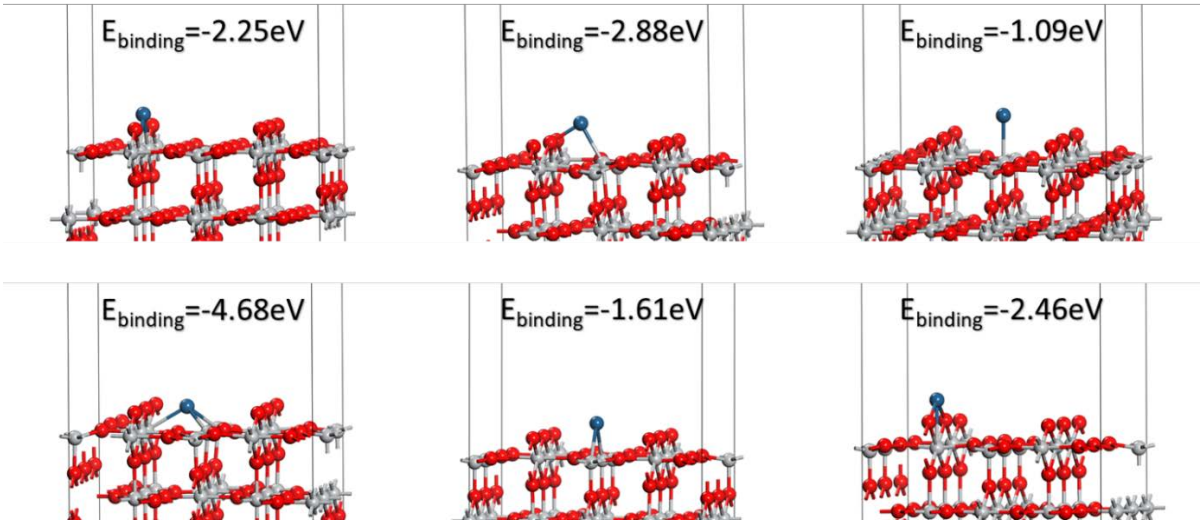

Figure S6.1.2 Barrier and reaction energy of diffusion of Pt out of the cationic vacancy site.

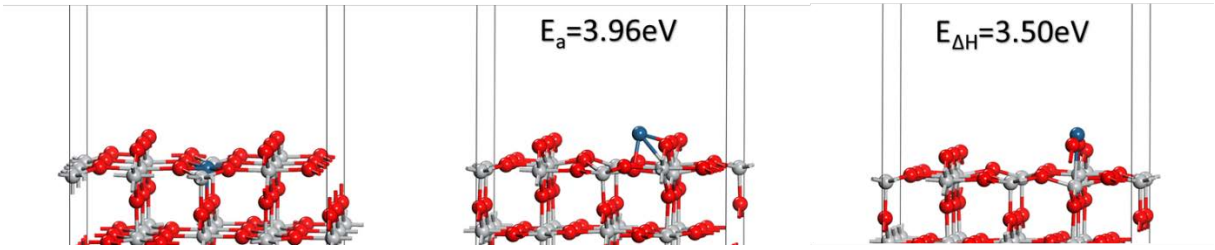

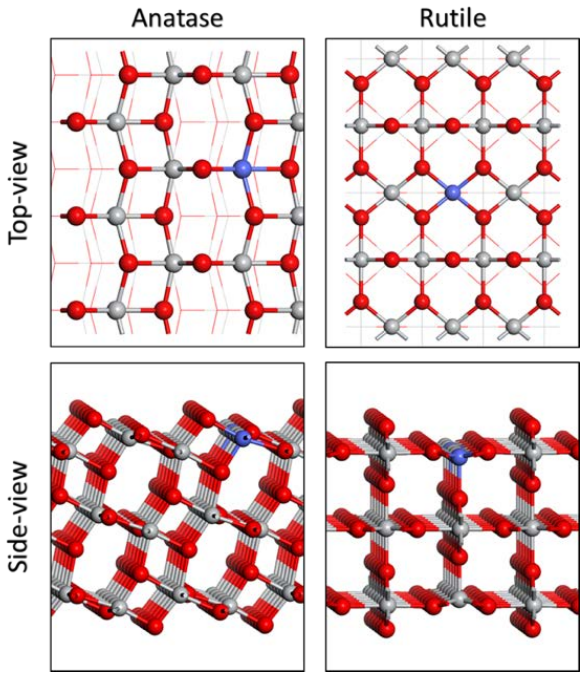

Figure S6.1.3 Side and top-view of anatase (101) and rutile (110) TiO_2. The anchoring site for the single atom is highlighted in blue.

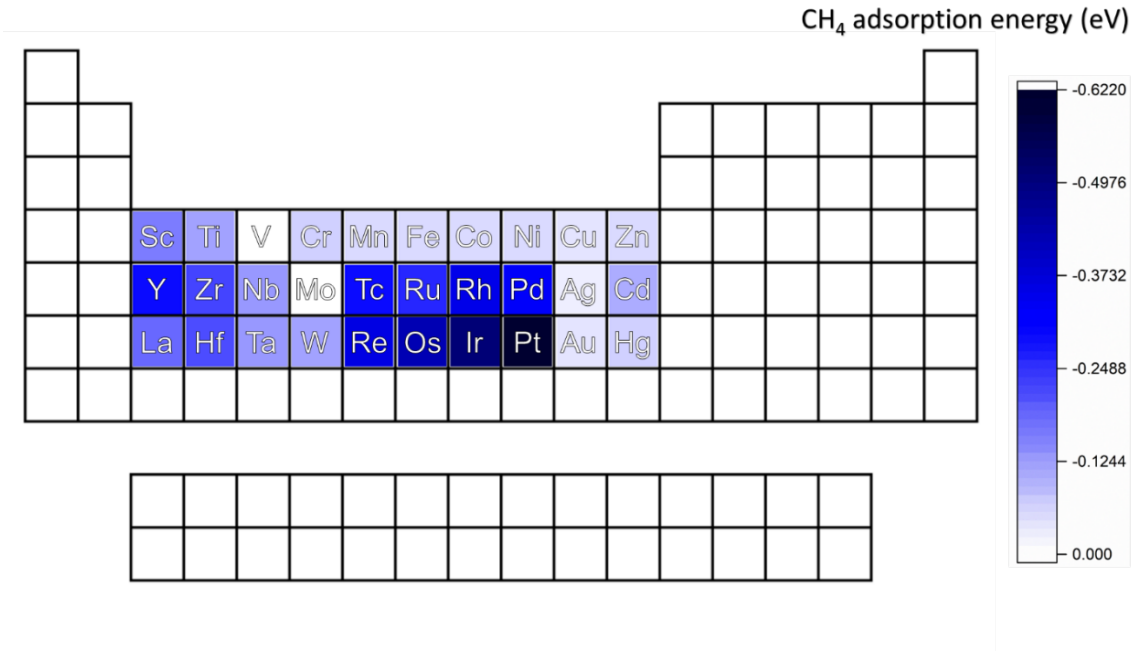

Figure S6.1.4 Heat map representing methane adsorption energies for each 3-5d single-atom sites on rutile TiO_2 (110).

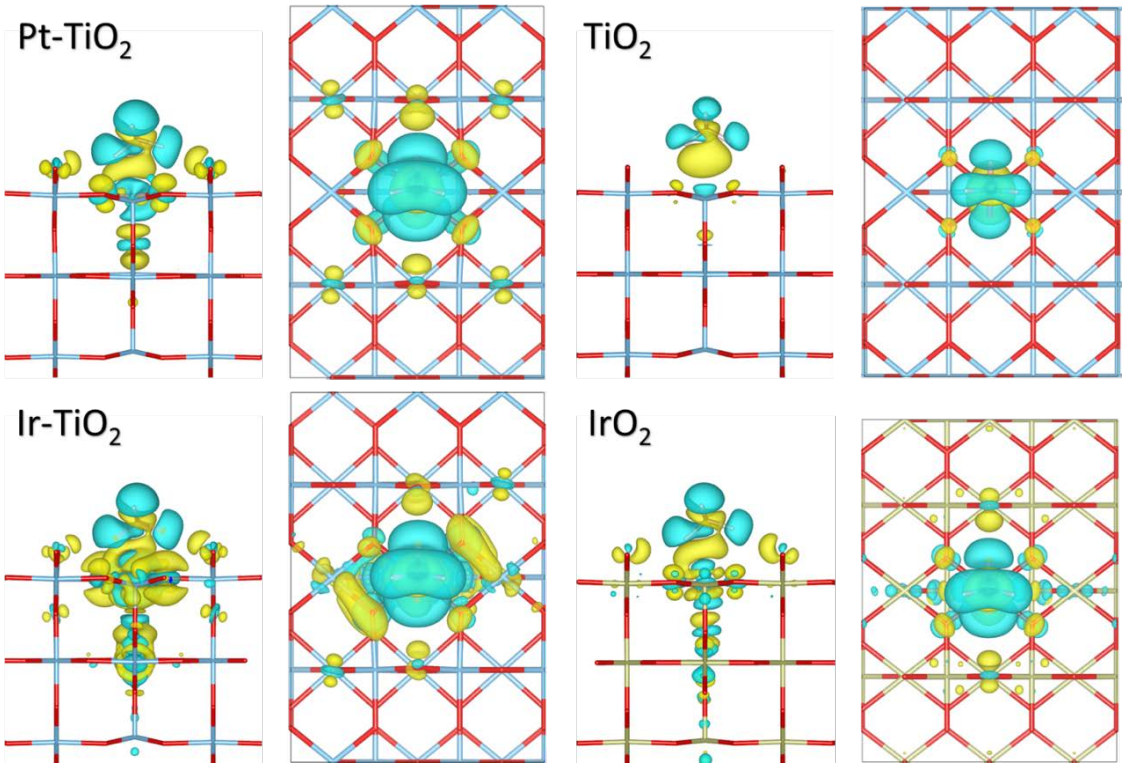

Figure S6.1.5 Side and top-views of the isosurface plot of the charge density difference for CH_4 adsorption on rutile Pt_1-TiO_2, Ir_1-TiO_2, IrO_2, and TiO_2 (110) surfaces.

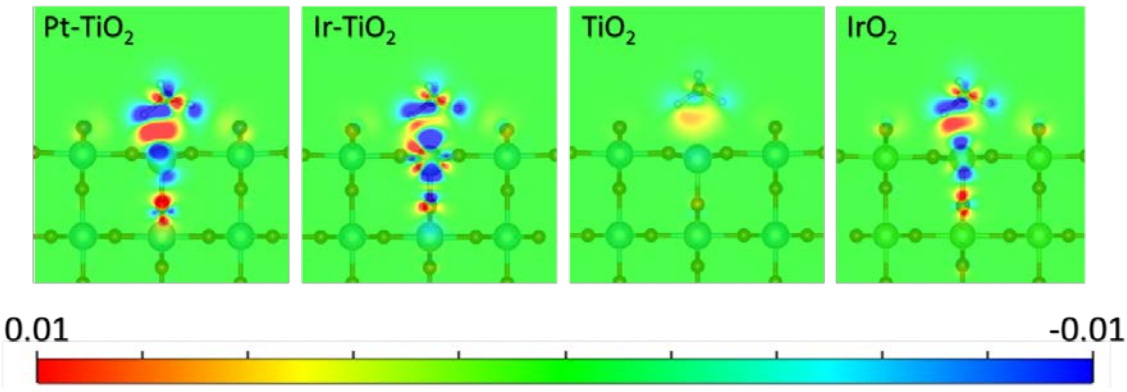

Figure S6.1.6 Side views of the 2-D charge density plot on the H_a-C-H_b plane with charge decrease in blue and charge increase in red for CH_4 adsorption on rutile on rutile Pt_1-TiO_2, Ir_1-TiO_2, IrO_2, and TiO_2 (110) surfaces.

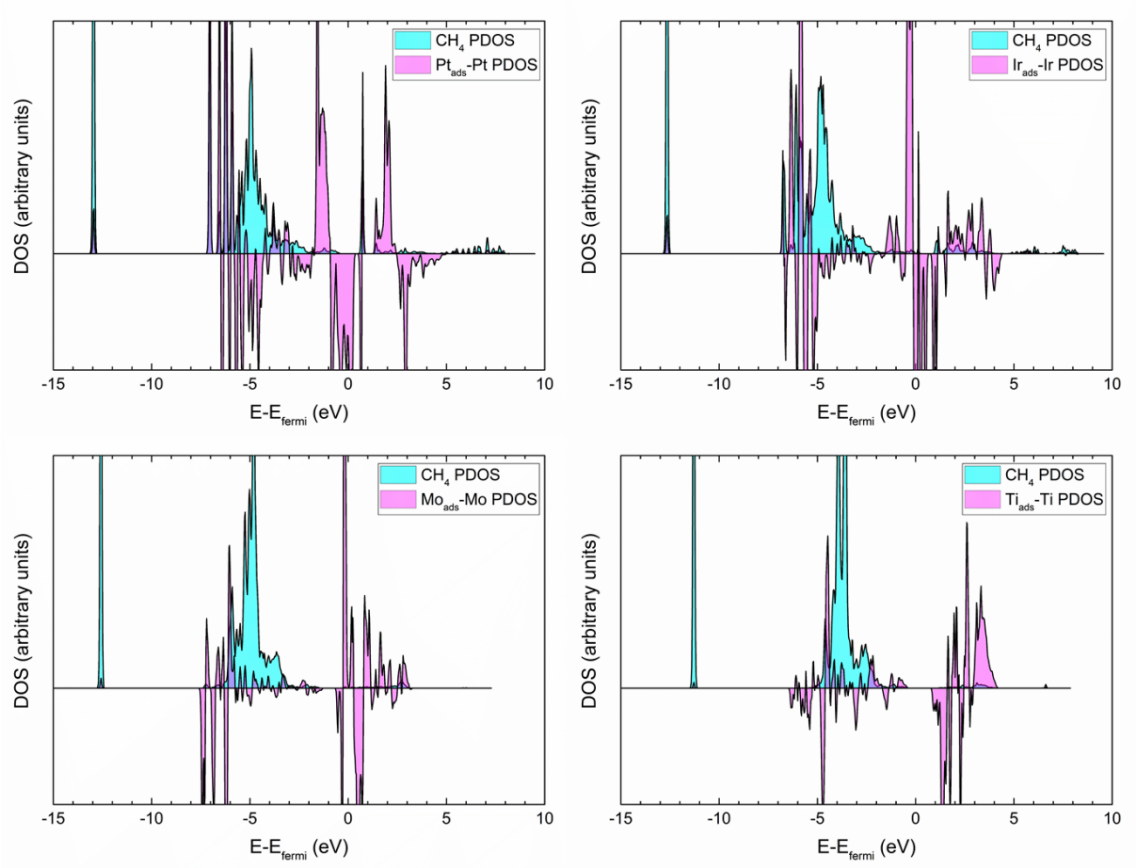

Figure S6.1.7 Local density of states of the adsorbed CH_4 and single-atom sites for Pt_1, Ir_1, and Mo_1 on rutile TiO_2(110), in comparison with the undoped rutile TiO_2(110).

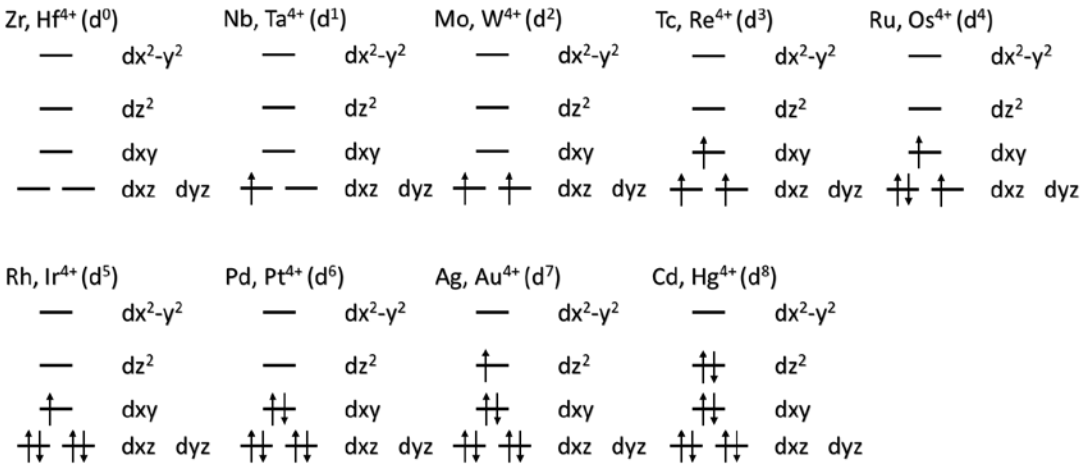

Figure S6.1.8 Diagram of most plausible d-orbital occupations of the 4-d and 5-d transition metal single atoms on rutile TiO_2(110), based on the 4+ oxidation state and computationally obtained electron magnetic moments for the single atoms.

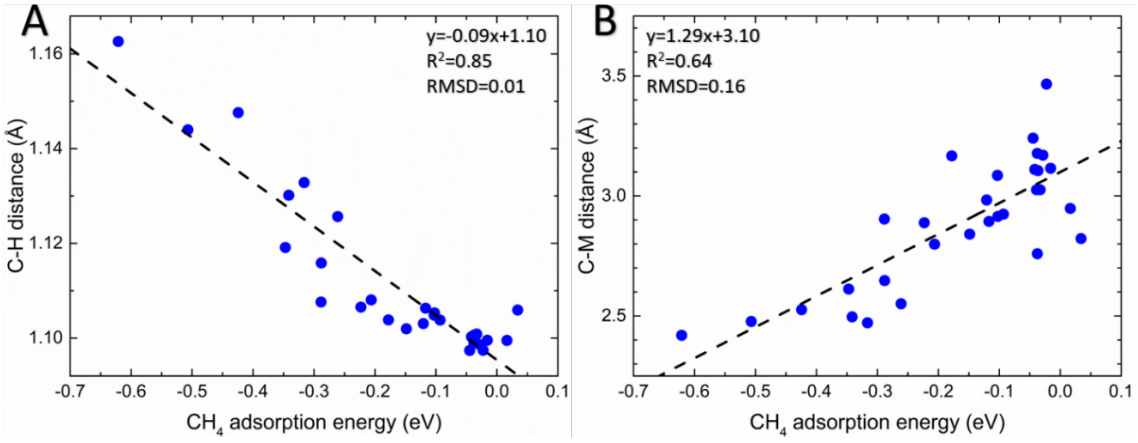

Figure S6.1.9 CH_4 adsorption on the M_1 (single atom) site on rutile TiO_2 (110) for M being various transition metals: (**A**) Correlation plot of C-H_a bond distance and CH_4 adsorption energy; (**B**) Correlation plot of C-M_1 distance and CH_4 adsorption energy. See Table S2 for the specifics of all data points.

Table S6.1.1 Binding energies of the dopant atoms into the cationic vacancy of TiO_2.

Dopant	$E_{binding}$(eV)
Ru	-15.64
Rh	-14.15
Pd	-10.99
Os	-16.64
Ir	-15.15
Pt	-12.95

Table S6.1.2 Comparison of CH_4 adsorption energies on the M_1, single-atom site on TiO_2 anatase (101) and rutile (110).

M_1	CH_4 ads. (eV)	
	Anatase	Rutile
Fe	-0.02	-0.04
Co	0.00	-0.04
Ni	-0.02	-0.03
Ru	-0.14	-0.26
Rh	-0.18	-0.34
Pd	-0.08	-0.32
Os	-0.21	-0.42
Ir	-0.31	-0.51
Pt	-0.18	-0.62

Table S6.1.3 Energetic and geometric parameters of methane adsorption on the M_1, single-atom site on rutile TiO_2(110).

M_1	CH_4 ads. E (eV)	C-M dis. (Å)	O-H_a dis. (Å)	O-H_b dis. (Å)	C-H_a dis. (Å)	C-H_b dis. (Å)	C-H diss. E (eV)	C-H act. E (eV)	Apparent act. E (eV)
Sc	-0.15	2.841	2.577	2.551	1.102	1.106	-0.44		
Ti (undoped)	-0.10	2.915	2.650	2.492	1.105	1.102	-0.02	0.87	0.76
V	0.02	2.948	2.620	2.458	1.099	1.097	0.00	0.96	0.97
Cr	-0.04	3.111	2.662	2.563	1.100	1.101	-0.37	0.81	0.77
Mn	-0.04	2.759	2.591	2.388	1.100	1.107	-1.08	0.52	0.48
Fe	-0.04	3.106	2.723	2.640	1.101	1.098	-0.35	1.06	1.03
Co	-0.04	3.177	2.740	2.644	1.099	1.100	-1.21	0.74	0.70
Ni	-0.03	3.026	2.702	2.591	1.101	1.098	-1.82	0.52	0.49
Cu	-0.03	3.170	2.817	2.866	1.099	1.101	-1.03		
Zn	-0.04	3.026	2.713	2.691	1.100	1.103	-0.56		
Y	-0.29	2.904	2.772	2.596	1.108	1.105	-0.47		
Zr	-0.22	2.888	2.602	2.515	1.107	1.106	0.22	0.80	0.58
Nb	-0.12	2.983	2.622	2.557	1.103	1.102	-0.12	0.88	0.76
Mo	0.03	2.822	2.557	2.474	1.106	1.106	-0.36	0.69	0.72
Tc	-0.29	2.647	2.520	2.375	1.116	1.105	-0.83	0.51	0.22
Ru	-0.26	2.551	2.546	2.310	1.126	1.101	-1.23	0.38	0.12
Rh	-0.34	2.496	2.538	2.277	1.130	1.102	-1.60	0.27	-0.07
Pd	-0.32	2.471	2.527	2.275	1.133	1.103	-2.28	0.13	-0.18
Ag	-0.02	3.115	2.907	2.860	1.100	1.103	-0.88		
Cd	-0.09	2.924	2.852	2.786	1.104	1.102	-0.42		
La	-0.18	3.167	3.270	3.161	1.104	1.101	-0.36		
Hf	-0.21	2.799	2.531	2.463	1.108	1.108	0.26	0.80	0.60
Ta	-0.12	2.894	2.583	2.515	1.106	1.104	-0.23	0.78	0.66
W	-0.10	3.085	2.689	2.605	1.105	1.101	-0.49	0.70	0.59
Re	-0.35	2.612	2.522	2.334	1.119	1.107	-0.83	0.47	0.12
Os	-0.42	2.526	2.568	2.277	1.148	1.099	-1.24	0.37	-0.05
Ir	-0.51	2.477	2.524	2.269	1.144	1.100	-1.63	0.23	-0.27
Pt	-0.62	2.419	2.535	2.212	1.163	1.100	-2.24	0.15	-0.47
Au	-0.02	3.466	3.185	3.093	1.097	1.099	-0.93		
Hg	-0.04	3.241	3.028	2.968	1.097	1.101	-0.34		

Table S6.1.4 Bader charges prior to and after adsorption of CH_4 on rutile $IrO_2(110)$, $TiO_2(110)$, and Ir_1-$TiO_2(110)$, and Pt_1-$TiO_2(110)$.

Pre-adsorption	M_{cus}	O_a	O_b	C	H_a	H_b
CH_4				-0.064	0.016	0.016
Rutile IrO_2	1.459	-0.707	-0.707			
Rutile TiO_2	2.026	-0.906	-0.906			
Ir_1-TiO_2	1.599	-0.904	-0.904			
Pt_1-TiO_2	1.453	-0.904	-0.904			
Post-adsorption						
Rutile IrO_2	1.465	-0.731	-0.733	-0.200	0.026	0.135
Rutile TiO_2	2.033	-0.918	-0.920	-0.151	0.030	0.070
Ir_1-TiO_2	1.558	-0.929	-0.931	-0.246	0.064	0.163
Pt_1-TiO_2	1.421	-0.933	-0.937	-0.222	0.073	0.204
Difference						
Rutile IrO_2	0.006	-0.024	-0.026	-0.136	0.010	0.119
Rutile TiO_2	0.006	-0.012	-0.015	-0.087	0.014	0.054
Ir_1-TiO_2	-0.041	-0.025	-0.027	-0.182	0.048	0.147
Pt_1-TiO_2	-0.032	-0.029	-0.033	-0.158	0.057	0.188

Table S6.1.5 Adsorption energy of methane to selected, isolated gas phase metals.

Atom	$E_{adsorption}$(eV)
Os	-0.11
Ir	-0.23
Pt	-0.13
Au	-0.01

Table S6.1.6 Comparison of methane adsorption energy (E_{ads}), activation-energy (E_a), and dissociation energy (ΔE) on rutile $TiO_2(110)$, and Ir_1-$TiO_2(110)$, and Pt_1-$TiO_2(110)$ for different functionals.

Functional	**Energetics**	**TiO_2**	**Ir_1-TiO_2**	**Pt_1-TiO_2**
PBE	E_{ads}	-0.10	-0.51	-0.62
	E_a	0.87	0.23	0.15
	ΔE	-0.02	-1.63	-2.24
PBE-D3	E_{Ads}	-0.39	-0.83	-0.95
	E_a	0.82	0.21	0.13
	ΔE	-0.05	-1.60	-2.22
optPBE-vdW	E_{Ads}	-0.37	-0.75	-0.84
	E_a	0.95	0.30	0.19
	ΔE	-0.04	-1.64	-2.27
SCAN	E_{ads}	-0.04	-0.76	-0.96
	E_a*	0.96	0.28	0.19
	ΔE	0.19	-1.68	-2.28
HSE06*	E_{ads}	-0.28	-0.48	-0.92
	E_a	1.03	0.12	0.25
	ΔE	-0.09	-2.09	-2.48

*Single point energies.

6.2 Role of substrate-single atom electronic coupling on methane complexation

6.2.1 Abstract

Recent experimental and theoretical evidence has demonstrated the formation of methane complexes on both bulk and single atom oxide surfaces with significant implications for catalysis and gas separation. Despite its potential chemical and practical importance, much remains to be explored regarding the factors determining strong methane complexation, and promising oxides with this appealing property remain exceedingly scarce. In our proposed model for methane complexation, any doped oxide can chemisorb methane so long as requirements for the metal center orbital energies and occupation are fulfilled, determined by their geometry in the oxide lattice and by their electron count or elemental identity. Using hybrid density functional theory, we validated this prediction by confirming strong methane complexation on a host of doped oxides, but also revealed a subtle interplay of electronic states on metallic oxides which can disrupt the complexation strength of the doped metal center. Whereas single atoms on wide-gap substrates performed best, those with a significant overlap of their conduction band with the single atom dz2 states instead exhibited complexation but with *positive* adsorption energies. Therefore, a third condition for methane complexation on doped oxides is revealed, requiring the substrate oxide conduction band to not overlap with the single atom states. This unique observation is the first indication of strong substrate-single atom electronic coupling

drastically affecting adsorption with significant implications in choosing suitable substrates for single atoms.

6.2.2 Introduction

Methane is an abundant and inexpensive resource with potential to be a viable source for energy or as industrial precursors.[1-3] Understanding the interaction of methane with solids is therefore a crucial first step towards designing materials with better performance for methane catalysis or capture. As a non-polar, inert molecule with a strong bond dissociation energy, its interaction with surfaces can be best described as weakly physisorbing in the vast majority of cases.[4] Methane *chemisorption*, on the other hand, while possible for certain inorganic complexes,[5] is still an emergent topic for surfaces.[6-7] Most prominently, methane was recently discovered to chemisorb and dissociate at cryogenic temperatures on rutile IrO_2 (110).[8-9]

Beyond IrO_2, no such oxide has been experimentally observed to exhibit the similar degree of activity thus far. Given the rarity of this phenomenon, a brute-force screening of potential solid surfaces for methane complex is impractical even by computational standards, much less through experimental means. Recently, we proposed that methane complex formation depends primarily on the d-orbital occupancy and geometry of the metal atom. For the square pyramidal metal site, a common surface geometry observed in oxides such as rutile, we expected a 6 d-electron system as most suitable for methane complexation by having an empty dz^2[8, 10-11] orbital to accept the electron donation from the C-H sigma bond, and a filled dxy orbital for the back-bonding

interaction into the C-H antibonding orbitals. Using rutile TiO_2 as a model substrate, we demonstrate by replacing or doping the surface Ti atoms with other transition metal single atoms, we can fulfill both geometry and electron occupancy requirements without resorting to bulk oxides. Namely, the Pt^{4+} doped in the TiO_2 framework is predicted to form strong methane complexes based on our model (Figure 1).

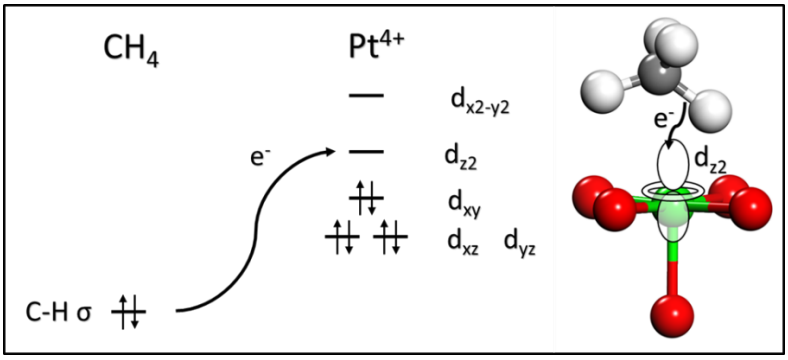

Figure 6.2.1 Schematic of methane complexation via C-H σ-bond donation into the critical dz2 orbital on square-pyramidal Pt^{4+} (green) in an oxide surface.

This prediction is confirmed by density functional theory (DFT) calculations, which found Pt-TiO_2 to have the strongest methane adsorption energy of -0.62 eV using PBE within the screened 3d, 4d, and 5d transition metals.[10] Of the two relevant orbitals dxy and dz2, the dz2 orbital filling was found to be the most sensitive for methane adsorption, with no adsorption possible as soon as it is partially occupied, such as in the case of the 7 d-electron systems Ag-TiO_2 and Au-TiO_2. These results clearly showed the single atom can be thought as behaving like a metal coordination center, with the lattice oxygen of the substrate behaving as the ligands in this complex, matching the similar interaction found between methane and inorganic complexes.[5] From these insights, methane complexation on surfaces can no longer be argued as remote or inaccessible.

Rather, prediction via intuitive principles of geometry and electron count is sufficient to reveal promising candidates. One must wonder then, if these rules are truly broadly applicable beyond the model doped TiO_2 system, and if other substrates can provide the same 'ligand' effect for the metal single atom.

6.2.3 Computational details

The density functional theory calculations were performed using the Vienna Ab Initio Simulation Package (VASP).[12-13] Unless otherwise noted, the calculations were performed with the Heyd-Scuseria-Ernzerhof screened hybrid functional (HSE06).[14] The Perdew-Burke-Ernzerhof (PBE)[15] functional was used for comparison cases. To focus on the chemical bonding contribution of the CH_4-Pt interaction, we opted out of using van der Waals corrections in this study. All calculations were performed with spin polarization. The projector-augmented wave method was used to describe the electron-core interaction.[12, 16] A kinetic energy cutoff of 450 eV was used for the plane waves. Due to the computational cost of hybrid functional calculations for geometric relaxations, the Brillouin zone was sampled at the gamma-point only for adsorption geometry and energy calculations. Comparison of gamma-point only adsorption energies with the a 3×2×1 Monkhorst-Pack[17] k-point sampling using gamma-point relaxed geometries showed close agreement.

A vacuum layer of 15 Å was added for the surface slabs along the z-direction; the slab contains a total of four layers, with the bottom two layers fixed in their bulk positions. The methane absorption energy (E_{ads}) is calculated with the equation $E_{ads} = E_{surface+CH4} - (E_{perfect\text{-}surface} + E_{CH4})$ where $E_{surface+CH4}$ is the energy of the surface slab with a

methane. The energies of E_{CH4} was computed by placing the adsorbate in a cubic cell with a 15 Å wide vacuum in each direction. Charge densities and isosurfaces were visualized using the VESTA program.[18]

6.2.4 Results

6.2.4.1 Geometry and electronic structure of methane complexation on rutile TiO_2

On rutile (110), the optimal bonding configuration for methane places the methane molecule directly above the single atom center (Figure 2a), with two C-H bonds facing downwards and two facing upwards. Methane complexation can be further characterized by significantly shortened distances between the methane molecule and the surface metal center, beyond the overlapping van der Waals (vdW) radius. In the prototypical case of Pt-TiO_2 (Figure 2b), the distance between the methane C and surface Pt was found to be only 2.406 Å, compared to the combined vdW radius of 3.45 Å for C-Pt. To counter the energetic penalty of the repulsive interactions with the surface at these distances, a strong interaction between the methane and surface Pt is necessary. This interaction is observed from charge density difference plots (Figure 2c, d) showing charge accumulation between the two molecules suggesting the formation of a chemical bond. In addition, a lengthening of the C-H bond can be observed from a gas phase length of 1.090 Å to 1.154 Å for the adsorbed complex. Finally, the adsorption energy obtained for the methane complex was found to be -0.75 eV. The adsorption energies, geometries and charge accumulation, obtained using the hybrid functional, are in line with those

obtained using GGA.[10] In the subsequent sections, we will demonstrate that this is not necessarily the case for any substrate.

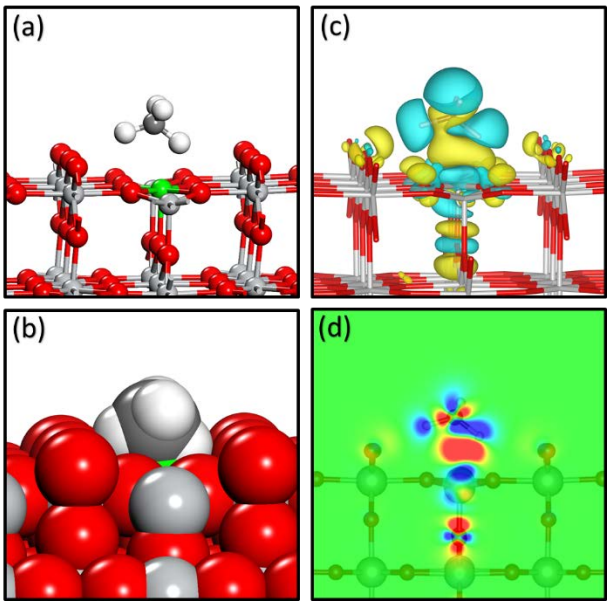

Figure 6.2.2 (a) Ball-and-stick and (b) CPK model adsorption geometries of CH_4 on Pt-TiO_2 (Pt = green, Ti = grey, O = red). (c) Isosurface plot of charge density difference from CH_4 adsorption and (d) 2D charge density difference plot along the H-C-H plane.

6.2.4.2 The methane adsorption conundrum – the failure of rutile Pt-IrO2

To move beyond the model case of rutile TiO_2, we study the impact of different substrates on the CH_4-Pt complexation starting with rutile IrO_2. The IrO_2 (110) surface has already been experimentally shown to adsorb methane, and here we verify these results with hybrid functional calculations showing an adsorption energy of -0.60 eV and similar adsorption geometries with Pt-TiO_2 (Figure 3a, b). One would expect then, that by replacing a surface Ir atom with Pt would result in similar if not stronger adsorption energies. Instead, methane was found to be non-interacting in its more stable adsorption

geometry with a C-Pt distance extending just beyond the vdW radius, with a length of 3.675 Å, and no corresponding lengthening of the C-H bonds can be observed (Figure 3c, d). A second adsorption geometry was observed with a C-Pt distance of 2.535 Å and a lengthened C-H bond length of 1.132 Å but a slightly positive adsorption energy of 0.07 eV . While this adsorption mode is a local minimum due to the complexation with the Pt; however, the CH_4-Pt interaction has been weakened to the extent where the energy is positive relative to the gas phase (i.e. the repulsive energy from steric interaction is greater than attraction from C-H donation).

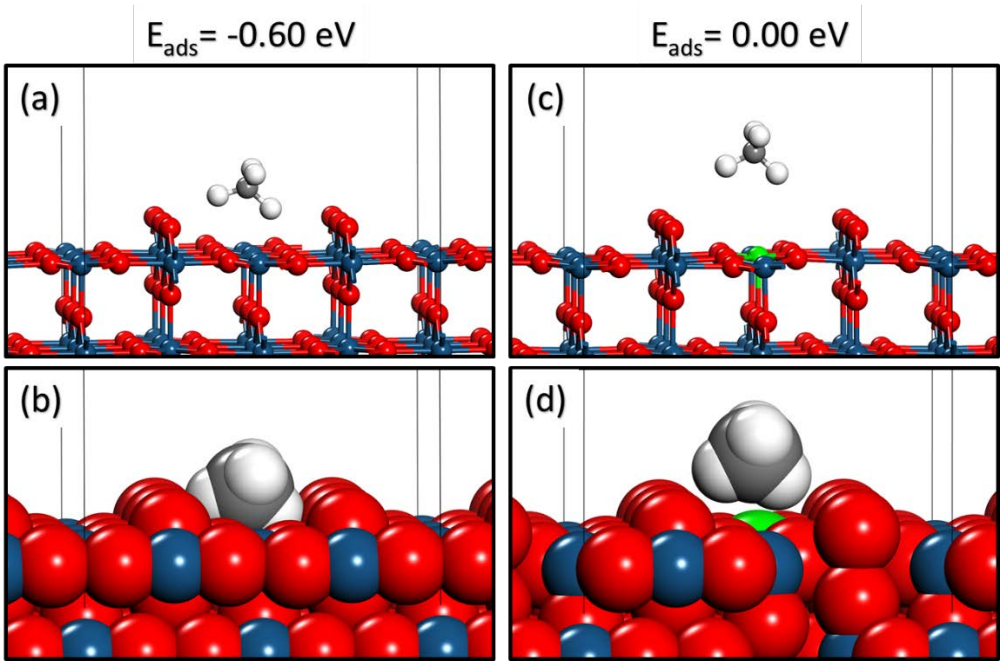

Figure 6.2.3 Adsorption energies and geometries of CH_4 on IrO_2, and Pt-IrO_2 (Pt = green, Ir = blue, O = red)

Within the model for methane complexation outlined previously (Figure 1), the reason for positive adsorption energy can be traced to a change or occupation of the dz2 orbital previously identified as responsible for bonding with CH_4. A naive hypothesis may suggest the oxidation state of Pt in IrO_2 may be different from that in TiO_2. Specifically, the Pt in Pt-IrO_2 may be in a 3+ or 2+ oxidation state in contrast with the 4+ state in Pt-TiO_2, leading to a one or two electron occupancy in the dz2 orbital. While assigning oxidation states remains an ongoing chemical challenge,[19] there are many reasons which suggest Pt is not in the 3+ or 2+ state. First, the magnetic moment of Pt was found to be 0.560 μB, which can neither be attributed to being 3+ or 2+. This result is also contrary to the case of Au^{4+} in Au-TiO_2 which is isoelectronic to Pt^{3+} (d=7 electrons), but was found to have a moment close to 1 μB from the previous study.[10] Second, the methane complex, with positive adsorption energies for Pt-IrO_2 was not observed in Au-TiO_2, demonstrating that the Pt in Pt-IrO_2 does not behave like a 7 electron system for methane interaction. Finally, $Pt^{3+}$is an uncommon oxidation state compared to Pt^{4+}, and it is furthermore unusual to expect the single atom to be reduced in the stochiometric rutile slab in the absence of reduction via an oxygen vacancy or other means.

Instead, we must look to other means to explain the positive methane complex formation energies, namely by the changes to the dz2 orbital in the electronic density of states (Figure 4). Returning once more to the model case of Pt-TiO_2, the empty Pt dz2 states above the Fermi level can be clearly visualized in the projected density of states plot (Figure 4a) which inhabit the region between the valence and conduction band of the

substrate, TiO_2. Similarly, in IrO_2 (Figure 4b), the dz2 states are also found above the fermi level, albeit in a less localized fashion – this may also explain why Pt-TiO_2 exhibits stronger methane chemisorption than IrO_2. In contrast, for Pt-IrO_2 (Figure 4c), the dz2 states appear disrupted, with many states being pushed below the Fermi level. Here we hypothesize this is due to the dz2 states of Pt occupying the same region as the conduction band of the substrate, IrO_2, leading to overlap or hybridization of the dz2 states and the formation of new hybrid states below the Fermi level. As the surface Ir-Pt distance is found to be just slightly beyond usual bonding distances at approximately 3.18 Å, interaction should be expected to occur.

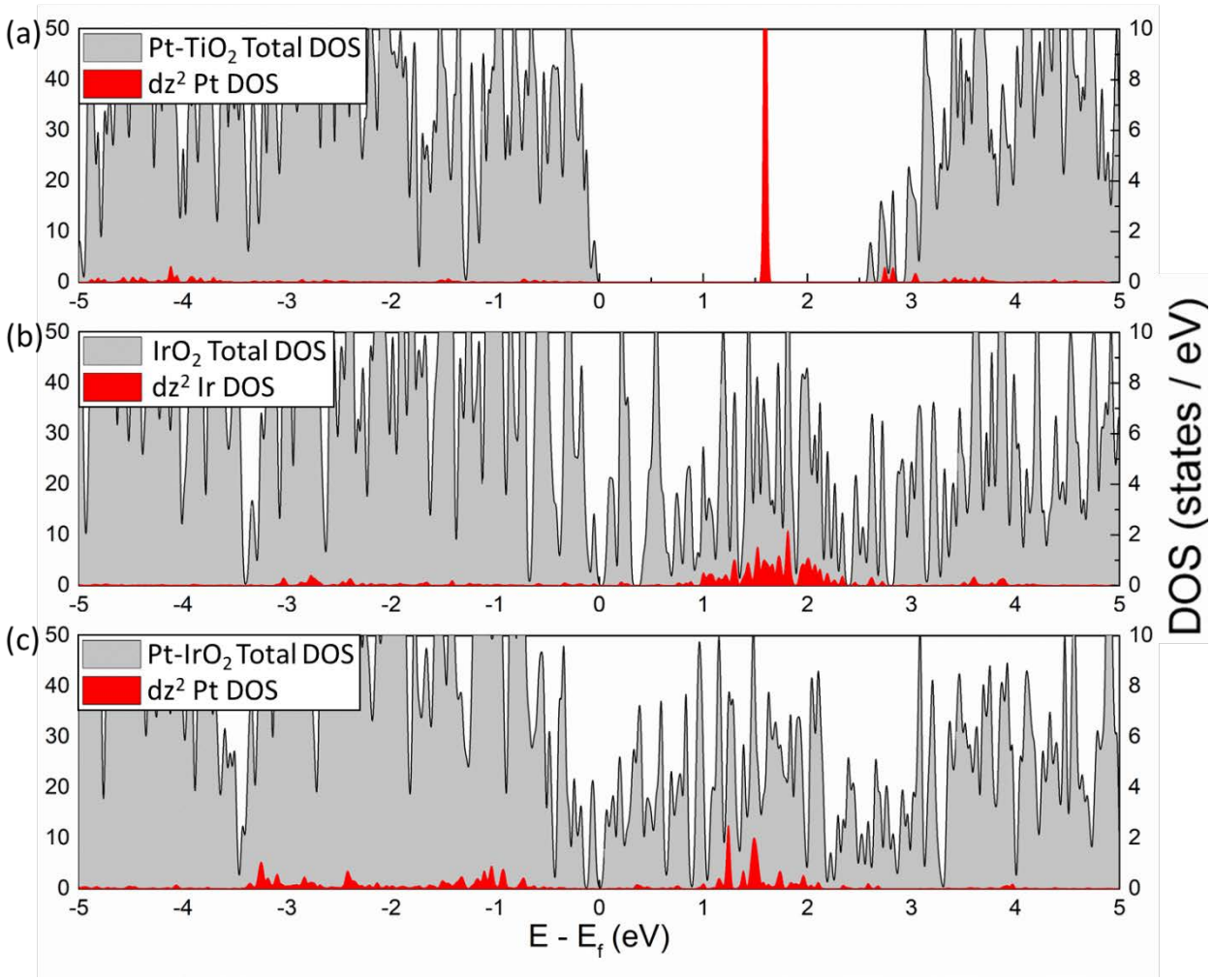

Figure 6.2.4 Density of states plots for (a) Pt-TiO_2, (b) IrO_2, and (c) Pt-IrO_2, showing the total DOS (left Y-axis) with the projected dz^2 DOS (right Y-axis) overlaid in red.

6.2.4.3 Adsorption on different rutile substrates

Table 6.2.1: Adsorption energy, substrate band gap, Pt magnetic moment and Pt Bader charge of single atom Pt on studied substrate rutile oxides

Substrate	E_{ads} (eV)	Band Gap (eV)	Pt Magnetic Moment (μB)	Bader Charge (e)
Pt-TiO_2	-0.75	2.8	0.000	1.59
Pt-VO_2	-0.36	1	0.036	1.55
Pt-CrO_2	-0.44	Half-metal	0.134	1.63
Pt-MnO_2	-0.30	0.1	0.021	1.63
Pt-RuO_2	-0.04	Metallic	0.503	1.42
Pt-OsO_2	-0.09	Metallic	0.582	1.36
Pt-IrO_2	0.00	Metallic	0.560	1.36
Pt-ZrO_2	-0.84	4.6	0.000	1.30
Pt-SiO_2	-1.00	6.8	0.000	1.66
Pt-GeO_2	-0.80	2.7	0.000	1.61
Pt-SnO_2	-0.68	2.1	0.000	1.59
Pt-PbO_2	-0.52	0.1	0.001	1.63

To verify this hypothesis as well as screen for additional suitable substrates for methane complexation, we extend our study to a wider range of rutile oxides (Table 1). These include Ti, V, Cr, Mn, Ru, Os, Ir, Ge, Sn, and Pb, which form stable rutile

oxides,[20] as well as Si which forms under high pressures, and a theoretical Zr rutile phase. From these oxides, roughly half are metallic while the remainder span from semimetals to insulators, which provides a suitable range of substrate environments to test CH_4-Pt complexation. Precisely as our hypothesis predicts, substrates with a metallic band gap disrupt CH_4-Pt complexation leading to more positive adsorption energies (Ru, Os, Ir). Meanwhile, substrates with the widest band gaps have the strongest methane adsorption energies (Ti, Zr, Si, Ge) and those with intermediate gaps fall somewhere in the middle (V, Mn, Sn, Pb). Cr being a unique and well-known half-metal, allows for moderate CH_4-Pt adsorption energy despite overlap with the dz2 states in one spin direction (Supplementary Figure 2). This clear correlation between band gap and CH_4-Pt adsorption energy once again strongly suggests the overlap between dz2 states and the conduction band as the prime culprit for disrupted interaction. Charge transfer, on the other hand, is insufficient to fully describe the extent of hybridization of the dz2 states, as Pt Bader charges are roughly similar across different substrates, nor does a less positive charge necessarily result in occupied dz2 states, such as ZrO_2.

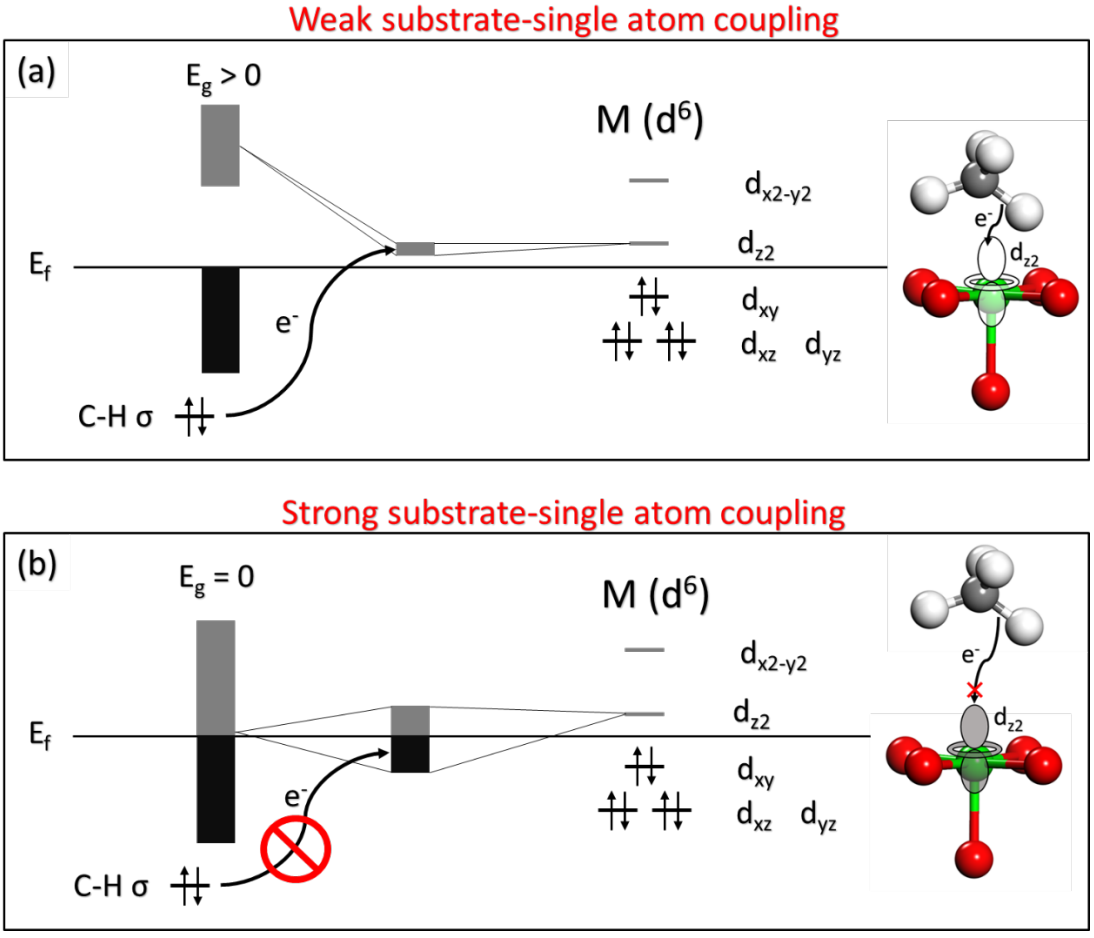

Figure 6.2.5 Model illustrating the interaction of (a) the non-zero gap oxide substrate and the (b) metallic oxide substrate d states above the Fermi level with the metal single atom d orbitals.

Therefore, the described interaction can be best explained by the model in Figure 5, which illustrates the difference between substrates with large band gaps with metallic ones. In the situation where the substrate band gap is sufficiently large (Figure 5a), the d orbitals of the metal single atom lie between the valence and conduction bands, and the coupling between the substrate metal d states in the conduction band with the single atom d orbitals is weak. Consequently, the dz2 orbital remains localized above the Fermi level,

allowing it to accept electrons from the C-H bond (as seen in Pt-TiO_2 in Figure 4a). On the other hand, when the substrate is metallic, the single atom d orbitals lie in the same energetic region as the substrate d states, which leads to a greater coupling or hybridization and a delocalization of dz2 orbital. This delocalization leads to dz2 states below the Fermi level which are subsequently occupied by the substrate electrons and hinders the interaction with the C-H bond (as seen in Pt-IrO_2 in Figure 4c).

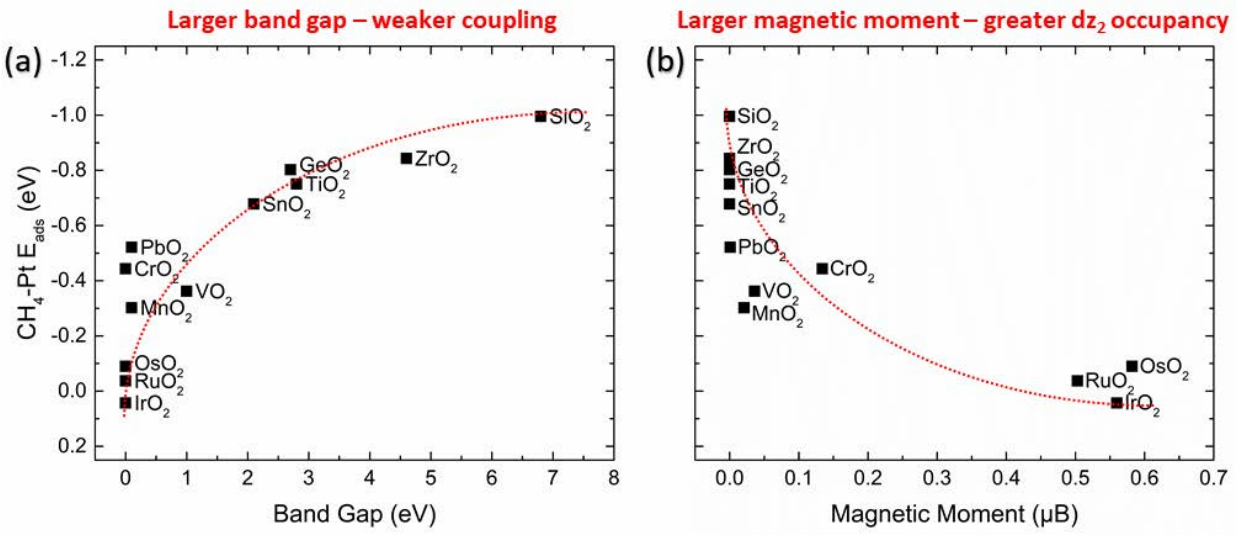

Figure 6.2.6 Plot of CH_4-Pt adsorption energy versus (a) the band gap of the substrate oxide and (b) the magnetic moment of the embedded Pt single atom.

To quantitatively illustrate the aforementioned model for the studied substrates in this work, we plot the CH_4-Pt adsorption energy versus the band gap of the substrate oxide and the magnetic moment of the embedded Pt single atom (Figure 6). First, a general trend can be observed for all studied substrates whereby a larger band gap leads to stronger CH_4-Pt adsorption while at zero band gap, denoting metallic systems, CH_4-Pt

adsorption can be observed to approach zero. This trend is the natural result of a larger band gap leading to a poorer energetic overlap between the conduction band and the d orbitals in the single atom. Second, dz2-conduction band coupling leads to hybridization and formation of new states below the Fermi level which become partially occupied, resulting in a nonzero magnetic moment on Pt single atom. The substrates with zero or close-to-zero moments have the strongest CH_4-Pt adsorption which decreases dramatically with even a small partial occupancy or moment in the Pt dz2 orbital. As the dative interaction between CH_4 and Pt is a two electron-two orbital process, any partial occupancy leads to strong electronic repulsion. Therefore, both band gap and Pt magnetic moment can be viewed as important descriptors for CH_4-Pt adsorption strength.

6.2.5 Discussion

Recent theoretical studies have speculated the chemical properties of a single atom on a substrate can be determined primarily by the local properties of the SA and the neighboring coordinating atoms.[21] By using these local properties such as the atom electronegativity, coordination number, and other parameters, predictions can be made on the basis of linear relationships[21-23] or via more complex machine-learned regression models.[24-26] However, the role of the substrate on the SA properties, beyond those deriving from the geometry and local properties of the SA adsorption site, is often overlooked. From the theoretical standpoint, methane complexation presents a useful probe process due to its extreme sensitivity towards the electronic properties of the

complexation site. From this study we therefore reveal a third requirement for CH_4-Pt adsorption, beyond the metal-oxygen geometry and d-electron count: the interaction between empty metal dz2 states and the conduction band should be avoided, primarily through substrates with sufficiently wide band gaps. We expect this substrate requirement to also play a role in the adsorption of other molecular species other than methane. A unique avenue for modulating the electronic or chemical properties of the single atom may also arise via the intrinsic or extrinsic tuning of the substrate band gap, with significant implications for designing more active single atom catalysts.

Another aspect to note is the importance of the computational method, in particular the DFT functional, in obtaining accurate predictions for methane chemisorption due to the routine underestimation of band gaps by GGA functionals. While GGA functionals such as PBE is sufficient for cases where the gap is sufficiently wide such that the conduction band rises far beyond the Pt atom dz2 states, such as TiO_2,[10] it must be used with caution for the strongly-correlated oxides VO_2, CrO_2, MnO_2 for which PBE fails. Furthermore, the failure of PBE for adsorption energies also extends to geometries, as the methane complexing adsorption mode (Figure 1) is no longer accessible in many cases, hence the need to perform both relaxations and energy calculations at the hybrid DFT level.

6.2.6 Conclusions

In this work, we use hybrid density functional theory calculations to explore the recently discovered Pt-CH_4 strong complexation on rutile oxides. While Pt-TiO_2 is shown

to be a strong methane complexing surface consistent with previous PBE results, Pt-IrO_2 exhibits positive adsorption energies despite IrO_2 being able to strongly chemisorb methane. We attribute this paradoxical behavior as being linked to the band gaps of the substrates rather than through simple oxidation state change or through charge transfer processes on the single atom. We hypothesized the overlap between Pt dz2 states and the substrate conduction band leads to coupling or hybridization, disrupting the states for interaction with the methane orbitals, which is clearly visible in the calculated density of states. A screening of a total of twelve rutile oxides spanning from metallic to insulating confirms this hypothesis by showing positive adsorption for the metallic substrates and exhibiting similarly disrupted dz2 states. Furthermore, we demonstrate our dz2-conduction overlap model is valid regardless of the method or functional used and highlight the need for a functional which can accurately predict band gaps for correct predictions of methane complexation. For edge-cases of substrates with small gaps, or for strongly-correlated oxides, regular GGA functionals such as PBE is shown to give disparate geometries and energies from the HSE06 results. For the first time in the literature, global electronic properties of the substrate are shown to play a major role in single atom properties beyond those obtained from just the local coordination, electronegativity or charge. These effects are quantum-mechanical in nature, as we have shown from the coupling and hybridization of the single atom-substrate electronic states, and are sensitive to proper treatment of the electron exchange and correlation energies

References

(1) Horn, R.; Schlögl, R. Methane Activation By Heterogeneous Catalysis. *Catal. Lett.* **2015,** *145*, 23-39.

(2) Ravi, M.; Ranocchiari, M.; van Bokhoven, J. A. The Direct Catalytic Oxidation of Methane to Methanol—A Critical Assessment. *Angew. Chem. Int. Ed.* **2017,** *56*, 16464-16483.

(3) Schwach, P.; Pan, X.; Bao, X. Direct Conversion of Methane to Value-Added Chemicals over Heterogeneous Catalysts: Challenges and Prospects. *Chem. Rev.* **2017,** *117*, 8497-8520.

(4) Latimer, A. A.; Kulkarni, A. R.; Aljama, H.; Montoya, J. H.; Yoo, J. S.; Tsai, C.; Abild-Pedersen, F.; Studt, F.; Nørskov, J. K. Understanding Trends in CH Bond Activation in Heterogeneous Catalysis. *Nature Mater.* **2017,** *16*, 225-229.

(5) Saillard, J. Y.; Hoffmann, R. Carbon-Hydrogen and Hydrogen-Hydrogen Activation in Transition Metal Complexes and on Surfaces. *J. Am. Chem. Soc.* **1984,** *106*, 2006-2026.

(6) Weaver, J. F. Surface Chemistry Of Late Transition Metal Oxides. *Chem. Rev.* **2013,** *113*, 4164-4215.

(7) Weaver, J. F.; Hakanoglu, C.; Hawkins, J. M.; Asthagiri, A. Molecular Adsorption of Small Alkanes on a PdO(101) Thin Film: Evidence of Sigma-Complex Formation. *J. Chem. Phys.* **2010,** *132*, 024709.

(8) Wang, C.-C.; Siao, S. S.; Jiang, J.-C. C–H Bond Activation of Methane via σ–d Interaction on the IrO_2 (110) Surface: Density Functional Theory Study. *J. Phys. Chem. C* **2012,** *116*, 6367-6370.

(9) Liang, Z.; Li, T.; Kim, M.; Asthagiri, A.; Weaver, J. F. Low-Temperature Activation of Methane on the IrO_2 (110) Surface. *Science* **2017,** *356*, 299-303.

(10) Fung, V.; Tao, F.; Jiang, D.-e. Low-Temperature Activation of Methane on Doped Single Atoms: Descriptor and Prediction. *Phys. Chem. Chem. Phys.* **2018,** *20*, 22909-22914.

(11) Tsuji, Y.; Yoshizawa, K. Adsorption and Activation of Methane on the (110) Surface of Rutile-type Metal Dioxides. *J. Phys. Chem. C* **2018,** *122*, 15359-15381.

(12) Kresse, G.; Furthmuller, J. Efficiency of Ab-Initio Total Energy Calculations for Metals and Semiconductors Using a Plane-Wave Basis Set. *Comput. Mater. Sci.* **1996,** *6*, 15-50.

(13) Kresse, G.; Furthmuller, J. Efficient Iterative Schemes for Ab Initio Total-Energy Calculations Using a Plane-Wave Basis Set. *Phys. Rev. B* **1996,** *54*, 11169-11186.

(14) Krukau, A. V.; Vydrov, O. A.; Izmaylov, A. F.; Scuseria, G. E. Influence of the Exchange Screening Parameter on the Performance of Screened Hybrid Functionals. *J. Chem. Phys.* **2006,** *125*, 224106.

(15) Perdew, J. P.; Burke, K.; Ernzerhof, M. Generalized Gradient Approximation Made Simple. *Phys. Rev. Lett.* **1996,** *77*, 3865-3868.

(16) Blöchl, P. E. Projector Augmented-Wave Method. *Phys. Rev. B* **1994,** *50*, 17953-17979.

(17) Monkhorst, H. J.; Pack, J. D. Special Points for Brillouin-Zone Integrations. *Phys. Rev. B* **1976,** *13*, 5188-5192.

(18) Momma, K.; Izumi, F. VESTA 3 for Three-Dimensional Visualization of Crystal, Volumetric and Morphology Data. *J. Appl. Crystallogr.* **2011,** *44*, 1272-1276.

(19) Walsh, A.; Sokol, A. A.; Buckeridge, J.; Scanlon, D. O.; Catlow, C. R. A. Oxidation states and ionicity. *Nature Mater.* **2018,** *17*, 958-964.

(20) Hiroi, Z. Structural Instability of the Rutile Compounds and its Relevance to the Metal–insulator Transition of VO_2. *Prog. Solid State Chem.* **2015,** *43*, 47-69.

(21) Xu, H.; Cheng, D.; Cao, D.; Zeng, X. C. A Universal Principle for a Rational Design of Single-atom Electrocatalysts. *Nat. Catal.* **2018,** *1*, 339-348.

(22) Fung, V.; Tao, F. F.; Jiang, D. E. General Structure-Reactivity Relationship for Oxygen on Transition-Metal Oxides. *J. Phys. Chem. Lett.* **2017,** *8*, 2206-2211.

(23) Calle-Vallejo, F.; Loffreda, D.; Koper, M. T.; Sautet, P. Introducing Structural Sensitivity Into Adsorption-Energy Scaling Relations by Means of Coordination Numbers. *Nat. Chem.* **2015,** *7*, 403-410.

(24) Li, Z.; Ma, X.; Xin, H. Feature Engineering of Machine-Learning Chemisorption Models for Catalyst Design. *Catal. Today* **2017,** *280*, 232-238.

(25) Nandy, A.; Duan, C.; Janet, J. P.; Gugler, S.; Kulik, H. J. Strategies and Software for Machine Learning Accelerated Discovery in Transition Metal Chemistry. *Ind. Eng. Chem. Res.* **2018,** *57*, 13973-13986.

(26) Janet, J. P.; Chan, L.; Kulik, H. J. Accelerating Chemical Discovery with Machine Learning: Simulated Evolution of Spin Crossover Complexes with an Artificial Neural Network. *J. Phys. Chem. Lett.* **2018,** *9*, 1064-1071.

7 Conclusions and outlook

7.1 Summary

We used first principles density functional theory to study alkane activation and conversion and approached this problem in several stages. We first began our study on the most active conventional system for alkane catalysis, metal oxides. In particular, we studied the complete ethane dehydrogenation pathway on the experimentally observed (111) surface of spinel Co_3O_4.[1] In agreement with the literature for propane dehydrogenation on Co_3O_4 (111),[2] the first C-H bond was favorably activated via a homolytic pathway by the lattice oxygen. This is followed by a second C-H activation and facile desorption of ethylene. The remaining hydroxyls can diffuse on the surface to cluster and form water, leaving a vacancy, which is refilled by molecular oxygen. The high activity of Co_3O_4 for ethane dehydrogenation could be traced to the low first C-H activation energy (0.62 eV), though we observed the water formation barrier was non-trivial to overcome in the overall reaction cycle. Comparing these results with ethane dehydrogenation on the less-stable (311) facet, we find even lower C-H activation barriers (0.40 eV) consistent with experimental observations of higher oxygen activity and methane oxidation ability of the (311) facet.[3] However, selectivity to ethylene on (311) is poorer in large part due to ethane dehydrogenating to form a deprotonated ethylene glycol intermediate on the surface instead of desorbing as ethylene, which is subsequently further oxidized to form CO_2. The importance of the first C-H activation energy and the oxygen activity were recognized as key catalytic descriptors for alkane

conversion in these two studies. Motivated by this insight, as well as a collaborative work on Si doping of Co_3O_4,[4] we turn to a systematic study of tuning the oxygen reactivity (and by extension the C-H activation activity) on Co_3O_4 by substitutionally doping the neighboring Co atoms with other elements.[5] We furthermore compare the differences in the effect of the dopant on replacing Co^{2+} ions on the (111) surface and Co^{3+} ions on the (311) surface. Consistent with our hypothesis, substitutional doping can tune the C-H activation barriers on the nearest neighbor oxygen sites with a direct correlation to its vacancy formation energy and hydrogen adsorption energies.

Out of these studies, we also observed a correlation between oxygen activity and C-H activation barriers contemporaneous with other works on C-H activation descriptors in the literarure.[6-7] We then sought to elucidate a link between oxygen activity and its more fundamental properties such as coordination and charge. In our subsequent study, we developed a descriptor containing the coordination number of the oxygen and its neighboring metal to predict both the local charge on the oxygen. From this property, we are able to predict the oxygen reducibility from vacancy formation and hydrogen adsorption energies, and finally correlate to C-H activation barriers with low error bars.[8] Though coordination number descriptors have been proposed in the past for metals,[9-10] this represents the first study to successfully correlate coordination in a metal oxide with reaction barriers. For comparing materials with different compositions (where coordination itself is not sufficient), we turn to electronic and energetic descriptors. We use hydrogen adsorption energy as a descriptor for methane oxidative coupling on different perovskite compositions.[11] As we expected, hydrogen adsorption energy is a

viable descriptor for C-H activation on perovskites, but it is also further capable of predicting methyl adsorption energy. Via the Lunsford mechanism for oxidative coupling,[12] ethylene is produced from gas phase methyl radicals; therefore we can identify active perovskite catalysts with low C-H activation barriers and methyl desorption barriers via a single descriptor of hydrogen adsorption. Finally, we try to elucidate the underlying electronic mechanism governing the adsorption strength of hydrogen and other radicals on the surface. Through a thorough analysis of the electronic structure and Crystal Orbital Hamilton Populations of perovskite surfaces before and after radical adsorption, we are able to demonstrate that adsorption leads to reduction of the oxide surface and occupation of M-O antibonding orbitals.[13] The stronger the M-O bond, the lower the adsorption energy due to the greater destabilizing effect of M-O antibonding occupancy. These descriptor-based studies provide powerful tools for the screening of metal oxide for alkane conversion based on easily and affordably obtained information such as coordination number, electronic structure and adsorption energy.

Additionally, to tackle to problem of alkane activation on sub-nanometer metal clusters, we first recognize the importance of accurately obtaining the cluster structure and local coordination information. We use basin-hopping global optimization to sample the potential energy surface and obtain low-energy structures of $Pt_{10\text{-}13}$ clusters.[14] From a sampling of 20000 locally-optimized structures, we compare the structural diversity between cluster sizes through a number of features including coordination number, interatomic distances and shape. We find Pt_{10} is unique in its cohort due to low structural diversity near the global minima as a possible ‘magic’ cluster compared to the more

fluxional $Pt_{11, 12, 13}$. In the low-energy region, the average coordination number of Pt_{10} is localized around 5.6-5.8, whereas for $Pt_{11, 12, 13}$ the range is expanded down to ~4.8. The presence of greater undercoordinated sites on $Pt_{11, 12, 13}$ suggests a greater catalytic activity. Therefore, we can explain the higher methane combustion ability of $Pt_{11, 12, 13}$ compared to Pt_{10}.[15-16]

In metal single atom systems, we explored heterolytic pathways for alkane activation. On rhodium single atom sites in ZSM-5, we find methane can be activated heterolytically over Rh-O_5 and Rh-O_4 sites. Further calculations find subsequent coupling of methyl and hydroxyl with carbon monoxide can occur to yield acetic acid in this catalyst.[17] Under certain, rare, conditions the heterolytic activation of methane was found to be complex-mediated, which can allow for methane activation at cryogenic temperatures.[18] Motivated by the experimental confirmation of this phenomenon on rutile IrO_2, we conducted a systematic study of metal doped rutile oxides to elucidate the underlying electronic properties which govern strong methane complexation and identify promising catalysts with similar or even better performance than IrO_2. In the first part of the work on a model TiO_2 substrate, we find Pd, Rh, Os, Ir, and Pt single atoms can activate methane at similar or lower temperatures than IrO_2. We further identify the interaction between methane and the d_{z2} orbitals of the single atom as key to chemisorption, which we show can be easily predicted from our d orbital occupation descriptor in a square pyramidal crystal field.[19] In the second part, by varying the composition of the substrate, we find a strong correlation between the substrate electronic properties and the methane complexation on the single atom.

7.2 Future directions

Gathering from our studies so far on alkane catalysis, we have obtained valuable insights on alkane activation and mechanistic pathways for their conversion to various industrially valuable products. Furthermore, we been successful in developing descriptors to quickly screen and predict materials with high alkane activation efficacy. For example, hydrogen adsorption energy and vacancy formation energy can be used to quickly predict C-H activation barriers on a variety of systems, including metal oxide surfaces on diverse terminations and metal doped oxides. From d-orbital occupancy, the elusive methane complexation property can be deduced on doped and bulk oxide surfaces.

However, there is nevertheless significant room for further development of computational studies in this area. First, the methodology used can be improved beyond conventional density functional theory and GGA functionals. Future studies with a greater focus on hybrid DFT, or even a number of beyond-DFT techniques such as the random-phase approximation (RPA) may be desired or even necessary for an accurate calculation of catalytically important properties such as vacancy formation energy. Second, to provide an even greater scope and impact of the descriptor approach, it is desirable to expand the calculations to the high-throughput level on larger databases of possible materials. In this aspect, more computationally efficient descriptors, such as those based on bulk or other fundamental properties may be crucial. Finally, it would be prudent to utilize the significant technological advances within the machine learning field in recent years to apply to the screening and prediction of better alkane conversion catalysts. While possible avenues for applying machine learning to catalysis are

numerous, with many appearances in the topical literature, more chemically-motivated approaches may yet offer significant advantages.

Utilizing these suggested improvements coupled with validation and corroboration to experimental results, the high throughput screening of complex materials can be within grasp. Which such efforts are now commonplace for catalysis on metal surfaces, significant technical challenges still prevent such an application to materials such as metal oxides or other metal compounds in general. Unlocking this barrier to these systems can significantly broaden our search space and lead to much higher functionality.

References

(1) Fung, V.; Tao, F.; Jiang, D. E. Understanding oxidative dehydrogenation of ethane on Co3O4 nanorods from density functional theory. *Catal. Sci. Technol.* **2016,** *6*, 6861-6869.

(2) Tyo, E. C.; Yin, C.; Di Vece, M.; Qian, Q.; Kwon, G.; Lee, S.; Lee, B.; DeBartolo, J. E.; Seifert, S.; Winans, R. E.; Si, R.; Ricks, B.; Goergen, S.; Rutter, M.; Zugic, B.; Flytzani-Stephanopoulos, M.; Wang, Z. W.; Palmer, R. E.; Neurock, M.; Vajda, S. Oxidative dehydrogenation of cyclohexane on cobalt oxide (Co_3O_4) nanoparticles: The effect of particle size on activity and selectivity. *ACS Catal.* **2012,** *2*, 2409-2423.

(3) Liu, J.; Fung, V.; Wang, Y.; Du, K.; Zhang, S.; Nguyen, L.; Tang, Y.; Fan, J.; Jiang, D.-e.; Tao, F. F. Promotion of catalytic selectivity on transition metal oxide through restructuring surface lattice. *Appl. Catal., B* **2018,** *237*, 957-969.

(4) Liu, J.; Zhang, S.; Zhou, Y.; Fung, V.; Nguyen, L.; Jiang, D.-e.; Shen, W.; Fan, J.; Tao, F. F. Tuning Catalytic Selectivity of Oxidative Catalysis through Deposition of Nonmetallic Atoms in Surface Lattice of Metal Oxide. *ACS Catal.* **2016,** *6*, 4218-4228.

(5) Fung, V.; Tao, F. F.; Jiang, D.-e. Trends of Alkane Activation on Doped Cobalt (II, III) Oxide from First Principles. *ChemCatChem* **2018,** *10*, 244-249.

(6) Kumar, G.; Lau, S. L. J.; Krcha, M. D.; Janik, M. J. Correlation of Methane Activation and Oxide Catalyst Reducibility and its Implications for Oxidative Coupling. *ACS Catal.* **2016,** *6*, 1812-1821.

(7) Latimer, A. A.; Kulkarni, A. R.; Aljama, H.; Montoya, J. H.; Yoo, J. S.; Tsai, C.; Abild-Pedersen, F.; Studt, F.; Nørskov, J. K. Understanding Trends in CH Bond Activation in Heterogeneous Catalysis. *Nature Mater.* **2017,** *16*, 225-229.

(8) Fung, V.; Tao, F. F.; Jiang, D. E. General Structure-Reactivity Relationship for Oxygen on Transition-Metal Oxides. *J. Phys. Chem. Lett.* **2017,** *8*, 2206-2211.

(9) Calle-Vallejo, F.; Martínez, J. I.; García-Lastra, J. M.; Sautet, P.; Loffreda, D. Fast Prediction of Adsorption Properties for Platinum Nanocatalysts with Generalized Coordination Numbers. *Angew. Chem. Int. Ed.* **2014,** *53*, 8316-8319.

(10) Ma, X.; Xin, H. Orbitalwise Coordination Number for Predicting Adsorption Properties of Metal Nanocatalysts. *Phys. Rev. Lett.* **2017,** *118*, 036101.

(11) Fung, V.; Polo-Garzon, F.; Wu, Z.; Jiang, D.-e. Exploring Perovskites for Methane Activation from First Principles. *Catal. Sci. Technol.* **2018,** *8*, 702-709.

(12) Lunsford, J. H. The Catalytic Oxidative Coupling of Methane. *Angew. Chem. Int. Ed.* **1995,** *34*, 970-980.

(13) Fung, V.; Wu, Z.; Jiang, D.-e. New Bonding Model of Radical Adsorbate on Lattice Oxygen of Perovskites. *J. Phys. Chem. Lett.* **2018,** *9*, 6321-6325.

(14) Fung, V.; Jiang, D.-e. Exploring Structural Diversity and Fluxionality of Ptn (n = 10–13) Clusters from First-Principles. *J. Phys. Chem. C* **2017,** *121*, 10796-10802.

(15) Trevor, D.; Cox, D.; Kaldor, A. Methane activation on unsupported platinum clusters. *J. Am. Chem. Soc.* **1990,** *112*, 3742-3749.

(16) Adlhart, C.; Uggerud, E. Reactions of platinum clusters Pt_n^+, n= 1–21, with CH_4: to react or not to react. *Chem. Commun.* **2006**, 2581-2582.

(17) Tang, Y.; Li, Y.; Fung, V.; Jiang, D.-e.; Huang, W.; Zhang, S.; Iwasawa, Y.; Sakata, T.; Nguyen, L.; Zhang, X.; Frenkel, A. I.; Tao, F. Single rhodium atoms anchored in micropores for efficient transformation of methane under mild conditions. *Nature Commun.* **2018,** *9*, 1231.

(18) Liang, Z.; Li, T.; Kim, M.; Asthagiri, A.; Weaver, J. F. Low-Temperature Activation of Methane on the IrO_2 (110) Surface. *Science* **2017,** *356*, 299-303.

(19) Fung, V.; Tao, F.; Jiang, D.-e. Low-Temperature Activation of Methane on Doped Single Atoms: Descriptor and Prediction. *Phys. Chem. Chem. Phys.* **2018,** *20*, 22909-22914.